

Synchrotron radiation studies of multicomponent metal oxides

Vladimir Martis

University College London

Department of Chemistry

Dutch-Belgium Beamline

(ESRF)

Thesis submitted for the degree of Doctor in Engineering

April 2012

Declaration

I, Vladimir Martis, confirm that the work presented in this thesis is my own except where indicated. Where information has been derived from other sources, I confirm that this has been indicated in the thesis.

Signed: _____

Abstract

The work described in this thesis is focused on the development of characterization methods for determining the structure of multicomponent metal oxides using synchrotron radiation techniques, in particular, X-ray Absorption Fine Structure (XAFS) and Energy Resolved Electron Yield X-ray Absorption Spectroscopy (EREY-XAS).

XAFS is a superior technique for determining the local structure of, for example, transition metals that are used as dopants in very low concentrations. It also provides information on early stages of crystallization processes before a material develops sufficient long range order.

Energy resolved XAS was developed as an alternative to conventional transmission and fluorescence techniques which probe mainly the bulk of materials. This techniques yield information about the local structure from the near surface region of materials. The other complementary techniques used for characterization of materials were XRD, Raman spectroscopy, X-ray Photoelectron Spectroscopy (XPS) and Scanning Electron Microscopy (SEM).

New insights about formation of Bi_2MoO_6 crystallites from an amorphous gel below 200°C were obtained with a novel in situ setup, in which XAFS and XRD was combined with RAMAN spectroscopy in a single experiment. Combined XRD/XAFS technique was used for determining the growth mechanism of Bi_2MoO_6 formed under hydrothermal conditions from an amorphous gel. The reaction kinetics was quantified by using the Avrami-Erofe'ev formalism.

The surface sensitive of EREY-XAS was performed on several materials in particular chromium doped Fe_2O_3 catalysts and cobalt substituted aluminophosphates such as CoAlPO-18 and CoAlPO-34. The sensitivity of technique was assessed by comparison with conventional XAS techniques and XPS.

Finally, the interactions of a synchrotron X-ray beam with a sample were studied. In particular, the effects of exposure to a monochromatic 10 keV X-ray beam on thermally induced crystallization of lithium disilicate glass were investigated.

Table of Contents

Synchrotron radiation studies of multicomponent metal oxides	1
Abstract	3
List of figures	7
List of Tables	17
List of Equations	18
Acknowledgments	19
List of publications	21
Chapter 1 Introduction	22
1.1 Introduction	22
1.1.1 Preparation of catalysts	27
1.1.2 Properties and characteristic of catalysts	28
1.1.3 Characterization of catalysts	30
Chapter 2 Experimental part	35
2.1 Chapter Overview	35
2.2 Origin of X-Rays	36
2.3 X-Ray Diffraction	37
2.4 Synchrotron radiation	38
2.5 Dutch–Belgium beamline at the ESRF	41
2.6 X-ray Absorption Fine Structure	44
2.6.1 XANES	52
2.6.2 EXAFS	53
2.6.3 EXAFS equation	54
2.7 Total Electron Yield X-ray Absorption Spectroscopy	59
2.8 Energy Resolved Electron Yield X-ray Absorption Spectroscopy	62
2.8.1 Description of electron yield detector vessel accommodating the GM64	64
2.8.2 Calibration of the electron yield detector	65

2.8.3	Analysis of energy-resolved XAS data.....	66
2.9	Other techniques	68
2.9.1	Raman spectroscopy	68
2.9.2	Scanning Electron Microscopy	69
2.9.3	X-ray photoelectron spectroscopy	69
Chapter 3	Combined XANES/XRD/RAMAN and EXAFS/XRD studies on Bi ₂ MoO ₆ formation	73
3.1	Chapter Overview	73
3.2	Introduction	74
3.3	Aims of the work	79
3.4	Experimental part	81
1.1.1	Hydrothermal synthesis of γ -Bi ₂ MoO ₆	81
3.4.1	XRD and SEM characterization	82
3.4.2	Combined HRPD/Raman/XAS	82
3.4.3	Combined EXAFS/XRD.....	84
3.4.4	XAFS data analysis.....	84
3.5	Results and discussion	85
3.5.1	Synthesis and XRD characterization	85
3.5.2	Combined HRPD/Raman/XAS	86
3.5.3	Combined EXAFS/XRD.....	99
3.5.4	EXAFS.....	103
3.5.5	Kinetic analyses.....	109
3.6	Conclusion.....	115
Chapter 4	Characterisation of Chromium doped Fe ₂ O ₃ Catalysts.....	120
4.1	Chapter Overview	120
4.2	Introduction	121
4.3	Aims of the work	122

4.4	Experimental part	122
4.4.1	Catalyst preparation	122
4.4.2	Catalyst characterization	123
4.4.3	XAFS data analysis.....	125
4.5	Results and discussion	126
4.6	Conclusion.....	145
Chapter 5	EREY–XAS and transmission XAS investigation of CoAlPOs	148
5.1	Chapter overview	148
5.2	Introduction	149
5.3	Aims of the work	153
5.4	Experimental part	154
5.4.1	Hydrothermal preparation of CoAlPO-18 and CoAlPO-34.....	154
5.4.1	XRD characterization	155
5.4.2	Transmission and Energy-Resolved Electron Yield XAS	155
5.4.3	XAFS data analysis.....	156
5.5	Results and discussion	157
5.6	Summary and Conclusion	169
Chapter 6	Effects of X-rays on crystal nucleation in Lithium disilicate	172
6.1	Chapter Overview	172
6.2	Introduction	173
6.3	Aims of the work	175
6.4	Experimental part	176
6.5	Results and discussion	178
6.6	Conclusion.....	190
Chapter 7	Conclusion and future work.....	194
Appendix A	High pressure gas rig.....	199

List of figures

Figure 1-1 Energy diagram illustrating the progress of a chemical reaction with and without a catalyst. The reaction without a catalyst requires a higher activation energy than does the catalysed reaction. There is no difference in free energy (ΔE) between catalysed and uncatalysed reactions ^[14]	25
Figure 2-1 The first ‘medical’ X-ray picture showing hand of Roentgen’ wife ^[2]	36
Figure 2-2 Production of synchrotron radiation at the ESRF. Electrons are produced and accelerated in a 200 MeV linear accelerator. Subsequently they are boosted in energy in the booster synchrotron to 6 GeV before injection in the main storage ring. .	39
Figure 2-3 Schematic lay-out of the optical system of BM26A ^[16] with a typical distances of optical elements from the radiation source. The monochromator is placed 28.5 m from the radiation source. The vertical focusing mirror is 31.5 m away from the source. The sample is positioned at 38 m from the radiation source.....	42
Figure 2-4 Schematic lay-out of the optical components in H-brunch, BM26B ^[21]	44
Figure 2-5 The photoelectric absorption process, whereby the core hole is created by the absorption of X-ray photon.....	45
Figure 2-6 A schematic illustration of an experimental setup for recording X-ray absorption in transmission or fluorescence mode using synchrotron X-ray beam. For further details the reader is referred to the text.....	47
Figure 2-7 Raw Cr K-edge XAS spectrum of $K_2Cr_2O_7$ recorded in transmission mode. The y-axis is related to absorption of X-rays by the sample and the x-axis is the energy of the incident X-ray photons.	48
Figure 2-8 Decay of the excited state in fluorescent X-ray emission. The probability of X-ray emission is directly proportional to absorption probability.....	49
Figure 2-9 Mo K-edge XAFS of a Mo foil recorded in transmission geometry.	50
Figure 2-10 Cr K-edge XANES spectra of $K_2Cr_2O_7$ in black and Cr_2O_3 in red representing Cr^{6+} and Cr^{3+} oxidations states respectively. The XANES spectrum of Cr_2O_3 shows a pre-edge doublet with very low intensity compared to $K_2Cr_2O_7$ which has an intense pre-edge peak. The latter is due to 1s–3d electronic transition. The pre-edge peak can be used as a signature identifying coordination geometry of chromium. The intense pre-edge peak in $K_2Cr_2O_7$ XANES indicates tetrahedral coordination of Cr^{6+} ions, while the pre-edge doublet in Cr_2O_3 suggests octahedrally coordinated Cr^{3+} ions.....	53

Figure 2-11 Schematic illustration of the photoelectrons (produced by photoelectric absorption), which are described as spherical waves propagating outward from the absorber atom (top). These photoelectrons waves are scattered from the neighbouring atoms producing backscattered waves. The interference between the outgoing and backscattered waves affects the probability of X-ray absorption by the absorber atom. 55

Figure 2-12 Isolated EXAFS $\chi(k)$ for a Mo foil. 56

Figure 2-13 Isolated k^3 -weighted EXAFS $\chi(k)$ for a Mo foil. 57

Figure 2-14 Amplitude of the Fourier transform data form Figure 2-13. 59

Figure 2-15 The first step during an Auger process^[38] is the removal of electrons from inner atomic levels created by ionisations due to X-ray photons. This creates a hole in the K-shell and causes an energetically unstable situation. The relaxation takes place by filling the hole with an electron from an L_1 shell. As a consequence the amount of energy ($K - L_1$) is released which can be given to another electron or emitted as a photon. If the second electron originating from the same shell or higher shell e.g. L_{23} has sufficient excess kinetic energy, it will be ejected from the surface to the vacuum or ambient, where its energy can be measured. The second electron is called an Auger electron and its energy is ($K - L_1 - L_{23}$). This Auger transition can be labelled KL_1L_{23} .
..... 60

Figure 2-16 The characteristic field lines associated with electron yield detection using the GMSD. The sample bias is set to a high negative potential which creates drift field accelerating the signal electrons towards the detector plate. The electron avalanche occurs because of ionization of the gas molecules by the accelerated electrons and is situated only a few micrometers from the detector plate^[45] 62

Figure 2-17 Detection of Auger electrons using GMSD detector at ambient conditions, where E is the energy of electron, e^- , escaping from the sample surface or bulk into ambient; $h\nu$ is the incident X-ray photon energy. 63

Figure 2-18 Cut away sketch of the electron yield detector^[51] 64

Figure 2-19 PHDs taken from X-ray intensity measurements without a sample at the start (left) and end (right) of an EXAFS scan. 65

Figure 2-20 Operation performed by Reduce software in order to obtain raw EYER-XAS data. 66

Figure 2-21 Typical PHD recorded at Ni K-edge showing sampled 4 different energy regions. 67

Figure 2-22 Normalized EYER XANES spectra of NiO/Ni film. The spectra were obtained from the Auger electron regions marked in Figure 2-21 using Reduce.	68
Figure 3-1 The three dimensional representation of γ -Bi ₂ MoO ₆ structure, where purple and green polyhedrons represent Bi ³⁺ and Mo ⁶⁺ species respectively, while O ²⁻ ions are red balls. The structure is built upon [Bi ₂ O ₂] ²⁺ layers sandwiched between layers of MoO ₆ octahedra.	76
Figure 3-2 In-situ hydrothermal cell that was used for isothermal hydrothermal reactions between 160 and 180°C throughout time resolved HRPD/Raman/XAS experiments. The γ -Bi ₂ MoO ₆ gel was loaded between two mica discs separated by a Teflon ring spacer and subsequently housed between two aluminium plates sealed with a lockable flange.	81
Figure 3-3 A scheme of HRPD/Raman/XAS setup as constructed on the Swiss-Norwegian beamlines at the ESRF ^[37] . The set-up is based upon a step scanning powder diffractometer equipped with an X-ray detector consisting of six independent counting chains. Raman instrument is dispersive spectrophotometer, Renishaw RA100, with Ar-ion laser and 1200 mm ⁻¹ grating. A Raman probe is connected to the instrument by optical fibres. XAS data are recorded with a Vortex fluorescence detector. The in situ cell is positioned with the respect to the incoming X-ray beam the way, that the X-ray beam hits a sample close to the bottom edge of the mica disc windows.	83
Figure 3-4 XRD pattern of Bi ₂ MoO ₆ collected at wavelength of 1.54 Å prepared in Teflon-lined autoclave at 170°C for 20 hours. The peak intensities are normalized on 131 diffraction peak. All peaks in the pattern can be indexed in orthorhombic crystal structure based on Theobald et.al. ^[42] XRD data. Therefore it can be assumed that the pure phase is formed. The hump at ~11° is due to the scattering from sample holder, that is, wrong slits setting of D4 diffractometer were used.	85
Figure 3-5 Mo K-edge XANES spectra collected during the isothermal heat treatment at 180°C under hydrothermal conditions. The features marked A and B are characteristic of Mo ⁶⁺ in tetrahedral and octahedral environment respectively. A clear increase in the tetrahedral pre-peak intensity and disappearance of the octahedral fingerprint are observed.....	86
Figure 3-6 Mo K-edge XANES spectra of model compounds, Na ₂ MoO ₄ ·2H ₂ O in red and (NH ₄) ₆ Mo ₇ O ₂₄ ·4H ₂ O in black, representing Mo ⁶⁺ in tetrahedral and octahedral geometry respectively. The XANES spectrum of Mo ⁶⁺ in tetrahedral geometry shows a distinct pre-edge peak due to 1s-3d electronic transition, while the pre-edge peak is	

suppressed in octahedrally coordinated Mo^{6+} ions. A weak shoulder on the top of the edge is due to 1s 5p electronic transition. 87

Figure 3-7 Raman spectra collected during the hydrothermal synthesis of $\gamma\text{-Bi}_2\text{MoO}_6$ at 180°C . The weak band at 711 cm^{-1} and the strong line at 1050 cm^{-1} can be assigned to NO_3^- anion. The bands at 881 and 897 cm^{-1} can be assigned to vibration of MoO_4^{2-} tetrahedra, while the strong lines at 802 cm^{-1} and two shoulders at 721 and 845 cm^{-1} are stretching modes of MoO_6 octahedra. 88

Figure 3-8 In-situ XRD patterns collected during the hydrothermal synthesis of $\gamma\text{-Bi}_2\text{MoO}_6$ at 180°C . The crystalline phase formed in the first minutes of the reaction can be assigned to Bi_2O_3 phase. After 23 minutes of the reaction this phase is gradually transformed into $\gamma\text{-Bi}_2\text{MoO}_6$ 89

Figure 3-9 A graphical representation of Bi_2O_3 distorted fluorite structure based on Rietveld refinement results, where red balls represent oxygen atoms and yellow balls bismuth atoms^[50]. 90

Figure 3-10 Rietveld refinement of XRD data for an intermediate phase which was formed after 9 min at 160°C during isothermal hydrothermal crystallization of $\gamma\text{-Bi}_2\text{MoO}_6$ from an amorphous gel. The refinement was carried out using I4/mmm space group with Bi in 2a (0, 0, 0) and O in 4d (0, 1/2, 1/4) and 75% occupancy of O site. In the Rietveld fit isotropic crystalline size model is used. An observed (black curve) and calculated (red curve) and difference profiles (green curve) are shown. 91

Figure 3-11 Rietveld refinement of XRD data for the crystalline $\gamma\text{-Bi}_2\text{MoO}_6$ formed under hydrothermal conditions from an amorphous gel after 184 min at 160°C . The refinement was carried out using the structural model derived by Theobald et al^[42]. In this model was necessary to allow anisotropic crystalline size broadening. An observed (black curve) and calculated (red curve) and difference profiles (green curve) are shown. 92

Figure 3-12 Selected HRPD patterns collected during the hydrothermal crystallization of $\gamma\text{-Bi}_2\text{MoO}_6$ at 160°C with the indexing of the Bragg peaks. Bragg Peaks marked with blue arrows correspond to the intermediate phase (Bi_2O_3) formed in a tetragonal unit cell ($a = 4.02\text{ \AA}$, $c = 5.69\text{ \AA}$), whereas black arrows are for the final $\gamma\text{-Bi}_2\text{MoO}_6$ crystallizing in an orthorhombic unit cell ($a = 5.50\text{ \AA}$, $b = 16.25\text{ \AA}$, $c = 5.42\text{ \AA}$). 93

Figure 3-13 Evolution of crystallite sizes formed at different temperatures as a function of time during the hydrothermal synthesis of $\gamma\text{-Bi}_2\text{MoO}_6$. In the initial stages of the reaction, the crystals are isotropic in the shape with the mean Bi_2O_3 particle sizes of

12.6±1.6 Å, 14.5±1.9 Å and 10.2±0.3 Å for temperatures of 160, 170 and 180°C respectively. Thereafter, the anisotropic growth with crystal sizes given in the figure takes place. The uncertainties are smaller than the symbol.	94
Figure 3-14 Changes in the volume fraction of Bi ₂ O ₃ and γ-Bi ₂ MoO ₆ phases present during the course of the reaction at 160, 170 and 180°C.	95
Figure 3-15 The graphical representation of γ-Bi ₂ MoO ₆ Aurivillius type structure viewed down to c-axis (on the left). Corner sharing MoO ₆ octahdra along a and c axis form infinite MoO ₄ ²⁻ layers that alternate with Bi ₂ O ₂ layers along b axis. On the right, a detailed view on MoO ₄ ²⁻ and Bi ₂ O ₂ ²⁺ layers viewed along b-axis.	98
Figure 3-16 Stacked plot of Mo K-edge XANES spectra of γ-Bi ₂ MoO ₆ recorded during hydrothermal crystallization at 140 °C. The pre-edge and the shoulder on the top of the edge are indicted by arrows B and A respectively. For a further explanation see the text.	100
Figure 3-17 Stacked XRD pattern recorded during hydrothermal crystallization of γ-Bi ₂ MoO ₆ gel at 140 °C with wavelength, λ=0.625 Å. The reflections in the first diffraction pattern can be assigned to Bi ₂ O ₃ phase which is gradually transformed to γ-Bi ₂ MoO ₆ during the course of the reaction.	100
Figure 3-18 Comparison of the Mo K-edge XANES of the amorphous gel and crystalline γ-Bi ₂ MoO ₆ with model compounds, Na ₂ MoO ₄ ·2H ₂ O and (NH ₄)Mo ₇ O ₂₄ ·4H ₂ O, representing molybdenum in tetrahedral and octahedral geometry respectively.	101
Figure 3-19 The variation of the pre-edge intensity during hydrothermal crystallization at 140, 150 and 160°C with time. The intensity was obtained by direct measurement of the maximum value of the pre-edge peak (arrow B) in XANES spectra plotted in Figure 3-16.	102
Figure 3-20 Post mortem XRD pattern of the crystalline γ-Bi ₂ MoO ₆ formed at 140°C during in-situ combined XAS/XRD experiment collected with lab XRD machine at the wavelength λ=1.54 Å. Indeed, the pure phase was formed.....	103
Figure 3-21 Fits to Mo K-edge EXAFS spectra of reference materials analysed in k-space (k ³ -weighted, background subtracted) together with corresponding Fourier transforms. The solid line is the experimental data and the dashed line is the best fit.	104
Figure 3-22 A fit to Mo K-edge EXAFS spectrum of ex-situ synthesised γ-Bi ₂ MoO ₆ together with corresponding Fourier transform. Data was analysed in k-space (k ³ -	

weighted, background subtracted). The solid line is the experimental data and the dashed line is the best fit.	105
Figure 3-23 A typical fit to Mo K-edge EXAFS spectra of γ -Bi ₂ MoO ₆ recorded after 18 min of the reaction at 140°C and a formed crystalline material upon the reaction completion. Data were analysed in k-space (after background subtraction, k ³ weighted). The solid line is the experimental data and the dashed line is the best fit.	106
Figure 3-24 Changes in short Mo–O bonds ($R_{\text{Mo-O}}$) (filled circles), long Mo–O bonds (open circles), coordination numbers (N) associated with short bonds (filled squares) and long bonds (open squares) as a function of crystallization time. The error bars are within the size of the used symbol ($\pm 0.01 \text{ \AA}$).....	108
Figure 3-25 Kinetic data for the growth of MoO ₆ species from MoO ₄ ²⁻ species. α -time curves were obtained from the isothermal hydrothermal crystallization of γ -Bi ₂ MoO ₆ gel at 140 °C (red square), 150 °C (blue circle) and 160 °C (green triangles). Solid lines are the non-linear least squares fits to Avrami-Erofe'ev expression shown in equation (Equation 3-1) performed in Origin.....	112
Figure 3-26 Arrhenius plot for determination activation energy.	113
Figure 3-27 SEM pictures of γ -Bi ₂ MoO ₆ gel itself and samples synthesised ex-situ by hydrothermal method at 180°C for 30 min and 70min and 20h.....	114
Figure 4-1 A typical Auger electron spectrum obtained at photon energy 6033 eV form HTS-200, whereby two different energy regions are indicated. The low energy region corresponds to Auger electrons escaping from the bulk, whereas in the high energy region they escape from near surface of the catalyst.	124
Figure 4-2 XRD patterns of HTS catalysts calcined at various temperatures showing crystalline and amorphous components. The crystalline component in samples was identified as haematite. The amorphous halo centred around $2\theta = 27^\circ$ is much reduced in the sample calcined at 500°C whilst the crystalline peaks have increased. This indicates a considerable increase in the degree of crystallinity.....	126
Figure 4-3 XPS data of the chromium containing iron oxide samples heated at various temperatures. For clarity only the Cr 2p spectra are shown which are normalised and corrected using carbon 1s binding energy. The split in the peaks between 575 and 580 eV indicates the presence of both Cr ³⁺ and Cr ⁶⁺	127
Figure 4-4 Transmission Fe K-edge XANES spectra of HTS catalysts calcined at various temperatures. The small pre-edge peak indicates the presence of octahedrally coordinated Fe ³⁺ ions.	128

Figure 4-5 Cr K-edge XANES of HTS catalysts and the reference materials containing Cr ⁶⁺ and Cr ³⁺ representing tetrahedral and octahedral geometry respectively. The pre-edge peak is used as signature identifying the coordination geometry of chromium species. (See text for further explanation).....	130
Figure 4-6 Cr K-edge EREY-XANES for HTS catalysts obtained from the near surface and bulk. The pre-edge peak indicates the coordination geometry of chromium species. See text for further explanation.	130
Figure 4-7 Cr K-edge fluorescence XANES of HTS-500 catalyst (solid line) and the fitted profile (dashed line) obtained by a linear combination least square fit to the Cr ₂ O ₃ and K ₂ Cr ₂ O ₇ reference materials. The catalyst contains 18% of Cr ⁶⁺ and 82% of Cr ³⁺	131
Figure 4-8 Variation of the pre-edge peak height of Cr K-edge XANES as a function of Cr ⁶⁺ /Total Cr. Total Cr is defined as mixture of Cr ³⁺ and Cr ⁶⁺ . Spectrum in red is without Cr ⁶⁺ i.e. 100 mol % Cr ³⁺ , in green contains 20 mol % of Cr ⁶⁺ , in blue 40 mol% of Cr ⁶⁺ , in brown 60 mol% of Cr ⁶⁺ , in pink 80 mol% of Cr ⁶⁺ and in black is solely Cr ⁶⁺	133
Figure 4-9 Plot of Cr ⁶⁺ /Total Cr versus pre-edge height. Data were fitted with a polynomial function $y=A+B_1x+B_2x^2$, where $A=-18.2\pm0.6$, $B_1=191.3\pm2.9$, $B_2=-59.9\pm3.0$ and $R=0.99$	134
Figure 4-10 Fe K-edge EXAFS spectra analysed in k-space (after background subtraction, k ³ -weighted) of HTS catalysts together with corresponding Fourier transforms. The solid line is experimental data and the dashed line is the best fit.....	138
Figure 4-11 Cr K-edge EXAFS spectra of reference materials, K ₂ Cr ₂ O ₇ and Cr ₂ O ₃ , analysed in k-space (after background subtraction, k ³ -weighted) and Fourier transforms of corresponding EXAFS spectra. The solid line is the experimental data and the dashed line is the best fit.....	139
Figure 4-12 Fourier transforms of k ³ weighted Cr K-edge EXAFS as a function of the atomic distance, R, for HTS catalysts calcined at various temperatures. See text for further explanation.....	140
Figure 4-13 Cr K-edge EXAFS spectra analysed in k-space (after background subtraction, k ³ -weighted) of HTS catalysts and Fourier transform of corresponding EXAFS spectra. The solid line is an experimental data and the dashed line is the best fit.	143

Figure 5-1 The 3D representation of the pore framework structures of AlPO-34 (CHA) and AlPO-18 (AEI), whereby cobalt will be introduced into the framework by the isomorph substitution for framework aluminium. Both structures have chabazitic cages as side pockets along the 0.38 nm diameter pores ^[13]	151
Figure 5-2 The generation of Brönsted acid sites in cobalt substituted aluminophosphates. The negatively charged framework is balanced by an equivalent number of positively charged extra-framework species such as quaternary ammonium cations and protonated amines ^[13]	152
Figure 5-3 Auger electron spectrum obtained at photon energy of 7 903 eV from CoAlPO-34 A, whereby two different energy regions are indicated. The low energy region, in which Auger electrons escape from the bulk, whereas the higher energy electrons emanate from the near surface region of the sample.	156
Figure 5-4 XRD patterns of the CoAlPO-34 samples A and B. The patterns are nearly identical which indicates that the crystalline framework of both materials is nearly identical.	157
Figure 5-5 XRD pattern of the CoAlPO-18 sample which resembles to AlPO-18 ^[31] pattern, monoclinic C2/c space group.....	158
Figure 5-6 Co K-edge XANES of CoAl ₂ O ₄ and C ₄ H ₆ CoO ₄ which have been used as reference materials representative of the tetrahedral or octahedral coordinated Co ²⁺ ions.	159
Figure 5-7 Comparison of the Co K-edge transmission and TEY–XAS spectra of CoAl ₂ O ₄ , as-prepared CoAlPO-18 and as-prepared CoAlPO-34 A and B. The comparison shows that spectra are very similar regarding the pre-edge feature and position of the main edge.	160
Figure 5-8 Co K-edge EREY–XANES for CoAlPO-34 A, CoAlPO-34 B and CoAlPO-18, where the spectrum from the bulk is plotted in red, whereas from the near surface is in blue. Co K-edge transmission XANES of all catalysts are shown in bottom right corner. The marginal differences indicate that there is no difference between the bulk and near edge with respect to the Co ²⁺ coordination.	161
Figure 5-9 Comparison of Co K-edge EREY and transmission EXAFS together with corresponding Fourier transforms for CoAlPO-34 A. Data were analysed in in k-space (after background subtraction, k ³ -weighted). The solid line is the experimental data and the dashed line is the best fit. It can be clearly observed that EREY–EXAFS amplitudes	

are comparable of that transmission. The EREY–EXAFS spectra are noisier, particularly at higher k-values. 165

Figure 5-10 Comparison of Co K-edge EREY and transmission EXAFS together with corresponding Fourier transforms for CoAlPO-34 B. Data were analysed in k-space (after background subtraction, k^3 -weighted). The solid line is the experimental data and the dashed line is the best fit. It can be clearly observed that EREY–EXAFS amplitudes are comparable of that transmission. The EREY–EXAFS spectra are noisier, particularly at higher k-values, but the data quality is sufficient for full EXAFS analyses. 166

Figure 5-11 Comparison of Co K-edge EREY and transmission EXAFS together with corresponding Fourier transforms for CoAlPO-18. Data were analysed in in k-space (after background subtraction, k^3 -weighted). The solid line is the experimental data and the dashed line is the best fit. It can be clearly observed that EREY–EXAFS amplitudes are comparable to that of transmission. The EREY–EXAFS spectra are much noisier, particularly at higher k-values, but data quality is sufficient for full EXAFS analyses. 167

Figure 6-1 Optical microscopy from samples exposed to a $0.4 \times 4.0 \text{ mm}^2$ (panel A) and a $0.4 \times 1.0 \text{ mm}^2$ sized X-ray beam (panel B). Panel A (left hand side) shows a not fully crystallized sample (heat treatment like sample LidiSi-3), panel B (right hand side) shows LidiSi-1 (fully crystallized). Only the central part of the areas marked ‘A’ in both panels have been exposed to the beam during the crystallization experiment (vertical direction). The areas marked ‘B’ have not been exposed to the direct beam. The black bar in panel A is $1 \pm 0.05 \text{ mm}$ in length. 179

Figure 6-2 SEM micrograph of a freshly cleaved LidiSi-3, which has not been exposed to the X-ray beam. The black area is the epoxy in which the sample was embedded. A textured surface layer is observed. In the bulk, small fairly monodisperse droplets can be seen. These are assumed to be homogeneously nucleated bulk crystallites. 181

Figure 6-3 SEM micrographs of the cross section of an area exposed to X-rays during the on-line experiment (panel A) and a non-exposed area (panel B) for LidiSi-5 embedded in epoxy (dark regions top and bottom of figure). The surface layers in the non-exposed sample are indicated by arrows. In the exposed area, there is hardly any evidence of a surface layer and the morphology is finer. 182

Figure 6-4 SEM micrograph of LidiSi-5 of the transition region between the non-exposed region (marked A) towards the exposed area (marked B). The non-exposed

area clearly shows the surface layer and the coarse morphology, while in the exposed area the surface layer is absent and the morphology is finer.....	183
Figure 6-5 The two dimensional diffraction patterns from a not fully crystallised sample (LidiSi-2) for the area exposed to the X-rays during the experiment (panel A) and the non-exposed area (panel B). The irregular radial intensity in panel B is typical for coarse grained samples.	184
Figure 6-6 Powder diffraction data from the non-exposed area (black curve) around $2\theta = 12^\circ$ scattering intensity is observed, which is due the amorphous halo (the dotted line is a guide to the eye). This intensity is absent in the curve taken in the exposed area (blue curve). The X-ray wavelength used was $\lambda = 0.7955 \text{ \AA}$	185
Figure 6-7 An example of Rietveld refinement plot of XRD data in this case for LidiSi-1, using the atomic coordinates derived by de Jong et.al. ^[21] , Ccc2 space group. An observed (black curve) and calculated (red curve) and difference profiles (blue curve) along with green lines indicating position of Bragg peaks are shown.....	186
Figure 6-8 Powder diffraction data comparisons between samples areas exposed to X-rays at different stages of the thermal treatment. The peak intensities are normalized on the 130 diffraction peak. The inset shows a magnified range where weaker 040 and 111 peaks are observed in the diffraction curves for the areas that were less or not exposed to X-rays during the experiment.....	187

List of Tables

Table 3-1 Structural parameters for α -, β - and γ -phases of bismuth molybdate.	77
Table 3-2 The Rietveld refinement results of HRPD patterns collected at 160°C.	95
Table 3-3 The Rietveld refinement results of HRPD patterns collected at 170°C.	96
Table 3-4 The Rietveld refinement results of HRPD patterns collected at 180°C.	97
Table 3-5 Avrami exponent (n) and rate of crystallization (k) derived from Avrami-Erofe'ev equation.	112
Table 4-1 Relative amounts of Cr^{6+} and Cr^{3+} in catalysts calcined at various temperatures. XANES and EXAFS refers to data measured in fluorescence.	132
Table 4-2 Determination of Cr^{6+}/Cr^{3+} atom ratio in HTS catalysts from fluorescence and EREY-XANES data using the pre-edge peak method and PCA. The resulting values are with an accuracy of 3% ^[21] for the pre-edge peak method and 8% for PCA.	135
Table 4-3 Fe K-edge and Cr K-edge EXAFS results for the HTS catalysts and chromium containing model compounds, where N is coordination number, R – inter-atomic distance between atom pairs, σ^2 – Debye Waller factor and R_{Fit} – goodness of fit.	144
Table 5-1 Synthetic conditions of CoAlPO-34 preparation; tetratethylammonium hydroxide was used as a template.	154
Table 5-2 Structural parameters obtained from analysis of transmission Co K-edge EXAFS data for the as-prepared catalysts and model compounds, where N is coordination number, R –bond distance, σ –standard deviation of bond distance, σ^2 –Debye-Waller factor and R_{Fit} –goodness of fit.	162
Table 5-3 Structural parameters obtained from the analysis of energy resolved Co K-edge EXAFS data for as-prepared catalysts, where N is coordination number, R – bond distance, σ –standard deviation of bond distance, σ^2 –Debye-Waller factor and R_{Fit} –goodness of fit.	164
Table 6-1 March parameter G_1^{-2} and the degree of the texture η as a function of the exposure to X-rays during the two step thermal treatment. The columns ‘pre-heat’ and ‘crystallization’ indicate if the sample was exposed to the radiation during these thermal stages.	188

List of Equations

Equation 2-1 <i>Bragg's law</i>	37
Equation 2-2 <i>Definition of Flux</i>	41
Equation 2-3 <i>Definition of Brightness</i>	41
Equation 2-4 <i>Definition of Brilliance</i>	41
Equation 2-5 <i>The kinetic energy of the photoelectron</i>	45
Equation 2-6 <i>Wavelength of the outgoing photoelectron</i>	46
Equation 2-7 <i>Beer Lambert's Law</i>	47
Equation 2-8 <i>Photon energy dependence of the absorption coefficient measured in ...</i>	49
Equation 2-9 <i>Normalization of the absorption coefficient in XAFS</i>	51
Equation 2-10 <i>Normalization of XAFS performed in the widely used data analysis program Athena using AUTOBK algorithm^[29]</i>	51
Equation 2-11 <i>Definition of the photoelectron wave vector</i>	56
Equation 2-12 <i>EXAFS equation</i>	57
Equation 2-13 <i>Mean square deviation of bond distances</i>	58
Equation 2-14 <i>Fourier transform</i>	58
Equation 2-15 <i>The kinetic energy of the emitted electron in XPS measurements</i>	69
Equation 3-1 <i>Avrami-Erofe'ev equation</i>	109
Equation 3-2 <i>Arrhenius equation</i>	109
Equation 3-3 <i>The amount of a single phase</i>	110
Equation 3-4 <i>The conversion fraction</i>	110
Equation 4-1 <i>Vegard expression for EXAFS</i>	135
Equation 6-1 <i>Adiabatic temperature rise</i>	177

Acknowledgments

During the course of this research project which was a joint collaboration between UCL and the Dutch-Belgium beamline, I have obtained support and guidance from many people that I wish to express to them my great gratitude.

First of all, I wish to give my greatest thanks to Prof Gopinathan Sankar, for taking me on board in this project and giving me an opportunity to work in this field. I appreciate his constant support, encouragement, understanding, knowledge sharing and enthusiasm throughout the years. I am delighted with his help during the thesis writing.

My big thanks go also to my industrial supervisor Dr Wim Bras for his guidance, for having me taught about the synchrotron, for his encouragement and writing scientific articles using “Dutch-English” and jokes. His character and dry jokes have made my stay at DUBBLE unforgettable. I really appreciate his time and the effort that he put in during the write up of my thesis. I am grateful to him for helping me to stay during the writing up period in Grenoble, and thus enabling me to experience one more ski season.

I would also like to say thanks to Dirk Detollenaere, who was always ready to help. Because of his outstanding experiences in electronics and software engineering, he was able to resolve all the technical problems that I encountered. It was pleasure to work on various projects with him because of his constant support and interest. I am grateful for his help outside of work and for making my first year at the ESRF very pleasant by taking me on skiing outings.

I would like to thank Sergey Nikitenko for his help, guidance and useful discussions regarding XAS instrumentations and data collections. I appreciate his help during my experiments and his effort to help me with technical issues during weekends. I would like to acknowledge Dr Portale Giuseppe not only for his help and support but also for useful discussions regarding scattering techniques and help with SAX. In addition, I would like to acknowledge Guy Lujckx, Dr Daniel Hermida Merino, Florian Ledrappier, and Muriel Rigolet for their help and support during my time at DUBBLE.

During my first research project I collaborated with the following people from the University of Lille: Chanapa Kongmark, Prof E.B. Richard and Prof R. Vannier.

I would like to say thanks to Prof Richard Oldman (UCL, JM) for our useful discussions, and his guidance.

I also would like to acknowledge John Lipp (STFC) for his help with e-yield detector and fruitful discussions.

I wish to give thanks to my brother, Martin, for his help during beamtime, valuable discussions, support and encouragement over the years.

I am grateful to all members of the KLB building, in particular: Rozie Sarip, Chao (Jeff) Shiang Yang, Jon Keeting, Nazarudin, Kerry Simmance and Andy Smith for brightening up my day. Special big thanks go to Tom Daley, Husn-Ubayda Islam and Alastair Smith for their support, help and encouragement during the last two years. I also appreciate their help for correcting my English. Big thanks go to those who helped me during beamtime.

Finally, I would like to thank my parents, Vladimir and Anna, for their enormous support and encouragement during all these years. I am very grateful for the support and encouragement from my sister, Zuzana, and friends: Jamie, Sophie, Kristina, Andy, Slava and Dima.

Thanks to you all.

List of publications

C. Kongmark, V. Martis, A. Rubbens, C. Pirovano, A. Lofberg, G. Sankar, E. Bordes-Richard, R.-N. Vannier and W. Van Beek, *Chemical communications* **2009**, 4850-4852; “Elucidating the genesis of Bi_2MoO_6 catalyst by combination of synchrotron radiation experiments and Raman scattering”

C. Kongmark, V. Martis, C. Pirovano, A. Löfberg, W. van Beek, G. Sankar, A. Rubbens, S. Cristol, R. N. Vannier and E. Bordes-Richard, *Catalysis Today* **2010**, 157, 257-262. “Synthesis of $\gamma\text{-Bi}_2\text{MoO}_6$ catalyst studied by combined high-resolution powder diffraction, XANES and Raman spectroscopy”

V. Martis, S. Nikitenko, S. Sen, G. Sankar, W. van Beek, Y. Filinchuk, I. Snigireva and W. Bras, *Crystal Growth & Design* **2011**, 2858-2865. “Effects of X-rays on crystal nucleation in lithium disilicate”

V. Martis, R. Oldman, R. Anderson, M. Fowles, T. Hyde, R. Smith, S. Nikitenko, W. Bras and G. Sankar, *Physical Chemistry Chemical Physics* **2012**, ID CP-ART-02-2012-040604.

V. Martis, G. Sankar, W. Bras, “Deriving reaction kinetics from time-resolved XANES for Bi_2MoO_6 photocatalysts formed under hydrothermal conditions” (ready to submit)

V. Martis, M. Martis, J. Lipp, W. Bras, G. Sankar “Energy resolved electron yield and transmission XAS studies on cobalt substituted aluminophosphates (CoAlPOs)”. (in preparation)

Chapter 1 Introduction

1.1 Introduction

The work described in this thesis is focused on the development of synchrotron radiation based characterization methods to determine the structure and function of multicomponent metal oxide catalysts. In particular, variations in X-ray Absorption Spectroscopy (XAS) such as Energy Resolved Electron Yield X-ray Absorption Spectroscopy (EREY-XAS) performed with an electron yield detector and a novel way of analysing reaction progress using EXAFS data have been the focus of research. These techniques were applied to model catalytic materials.

XAS is a versatile technique for determining the local structure in a wide range of materials among which are transition metals that are used as dopants in very low concentrations in catalysts. Since there is no requirement for long range order to exist spectroscopy techniques can also provide information on the early stages of crystallization processes before a material develops sufficient long range order which would allow it to be studied, for instance, with X-Ray diffraction (XRD). In addition, the detailed analysis of Extended X-ray Absorption Fine Structure (EXAFS) yields information on bond distances, coordination numbers, and identity of neighbouring atoms, which are unobtainable from the other techniques, for instance, XRD. EREY-XAS was developed as an alternative to conventional transmission and fluorescence techniques which mainly probe the bulk of materials. This technique yields information about the local structure from the near surface region of materials. The other complementary techniques used for characterization of materials were XRD, Raman spectroscopy and Scanning Electron Microscopy (SEM). A detailed description of the techniques and basic operational principles, which were used for catalytic materials in this thesis are presented in Chapter 2. To gain deeper understanding of the structure and active sites of the catalysts and to determine the relationship between active metal sites and overall catalytic performance, it was necessary to use all these techniques.

Catalysis is the ability to increase the rate of a chemical reaction, that is, the rate at which equilibrium is attained. This is achieved by employing a catalyst, usually present in small quantities, that permits reactions to take place more effectively or under milder conditions than would be required in the absence of catalysts^[1]. Ideally, the catalyst is not consumed during the chemical reaction and chemically unchanged at the end of the reaction, and therefore it is a species that mediates changes in the chemical state. In an ideal situation when the reaction has finished, the same mass of catalyst is present as it was at the beginning and the catalyst has the same environment as before the initiation of the reaction. The use of a catalyst leads to a process that is more energy efficient, uses feedstock more efficiently as undesired products are minimised, and pollution is reduced. Hence, catalysis has a crucial role for efficient utilization of limited resources in an environmentally responsible manner.

Catalysis has a big impact not only on quality of life but also on sustained economic growth. More than 90% of the chemical manufacturing processes currently in use throughout the world utilize catalysts in one form or another, for instance: food, medicine, fabrics, building materials and fuels are produced by heterogeneous catalytic reactions. The world's four most successful industrial sectors are petroleum, chemical production, energy generation and food production, all of which rely on the use of catalysts.

The applications of catalysis are numerous. A few examples of the usages of catalysts, which have profoundly impacted upon the daily lives of humans, are presented.

- 1) The production of syngas (a mixture of CO and H₂) and hydrogen are essential reactions for the synthesis of many chemicals. The high temperature water gas shift reaction^[2] used in the process utilizes chromium doped iron oxide catalysts, the structure of which was studied in this thesis and the results are presented in Chapter 4. This reaction is important for lowering CO content during the conversion of natural gas or liquid hydrocarbons to hydrogen^[3]. The resulting syngas is subsequently converted to liquid fuels and other chemicals using the Fisher-Tropsch process^[4]. Hydrogen is currently considered to be the most promising candidate as a clean energy carrier as a result, car manufactures are developing hydrogen fuelled vehicles^[5]. In addition, high purity hydrogen is

required for the operation of low temperature polymer electrolyte membrane fuel cells (PEMFCs)^[6]. For these reasons, the production and purification of hydrogen has a leading position in industrial technology, and is also an essential component of many other industrial processes.

- 2) Catalysts are used for environmental protection. Examples of these are the catalytic converters which are fitted to vehicles in order to reduce emissions of deleterious carbon monoxide, hydrocarbons and nitrogen oxides^[7]. Moreover, they are used for treatment of industrial effluents and they are instrumental in abating the discharge of harmful chemicals to the biosphere.

- 3) It is difficult to imagine life without synthetic polymers which are used for applications including paints, adhesives, packing, textiles and fibres. All of these materials depend on catalysis for their production. For example, bismuth molybdate^[8] catalyst (see Chapter 3) is used for the production of acrolein and acrylonitrile^[9]. Acrylonitrile is utilized to produce plastics that are impermeable to gases and ideal for shatterproof bottles that hold chemicals and cosmetics or clear 'blister packs' that keep meats fresh. It is also a component in plastic resins, paints, adhesives and coatings. Acrolein is used as a chemical intermediate in the production of acrylic acid and its esters. Cobalt substituted aluminophosphates, for instance, CoAlPO-18 and CoAlPO-34 are used as a catalysts for the conversion of methanol to light olefins^[10, 11]. The Co-AlPO-34 catalyst showed an excellent activity for the selective oxidation of *n*-hexane, with production of adipic acid^[11, 12], which is used as a precursor for the production of nylon^[13]. The structural studies on these catalysts are described in Chapter 5.

In summary, it can be said that catalysis are key elements in both the economic and environmental viability of the chemical industry.

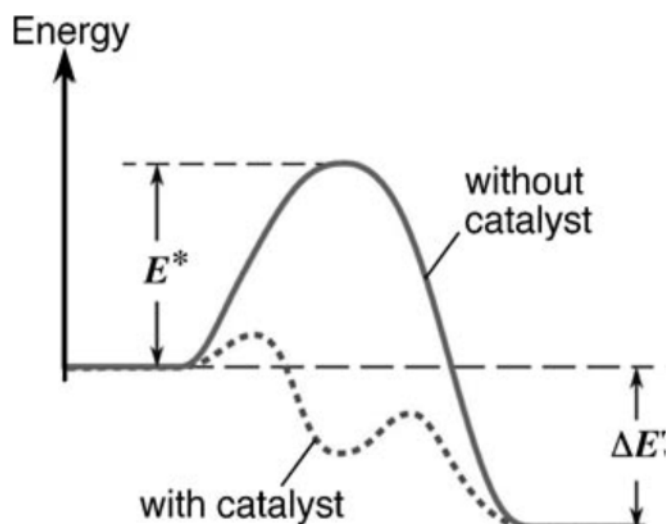


Figure 1-1 Energy diagram illustrating the progress of a chemical reaction with and without a catalyst. The reaction without a catalyst requires a higher activation energy than does the catalysed reaction. There is no difference in free energy (ΔE) between catalysed and uncatalysed reactions^[14].

A chemical reaction involves breaking bonds between atoms and the formation of new ones. This process is associated with the transformation of energy as shown in the energy diagram in Figure 1-1, in which the progress of a reaction $A + B \rightarrow C$ is schematically demonstrated. The activation energy, E_a , that needs to be surmounted is usually provided by thermal energy, kT , with k being Boltzmann's constant and T the temperature and hence not all molecular encounters will result in a successful reaction. An increase of the reaction probability (rate) can be achieved by either increasing the temperature or by lowering the activation energy, E_a . The latter situation is achieved when a catalyst is used. Through the formation of intermediate compounds with the molecules involved in the reaction, the catalyst provides alternate reaction paths as sketched by the dashed line in Figure 1-1. The dashed line is associated with smaller activation barriers and hence a higher overall reaction rate. In the last step, the product molecules are separated from the catalyst, which is now available for the next reaction cycle.

If the reacting molecules and the catalysts are in the same (gaseous or liquid) phase, the effect is called homogeneous catalysis. The main disadvantage of homogeneous

catalysis is the need to separate the product from the reactants and catalyst. In addition, there is large loss of catalyst in an industrial process, which can be expensive if, metals such as platinum or gold are used as catalysts. As an example of homogenous catalyst in living systems, macromolecules (enzymes) can be taken^[15].

On the other hand, in heterogeneous catalysis a catalyst is in a different phase from the reactants, that is, the reactants are in the gas or liquid phase and pass over the surface of a solid, upon which the reactions take place. The main benefit of this method is that there are no separations problems, the catalysts have a longer lifetime and a potential regeneration is more easily possible. The major disadvantages of using such catalysts can be a reduced number of active sites, the possibility of products sticking to the surface, blocking active sites and thereby preventing further reactions.

The principle of heterogeneous catalysis is that the atoms in the surface layer of a solid have fewer neighbours than those in the bulk and hence they are chemically unsaturated and may form new bonds with suitable molecules from the adjacent gas or liquid phase. In this step, existing bonds will be modified or may even be broken (dissociative chemisorption). The surface species formed may jump from one site to neighbouring sites, then may react with others; the newly formed molecules eventually leave the surface (desorption). This method is suitable for a continuous flow reactor. One of the most important applications of this principle was realized more than 100 years ago by F. Haber in the reaction of ammonia formation. In this reaction, nitrogen reacts with hydrogen producing ammonia using an osmium catalyst in a high pressure flow apparatus^[16]. This industrial process became only feasible due to the usage of catalysts to increase the ammonia yields. Since ammonia is used in the production process of many fertilizers, this discovery caused an agricultural revolution because one became independent of scarce natural sources of fertilizers like guano.

Catalysis has been identified as one of the most important tools for implementing green chemistry^[17]. The key benefits include lower energy requirements, catalytic versus stoichiometric amounts of materials, increased selectivity, and decreased use of processing and separation agents as well as the use of less toxic materials. In particular, heterogeneous catalysis is very beneficial for green chemistry by providing the ease of separation of product and catalysts, thereby eliminating the need for separation through

distillation or extraction. In addition, environmentally friendly catalysts such as zeolites and metal oxides catalysts can replace more hazardous catalysts currently in use.

1.1.1 Preparation of catalysts

In general, the majority of catalysts are synthesised either through precipitation, coprecipitation or hydrothermal method. Precipitation is the sedimentation of a solid material (a precipitate) from a liquid solution in which the material is present in amounts greater than its solubility in the liquid. Precipitation methods are frequently used for preparation of catalyst support materials. These materials include aluminium, silicon oxides and iron oxides. The main advantage of precipitation for the preparation of such materials is the purity of the product materials and the flexibility of the process with respect to the final product quality.

An alternative preparation method is co-precipitation. Coprecipitation is the simultaneous precipitation of a normally soluble component from the same solution by formation of mixed crystals, by adsorption, occlusion or mechanical entrapment. In many cases, both components to be precipitated are essentially insoluble under precipitation conditions, although their solubility limits might differ substantially. Therefore, the term coprecipitation is used for simultaneous precipitation of more than one component^[18]. This method is suitable for the generation of a homogenous distribution of catalysts components or for the creation of precursors with a definite stoichiometry, which can be easily converted to the active catalyst. If the precursor for the final catalyst is a stoichiometrically defined compound of the constituents of the catalyst, a calcination and/or reduction step is necessary to produce small and closely packed mixed crystallites. On one hand, the main benefit of this method is that a good dispersion of catalysts components is obtained. On the other hand, this preparation method is associated with the higher technological demands as well as the difficulties in monitoring the quality of the precipitated product during production.

Lastly, hydrothermal method is relatively cheap way of producing highly crystalline solids under mild hydrothermal conditions. Hydrothermal preparation is widely used for

the preparation of zeolites^[19] as well as catalytic materials. This method is discussed in more detail in Chapter 3, where Bi₂MoO₆ catalyst was produced by this method.

1.1.2 Properties and characteristic of catalysts

Besides fundamental properties of catalysts such as activity, selectivity and stability, industrially relevant catalysts also have to be regenerable, reproducible, mechanically and thermally stable, economical, and possess suitable morphological characteristics^[20].

Activity

A high activity is reflected either in high productivity from relatively small reactors and catalyst volumes or by carrying out catalytic reactions under mild operating conditions, that is, a lower temperatures that enhance selectivity and stability if the thermodynamics are more favourable.

Selectivity

High selectivity produces high yields of a desired product while suppressing undesirable competitive and consecutive reactions. This means that the texture of the catalysts, i.e. pore volume and distribution, are responsible for reducing these selectivity limitations.

Stability

A catalyst with a good stability will change very slowly over time under operating conditions and regeneration. Indeed, according to theory a catalyst remains unaltered during reaction. However, in practice, this is not the case and catalysts gradually lose activity, selectivity and mechanical strength due to several factors^[20]:

- a) Coke forms on some catalysts as a consequence of parasitic reactions of hydrogenolysis, polymerization, cyclization, and hydrogen transfer.
- b) Reactants, products and poisons may attack active agents or the support.
- c) The crystals of a deposited metal can become enlarged or regrouped. A change in the crystalline structure of the support can cause a loss of mechanical strength.

- d) Progressive adsorption of trace poisons in the feed or products may reduce activity. This is a typical problem in industrial feedstocks that are rarely pure materials, but mixtures containing portions of impurities that must be eliminated beforehand so that the catalyst can be used.

Morphology

The external morphological characteristics of a catalyst such as shape and grain size must be tailored to the corresponding process. For instance, for boiling bed reactors a spherical shape is desirable because it reduces problems with attrition and abrasion. In a fluid bed, spherical powder with well determined grain size distribution is preferred, as this limits attrition and good fluidization can be obtained. In a fixed bed, beads, rings or pellets can be used. Their shapes and dimensions have an influence on the pressure drop through the bed. The appropriate pressure drop ensures an even distribution of the reaction fluid across the catalytic bed. Furthermore, the grain density which depends on pore volume is particularly important for filling the reactors and the cost of the catalyst as it is sold by weight.

Mechanical strength

The mechanical strength of a catalyst is determined by its resistance to crushing. This ensures that the catalyst passes undamaged through the catalyst bed.

Thermal characteristics

For a certain type of catalyst the thermal conductivity and specific heat have to be taken into account. Temperature gradients within the grain as well as in the catalytic bed for endothermic and exothermic reactions can be reduced using the catalytic mass with a high thermal conductivity. However, in some cases the specific heat of a catalyst is very important, because a high specific heat enables the catalyst to carry a large thermal load from the combustion back to an endothermic reaction, where it is usefully consumed.

Regenerability

All catalysts age and thus their activities and selectivities degrade over a period of time. As a consequence, they must be regenerated through a treatment that partially restores their catalytic properties. In general, this treatment includes burning off carbon and, scrubbing with suitable gases which can desorb reversible poisons.

Reproducibility

Reproducibility of a catalyst is essential for manufacturers that want to be assured of the properties of the catalysts. Further consideration must be made during development as there are often issues with scaling up the production from a laboratory setting to an industrial environment.

1.1.3 Characterization of catalysts

There are still many industrial catalysts currently in use which have been empirically developed, that is, the exact reason why they are active is not exactly known. In order to improve existing catalysts and develop new ones there is growing need to investigate the structure of these catalysts in order to gain a better understanding of the function-reactivity relationship. The main aim of catalysis research is to characterize the local environment of catalytically active centres and reaction intermediates formed during reactions. For a further understanding of catalysis at an atomic level, it is crucial to obtain information about the structure of the active sites during reaction conditions and in the presence of reacting molecules^[12, 21].

The majority of catalysts are disordered with structurally ill-defined phases. One way to tackle this complex problem is to prepare structurally well-defined model catalytic systems, which can provide more insights into inactivity, scaling problems or the formation of chemical species that are hazardous to the environment. Afterwards, it is essential to perform a detailed characterization in which often synchrotron radiation based technique play an essential role. In particular, X-ray Absorption Fine Structure (XAFS) and X-ray Diffraction (XRD) can be mentioned here. XRD gives information on the crystallinity and long range order of atoms in a catalyst, while the main advantage of using XAFS lies in the study of amorphous and polycrystalline structures of catalysts at an atomic scale. The benefits of using XAFS are shown in Chapter 4, in which studies on iron oxide doped with chromium catalysts are reported. More importantly, XAFS spectroscopy has shown that the structure of the catalyst, in particular the structure of the active sites, is different in ‘real’ catalysts at reaction temperatures and pressures compared to model systems.

State of the art time resolved *in-situ* XAFS and XRD techniques can be used for following catalytic reactions under reaction (operando) conditions. Formation of active sites, reaction intermediate states and changes in the inter-atomic distances due to reaction of molecules can be observed, while *on-line* analysis during the activation of catalysts and catalytic reactions are performed. It is vital that the catalyst characterization is performed during catalysis because of the strong dependence of the catalyst structure on the gaseous environment. This allows for the drawing of more direct conclusions on the relationship between the structure and the activity. For this reason, a high pressure gas rig was built on DUBBLE (BM26A) at the ESRF (see Appendix A for the scheme of the gas rig). *In-situ* investigations of catalysts under realistic reaction conditions are crucial for understanding the catalyst's behaviour since the structure of *in-situ* catalysts is very different from that *ex-situ* or post mortem. Therefore, it is logical to develop other characterization methods as well as a combination of techniques which can be used under relevant reaction conditions.

The first *in-situ* combined XRD and XAFS measurements on a sample undergoing catalysis were performed in 1991 at the synchrotron laboratory in Daresbury, UK^[22]. This pioneering work showed that *in-situ* combined XAFS/XRD is a powerful tool for investigating structures of materials under operando conditions. Since then, this experimental setup has been routinely applied to catalysis research^[23]. Further, this 'standard' XAFS/XRD setup has been modified by adding other single experimental techniques such as Raman scattering which is described in detail in Chapter 3. Other combination of techniques besides XAFS/XRD includes small angle scattering SAXS/WAXS/XAFS^[24] and an ultraviolet visible spectroscopy setup, UV-VIS/XAFS/XRD^[25]. Recently, it has been reported a setup that coupled three spectroscopic techniques such as energy-dispersive XAFS, UV-VIS and Raman^[26].

In this thesis, an experimental setup known as Electron Yield Energy Resolved XAFS (EYER-XAFS) is described which is capable of providing information from the near surface region of a catalyst. The fundamental principles of characterization methods are explained in Chapter 2 and in chapter 5 an application of technique to catalysts research is demonstrated on cobalt substituted aluminophosphates (CoAlPOs) which were taken as example catalysts.

As can be seen, employing synchrotron radiation techniques utilizing powerful X-ray beams is beneficial for catalysis research, and the structural information obtained under relevant operando conditions are unavailable from other techniques. However, one should take special care to note how long a studied sample should be exposed to X-ray beams, since X-rays can interact with sample atoms. In Chapter 6 serendipitous results of the interaction of X-rays produced by bending magnet radiation with lithium disilicate glass is described.

Apart from catalysis research, *in situ* XAFS/XRD can also be employed to study the formation of a material under mild hydrothermal conditions from an amorphous gel^[27]. In combination with an *ex-situ* method, this can be a powerful tool for designing new materials as their properties can be tailored to an appropriate process. Such hydrothermal reactions have been successfully carried out as shown in Chapter 3.

References

- [1] in *Catalysis*, Vol. (Ed. <http://www.catalysis.org/>).
- [2] C. Ratnasamy and J. P. Wagner, *Catalysis Reviews: Science and Engineering* **2009**, *51*, 325-440.
- [3] C. Rhodes, G. J. Hutchings and A. M. Ward, *Catalysis Today* **1995**, *23*, 43-58.
- [4] T. Riedel, M. Claeys, H. Schulz, G. Schaub, S.-S. Nam, K.-W. Jun, M.-J. Choi, G. Kishan and K.-W. Lee, *Applied Catalysis A: General* **1999**, *186*, 201-213; M. Bayat, M. R. Rahimpour and B. Moghtaderi, *Journal of Natural Gas Science and Engineering* **2011**, *3*, 555-570; H. Schulz, *Applied Catalysis A: General* **1999**, *186*, 3-12; A. A. Adesina, *Applied Catalysis A: General* **1996**, *138*, 345-367.
- [5] D. Sáinz, P. M. Diéguez, C. Sopena, J. C. Urroz and L. M. Gandía, *International Journal of Hydrogen Energy* **2012**, *37*, 1781-1789; L. F. Brown, *International Journal of Hydrogen Energy* **2001**, *26*, 381-397.
- [6] N. A. Koryabkina, A. A. Phatak, W. F. Ruettinger, R. J. Farrauto and F. H. Ribeiro, *Journal of Catalysis* **2003**, *217*, 233-239.
- [7] S. H. Oh and J. E. Carpenter, *Journal of Catalysis* **1986**, *101*, 114-122; J. T. Kummer, *Progress in Energy and Combustion Science* **1980**, *6*, 177-199; W. D. J. Evans and A. J. J. Wilkins, *Science of The Total Environment* **1987**, *59*, 97-112.
- [8] P. A. Batist and Hj, *Journal of Chemical Technology and Biotechnology* **1979**, *29*, 451-466.
- [9] P. Courtine and E. Bordes in *Studies in Surface Science and Catalysis*, Vol. Volume 110 Elsevier, **1997**, pp. 177-184; B. Delmon in *Studies in Surface Science and Catalysis*, Vol. Volume 110 Elsevier, **1997**, pp. 43-59; R. K. Grasselli, M. Che and G. C. Bond in *Studies in Surface Science and Catalysis*, Vol. Volume 21 Elsevier, **1985**, pp. 275-285; R. K. Grasselli, *Applied Catalysis* **1985**, *15*, 127-139; R. K. Grasselli, *Catalysis Today* **2005**, *99*, 23-31.
- [10] J. Chen and J. M. Thomas, *Journal of the Chemical Society, Chemical Communications* **1994**, 603-604; Y. Xu, C. P. Grey, J. M. Thomas and A. K. Cheetham, *Catalysis Letters* **1990**, *4*, 251-260.
- [11] J. M. Thomas, R. Raja, G. Sankar and R. G. Bell, *Nature* **1999**, *398*, 227-230.
- [12] J. M. Thomas and G. Sankar, *Accounts of Chemical Research* **2001**, *34*, 571-581.
- [13] M. H. Thiemens and W. C. Troglor, *Science* **1991**, *251*, 932-934.
- [14] G. Ertl, *Angewandte Chemie-International Edition* **2008**, *47*, 3524-3535.
- [15] G. M. Whitesides and C.-H. Wong, *Angewandte Chemie International Edition in English* **1985**, *24*, 617-638; C. H. Wong and G. M. Whitesides, *Enzymes in Synthetic Organic Chemistry*, Pergamon, **1994**, p. 1-39.
- [16] F. Haber, *Zeitschrift fur Elektrochemie* **1910**, *16*, 244-246.
- [17] P. T. Anastas and M. M. Kirchoff, *Accounts of Chemical Research* **2002**, *35*, 686-694.
- [18] J. B. Clarke, J. W. Hastie, L. H. E. Kihlberg, R. Metselaar and M. M. Thackeray, *Pure and Applied Chemistry* **1994**, *66*, 577-594.
- [19] R. M. Barrer, *Zeolites* **1981**, *1*, 130-140; H. Lechert in *The pH-value and its importance for the crystallization of zeolites*, Vol. 2 (Ed. H. Robson), Elsevier, London, **2001**, pp. 33-38; M. E. Davis, *Industrial & Engineering Chemistry Research* **1991**, *30*, 1675-1683; J. Weitkamp, *Solid State Ionic* **1999**, *131*, 175-188; S. T. Wilson, B. M. Lok and E. M. Flanigen, *Journal of American Chemical Society* **1988**, *196*, 207-211.
- [20] G. Ertl, H. Knozinger and J. Weitkamp, *Preparation of Solid Catalysts*, WILEY-VCH Verlag GmbH Weinheim, **1999**, p. 65-83.

- [21] J. M. Thomas and G. Sankar, *Journal of Synchrotron Radiation* **2001**, *8*, 55-60; S. T. Korhonen, D. W. Fickel, R. F. Lobo, B. M. Weckhuysen and A. M. Beale, *Chemical communications* *47*, 800-802.
- [22] J. W. Couves, J. M. Thomas, D. Waller, R. H. Jones, A. J. Dent, G. E. Derbyshire and G. N. Greaves, *Nature* **1991**, *354*, 465-468.
- [23] G. Sankar, M. A. Roberts, J. M. Thomas, G. U. Kulkarni, N. Rangavittal and C. N. R. Rao, *Journal of Solid State Chemistry* **1995**, *119*, 210-215; G. Sankar and J. M. Thomas, *Topics in Catalysis* **1999**, *8*, 1-21; K. Simmance, G. Sankar, R. G. Bell, C. Prestipino and W. v. Beek, *Physical Chemistry Chemical Physics* **2009**, *12*, 559-562; G. Sankar, J. M. Thomas, F. Rey and G. N. Greaves, *Journal of the Chemical Society, Chemical Communications* **1995**, 2549-2550; G. Sankar, J. M. Thomas and C. R. A. Catlow, *Topics in Catalysis* **2000**, *10*, 255-264; S. Poulston, T. I. Hyde, H. Hamilton, O. Mathon, C. Prestipino, G. Sankar and A. W. J. Smith, *Physical Chemistry Chemical Physics* **2011**, *12*, 484-491; A. J. Dent, M. Oversluizen, G. N. Greaves, M. A. Roberts, G. Sankar, C. R. A. Catlow and J. M. Thomas, *Physica B* **1995**, *209*, 253-255; J. D. Grunwaldt and B. S. Clausen, *Topics in Catalysis* **2002**, *18*, 37-43; A. M. Beale, L. M. Reilly and G. Sankar, *Applied Catalysis A: General* **2007**, *325*, 290-295; A. M. Beale, M. T. Le, S. Hoste and G. Sankar, *Solid State Sciences* **2005**, *7*, 1141-1148; L. M. Reilly, G. Sankar and C. R. A. Catlow, *Journal of Solid State Chemistry* **1999**, *148*, 178-185.
- [24] A. M. Beale, A. M. J. van der Eerden, S. D. M. Jacques, O. Leynaud, M. G. O'Brien, F. Meneau, S. Nikitenko, W. Bras and B. M. Weckhuysen, *Journal of the American Chemical Society* **2006**, *128*, 12386-12387; S. Nikitenko, A. M. Beale, A. M. J. van der Eerden, S. D. M. Jacques, O. Leynaud, M. G. O'Brien, D. Detollenaere, R. Kaptein, B. M. Weckhuysen and W. Bras, *Journal of Synchrotron Radiation* **2008**, *15*, 632-640; W. Bras, S. Nikitenko, G. Portale, A. M. Beale, A. v. d. Eerden and D. Detollenaere, *Journal of Physics: Conference Series* **2010**, *247*, 012047.
- [25] G. Sankar, S. Fiddy, A. M. Beale, I. Harvey, S. Hayama and G. Bushnell-Wye, *AIP Conference Proceedings* **2007**, *882*, 585-587.
- [26] A. M. Beale, A. M. J. van der Eerden, K. Kervinen, M. A. Newton and B. M. Weckhuysen, *Chemical communications* **2005**, 3015-3017.
- [27] A. M. Beale and G. Sankar, *Chemistry of Materials* **2003**, *15*, 146-153; A. M. Beale, M. G. O'Brien, M. Kasunic, A. Golobic, M. Sanchez-Sanchez, A. J. W. Lobo, D. W. Lewis, D. S. Wragg, S. Nikitenko, W. Bras and B. M. Weckhuysen, *Journal of Physical Chemistry C* *115*, 6331-6340; M. A. Newton and W. van Beek, *Chemical Society Reviews* *39*, 4845-4863.

Chapter 2 Experimental part

2.1 Chapter Overview

The experimental techniques employed to study materials within this thesis are described in this chapter. The chapter starts with a brief introduction to X-rays and X-ray diffraction. In the next part the phenomenon of synchrotron radiation and a typical experimental facility, i.e. a beamline at the synchrotron are described. Moreover, synchrotron radiation techniques such as conventional X-ray absorption spectroscopy and energy resolved electron yield X-ray absorption spectroscopy are discussed more in detail since these are particularly relevant for the work described in this thesis. Other experimental techniques used for this work such as Scanning Electron Microscopy, X-ray photoemission spectroscopy and Raman spectroscopy, which are all routinely used in sample characterization, are only briefly discussed.

2.2 Origin of X-Rays

X-rays were first observed by Wilhelm Conrad Röntgen^[1] in 1895 during his studies of fluorescence induced by radiation from a cathode ray tube. They obtained their name because of the fact that their nature was unknown at the time. Röntgen discovered that X-rays penetrate many substances. Accidentally he found out that X-rays cannot pass through metal when he inadvertently left a key in a book which was used as a radiation target. In 1895 he made a famous image of his wife's hand as illustrated in Figure 2-1 by irradiating her hand over a photographic plate. For his discovery of X-rays he was honoured with the first Nobel Prize for Physics in 1901.



Figure 2-1 The first 'medical' X-ray picture showing hand of Roentgen' wife^[2].

Conventionally, X-rays are produced by X-ray tubes. X-rays are generated when an electron beam (produced by heating a metal filament) accelerated across a high voltage field bombards a stationary or rotating solid metal anode. A broad spectrum of X-rays is generated by electrons which are being decelerated or stopped in the metal. This continuous (bremsstrahlung) radiation spectrum has a maximum energy that corresponds to a high voltage applied to the tube^[3].

In addition, when an electron beam with sufficient energy beam strikes the anode, an electron from the target atom can be raised to a higher orbit or even be completely ejected. This creates vacancies in the inner shell (K-shell) which are subsequently filled by an electron from an outer shell (L- or M-shells) emitting continuous spectrum of X-rays with characteristic energy equal to the difference in energy between the two shell (K_{α} or K_{β})^[3]. For experiments requiring a monochromatic beam, the K_{α} line is often used, because it is several orders of magnitude more intense than the bremsstrahlung.

2.3 X-Ray Diffraction

The phenomenon of X-ray diffraction (XRD) by crystals was discovered in 1912 by Max von Laue. The diffraction condition in a mathematical form which is known as the Bragg law, was formulated by Lawrence Bragg in the same year^[4].

Equation 2-1 *Bragg's law*

$$n\lambda = 2d \sin \theta$$

where θ is the angle of the incident /reflection to the planes, the d_{hkl} is the lattice plane spacing, λ is the wavelength and n is order of reflection.

X-ray diffraction^[4, 5] from matter is based on elastic scattered X-rays, i.e. the wavelength of the scattered X-rays does not change when the X-rays are scattered by the electrons in atoms. Due to the wave nature of X-rays, the scattered X-rays from the sample can interfere with each other such that the intensity distribution is determined by the wavelength, the incident angle of the X-rays and the atomic arrangement of the sample structure, in particular the long range order of crystalline structures. A prerequisite to be able to derive structural information is that the coherence length of the waves is larger than the distance between two scattering objects.

If the atoms are arranged in a periodic order (crystals), the diffracted waves will consist of sharp interference maxima (peaks) with the same symmetry as in the distribution of atoms. The illustration of space distribution of the scattered X-rays is referred to as an X-ray diffraction pattern. The long-range structure of the material can be determined at

an atomistic level by analysing the diffraction pattern. Phase identification is performed by matching (indexing) the positions of the diffraction peaks in XRD pattern to known pattern in a database such as the International Centre for Diffraction Data (ICDD) PDF database^[6]. Moreover, from analysis of XRD data, degree of crystallinity, lattice parameters, particle sizes and texture in samples can be determined. In this thesis, the analysis of XRD data was carried out by Rietveld profile refinement method^[7] using the program Fullprof^[8]. This method uses a least-squares minimisation process for the experimental data, in which the peak intensities are treated as arbitrary values. The aim of the refinement is to match theoretical diffraction pattern (simulated from a known structural model) to that of the (observed) experimental data.

2.4 Synchrotron radiation

Synchrotron radiation^[9] is electromagnetic radiation emitted by electrons moving at relativistic velocities along a curved trajectory. The name ‘synchrotron radiation’ is derived from the electron synchrotron, which is the kind of particle accelerators where the radiation was observed for the first time. An electron accelerator emits synchrotron radiation in a very broad range of photon energies from microwaves to hard X-rays. It provides electromagnetic radiation in spectral regions for which no other usable sources exist. The history of synchrotron radiation can be traced back to the classic treatment of the emission of electromagnetic radiation by accelerated charged particles^[10]. Early theoretical work on the radiation emitted by electrons in circular orbits was motivated by the pre-Bohr attempts to develop atomistic models and explain the atomic spectra^[11]. In the early 1940’s, synchrotron radiation was identified as the key factor limiting the energy achievable with accelerators such as the betatron^[12]. For that reason, synchrotron radiation first appeared in science as a technical problem in accelerator physics. The electromagnetic radiation emitted by a synchrotron was first seen in 1946 at the General Electric Laboratories. The observation was made at the 70-MeV electron synchrotron in Schenectady. Until the late 1950’s, the study of synchrotron radiation was primarily motivated by its negative role in electron accelerator technology. In 1956, an article published by Tombouljian and Hartman^[13] supported that it was potentially a useful radiation source for research tools.

Moreover, synchrotron radiation is naturally occurring phenomenon especially in cool stars^[14]. They have a surface temperature of few thousand degrees, and are surrounded by hotter atmosphere of ionised gases (plasma) known as the corona. The hot gases in the corona emit thermal radiation as X-rays, which reach peak during flares. However, radio waves are produced through interactions between electrons and the magnetic field of the coronal plasma. Thus, the radio waves, i.e. synchrotron radiation, which is emitted when energetic electrons spiral in the strong magnetic fields in the corona can be observed and is an important research tool for radioastronomy.

Synchrotron radiation, for instance the X-ray beams at the ESRF (European Synchrotron Radiation Facility) is produced in a storage ring (844 m in a length), where electrons are injected at 6 GeV from a booster synchrotron and kept circulating at that energy (Figure 2-2). The speed of electrons in the storage ring almost matches that of light. The storage ring feeds the X-ray beam into experimental stations called beamlines, equipped with instruments and techniques, each for a specific type of research.

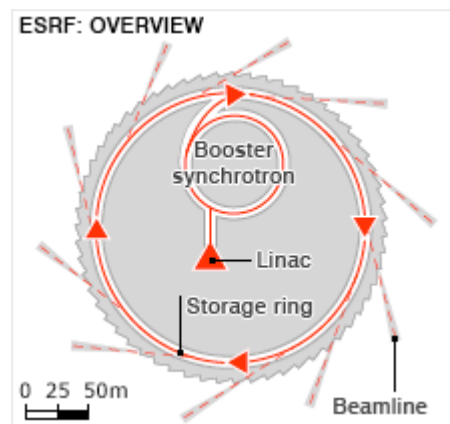


Figure 2-2 Production of synchrotron radiation at the ESRF. Electrons are produced and accelerated in a 200 MeV linear accelerator. Subsequently they are boosted in energy in the booster synchrotron to 6 GeV before injection in the main storage ring.

The storage 'ring' is actually a polygon consisting of straight and curved sections. In the straight sections one can place insertion devices whereas curved sections are constructed with bending magnets. In the bending magnets with the magnetic fields of

either 0.4 or 0.8 Tesla is the radiation emitted by the electrons. The bending trajectory is necessary to keep the electrons in a closed orbit. The production of synchrotron radiation is a by-product of this function. The spectral characteristics of the radiation depend on ring parameters such as energy and the radius of curvature.

Characteristics of synchrotron radiation emitted by bending magnets^[9]:

- a) High intensity
- b) High collimation – the emission is confined to a narrow range of vertical angles, centred at the plane of the reference electron orbit.
- c) A wide spectral range – photon energies in the infrared, visible, near ultraviolet, vacuum ultraviolet, soft X-ray and hard X-ray

The other characteristics of the synchrotron radiation is the time structure, i.e. short pulses of the order of nanoseconds separated by longer intervals and the elliptical polarization outside the plane.

Insertion devices consist of a series of magnets inserted in the straight sections of the storage ring. These magnets, wigglers and undulators, are arranged in such a way that the perturbation of the electron orbits outside the magnetic device is minimised. A wiggler forces the electrons over a sinusoidal path with a small radius of curvature in a magnetic field of 5 Tesla. This is required for extending the energy range and increasing the intensity of synchrotron radiation at the high energy end of the spectrum. However, the majority of modern synchrotron sources use undulators instead of wigglers. An undulator consists of many (50-100) alternating low field magnetic poles in which, unlike a wiggler, the radiation of each pole is coherent with the other poles and thus creates a very high, but non continuous wavelength spectrum. This produces a series of inward and outward electron accelerations ‘undulations’. The radiation obtained from undulators has very high brilliance at specific photon energies.

The quality of the X-ray beam can be described in terms of well-defined quantities of high flux (a large number of photons), high brightness (also well collimated), high brilliance (also a small size and well collimated).

Equation 2-2 Definition of Flux

$$Flux = \frac{Photons / sec\ ond}{(0.1\% bandwidth)}$$

Equation 2-3 Definition of Brightness

$$Brightness = \frac{Photons / sec\ ond}{(mrad)^2 (0.1\% bandwidth)}$$

Equation 2-4 Definition of Brilliance

$$Brilliance = \frac{Photons / sec\ ond}{(mrad)^2 (mm^2)(0.1\% bandwidth)}$$

The 0.1 % bandwidth term refers to the photon energy range which is used for comparison of spectral distribution of X-ray sources. It is defined as a fixed relative energy bandwidth. There are several reasons why the relative rather than absolute bandwidth is chosen. First, monochromator crystals are perfect crystals. The relative bandwidth for a perfect crystal in symmetric reflection geometry is independent of the photon energy and depends only on the Miller indices of the reflection. In general, one defines the figure-of-merit for the source as indicated in Equation 2-4. The $mrad^2$ refers to radiation solid angle delivered from the source, and mm^2 term to the cross sectional area. The spectral brightness of synchrotron radiation produced at magnet dipoles reaches maximum brightness of around 10^{14} photons/sec/ $mrad^2/mm^2/0.1\%$ bandwidth.

2.5 Dutch–Belgium beamline at the ESRF

The ESRF is a fundamental research institute situated in Grenoble, French Alps. It was founded in 1988 by 12 European countries (France, Germany, Italy, United Kingdom, Spain, Denmark, Finland, Norway, Sweden, Belgium, Netherlands and Switzerland). Since then seven more countries have joined the group. The ESRF was the world's first high energy third-generation X-ray source. It started regular operation for users in 1994. There are currently 41 beamlines in the operation. A typical design of a bending magnet

beamlines can be seen at the Dutch–Belgium beamlines (DUBBLE, BM26). DUBBLE was officially open for users in 2000.

The DUBBLE beamlines are designed in such a way that the X-ray radiation is split into two branches such as hard (H)-branch and soft (S)-branch^[15]. The (H)-branch receives radiation of a 0.8 Tesla bending magnet and accommodates small and wide angle X-ray scattering (SAXS/WAXS) The (S)-branch receives radiation from a 0.4 Tesla bending magnet and has consequently a somewhat softer X-ray spectrum. On it is placed X-ray absorption spectroscopy (XAS) station. Both branches can operate independently. Each branch has a shutter in the optics hutch allowing the entry into the corresponding experimental hutch without stopping the other beam line. In order to minimise possible interference, the vacuum of the two branches is separated by two fixed Be windows immediately after the common splitter vessel.

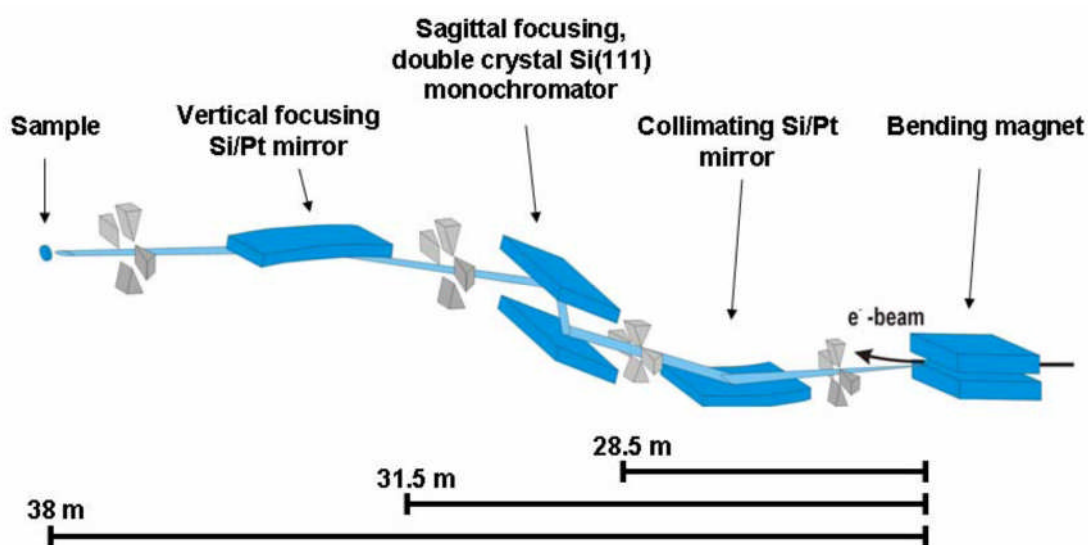


Figure 2-3 Schematic lay-out of the optical system of BM26A^[16] with a typical distances of optical elements from the radiation source. The monochromator is placed 28.5 m from the radiation source. The vertical focusing mirror is 31.5 m away from the source. The sample is positioned at 38 m from the radiation source.

The optical lay-out of the beamline BM26A^[16] (S-branch) is represented in Figure 2-3. The beamline receives 2 mrad of the radiation fan from radiation source of 0.4 Tesla ESRF bending magnet^[17].

The first optical element is a collimating mirror which is presently being installed but has not been used in the experiments described in this work. It has surface grooves in horizontal direction filled with GaIn alloy on the surface parallel to the X-ray beam. A cooling blade is inserted into the grooves of the collimating mirror, so that side cooling is obtained without any mechanical constraints which could affect a required bending accuracy. The mirror is made of 2 strips of optical surface. One of the surfaces is the bare Si surface and the other one is Pt coated strip along the length of the mirror. The function of this mirror is to intercept a larger part of the radiation fan and to create a parallel beam which is favourable in reducing the energy bandwidth. The second optical element is the water cooled, sagittal focusing, double crystal Si(111) monochromator which has the option of sagittal, i.e. horizontal, focusing. In XAS experiments the sagittal focussing is not used and thus the sagittally focussing second crystal is kept flat. This monochromator produces a monochromatic beam in the range 5-32 keV. The distance between a sample and the radiation source is 38 m. After the monochromator a vertically focusing mirror is inserted with Si/Pt coating. The surface of the mirrors is polished to roughness of 1.5 Å with slope error less than 1.5 μrad. The function of the mirror is to reduce the amount of higher harmonic radiation transmitted by the monochromator and to focus the beam in the vertical plane.

In the experimental hutch X-ray spectroscopy experiments are carried out in either the transmission or fluorescence configuration. For experiments performed in the transmission mode low-noise ionization chambers are used, which are read out by low-noise current preamplifiers, Novelec SA, This signal voltage is converted by voltage to frequency converters (0-1MHz) and generate an output which is connected to a scaler unit. The amplification of the signal is controlled over a range of up to six orders of magnitude from 0.1 nA to 10 μA.

Fluorescence measurements are performed using a nine element monolithic Ge fluorescence detector with digital XPRESS-X-ray signal processing electronics^[18]. In combined XAS/XRD experiments, the XRD data are recorded using a positive sensitive curved gaseous INEL CPS 590 detector^[19].

The other branch, H-brunch, of the beamline accommodates SAXS/WAX experiments. The schematic layout of the BM26B is illustrated in Figure 2-4. The beam line receive 2

mrad of the radiation fan of an 0.8 Tesla bending magnet. The first optical element is a double crystal sagittal focussing monochromator, placed at 33 m from the source. It produces a monochromatic beam in the range 5-20 keV. The second optical element is a flat single crystal mirror placed at 37 m from the source. The mirror is made of two strips of optical surface. One of these strips is with the bare Si surface; the other one is coated with Pt. The sample is positioned at 48 m from the radiation source. In the experimental hutch a maximum sample to detector distance^[20] of 8 m can be achieved which is required to detect the low angle scattered radiation which contains information about larger (> 5 nm) structural features in the sample.

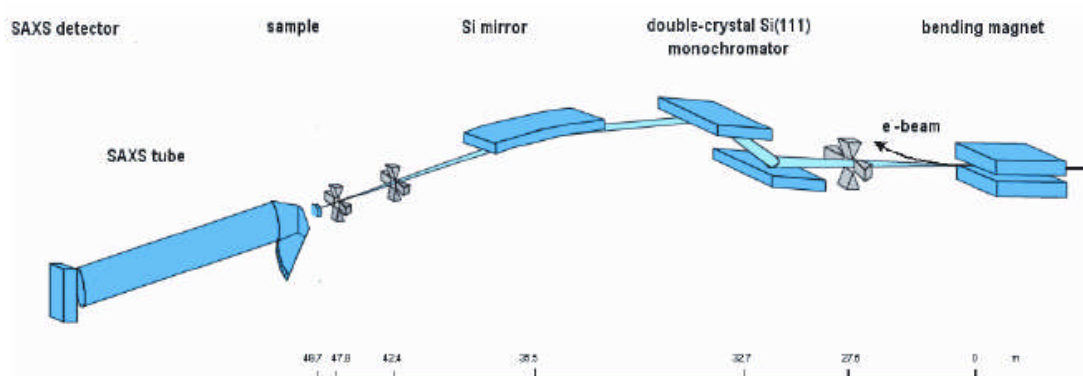


Figure 2-4 Schematic lay-out of the optical components in H-brunch, BM26B^[21].

The SAXS/WAXS^[16] data can be recorded simultaneously using a combination of two detectors. The SAXS data can be collected either by a gas filled quadrant detector or a Pilatus 1M detector. The WAXS patterns are currently acquired using a Pilatus 300K-W or CCD based X-ray digital camera, FReLoN 2000.

2.6 X-ray Absorption Fine Structure

X-ray absorption fine structure (XAFS) is a powerful tool for studying the structure of materials in chemistry, materials science, physics, biology and medicine. XAFS^[22] is a spectroscopic technique which provides information on the electronic and structural properties of crystalline, poly-crystalline and highly disordered materials. In principle

the XAFS information can be obtained for every element in the periodic table, as long as atoms have core level electron transitions in the energy range available on the beamline.

XAFS spectra are especially sensitive to the elemental oxidation state, coordination chemistry, distances, coordination numbers and species of atoms immediately surrounding the selected element. X-ray absorption in the photon energy range up to 40 keV is dominated by photoelectron absorption^[23].

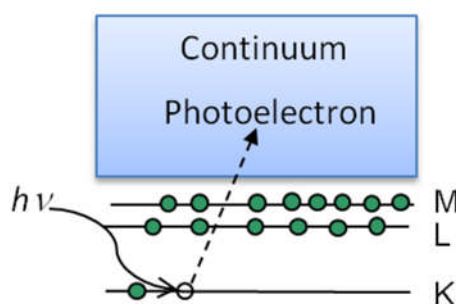


Figure 2-5 The photoelectric absorption process, whereby the core hole is created by the absorption of X-ray photon.

In the absorption process the photon is completely absorbed. Its energy is transferred to excite photoelectrons which leave behind a core hole in the atom. If all the absorbed photon energy goes into exciting a single core electron then kinetic energy can be represented by following expression:

Equation 2-5 The kinetic energy of the photoelectron

$$E_k = h\nu - E_b$$

where E_k – the kinetic energy of the excited photoelectron, $h\nu$ is the photon energy, E_b – the electron’s binding energy in the atom.

The outgoing photoelectron can be represented as a spherical wave with wavelength, λ ^[24]

Equation 2-6 *Wavelength of the outgoing photoelectron*

$$\lambda = \frac{2\pi}{k}$$
$$k = \sqrt{\left(\frac{8\pi^2m}{h^2}\right)(h\nu + E_0 - E_{edge})}$$

where k is the wave vector, m – electron mass and h – Planck's constant.

When the energy of the incoming photons is large enough to excite an electron from a deeper core level to a vacant excited state or to the continuum a sharp rise in the absorption intensity appears. The latter occurs because at energies below the edge X-ray photons do not have enough energy to excite electrons from, for instance, the $1s$ orbital, while above it they do. This sharp rise in absorption is marked as an absorption edge. At the absorption edge E_{edge} is kinetic energy of the electron E_k equal to E_0 – zero point energy or threshold energy which is the minimum photon energy required to eject an electron out of a particular atomic state. Any element of the Periodic table has a characteristic X-ray absorption edge energy, which is labelled according to the particular core level which is excited; for example K-edge corresponds to excitation of an electron from $1s$ orbital, while $2s$, $2p_{1/2}$ and $2p_{3/2}$ orbitals from L_{1-} , L_{2-} and L_{3-} edges respectively. Therefore, the position of the edge sensitively depends on the electronic structure of the absorber. This information can be used to identify for instance the chemical state of the atomic species.

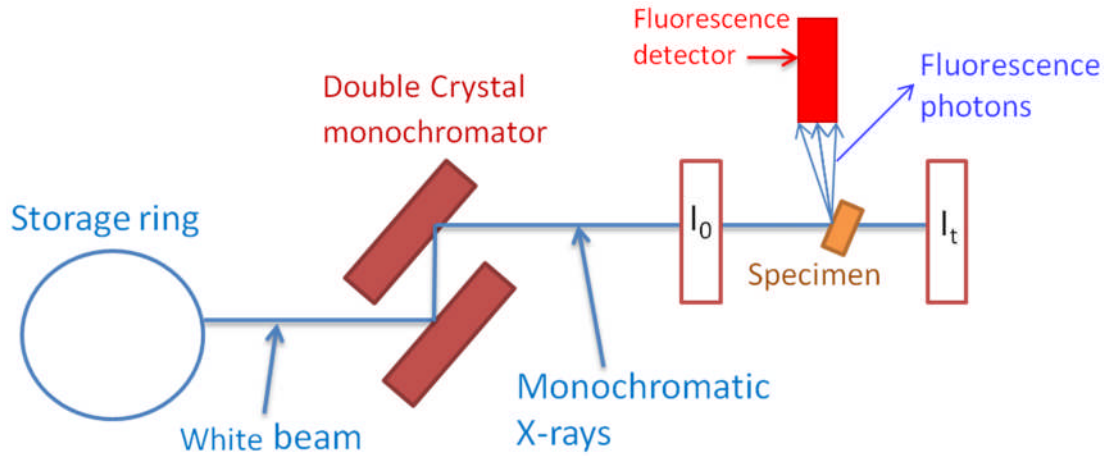


Figure 2-6 A schematic illustration of an experimental setup for recording X-ray absorption in transmission or fluorescence mode using synchrotron X-ray beam. For further details the reader is referred to the text.

In general for appropriately thin specimens with adequate atomic doping, the measurements of the X-ray absorption are performed in transmission geometry. In this case, X-rays with definite energy pass through a thin specimen and the ratio of incoming and transmitted X-ray beam is measured as function of photon energy. Some of the X-rays are absorbed by the atoms in the specimen, causing excitation or ejection of a core electron. This absorption can be quantified by comparing the incident beam intensity, I_0 , to the transmitted beam intensity, I_t . Once the absorption is determined for one energy of the incident X-rays, the energy is slightly increased and the process repeated. By stepping through of range energies an absorption spectrum is created, as shown in Figure 2-7. The measurement of X-ray absorption coefficient, μ , as a function of a photon energy E above the threshold of an absorption edge is calculated by Beer Lambert's Law.

Equation 2-7 Beer Lambert's Law

$$I_t = I_0 e^{-\mu(E)x}$$

where $\mu(E)$ is the linear absorption coefficient which describes absorption of the photons and x a specimen thickness, I_0 is the incident beam intensity and I_t is the

transmitted beam intensity. The variations on the Lambert-beer law due to the outer electron orbits define the EXAFS spectrum.

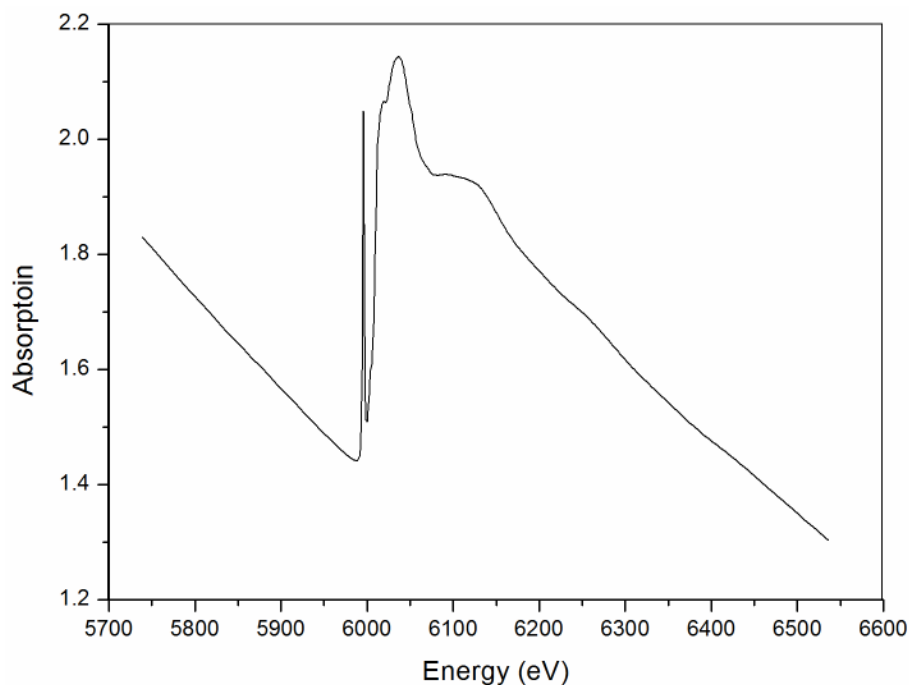


Figure 2-7 Raw Cr K-edge XAS spectrum of $K_2Cr_2O_7$ recorded in transmission mode. The y-axis is related to absorption of X-rays by the sample and the x-axis is the energy of the incident X-ray photons.

A typical experimental setup is illustrated in Figure 2-6. The absorption signal is measured by monitoring I_t and I_0 with suitable detectors, in this instance ionisation chambers, in which ion pairs are collected from the gases. In this process particles passing through a gas create both excited molecules and ionized molecules along its path. After a neutral molecule is ionized, the resulting positive ion and free electron are called ion pair. The ion pair serves as the basic constituent of the electrical signal generated by the ion chamber^[23]. The full XAFS spectrum is acquired by stepping the monochromator through the required energy range (Figure 2-7).

An alternative technique for measuring absorption is the detection of the fluorescence photons and electrons emitted by radiative decay of the core holes produced by X-ray

absorption events^[25]. Fluorescence is preferable for dilute specimens, i.e. low concentrations of elements in specimens, which cannot be measured in transmission.

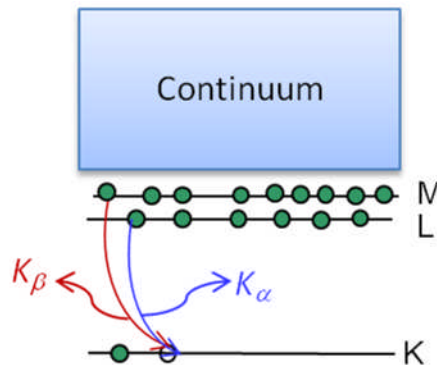


Figure 2-8 Decay of the excited state in fluorescent X-ray emission. The probability of X-ray emission is directly proportional to absorption probability.

Fluorescence^[3] radiation results from an electron from an outer shell (L shell) filling the core hole created by the absorption of an X-ray photon. This results in the emission of a photon with energy equal to the difference in the binding energies of the K and L electrons. The emitted radiation for the K shell is dominated by K α radiation. The energy of this radiation is characteristic of the absorbing element. The background consists of elastically and inelastically scattered radiation with higher photon energies than the fluorescent line. Thus, a fluorescence detector has to be able to discriminate between the signal from a fluorescence line and the background. In X-ray fluorescence measurements the measured signal is dictated by escape depth of the fluorescing X-rays. The probability of fluorescence is proportional to the absorption probability. Hence, the absorption coefficient as a function of photon energy can be expressed as the ratio of the incident X-ray intensity and the intensity of fluorescence X-rays.

Equation 2-8 Photon energy dependence of the absorption coefficient measured in fluorescence

$$\mu(E) = \frac{I_f}{I_0}$$

I_f – the intensity of fluorescence X-rays, I_0 – the intensity of incoming X-rays, $\mu(E)$ – the absorption coefficient

If a specimen measured in fluorescence geometry is thick and dense, i.e. the concentration of the absorbing species is too high, the self-absorption effect occurs^[26]. This means that a large proportion of the fluorescence radiation formed in the material is absorbed in the sample. As a result the fine-structure oscillations in XAFS spectrum are suppressed.

A typical XAFS spectrum, in this instance for a Mo foil, measured in transmission geometry is shown in Figure 2-9. The XAFS spectrum can be divided into two parts: X-ray Absorption Near Edge Structure (XANES) and Extended X-ray Absorption Fine Structure (EXAFS). XAFS is a unique signature of a given material, in that it depends not only on the detailed atomic structure but also the electronic and vibrational properties of the material^[27].

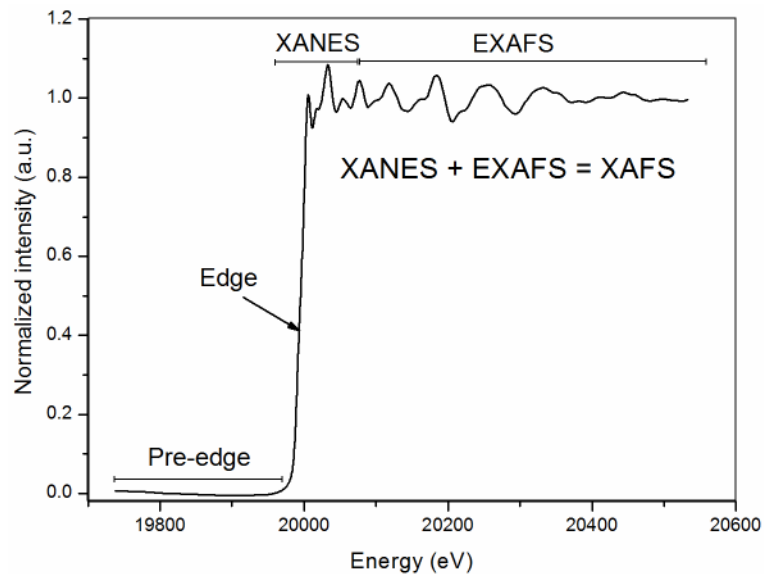


Figure 2-9 Mo K-edge XAFS of a Mo foil recorded in transmission geometry.

In order to retrieve structural information from XAFS data, it is necessary to separate the XAFS, i.e. $\chi(E)$ from the measured absorption $\mu(E)$, which represents the fractional modulation in the X-ray absorption coefficient^[28] (Equation 2-9).

Equation 2-9 *Normalization of the absorption coefficient in XAFS*

$$\chi(E) = \frac{\mu(E) - \mu_0(E)}{\mu_0(E)}$$

where $\mu(E)$ is the experimentally determined absorption coefficient and $\mu_0(E)$ is the 'background' absorption, i.e. the absorption of an 'isolated atom' which would be observed in the absence of XAFS effects. $\mu_0(E)$ cannot be measured directly and therefore it is approximated by fitting a smooth spline function through the data. Division by μ_0 normalizes the XAFS oscillations per atom and thus the XAFS spectrum is an average structure based upon the ensemble of the absorbing atoms. The determination of $\mu(E)$ consists of three steps^[29]. First one removes the pre-edge background, in which most of the energy dependence of the absorption other than that from the absorption edge of interest is eliminated. The second step is the normalization to the edge jump. The final step is the post edge background removal, whereby a smoothly varying background function which approximates the absorption from the isolated atom, $\mu_0(E)$, is subtracted from $\mu(E)$ to give $\chi(E)$. In fact, Equation 2-9 is not commonly used to extract $\chi(E)$ because the factor $\mu_0(E)$ in the denominator cannot be calculated accurately especially near absorption edge, E_0 ^[25]. In practice, the edge step normalization is performed and $\mu_0(E)$ in the denominator is replaced by $\mu_0(E_0)$ ^[30]. The $\mu_0(E_0)$ is the value of the background function evaluated at the edge energy.

Equation 2-10 *Normalization of XAFS performed in the widely used data analysis program Athena using AUTOBK algorithm^[29]*

$$\chi(E) = \frac{\mu(E) - \mu_0(E)}{\mu_0(E_0)}$$

Normalization of XAFS is an important process of standardising data treatment with respect to variations in sample preparations, sample thicknesses, absorber concentrations. Normalized data can be compared regardless of the details of the experiment.

2.6.1 XANES

The XANES region in a XAFS spectrum extends to about 50 eV beyond the absorption edge. A typical Cr K-edge XANES spectra of model compounds, $\text{K}_2\text{Cr}_2\text{O}_7$ and Cr_2O_3 , representing Cr^{6+} and Cr^{3+} oxidation states is shown in Figure 2-10. XANES spectrum provides information about coordination chemistry (regular, distorted octahedral, tetrahedral coordination), molecular orbitals ($p-d$ orbital hybridization), band structure (the density of available electronic states) and multiple scattering (multiple bounces of the photo-electron). An important application of XANES is to use the shift of the edge position to determine valence state of the absorbing atom. In addition, height and position of pre-edge peak can be reliably used to empirically determine oxidation states and coordination chemistry. These approaches of assigning formal valence states and coordination environments based on the edge and pre-edge features makes XANES a fingerprinting technique. Since the theoretical modelling of the XANES spectrum is complex, analyses of XANES are based on linear combinations of known spectra from 'model compounds' which can provide ratios of valence states or phases.

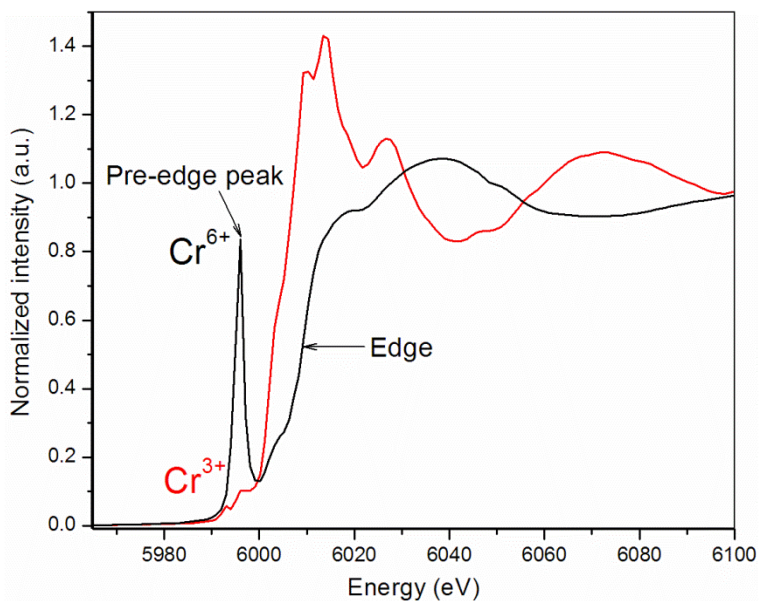


Figure 2-10 *Cr K-edge XANES spectra of $K_2Cr_2O_7$ in black and Cr_2O_3 in red representing Cr^{6+} and Cr^{3+} oxidations states respectively. The XANES spectrum of Cr_2O_3 shows a pre-edge doublet with very low intensity compared to $K_2Cr_2O_7$ which has an intense pre-edge peak. The latter is due to $1s-3d$ electronic transition. The pre-edge peak can be used as a signature identifying coordination geometry of chromium. The intense pre-edge peak in $K_2Cr_2O_7$ XANES indicates tetrahedral coordination of Cr^{6+} ions, while the pre-edge doublet in Cr_2O_3 suggests octahedrally coordinated Cr^{3+} ions.*

2.6.2 EXAFS

EXAFS refers to the oscillatory variations of the X-ray absorption as a function of photon energy beyond the absorption edge. The oscillatory variations in EXAFS were the first time explained by Kronig^[31] in 1932, who attributed it to the influence of the neighbouring atoms on the transition matrix elements in the short range order effect^[27]. Following the pioneering work of Sayers, Stern and Lytle^[32] in 1971 it was recognized that that wiggles in the EXAFS spectra could be used to obtain qualitative information about the local structure around an absorbing atom from a short range order theory.

2.6.3 EXAFS equation

The simplest EXAFS theory is based on the single scattering approximation^[27]. In this approximation the photoelectron created in the absorption process is viewed as a spherical wave that spreads out through the solid, much as a rock thrown in a pond creates and expands spherical wave in water. In the same way that water waves reflect off of any obstacles in the pond and in turn, reflect other waves back toward the original point of the splash, so will other atoms reflect the electron wave back towards the original atom. The amplitude of all reflected electron waves at the absorbing atom add either constructively or destructively to the outgoing photoelectron wave and hence modulate the matrix element between the initial and final states that controls the strength of the transition, as shown in Figure 2-11. Because this interference pattern changes with the energy of the photoelectron, the matrix element and consequently the absorption will exhibit similar oscillations^[27].

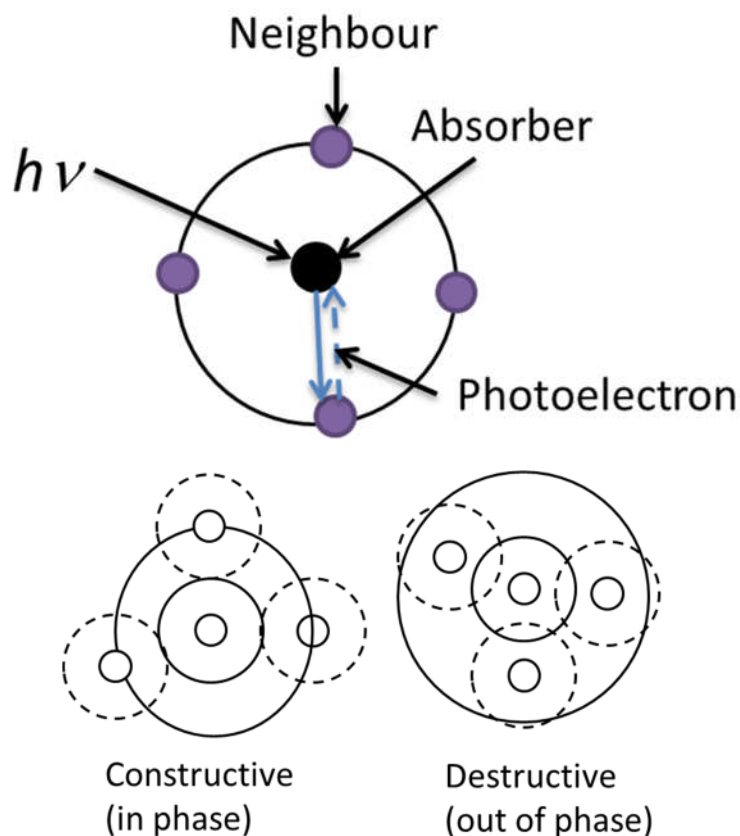


Figure 2-11 Schematic illustration of the photoelectrons (produced by photoelectric absorption), which are described as spherical waves propagating outward from the absorber atom (top). These photoelectrons waves are scattered from the neighbouring atoms producing backscattered waves. The interference between the outgoing and backscattered waves affects the probability of X-ray absorption by the absorber atom. When the waves are out of phase, this causes a minimum in the oscillatory part of the absorption coefficient, because the outgoing and backscattered waves meet at a minimum at the absorbing atom. A maximum in the oscillatory part of the absorption coefficient is produced when the outgoing and backscattered waves are in phase and meet at a maximum at the absorbing atom. The final phase is defined by the path length of both waves. Therefore, the interference pattern is determined by the distance to the neighbouring atoms.

Since EXAFS can be best understood in terms of the wave behaviour of the photoelectron created in the absorption process, it is common to convert X-ray energy to k , the wave number of the photoelectron, i.e. $\chi(E)$ to $\chi(k)$.

Equation 2-11 Definition of the photoelectron wave vector

$$k = \sqrt{\frac{2m(E - E_0)}{\hbar^2}}$$

where, E_0 is the absorption edge energy and m is the electron mass.

Consequently, EXAFS, $\chi(k)$, refers to the oscillations as a function of photoelectron wave number. The EXAFS extracted from Mo K-edge in this way, for a Mo-foil is shown in Figure 2-12. To emphasise the oscillations, $\chi(k)$ is multiplied by a power of k typically k^3 , as shown in Figure 2-13. In addition to that, it compensates for attenuation of EXAFS at higher k values and prevents the large oscillations at low k values.

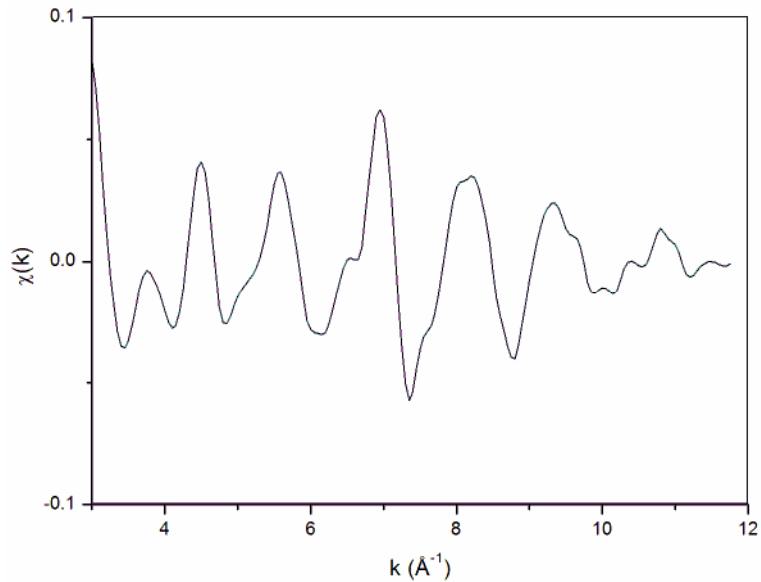


Figure 2-12 Isolated EXAFS $\chi(k)$ for a Mo foil.

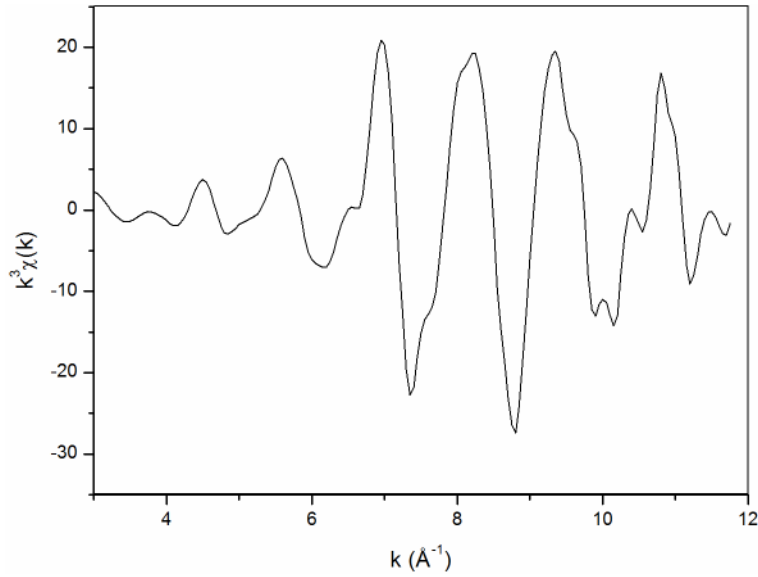


Figure 2-13 Isolated k^3 -weighted EXAFS $\chi(k)$ for a Mo foil.

The EXAFS spectrum can be thought of to be composed of a weighted addition of a range of waves with different wavelengths/frequencies. The different frequencies apparent in the oscillations in $\chi(k)$ correspond to different near neighbour coordination shells which can be described and modelled according to the EXAFS equation.

Equation 2-12 EXAFS equation

$$\chi(k) = \sum_j \frac{N_j f_j(k) S_0^2}{k R_j^2} e^{-2k^2 \sigma_j^2} \sin[2kR_j + \delta_j(k)]$$

where j represents the individual coordination shell of identical atoms at approximately the same distance from the central atom. $f_j(k)$ and $\delta_j(k)$ are scattering properties of the atoms neighbouring the excited atom i.e. $f_j(k)$ is the magnitude of the backscattering amplitude of the neighbouring atom and $\delta_j(k)$ is the electronic phase shift due to the atomic potentials. These scattering factors depend on the atomic number, Z , of the neighbouring atom. N_j is the coordination number of the j^{th} shell. R_j is the mean distance between the absorbing atom and the j^{th} shell. σ_j^2 is the Debye-Waller factor for the j^{th} shell, i.e. the mean square displacement in bond distance R due to thermal motion and structural disorder. It can be represented in a good approximation as superposition of

static (σ_s^2) and dynamic (σ_d^2) terms (Equation 2-13). k is the photoelectron wave vector defined by Equation 2-11. The S_0^2 term, (in EXCURVE98 called AFAC), is an amplitude reduction factor representing many body effects such as central atom shake up, (excitation of other electrons along with the photoelectron) and shake off (ionisation of weakly bound electrons by the photoelectrons) excitations in which more than one electron is excited in a transition^[24, 27]. Typically, S_0^2 has a value between 0.7 and 1. The factor of 2 in the term $2kRj$ in equation 1.12 is present because the photoelectron needs to travel from the absorbing atom to the scattering atom and back.

Equation 2-13 *Mean square deviation of bond distances*

$$\sigma^2 = \sigma_s^2 + \sigma_d^2$$

From the EXAFS equation N , R and σ^2 can be determined if one knows the scattering amplitudes $f(k)$ and phase shift $\delta(k)$. For a specific structural model these factors can be calculated. Obviously this is a rather elaborate process and for this reason the programs^[33], FEFF^[34] and EXCURVE98^[35] have been developed and are used in the analysis of the data presented in this work

Although a complete description of the EXAFS oscillations in Figure 2-13 can be described by Equation 2-12, it is not particularly convenient for visualizing the information from an EXAFS spectrum. Therefore, Fourier transform defined in Equation 2-14 can be used to separate the neighbouring atoms according to their distances from the central atom.

Equation 2-14 *Fourier transform*

$$FT(R) = \frac{1}{\sqrt{2\pi}} \int_{k_{min}}^{k_{max}} k^n \chi(k) e^{i2kR} dk$$

The Fourier transform of the EXAFS spectrum gives a ‘pseudo’ radial distribution function defined in R -space. The distance in the FT is about 0.2-0.5 Å shorter than the actual distance due to energy dependence of the phase factors in the sin function

(Equation 2-12), therefore, the magnitude of the FT (Figure 2-14) is only related to radial distribution function. The FT can be taken with different k weightings (multiplication by k^n). This can be used to distinguish between high and low Z scatterers around absorbing atom. Weighting of the Fourier transformation emphasise the important scatterer in a specific region.

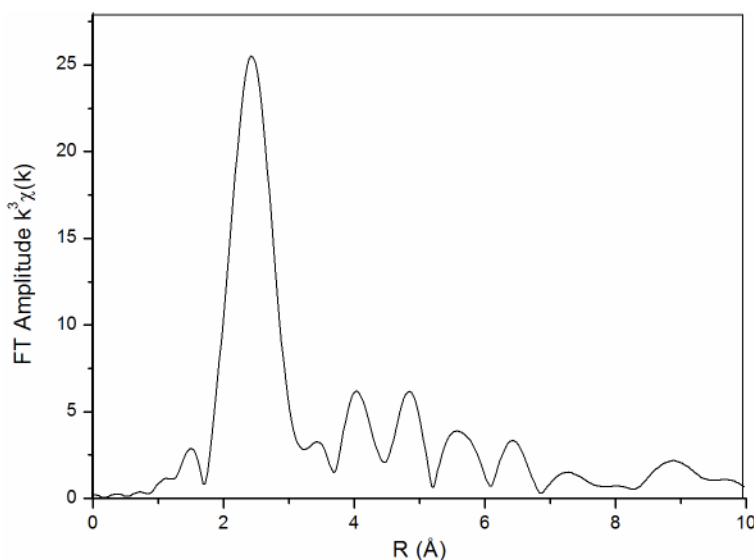


Figure 2-14 Amplitude of the Fourier transform data form Figure 2-13.

Analyses of the EXAFS data renders unique information on the local environment of the absorbing atom, in particular, the distances and coordination numbers of the shells of atoms immediately surrounding the absorbing species which are in some cases unavailable from other techniques. Bond distances can be obtained with accuracy less than 0.01Å for the first coordination shell^[25].

2.7 Total Electron Yield X-ray Absorption Spectroscopy

Total electron yield X-ray absorption spectroscopy (TEY-XAS) renders near surface EXAFS data which are obtained by direct measurements of the photo electric current when a sample is exposed to X-ray^[36]. TEY-XAS is an indirect measurement of the absorbed intensity, in this instance number of the number of Auger electrons emitted during the core hole decay, as a function of photon energy. Detection of Auger electrons

can be performed under vacuum conditions^[36] or in gaseous environments^[37]. The simple experiment consists of measuring the drain current from the sample while maintaining a moderate electric field over the sample using a biased counterelectrode.

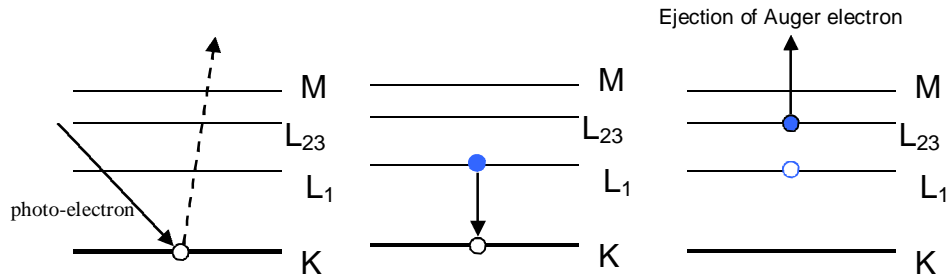


Figure 2-15 The first step during an Auger process^[38] is the removal of electrons from inner atomic levels created by ionisations due to X-ray photons. This creates a hole in the K-shell and causes an energetically unstable situation. The relaxation takes place by filling the hole with an electron from an L₁ shell. As a consequence the amount of energy ($K - L_1$) is released which can be given to another electron or emitted as a photon. If the second electron originating from the same shell or higher shell e.g. L₂₃ has sufficient excess kinetic energy, it will be ejected from the surface to the vacuum or ambient, where its energy can be measured. The second electron is called an Auger electron and its energy is ($K - L_1 - L_{23}$). This Auger transition can be labelled KL_1L_{23} .

When photoelectron absorption takes place, the atom is left with a vacancy in its electron shell. This vacancy is filled with an electron from an outer shell, but in some cases the energy excess that is released is sufficient to eject another electron from the same or higher shell. The free electrons that are created in this way are called Auger electrons^[39] (Figure 2-15). Their energy is given by the difference between the original atomic excitation energy and the binding energy of the shell from which electron was ejected. Auger electrons show a discrete energy spectrum with different energy groups corresponding to different initial and final state. Auger electrons emission is preferred for light Z-elements which have small electron binding energies. The relative probability of non-radioactive decay of single core vacancy depends on the atomic number of the absorbing species and have been tabulated by Krause^[40].

TEY experiments under non vacuum conditions can be carried out using an ionization chamber with wire anode detectors operating with ‘standard’ gas mixtures commonly used in proportional counters. ‘Standard’ gas mixtures are typically small proportions of alkane quencher gases in a noble gas. However, these detectors have some drawbacks and it is not possible to measure the electron energy. Therefore, these detectors have been replaced by a gas microstrip detector (GMSD) initially developed by Oed^[41] for position sensitive detectors but later adapted for energy discriminating electron yield XAFS at ambient pressures. The GMSD consists of a glass plate, lithographed with a pattern of 10 μ m wide anode strips interleaved with 90 μ m wide cathode strips, with a pitch of 300 μ m. Strips are bussed into groups with the active counting area of 12mm x 6mm^[42]. If one group of these strips is held at a high positive potential with respect to the neighbouring strips, in a suitable gas atmosphere these strips function as the anodes of an avalanching gas counter and can produce a gain of $\sim 10^3$ charges per initially formed electron. With appropriate amplifier and counting electronics, the GMSD accept electron impingement rates of 250 kHz/mm² with negligible loss of gain and 12 % energy resolution at X-ray energies of 8 keV^[41, 43].

The basic operating principle of detectors which use a gas mixture as detecting and signal amplification medium relies on the fact that a charged particle moving rapidly through the gas causes ionizations along its path and creating ion-electron pairs. If an electric field is applied across the gas volume, the electrons and positive ions will move toward anode and cathode respectively, thus producing a detectable electrical signal. Photons may be detected when a primary ionizing interaction with a gas molecule takes place. This produces a fast electron which then causes further ionization along its path. By adapting the configuration of the electric field, gas filled detectors may be operated in a variety of different modes^[44].

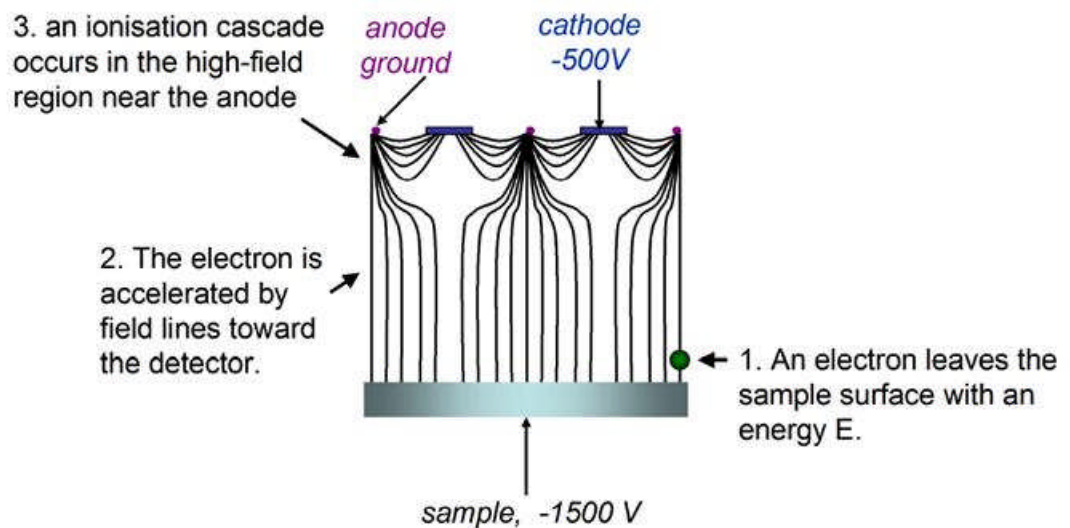


Figure 2-16 The characteristic field lines associated with electron yield detection using the GMSD. The sample bias is set to a high negative potential which creates drift field accelerating the signal electrons towards the detector plate. The electron avalanche occurs because of ionization of the gas molecules by the accelerated electrons and is situated only a few micrometres from the detector plate^[45].

If the electric field in gas filled proportional detector is sufficiently high electrons are accelerated to a point, where they are capable of causing further ionization (Figure 2-16). This results in avalanche of electrons which amplifies the original signal^[42]. The size of the ionization avalanche is proportional to the initial kinetic energy of the detected electrons as they leave the sample surface. Since the detector is operated as proportional counter measuring electron energies, it is possible to discriminate between electron energies via analysis of the charge pulse intensities.

2.8 Energy Resolved Electron Yield X-ray Absorption Spectroscopy

On the basis of the functional principles behind the GMSD Rayment et al.^[43] have developed a technique known as Energy resolved electron yield X-ray absorption spectroscopy (EREY-XAS). The basic concept of the technique is that the Auger electrons lose energy by various inelastic collision processes as they propagate to a surface. Therefore, the emergent electron energy profile contains information about the

structure as a function of depth from the surface. In other words, electrons emitted with energies close to the Auger energy must have originated close to the surface, and conversely those emerging with low energy most probably originated from the bulk of the material (Figure 2-17).

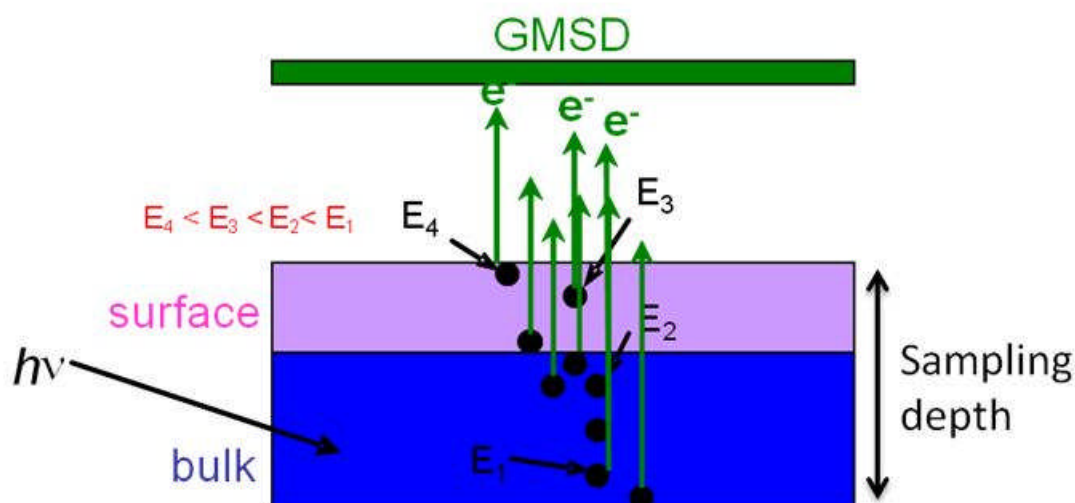


Figure 2-17 Detection of Auger electrons using GMSD detector at ambient conditions, where E is the energy of electron, e^- , escaping from the sample surface or bulk into ambient; $h\nu$ is the incident X-ray photon energy.

With the GMSD detector it is possible to detect electrons at ambient atmosphere pressures by using the sample like an internal photocathode for gas flow ionisation detector^{[46],[43]}. The signal measured by this technique is total electron yield (TEY), modified by electron multiplication in the gas phase due to impact ionization events^[37]. The TEY includes contributions from secondary electrons, inelastically scattered Auger electrons, elastic Auger electrons and a negligibly small number of photoelectrons^[37]. The Auger contributions dominate the signal in gaseous environments, because they can only escape from a thin layer near the sample surface. Typical escape depths for Auger electrons are between 100 Å and 1000 Å, thus enabling studies of epitaxially grown films^[47], corrosion layers^[48] and thin film bilayers^[49]. The maximum surface sensitivity in an electron yield experiment is achieved by selective detection of the elastic and quasi-elastic Auger electrons in the high energy region of the TEY spectrum^[50].

In addition, Rayment et.al.^[43] improved the design of the GMSDs in the way that these detectors could be operated not only with the gas mixtures normally used in proportional counters but also with the majority of gas mixtures used in common catalytic reactions^[51], for instance, CO₂, O₂, H₂, H₂O as long as they are mixed with a small percentage of isobutene (5%) in helium.

2.8.1 Description of electron yield detector vessel accommodating the GMSD

A schematic view of the detector assembly is shown in Figure 2-18. It consists of a stand for mounting the vessel onto a goniometer. A bottom flange holds the sample at the center of rotation. It also accommodates the gas inlet and outlet and an electrical feed-through for the sample bias.

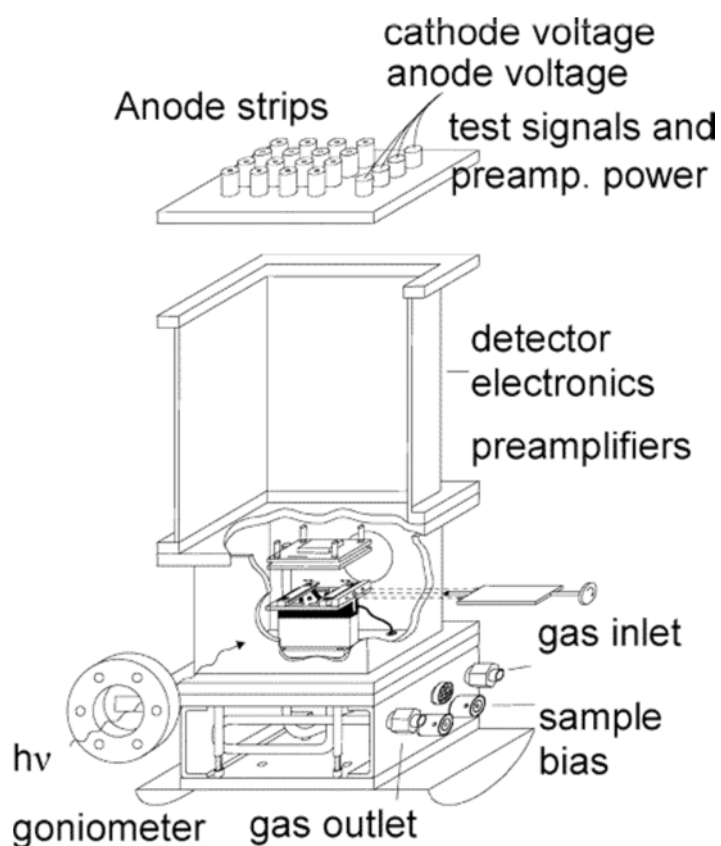


Figure 2-18 Cut away sketch of the electron yield detector^[51].

The GMSD is mounted on the top flange facing down towards the sample, leaving a gap of 11 mm between the sample and the detector plate. All electrical connections to the GMSD come through this top plate from an electronic enclosure mounted on the outside of the flange. The electronic enclosure is made of aluminum. It houses and shields a set of preamplifiers, shaping amplifiers, and high-voltage and low-voltage power supply filtering. Sample changing takes place through a side flange, while the system remains mounted and aligned on the beamline. Studied samples can be thin films, powder pressed into a pellet in graphite and powder deposited onto flat substrate.

2.8.2 Calibration of the electron yield detector

During electron yield energy resolved EXAFS experiments it is necessary to calibrate the detector. This is done by recording spectrum from the detector whilst the sample is moved out of the beam and the counts that are recorded on the GMSD are the result solely of interactions of the X-ray beam with the detection gas. This produces a spike at definite energy of the incoming photons. The actual signal resembles a Gaussian distribution. The position of the peak is used to calibrate the energy scale of the Pulse Height Distribution (PHD) spectra, whilst the peak full-width at half maximum (FWHM) gives the instrumental broadening.

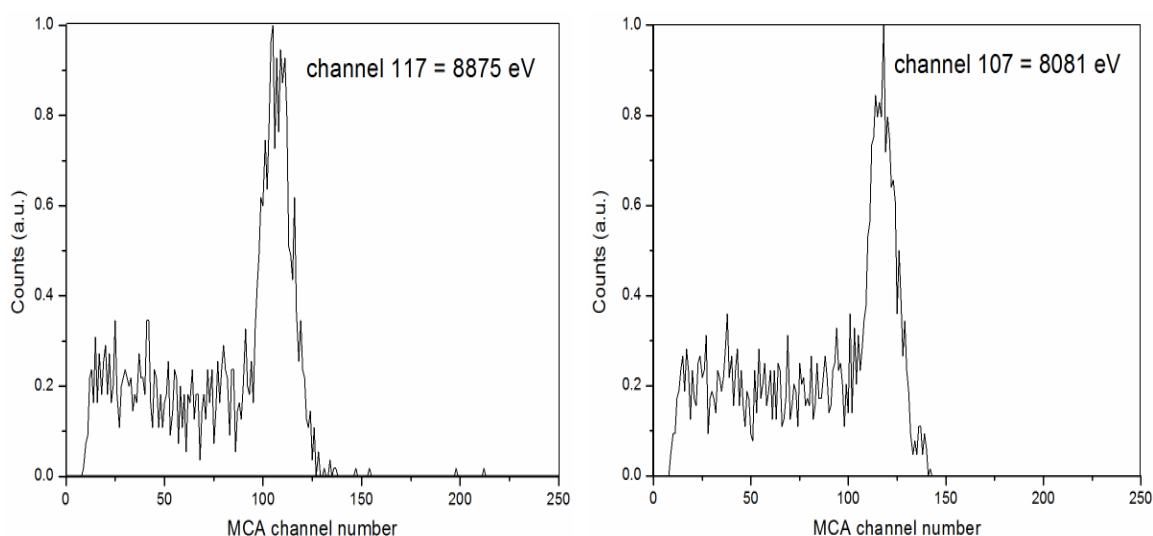


Figure 2-19 PHDs taken from X-ray intensity measurements without a sample at the start (left) and end (right) of an EXAFS scan.

In Figure 2-19 PHD spectra collected at the start and end of EXAFS scan, whilst the sample was moved out of the X-ray beam are shown. These spectra were used for calibrating the electron energy scale with respect to detector channel, as shown in Figure 2-21.

2.8.3 Analysis of energy-resolved XAS data

To obtain pulse height distributions (PHDs) as a function of the monochromator position a program named *Reduce* was developed. The program was written by John Lipp, STFC, UK. This program combines information from the station computer with data collected by the electron yield detector. The various steps performed during this process are summarized in Figure 2-20.

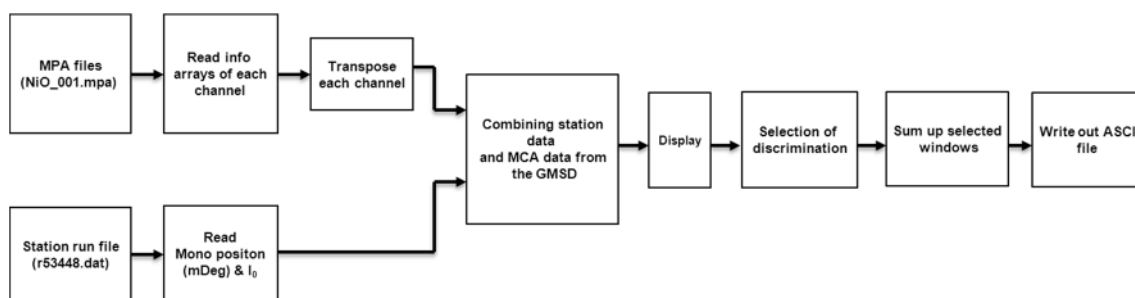


Figure 2-20 Operation performed by *Reduce* software in order to obtain raw EYER–XAS data.

First, the *Reduce* software requires inputting information such as which set of multichannel analyser (MCA) files corresponds to which EXAFS scan. After combining the two sets of data (station data e.g. r56448.dat and MCA data e.g. NiO_001.mpa), a 2D matrix is obtained which gives information on the PHD at each step of the monochromator. The 2D matrix contains a summed up data from all channels of the MCA. However, if one of the channels did not work properly, it can be omitted. In the next step the MCA data are divided into different Auger electron energy regions (Figure 2-21) and the number of counts within each region is integrated. The decision how to divide PHDs is based on the quality of data, i.e. signal to noise ratio and objectives of the study. Once EYER–EXAFS spectra for total electron yield and

different Auger electron energy regions are generated, they can be saved in ASCII file format. Last step is to divide the total electron yield data and EYER–XAFS by I_0 (in Origin or Excel). Finally, EYER–XAFS spectra can be processed by standard procedures for XAFS analysis. The normalized EYER–XANES are shown in Figure 2-22. In this instance the data obtained with a NiO/Ni thin film sample, which was used for calibration of the electron yield detector, is presented. Its bilayer structure consisted of 150 nm thick Ni layer covered by NiO overlayer with thickness of 25 nm deposited onto a Si(100) substrate. Recorded data were used as ‘internal standards’ which were compared to that in literature during the implementation of the electron yield detector on the EXAFS beamline (BM26A) and subsequent data analyses. The results of the analyses were in good agreement with those reported in the literature^[43, 49] and will be not discussed farther since there was not the subject of this thesis.

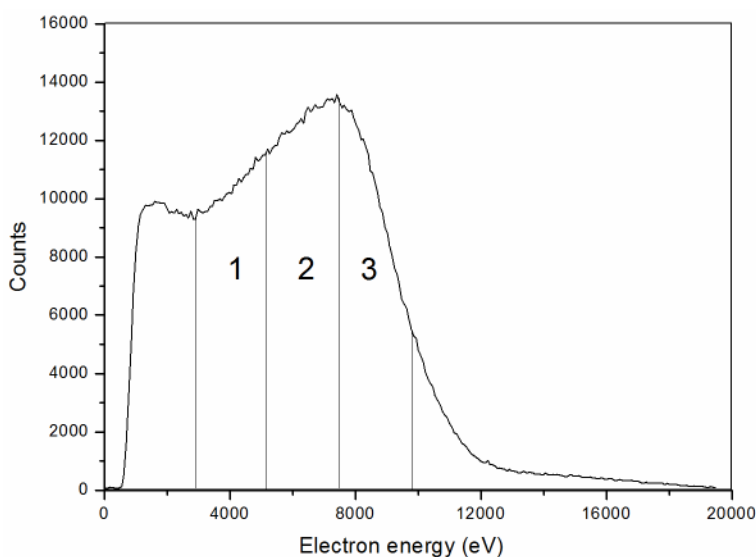


Figure 2-21 Typical PHD recorded at Ni K-edge showing sampled 4 different energy regions.

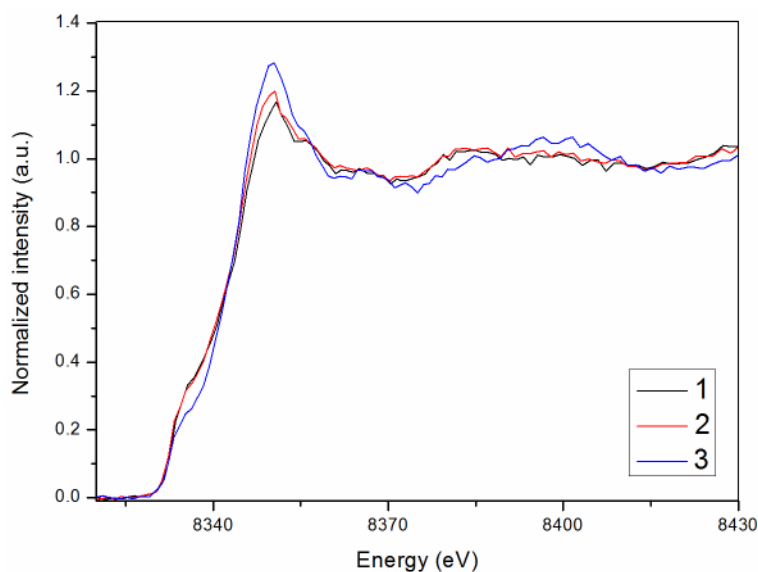


Figure 2-22 Normalized EYER XANES spectra of NiO/Ni film. The spectra were obtained from the Auger electron regions marked in Figure 2-21 using Reduce.

2.9 Other techniques

2.9.1 Raman spectroscopy

Raman spectroscopy is a spectroscopic technique based on inelastic scattering of an intense monochromatic and coherent light from a laser in the visible, near infrared or near ultraviolet range. In the inelastic scattering process the frequency of photons in monochromatic light changes upon interaction with sample atoms. Photons produced by laser light are absorbed by the sample and then reemitted. Frequency of reemitted photons is shifted up or down in comparison with original monochromatic frequency. This shift provides information about vibrational, rotational and other low frequency transitions in molecules. The vibrational information is specific to the chemical bonds and symmetry of molecules. The information is related to the chemical bonds, symmetry of molecules, and the nature of chemical species present in the gas, solid or liquid phase. In general, Raman spectra are used as fingerprints to identify the presence of molecular species in samples^[52].

2.9.2 Scanning Electron Microscopy

The information about the microstructural characteristics of solid objects in a sample can be obtained from Scanning electron Microscopy (SEM) technique. This microscope technique is capable of obtaining images from the sample surface and bulk. From SEM images can be obtained information about samples morphology, particles shapes, dimensions and their distribution in the material. In a typical experiment, the sample is exposed to the electron beam under vacuum conditions. SEM images are obtained as a result of interaction the electron beam with the sample, whereby a number of scattering and emission events take place^[53].

2.9.3 X-ray photoelectron spectroscopy

X-ray photoelectron Spectroscopy (XPS) is a surface sensitive technique that renders information about the elemental chemical composition, electronic states of species embedded within the top atomic layer of a material^[54] and is thus renders complementary results to EYER. XPS is based on the irradiation of a sample in ultra-high vacuum conditions by soft monochromatic X-rays typically Al K_α ($h\nu=1486.5$ eV) and analysing the energy of the detected electrons. The spectrum is obtained by plotting the number of detected electrons per energy interval versus their kinetic energy. Since the mean free path of electrons in solids is very small, the detected electrons originate from only the top few atomic layers (1 to 10 nm) of a material. The interaction of photons with sample atoms in the surface region can be described by the photoelectric effect. The kinetic energy of the emitted electrons can be expressed as follow^[55]:

Equation 2-15 *The kinetic energy of the emitted electron in XPS measurements*

$$E_k = h\nu - E_b - \phi_s$$

where $h\nu$ the energy of the incoming photons, E_k is the binding energy of the atomic orbital from which the electron originates, and ϕ_s is the spectrometer work function.

Quantitative data of the XPS measurements can be obtained from peak heights or peak areas. Identification of chemical states is made from exact measurements of peak positions and separations^[54].

References

- [1] W. C. Rontgen, *Science of radiology*, Springfield, IL **1933**, 1-14.
- [2] L. Zehnder in *First X-ray picture: The hand of Roentgen wife*, Vol. Wikipedia, **1896**.
- [3] J. Als-Nielsen and D. McMorrow, *Elements of Modern X-ray Physics*, Wiley, **2001**, p. 1-29.
- [4] B. B. He, *Two Dimensional X-Ray Diffraction*, John Wiley & Sons, **2009**, p. 1-25.
- [5] P. E. Ewald, *International Union of Crystallography* **1962**, 31-73.
- [6] in *International Centre for Diffraction Data (ICDD) PDF-2*, Vol. **Realese 2003**.
- [7] H. Rietveld, *Acta Crystallographica* **1967**, 22, 151-152.
- [8] J. Rodriguez-Carvajal, *Physica B.*, **1993**, 192, 55-69; J. Rodriguez-Carvajal, *Commission on Powder Diffraction (IUCr), Newsletter* **2001**, 26, 12-19; Rodriguez-Carvajal Juan, *An Introduction to the Program FullProf 2000 (Version July 2001)*, <http://www.ill.eu/sites/fullprof/php/tutorials.html>, **2001**, p.
- [9] G. Margaritondo, *Introduction to Synchrotron Radiation*, **1988**, p. 9-45.
- [10] P. M. Larmor and A. Lienard, *L' Eclairage Electrique* **1898**, 16, 106.
- [11] G. A. Schott, *Annals of Physics* **1907**, 24, 635.
- [12] D. Ivanenko and I. Y. Pomeranchouk, *Physical Review* **1944**, 65, 343.
- [13] D. H. Tombouljian and P. L. Harman, *Physical Review* **1956**, 102, 1423.
- [14] A. O. Benz, *Nature* **2001**, 410, 310-311.
- [15] M. Borsboom, W. Bras, I. Cerjak, D. Detollenaere, D. Glastra van Loon, P. Goedtkindt, M. Konijnenburg, P. Lassing, Y. K. Levine, B. Munneke, M. Oversluizen, R. van Tol and E. Vlieg, *Journal of Synchrotron Radiation* **1998**, 5, 518-520.
- [16] S. Nikitenko, A. M. Beale, A. M. J. van der Eerden, S. D. M. Jacques, O. Leynaud, M. G. O'Brien, D. Detollenaere, R. Kaptein, B. M. Weckhuysen and W. Bras, *Journal of Synchrotron Radiation* **2008**, 15, 632-640.
- [17] M. Altarelli, *Physica Scripta* **1991**, T34, 73-76.
- [18] G. Derbyshire, K. C. Cheung, P. Sangsingkeow and S. S. Hasnain, *Journal of Synchrotron Radiation* **1999**, 6, 62-63.
- [19] W. Bras, G. E. Derbyshire, A. J. Ryan, G. R. Mant, A. Felton, R. A. Lewis, C. J. Hall and G. N. Greaves, *Nuclear Instruments & Method in Physics Research Section a-Accelerators* **1993**, 326, 587-591.
- [20] W. Bras, *Journal of Macromolecular Science: Physics B* **1998**, 37, 557-566.
- [21] W. Bras, I. P. Dolbnya, D. Detollenaere, R. Van Tol, M. Malfois, G. N. Greaves, A. J. Ryan and E. Heeley, *Journal of Applied Crystallography* **2003**, 36, 791-794.
- [22] D. C. Koningsberger and R. Prins, *X-ray Absorption: Principles, Applications, Techniques of EXAFS, SEXAFS, and XANES*, Wiley, **1988**, p. 443-572.
- [23] G. F. Knoll, *Radiation detection and measurements*, John Wiley & Sons, Inc., **1988**, p. 131-156.
- [24] D. C. Koningsberger, B. L. Mojet, G. E. van Dorssena and D. E. Ramaker, *Topics in Catalysis* **2000**, 10, 143-155.
- [25] D. C. Koningsberger and R. Prins, *X-ray absorption. Principles applications, techniques of EXAFS, SEXAFS, and XANES*, Jon Wiley & Sons, **1992**, p. 443-572.
- [26] G. Almkvist, K. Boye and I. Persson, *Journal of Synchrotron Radiation* 17, 683-688.
- [27] J. J. Rehr and R. C. Albers, *Reviews of Modern Physics* **2000**, 72, 621-654.
- [28] B. K. Teo, *EXAFS: Basic Principles and Data Analysis*, **1986**, p. 114-157.
- [29] M. Newville, P. Livins, Y. Yacoby, J. J. Rehr and E. A. Stern, *Physical Review B* **1993**, 47, 14126-14131.
- [30] B. Ravel and M. Newville, *Journal of Synchrotron Radiation* **2005**, 12, 537-541.

- [31] R. D. L. Kronig, *Zeitschrift für Physik A Hadrons and Nuclei* **1931**, 70, 317-323.
- [32] D. E. Sayers, E. A. Stern and F. W. Lytle, *Physical Review Letters* **1971**, 27, 1204.
- [33] M. Vaarkamp, I. Dring, R. J. Oldman, E. A. Stern and D. C. Koningsberger, *Physical Review B* **1994**, 50, 7872-7883.
- [34] J. Mustre de Leon, J. J. Rehr, S. I. Zabinsky and R. C. Albers, *Physical Review B* **1991**, 44, 4146-4156.
- [35] N. Binsted and S. S. Hasnain, *Journal of Synchrotron Radiation* **1996**, 3, 185-196; S. J. Gurman, N. Binsted and I. Ross, *Journal of Physics C-Solid State Physics* **1984**, 17, 143-151.
- [36] A. Erbil, G. S. Cargill III, R. Frahm and R. F. Boehme, *Physical Review B* **1988**, 37, 2450-2464.
- [37] L. M. Schroeder, G. D. Moggridge, R. M. Ormerod, T. Rayment and R. M. Lambert, *Surface Science* **1995**, 324, L371-L377.
- [38] J. C. Riviere, *Contemporary Physics* **1973**, 14, 513-539.
- [39] Landman U. and Adams D.L., *Proceedings of National Academy of Sciences* **1976**, 73, 2550-2553.
- [40] M. O. Krause, *Journal of Physical and Chemical Reference Data* **1979**, 8, 307-327.
- [41] A. Oed, *Nuclear Instruments and Methods in Physics Research A263* **1988**, 351-359.
- [42] J. E. Bateman, J. F. Connolly, G. E. Derbyshire, D. M. Duxbury, J. Lipp, J. A. Mir, R. Stephenson, J. E. Simmons and E. J. Spill in *Gas Microstrip X-Ray detectors for application in synchrotron radiation experiments, Vol. RAL-TR-1999-056* Rutherford Appleton Laboratory, Didcot, **1999**.
- [43] T. Rayment, S. L. M. Schroeder, G. D. Moggridge, J. E. Bateman, G. E. Derbyshire and R. Stephenson, *Review of scientific instruments* **2000**, 71, 3640-3645.
- [44] J. E. Bateman, R. Barlow, G. E. Derbyshire, J. A. Mir and R. Stephenson in *High gain gas microstrip detectors for soft X-ray detection, Vol. RAL-TR-2001-031* Rutherford Appleton Laboratory, Didcot, **2001**.
- [45] B. Abbey in *Vol. PhD* University of Cambridge Cambridge, **2006**.
- [46] S. L. M. Schroeder, G. D. Moggridge, R. M. Ormerod, R. M. Lambert and T. Rayment, *Physica B: Condensed Matter* **1995**, 208-209, 215-216.
- [47] Y. U. Idzerda, W. T. Elam, B. T. Jonker and G. A. Prinz, *Physical Review Letters* **1989**, 62, 2480.
- [48] F. W. Lytle, R. B. Gregor, G. L. Bibbins, K. Y. Blohowiak, R. E. Smith and G. D. Tuss, *Corrosion Science* **1995**, 37, 349-369.
- [49] B. Abbey, J. D. Lipp, Z. H. Barber and T. Rayment, *Journal of Applied Physics* **2006**, 99, 124914-124919.
- [50] A. Erbil, G. S. Cargill, R. Frahm and R. F. Boehme, *Physical review B* **1988**, 37, 2450-2465; Schroeder L.M., *Solid State Communications* **1996**, 98, 405-409.
- [51] A. Vollmer, J. D. Lipp, J. R. I. Lee, G. E. Derbyshire and T. Rayment, *Analytical Chemistry* **2003**, 75, 6571-6575.
- [52] E. Smith and G. Dent, *Modern Raman spectroscopy: A practical approach*, John Wiley & Sons, Inc., **2005**, p. 135-172.
- [53] H. Todokoro, M. Ezumi, Y. Ose and N. Suzuki in *Scanning Electron Microscope, Vol. 7,399,966* (Ed. U. S. Patent), Hitachi, Ltd., Tokyo, Japan, **2008**.
- [54] C. D. Wagner, *Handbook of X-ray Photoelectron Spectroscopy*, Perkin-Elmer, **1981**, p. 1-43.
- [55] A. A. Verberckmoes, B. M. Weckhuysen and R. A. Schoonheydt, *Microporous and Mesoporous Materials* **1998**, 22, 165-178.

Chapter 3 Combined XANES/XRD/RAMAN and EXAFS/XRD studies on Bi₂MoO₆ formation

3.1 Chapter Overview

In this chapter, it is shown that the combination of High Resolution Powder Diffraction (HRPD) with Raman and X-ray absorption Near Edge Structure (XANES) in a single experimental setup can be a powerful tool for studying structural changes in chemical reactions. As examples reactions which take place under mild hydrothermal conditions are given. More importantly, it is shown that high quality HRPD data can be obtained simultaneously and be used for identifying intermediate phases present during the course of the reactions.

It is also shown that combined EXAFS/XRD (Extended X-ray Absorption Fine Structure and X-ray Diffraction) experiments can be performed as long as reaction conditions are carefully controlled. In this case, this was achieved by slowing down the reaction process by lowering the crystallization temperatures. The instrumental time-resolution required to obtain an appropriate data quality was matched to the time scale relevant for the chemical reaction kinetics.

In addition, the methodology for deriving reaction kinetics from XANES is described. Using these procedures the reaction kinetics of γ -Bi₂MoO₆, formed from an amorphous gel was obtained.

3.2 Introduction

Bismuth molybdates belonging to $\text{Bi}_2\text{O}_3 \cdot n\text{MoO}_3$ system, where $n = 3$ (α -phase), $n = 2$ (β -phase) and $n = 1$ (γ -phase), are industrially used for the selective oxidation of lower olefins, in particular, the selective oxidation of propylene to acrolein, the ammoxidation of propene to acrylonitrile and the oxidative dehydrogenation of n-butane to 1,3-butadiene^[1, 2].

Industrial development of oxidation catalysts started with a patent by Herne and Adams^[3] in 1948, who produced acrolein from propylene using copper oxide catalysts. In 1960 Veath et al.^[4] reported the (amm)oxidation of propene to acrolein and acrylonitrile by using a bismuth phosphomolybdate catalyst. This catalyst composition was 50% $\text{Bi}_9\text{PMo}_{12}\text{O}_{52}$ /50% SiO_2 . Silica gel acted as support to prevent disintegration of the active material in fluidised bed operation.

Simultaneously researchers at the Standard Oil Company of Ohio were working on the development of selective (amm)oxidation catalysts of light hydrocarbons. Their research concept was based on simple hypotheses^[5]. They postulated that the lattice oxygen of multivalent transition metal oxides can serve as a more versatile and more selective oxidizing agent than gaseous dioxygen. Therefore, the reactive surface lattice oxygens must be structurally isolated from each other in defined groupings on a catalyst surface to achieve selectivity. The number of oxygens in a given isolated grouping (domain) would determine the reaction channel through the stoichiometry requirements imposed on the reaction by the availability of oxygens or lack at the reaction site^[6]. Furthermore, the metal oxygen bond energy of the active oxygen atoms must be in a range where rapid removal (hydrocarbon oxidation) and addition (regeneration by oxygen) can occur (appropriate bond lengths). This accounted for the fundamental principles behind the development of $\text{Bi}_9\text{PMo}_{12}\text{O}_{52}/\text{SiO}_2$ catalysts. This was the first commercial ammoxidation catalyst based on concept of cooperation of phases. In this concept the two phases, $\alpha\text{-Bi}_2\text{Mo}_3\text{O}_{12}$ and $\gamma\text{-Bi}_2\text{MoO}_6$, cooperated with each other. It was postulated that the catalytic function was performed by the α -phase while reoxidation function by γ -phase^[7]. From 1960 onwards, the expensive and inefficient process for manufacturing acrylonitrile was replaced by the new ‘SOHIO process’ in which propylene, ammonia and air reacted together over $\text{Bi}_9\text{PMo}_{12}\text{O}_{52}/\text{SiO}_2$ catalyst.

The realization that such benefits as higher product yields of acrolein and acrylonitrile can be obtained through phase cooperation, led in the 1970s towards research into the development of multiphase and multicomponent mixed metal oxide catalysts including bismuth molybdate which turned out to be a key catalyst component^[8, 9]. The general formula of multicomponent and multiphase bismuth molybdates can be described as follow: Mo-Bi-M^{II}-M^{III}, where M^{II} = Co²⁺, Ni²⁺ and M^{III} = Fe³⁺, Cr³⁺. These metal cations can be concentrated in the bulk or in the surface layers of catalyst particles depending on compositions, atomic ratios, preparation methods and conditions. Research in these complicated catalyst structures has led to a better understanding and consequently has had a positive effect on the total yield of acrolein and acrylonitrile. At present the yields in commercial plants can exceed 80 %^[9].

Recently, it has been reported that γ -Bi₂MoO₆, exhibits high photocatalytic activity under visible light^[10, 11]. In this instance, γ -Bi₂MoO₆ produced by hydrothermal method showed very good photocatalytic activity for degradation of N,N, N',N' –tetraethylated rhodamine (RhB) under visible-light radiation^[10]. More importantly, catalytic efficiency and stability can be achieved using visible light radiation which accounts for about 43% of incoming solar energy compared to that of traditionally used ultraviolet light which accounts for only 4%.

Even though bismuth molybdate has exceptional catalytic properties, research in the field has continued and has focused on investigations of the Bi₂O₃ · MoO₃ system and the crystalline structures of the different phases. The first phase diagrams were proposed by Chen and Smith^[12] and Egashira et al.^[13], who studied stoichiometric compositions of various solids belonging to the Bi₂O₃ · MoO₃ system after the materials were subjected to different heat treatments. Afterwards, Snyder et al.^[14] re-examined the phase diagrams and concluded that the most stable and catalytically active phases are α -Bi₂Mo₃O₁₂, β -Bi₂Mo₂O₉, and γ -Bi₂MoO₆.

Although the compositions as well as the catalytic properties of these three phases are very similar, their structures are quite different. Their crystal structures are compared in Table 3-1. All three phases can be derived from the fluorite structure^[15]. The α -phase is described as a defect scheelite structure, in which the Mo⁶⁺ ions are surrounded by five oxygen atoms in an asymmetric Mo-O₅ coordination environment. The β -phase is

described as defective fluorite structure, where Mo^{6+} ions are in an almost regular MoO_4 tetrahedral environment. The structure is built from regular MoO_4 tetrahedra and BiO_8 polyhedra.

The crystal structure of $\gamma\text{-Bi}_2\text{MoO}_6$ is discussed in detail, since it is the primary subject of this work. The structure of $\gamma\text{-Bi}_2\text{MoO}_6$ belongs to the Aurivillius family represented by $(\text{Bi}_2\text{O}_2)_x^{2+} (\text{Bi}_{n-1}\text{Mo}_x\text{O}_{3n+1})^{2-}$ with $x = 1$. The structure consists of layers of corner-sharing MoO_6 octahedra separated by Bi_2O_3 layers. The three dimensional view of the structure is shown in Figure 3-1. There are three types of oxygen surroundings in the structure. The first type of the oxygen environment is within the molybdenum octahedral layer bridging two molybdenum atoms^[16]. The second type is entirely contained within the Bi layer, bridging four metal atoms. The third type bridges the molybdenum and bismuth layers; they are bonded to one molybdenum and two bismuth atoms each^[16].

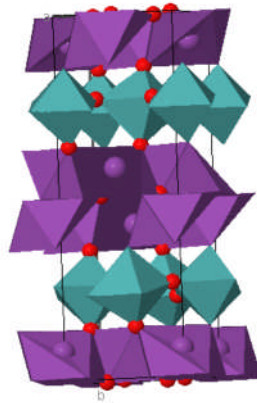


Figure 3-1 *The three dimensional representation of $\gamma\text{-Bi}_2\text{MoO}_6$ structure, where purple and green polyhedrons represent Bi^{3+} and Mo^{6+} species respectively, while O^{2-} ions are red balls. The structure is built upon $[\text{Bi}_2\text{O}_2]^{2+}$ layers sandwiched between layers of MoO_6 octahedra.*

Table 3-1 Structural parameters for α -, β - and γ -phases of bismuth molybdate.

Empirical Formula	$\text{Bi}_2\text{Mo}_3\text{O}_{12}$	$\text{Bi}_2\text{Mo}_2\text{O}_9$	Bi_2MoO_6
Phase	α	β	γ
Crystal Structure	Monoclinic	Monoclinic	Orthorhombic
Space Group	$P2_1/c$	$P2_1/n$	$Pca2_1$
a [Å]	7.7104 (3)	11.972(3)	5.4896(3)
b [Å]	11.5313(4)	10.813(4)	16.22658 (7)
c [Å]	11.9720(5)	11.899(2)	5.5131(3)
α [°]	90	90	90
β [°]	115.276(3)	90.13(2)	90
γ [°]	90	90	90
Determined by	Theobald ^[18]	Chen ^[19]	Theobald ^[20]

The low temperature form, γ - Bi_2MoO_6 , is a naturally occurring mineral Koechlinite which undergoes phase transformations at elevated temperatures^[17, 18]. These phase transformations were investigated in detail by Sankar et.al.^[17] employing *in-situ* combined XAS/XRD techniques. The first transformation is to an intermediate phase, generally referred as γ'' - phase. The transformation starts at 570°C but it is reversible up to 610°C. The second transformation, at higher temperature $\sim 750^\circ\text{C}$, is to the stable γ' -phase^[19]. These reveal that the intermediate phase (γ'' - phase) contains Mo^{6+} in highly distorted octahedra which are on the verge to transform into tetrahedra. On further heating, the γ'' -phase transformed irreversibly to the γ' -phase, whereby Mo^{6+} ions were tetrahedrally coordinated^[17]. These structural changes were also confirmed by Buttrey et.al.^[20], who carried out high resolution X-ray scattering and neutron powder diffraction studies.

γ - Bi_2MoO_6 catalyst can be prepared either by solid state routes or by more conventional co-precipitation and hydrothermal methods. The solid state method methods have been traditionally used to prepare bimetallic oxides using single oxides of the metals^[21]. The method involves grinding together appropriate metal oxides, Bi_2O_3 and MoO_3 , in correct stoichiometric ratios and heating up at the appropriate temperatures. The phase

is formed mainly via diffusion of atoms at the interface between the reactants. The main advantage of this preparation method is its simplicity. However, there are a number of disadvantages such as long preparation times because reactions only are occurring at the surface of relatively large particles, the presence of impurities, and formation of unwanted phases due to poor mixing.

The precursors occurring in the co-precipitation method are synthesised from aqueous solutions of Bi^{3+} salts and ammonium heptamolybdate. During the co-precipitation step, the pH of the mixed solution is precisely controlled and adjusted by adding drops of ammonium hydroxide. The formed precipitate is then washed with distilled water and filtered. The resulting solid product is dried at 100°C for several hours. To improve the purity, crystallinity, surface acidity and morphology of catalyst particles, these solid products have to be calcined for several hours at target temperatures between $400\text{--}700^\circ\text{C}$ ^[2, 16, 22]. The drawbacks of this method are that the morphology, the purity, surface texture, grain sizes and shapes can be difficult to control. Also in the case of $\gamma\text{-Bi}_2\text{MoO}_6$, the inactive $\gamma'\text{-Bi}_2\text{MoO}_6$ can be formed during the heating process.

On the other hand, preparation of these materials by hydrothermal methods, whereby mixtures of inorganic salts are dissolved in liquid reagents and are allowed to react at relatively low temperatures ($<200^\circ\text{C}$) under controlled pressure and pH, have been successfully carried out^[23-25]. This method is not only a relatively cheap way of engineering materials under mild conditions, but also an efficient way to control synthesis. The resulting crystalline porous solids have a high degree of crystallinity, large surface area, and controlled particle and pore sizes. This compares favourably to traditional methods like co-precipitation or solid state methods where the calcination of samples at elevated temperatures can induce particle sintering which is undesired in particular in the field of photocatalysis and catalysis.

To gain a deeper understanding of the reactions leading to the formation of a useful catalyst, the determination of the reaction kinetics is a logical first step to take. However, information on the early stages of structure development is in many cases still lacking due to the difficulties to find experimental techniques that render information on the still poorly ordered material on the required (nanometer) length scale. Only once the material has further developed, X-ray or neutron scattering/diffraction techniques can

provide real time information on the growth mechanism^[24]. A technique which is particularly useful for the study of the early stages of structure formation, before the material has developed sufficient long range order is X-ray spectroscopy. In-situ X-ray absorption spectroscopy (XAS) can render information about the local chemical environment of probe metal atoms and can be used to study hydrothermally crystallizing systems under real reaction conditions^[17, 24, 26, 27]. Extended X-ray Absorption Fine Spectroscopy (EXAFS) yields information about the local structure of specific probe atoms embedded in the structure^[28]. The coordination numbers, inter-atomic distances and Debye-Waller factors can be determined. Investigation of the near edge part of the XAS spectrum (XANES) can provide information about surrounding atomic geometry of an element of interest as well as its oxidation state. Unfortunately, the study of these structure forming hydrothermal reactions with only a single method will not give a comprehensive picture about the formation process. For a comprehensive understanding of the crystallization process complementary techniques such as X-ray diffraction (XRD), which provides information about the long range ordering and phase purity of the materials, can be used. These techniques are sensitive towards different stages of the formation of crystalline solids; therefore, their combination in a single experiment is powerful tool for monitoring changes during the course of reaction^[24, 27, 29, 30]. However, if one wants to carry out the subsequent characterization in order to confirm chemical states of species embedded in a sample, other complementary techniques such as Raman have to be used in the home laboratory. During the ex-situ characterization process samples are carried around, mounted into different sample holders. In this case, precursor gels need to be freshly prepared which can be time consuming, and more importantly, the resulting information do not have to be necessary corroborative and consistent. One way to overcome these difficulties is to combine other single techniques, for instance, Raman into one experimental setup and thus obtain a comprehensive picture about formation of a desired material.

3.3 Aims of the work

The first aim of this chapter is to precisely determine the nature and structure of intermediate phases that occur and the structural modifications that take place during the

growth process of γ -Bi₂MoO₆ crystallites under mild hydrothermal conditions from an amorphous gel. To do so, it is necessary to obtain high quality and high resolution powder diffraction (HRPD) combined with XANES and Raman scattering in a single experimental setup. In the past similar *in-situ* studies on hydrothermal crystallization of γ -Bi₂MoO₆ have been carried out using Energy Dispersive XRD (EDXRD), in which direct formation of γ -Bi₂MoO₆ was reported^[23]. However, it has been subsequently reported in the literature^[31] that the presence of an intermediate phase during formation γ -Bi₂MoO₆ was observed employing combined XAS/XRD measurements during heating γ -Bi₂MoO₆ precursors prepared by co-precipitation method. However, this intermediate phase was not identified.

The second aim is to provide more insights into formation of γ -Bi₂MoO₆ under hydrothermal conditions employing combined EXAFS/XRD measurements. In this case, structural changes around molybdenum are investigated in detail using EXAFS which was not possible with data recorded during the HRPD/Raman/XANES experiments. Additionally, a method for deriving the reaction kinetics from XANES data is described. The reaction kinetics of γ -Bi₂MoO₆ was quantified by using the Avrami-Erofe'ev formalism in which the pre-edge XAS intensity was used as a measure for the progress of the reaction.

3.4 Experimental part

3.4.1 Hydrothermal synthesis of $\gamma\text{-Bi}_2\text{MoO}_6$

According to a recipe by Beale and Sankar^[23], stoichiometric amounts of bismuth nitrate solution (2.32g Bi_2O_3 (Riedel de Haen) dissolved in 5.8 ml (65% HNO_3)) was mixed with ammonium heptamolybdate solution (0.88g $(\text{NH}_4)_6\text{Mo}_7\text{O}_{24}\cdot 4\text{H}_2\text{O}$ (Janssen Chimica, 99%) dissolved in 5.6 ml 28% NH_4OH) under continuous magnetic stirring to produce a homogenous mixture. The pH was adjusted to pH 9 by adding ammonia hydroxide. The resulting gel was aged for 30 min before was transferred into a Teflon-lined autoclave for hydrothermal treatment. The autoclave was sealed and placed in a pre-heated oven at 170°C for several hours. The resulting product was filtered, washed and dried in the oven at 100°C .

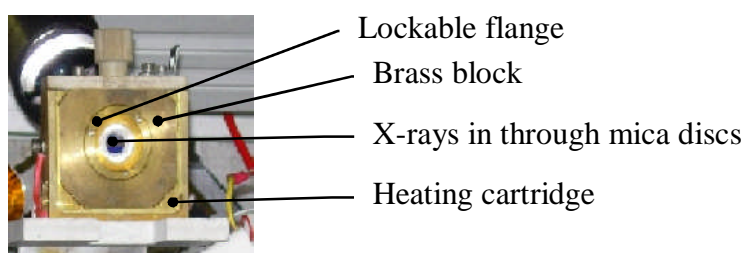


Figure 3-2 *In-situ hydrothermal cell that was used for isothermal hydrothermal reactions between 160 and 180°C throughout time resolved HRPD/Raman/XAS experiments. The $\gamma\text{-Bi}_2\text{MoO}_6$ gel was loaded between two mica discs separated by a Teflon ring spacer and subsequently housed between two aluminium plates sealed with a lockable flange.*

For on-line in-situ experiments a hydrothermal cell was used, which is shown in Figure 3-2 instead of a Teflon-lined autoclave. The hydrothermal cell made use of a Teflon ring as a spacer. 50 microns thick mica disks were used as windows. The bismuth molybdate gel, spacer and window material were housed between 2 aluminium plates that were sealed with a lockable flange system. The cell could maintain autogenous pressure in the desired temperature range. The assembly was housed in a brass block which was temperature controlled using 4x30W cartridge heaters.

3.4.2 XRD and SEM characterization

Ex-situ analyses on prepared samples as well as fully reacted samples from on-line experiments were carried out by XRD and Scanning Electron Microscopy (SEM). XRD patterns were collected at room temperature with a Bruker AXS D8 Advance diffractometer in the 5-70° range (step 0.02°, 2 s/step) using CuK α radiation ($\lambda=1.54$ Å). XRD patterns were also recorded by D4 Endeavor utilising CuK α radiation ($\lambda=1.54$ Å) in the range 5–50° with a step of 0.04°. Data were processed using DIFFRACplus EVA or Match software and compared with ICDD PDF files (PDF2, release 2003). A Scanning Electron Microscope Hitachi S4700 SEM was used to examine the microstructural features of synthesised samples.

3.4.3 Combined HRPD/Raman/XAS

In-situ time resolved HRPD/Raman/XAS measurements were performed at the Swiss-Norwegian beamline (SNBL, BM1B) at the ESRF. The experimental setup is shown in Figure 3-3. The beamline is equipped with a Si (111) monochromator.

The XANES transmission spectrum of a molybdenum foil was used for energy calibration. XAS fluorescence spectra were collected at the Mo K-edge using a Vortex EM fluorescence detector with Xia digital electronics. The collection time for a XANES spectrum was 378 seconds. XANES data were processed using the Athena software^[32], as described in Chapter 2.

The HRPD data were collected with the standard BM1B setup equipped with a six crystal analyser array mounted on a 2-circle diffractometer ensuring an intrinsic resolution (FWHM) of approximately 0.01°. HRPD patterns were collected at 0.5 Å wavelength in the 2 θ range 8 to 17.5° with a step of 0.003° and 150 ms/step counting time. The total time for the collection of a pattern was 475 seconds. Data were refined with the Fullprof suite^[33]. The Thompson-Cox-Hastings pseudo-Voigt profile function was used^[34]. The resolution of the instrument was determined from a

LaB₆ XRD pattern. HRPD results were reported by C. Kongmark^[35, 36] which was collaborative work between University College London and University of Lille.

Raman scattering was carried out on a dispersive InVia Renishaw spectrophotometer with a 532 nm exciting line and 1200 lines/nm grating. A standard Raman RP10 probe with long distance objective was connected to the spectrophotometer by optical fibers^[37] Raman spectra were recorded in the 100-1200 cm⁻¹ range for 132 seconds with 70 mW laser power. Labspec program was used to normalize and determine the surface area of Raman lines.

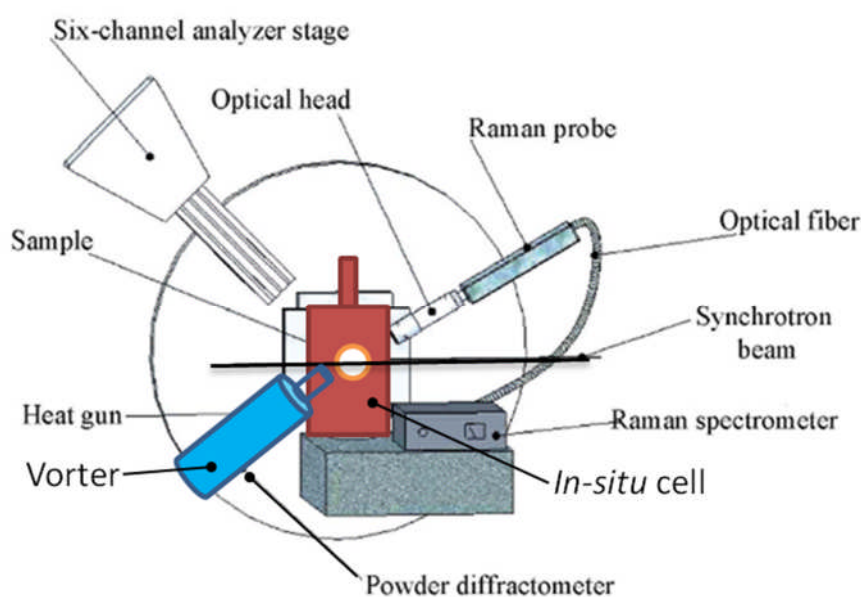


Figure 3-3 A scheme of HRPD/Raman/XAS setup as constructed on the Swiss-Norwegian beamlines at the ESRF^[37]. The set-up is based upon a step scanning powder diffractometer equipped with an X-ray detector consisting of six independent counting chains. Raman instrument is dispersive spectrophotometer, Renishaw RA100, with Ar-ion laser and 1200 mm⁻¹ grating. A Raman probe is connected to the instrument by optical fibres. XAS data are recorded with a Vortex fluorescence detector. The in situ cell is positioned with the respect to the incoming X-ray beam the way, that the X-ray beam hits a sample close to the bottom edge of the mica disc windows.

During the course of hydrothermal reaction XANES and HRPD data were collected sequentially, while Raman spectra were recorded continuously every 120 seconds.

3.4.4 Combined EXAFS/XRD

Combined time-resolved EXAFS/XRD experiments were performed at the Dutch-Belgian beamline (BM26A) at the ESRF^[30]. The beamline is equipped with a Si(111) double crystal monochromator.

EXAFS data were acquired in step scans over a k range (k being the wave vector number of the X-ray excited chromium photoelectron) from 3 \AA^{-1} to 12 \AA^{-1} . The XANES transmission spectrum of a molybdenum foil was used for energy calibration. XRD data were collected at a wavelength of 0.625 \AA ($19\,837 \text{ eV}$).

A position sensitive INEL detector was used to collect the time-resolved XRD-data^[27]. The acquisition time for each pattern was 150 seconds. A typical EXAFS-XRD cycle lasted 1110 ± 60 seconds. XRD data were calibrated using Si diffraction standard.

3.4.5 XAFS data analysis

EXAFS data were normalized in Athena^[32] and subsequent curve fitting was performed in EXCURVE98^[38], as described in Chapter 2. Phase shifts and backscattering factors were calculated from atomic potentials using EXCURVE98. The EXAFS data were analysed using the single scattering wave approximation^[39]. Refinement was carried out using k^3 weighting in the range from 3.3 to 11.2 \AA^{-1} . The AFAC fitting parameter in EXCURVE98 was derived from the best fit to EXAFS data from a Mo-foil and set to 1. AFAC represents the average proportion of excitations which contribute to EXAFS and is used to determine the amplitude reduction due to many electron processes. In the initial structural model, coordination numbers were fixed to crystallographic values. When refined, the refined coordination numbers were generated with less than 20% uncertainties^[40]. Throughout a whole cluster refinement the coordination numbers were fixed, in order to avoid inducing correlations between coordination number and the Debye-Waller factor.

3.5 Results and discussion

3.5.1 Synthesis and XRD characterization

Co-precipitation and hydrothermal preparations of the bismuth molybdate catalyst were carried out in order to test and optimise synthesis conditions. First, the co-precipitation method was used to prepare a pure phase γ - Bi_2MoO_6 according to procedures described in the literature^[41]. Afterwards several batches of samples with various reaction times under mild hydrothermal conditions (below 200°C) were prepared. These *ex-situ* investigations revealed that high pH (≥ 7) and high concentration of bismuth (Bi/Mo=2/1) lead to the formation γ - Bi_2MoO_6 . Figure 3-4 shows a typical XRD pattern of γ - Bi_2MoO_6 prepared by hydrothermal reaction, 20 hours at 170 °C, in a Teflon-lined autoclave. In the figure, the peak intensities are normalized on 131 diffraction peak. XRD contains reflections which can only be assigned to γ - Bi_2MoO_6 , that is, the pure phase is formed.

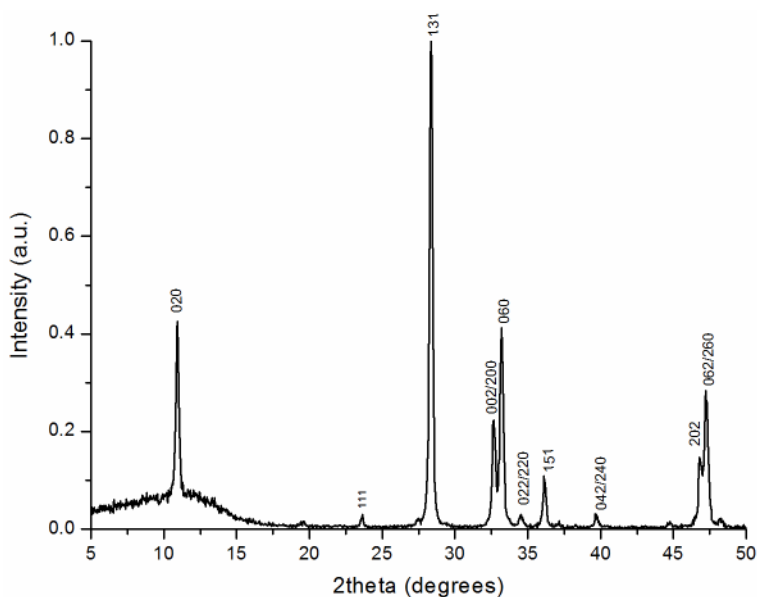


Figure 3-4 XRD pattern of Bi_2MoO_6 collected at wavelength of 1.54 Å prepared in Teflon-lined autoclave at 170°C for 20 hours. The peak intensities are normalized on 131 diffraction peak. All peaks in the pattern can be indexed in orthorhombic crystal structure based on Theobald *et.al.*^[42] XRD data. Therefore it can be assumed that the pure phase is formed. The hump at $\sim 11^\circ$ is due to the scattering from sample holder, that is, wrong slits setting of D4 diffractometer were used.

3.5.2 Combined HRPD/Raman/XAS

The γ - Bi_2MoO_6 gel was on-line subjected to isothermal hydrothermal heat treatments of 160 and 180°C respectively. Mo K-edge XANES, stacked plots of Raman spectra and HRPD patterns recorded during the course of hydrothermal reaction at 180°C are shown in Figure 3-5, Figure 3-7, and Figure 3-8 respectively.

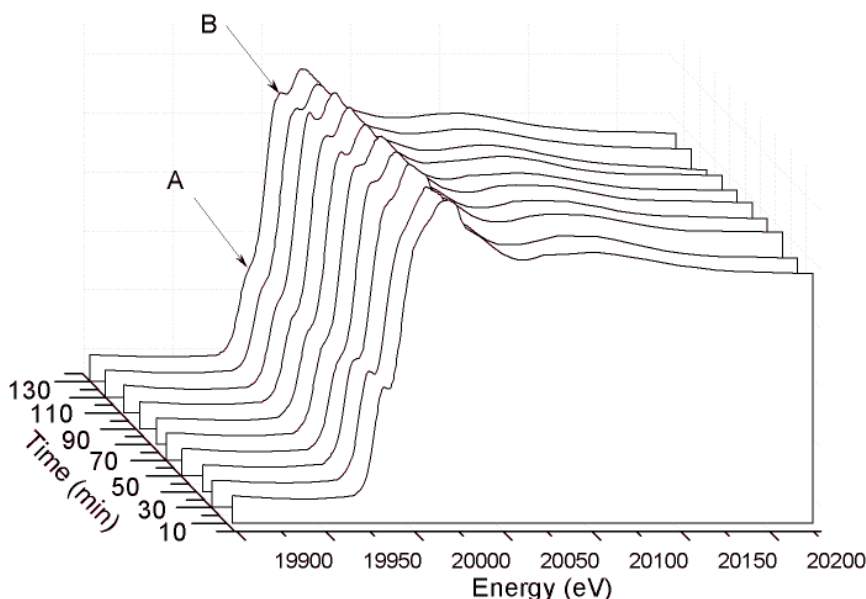


Figure 3-5 Mo K-edge XANES spectra collected during the isothermal heat treatment at 180°C under hydrothermal conditions. The features marked A and B are characteristic of Mo^{6+} in tetrahedral and octahedral environment respectively. A clear increase in the tetrahedral pre-peak intensity and disappearance of the octahedral fingerprint are observed.

Figure 3-5 depicts the Mo K-edge XANES recorded during the formation of γ - Bi_2MoO_6 . The first XANES spectrum was taken 6 minutes after the start of the reactions. This spectrum contains a distinct pre-edge peak (arrow A) and a weak shoulder on the top of the edge (arrow B). The features A and B are regarded as characteristic of XANES and corresponds to $1s$ to $4d$ and $1s$ to $5p$ quadrupole transitions^[23, 43]. The XANES spectrum resembles to that of $\text{Na}_2\text{MoO}_4 \cdot 2\text{H}_2\text{O}$ in terms of local structure, i.e. tetrahedrally coordinated Mo^{6+} ions. For clarity, comparison of the XANES of model compounds, $\text{Na}_2\text{MoO}_4 \cdot 2\text{H}_2\text{O}$ and $(\text{NH}_4)_6\text{Mo}_7\text{O}_{24} \cdot 4\text{H}_2\text{O}$, representing

Mo⁶⁺ in tetrahedral and octahedral geometry is shown in Figure 3-6. The XANES spectrum taken after 130 min of the reaction shows a small pre-edge peak, which is a typical for Mo⁶⁺ species in octahedral coordination^[23]. The spectrum is similar to that of (NH₄)₆Mo₇O₂₄·4H₂O in terms of local environment, as shown in Figure 3-6. The decrease in the pre-edge intensity (arrow A) and the increase in the intensity of shoulder on the top of the edge (arrow B) accounts for the conversion of tetrahedral to octahedral molybdenum during the course of the reaction. Previously, it has been shown, that the Mo⁶⁺ ions in the γ -Bi₂MoO₆ structure are in a distorted octahedral coordination environment^[42], and therefore, it can be concluded that this phase is indeed formed.

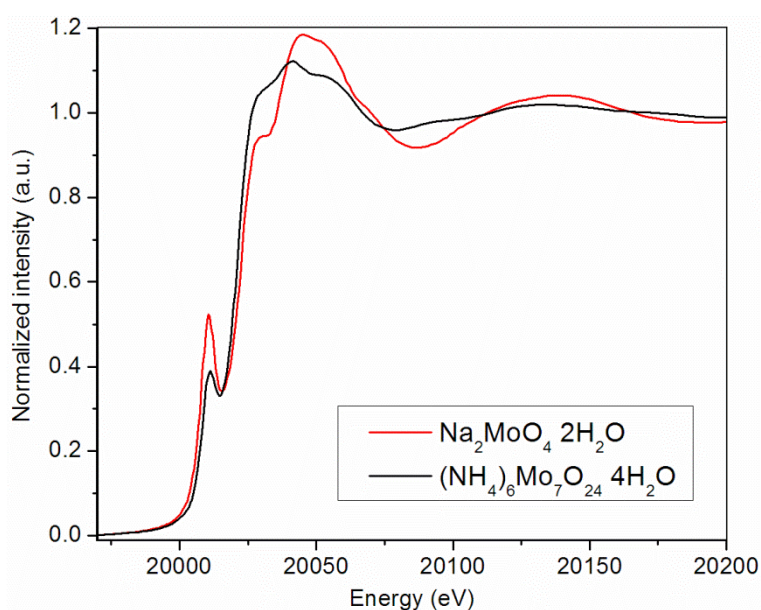


Figure 3-6 Mo K-edge XANES spectra of model compounds, Na₂MoO₄·2H₂O in red and (NH₄)₆Mo₇O₂₄·4H₂O in black, representing Mo⁶⁺ in tetrahedral and octahedral geometry respectively. The XANES spectrum of Mo⁶⁺ in tetrahedral geometry shows a distinct pre-edge peak due to 1s-3d electronic transition, while the pre-edge peak is suppressed in octahedrally coordinated Mo⁶⁺ ions. A weak shoulder on the top of the edge is due to 1s 5p electronic transition.

Raman spectra measured during the hydrothermal reaction at 180°C are illustrated in Figure 3-7. The weak band at 711 cm⁻¹ and the strong line at 1050 cm⁻¹ can be assigned to the N–O angular deformation and symmetric stretching modes of NO₃⁻ anion respectively^[44] and evidence the presence of nitrate species in the first minutes

of reaction which partially remained till completion. The spectrum of $\gamma\text{-Bi}_2\text{MoO}_6$ shows a strong line at 793 cm^{-1} with two shoulders located at $789, 814\text{ cm}^{-1}$ assigned to the stretching modes of Mo–O bond. In the orthorhombic cell, the distortion of molybdate octahedron can also generate other components with medium intensity at 721 and 845 cm^{-1} for the vibration of free species^[42]. Lines observed between 270 and 360 cm^{-1} , including $283, 327$ and 354 cm^{-1} can be assigned to the different components of the bending modes of MoO_6 octahedral unit^[45, 46].

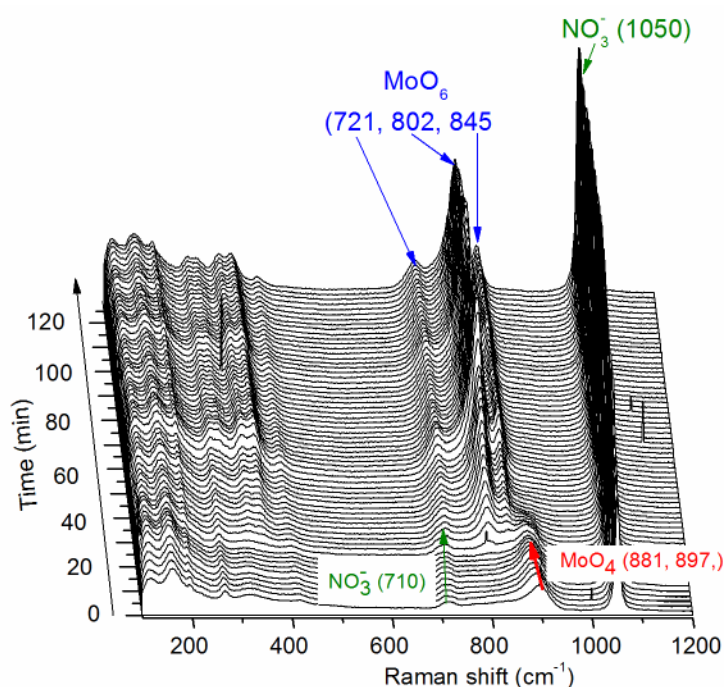


Figure 3-7 Raman spectra collected during the hydrothermal synthesis of $\gamma\text{-Bi}_2\text{MoO}_6$ at 180°C . The weak band at 711 cm^{-1} and the strong line at 1050 cm^{-1} can be assigned to NO_3^- anion. The bands at 881 and 897 cm^{-1} can be assigned to vibration of MoO_4^{2-} tetrahedra, while the strong lines at 802 cm^{-1} and two shoulders at 721 and 845 cm^{-1} are stretching modes of MoO_6 octahedra.

The evolution of molybdenum coordination during the hydrothermal synthesis is most clear in the $650\text{-}975\text{ cm}^{-1}$ spectral range, where there is no overlap by Bi–O group vibrations. Isolated MoO_4^{2-} tetrahedron in the starting gel are characterized by a broad band at 897 cm^{-1} and a weak line at 841 cm^{-1} which correspond to symmetric and anti-symmetric Mo–O stretching motions of the free ion^[47]. In the first 20 minutes of

reaction, the 897 cm^{-1} line shifts to 881 cm^{-1} and then it remains at this position. This shift is interpreted to be due to the lengthening of Mo–O bond and it probably accounts for structural rearrangements. The final value is close to 880 cm^{-1} , and can be assigned to the vibration of MoO_4^{2-} tetrahedra in the CaMoO_4 structure^[46]. After 30 minutes of reaction the intensity of the 881 cm^{-1} line decreases while new lines appear at 721 , 802 and 845 cm^{-1} . The latter are assigned to the Mo–O stretching modes of distorted MoO_6 octahedra in $\gamma\text{-Bi}_2\text{MoO}_6$, as previously mentioned.

Since no modifications of Raman bands are observed at the low wavenumbers, i.e. Bi–O bands below 270 cm^{-1} , it can be concluded that there is no significant modification of the local environment around bismuth during the synthesis. This is in agreement with Raman studies on the various substitutions of metal oxide compounds^[48]. It means that $\text{Bi}_2\text{O}_2^{2+}$ layers are already formed at the beginning of the reaction (3 minutes after heating), and these layers remain till the end of the reaction as a part of $\gamma\text{-Bi}_2\text{MoO}_6$ framework.

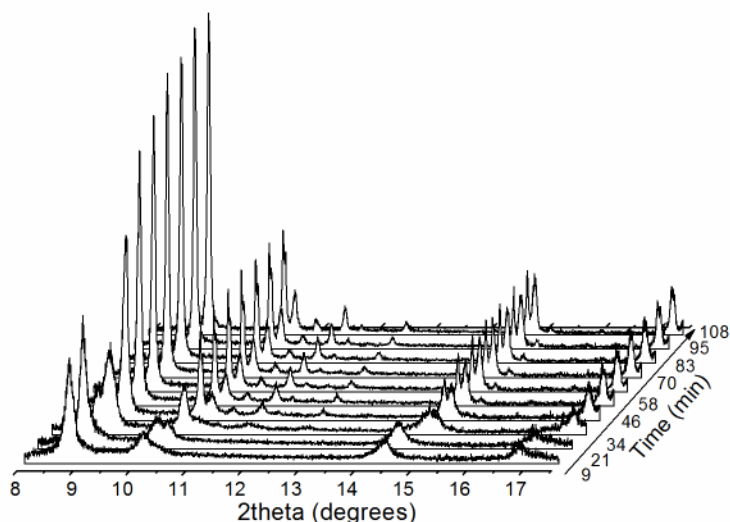


Figure 3-8 *In-situ XRD patterns collected during the hydrothermal synthesis of $\gamma\text{-Bi}_2\text{MoO}_6$ at 180°C . The crystalline phase formed in the first minutes of the reaction can be assigned to Bi_2O_3 phase. After 23 minutes of the reaction this phase is gradually transformed into $\gamma\text{-Bi}_2\text{MoO}_6$.*

Figure 3-8 shows the stacked HRPD patterns collected at 180°C during the hydrothermal reaction. From this plot it can be deduced that a crystalline phase was

formed in the first few minutes of the reaction. Irrespective of the reaction temperature two steps of phase formation were observed. After 21 minutes of reaction the diffraction pattern was characterized by reflections at 2θ ca. 8.8° , 10.2° and 14.4° which could be assigned to Bi_2O_3 . The fluorite structure of Bi_2O_3 ^[49] (with cell parameter $a = 5.6595 \text{ \AA}$ in the cubic lattice) was initially used to refine the HRPD data for the intermediate phase. However, a good fit was obtained only when the structure was compressed along the [001] direction. The refinement could finally be performed in $I4/mmm$ space group, with Bi in 2a (0, 0, 0) and O in 4d (0, 1/2, 1/4) and 75% occupancy of O site^[36]. Bismuth was only considered in the 2a site, although the presence of Mo could not be excluded. The initial diffraction patterns could be indexed to a tetragonal unit cell with parameters^[36]: $a = 4.022 \text{ \AA}$ ($a_F = a \cdot 2^{1/2} = 5.688 \text{ \AA}$ in the cubic fluorite lattice) and $c = 5.570 \text{ \AA}$. The relationship between the distorted fluorite unit cell and the tetragonal unit cell is illustrated in Figure 3-9.

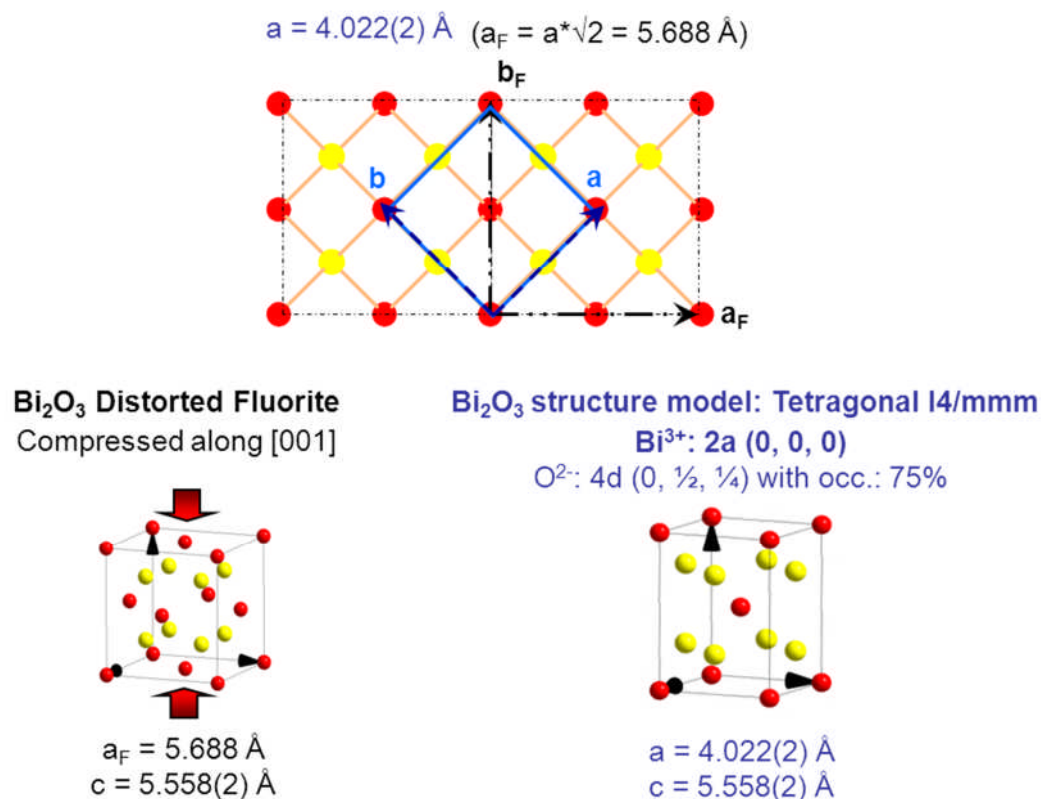


Figure 3-9 A graphical representation of Bi_2O_3 distorted fluorite structure based on Rietveld refinement results, where red balls represent oxygen atoms and yellow balls bismuth atoms^[50].

A typical fit to XRD data for an intermediate phase is shown in Figure 3-10. An isotropic model was used to refine the Bi_2O_3 crystallite size, which revealed that about 10.2 ± 0.3 nm sized particles are present in the system.

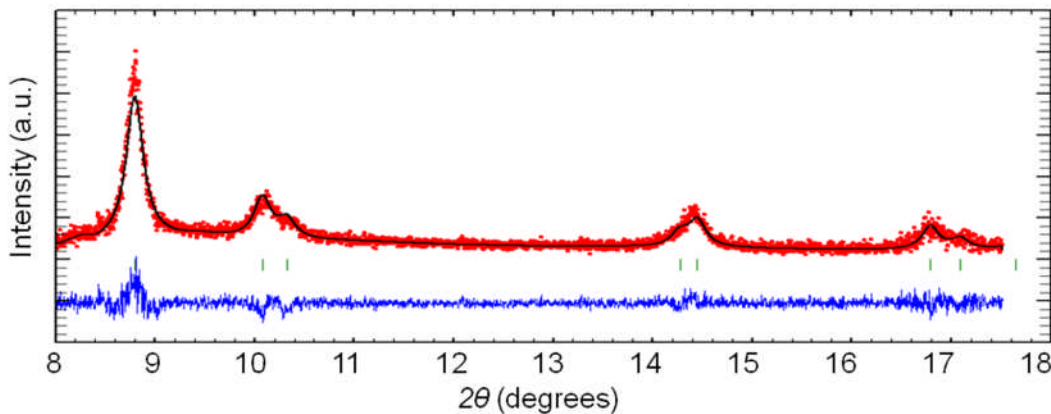


Figure 3-10 Rietveld refinement of XRD data for an intermediate phase which was formed after 9 min at 160°C during isothermal hydrothermal crystallization of $\gamma\text{-Bi}_2\text{MoO}_6$ from an amorphous gel. The refinement was carried out using $I4/mmm$ space group with Bi in $2a$ (0, 0, 0) and O in $4d$ (0, 1/2, 1/4) and 75% occupancy of O site. In the Rietveld fit isotropic crystalline size model is used. An observed (black curve) and calculated (red curve) and difference profiles (green curve) are shown.

23 minutes after the onset of the reaction at 180°C , the Bi_2O_3 phase gradually transforms into $\gamma\text{-Bi}_2\text{MoO}_6$. During the transformation, the intensity of the peaks corresponding to the distorted fluorite form of Bi_2O_3 is decreased but without observable changes in the unit-cell parameters. The reaction was completed after 95 minutes.

The structure of $\gamma\text{-Bi}_2\text{MoO}_6$ was refined using the structural model proposed by Theobald et al.^[42]. Similar to the case of Bi_2O_3 phase, only the unit cell, the overall Debye-Waller parameters and crystalline size were refined. A typical fit to XRD of the resulting crystalline $\gamma\text{-Bi}_2\text{MoO}_6$ is illustrated in Figure 3-11.

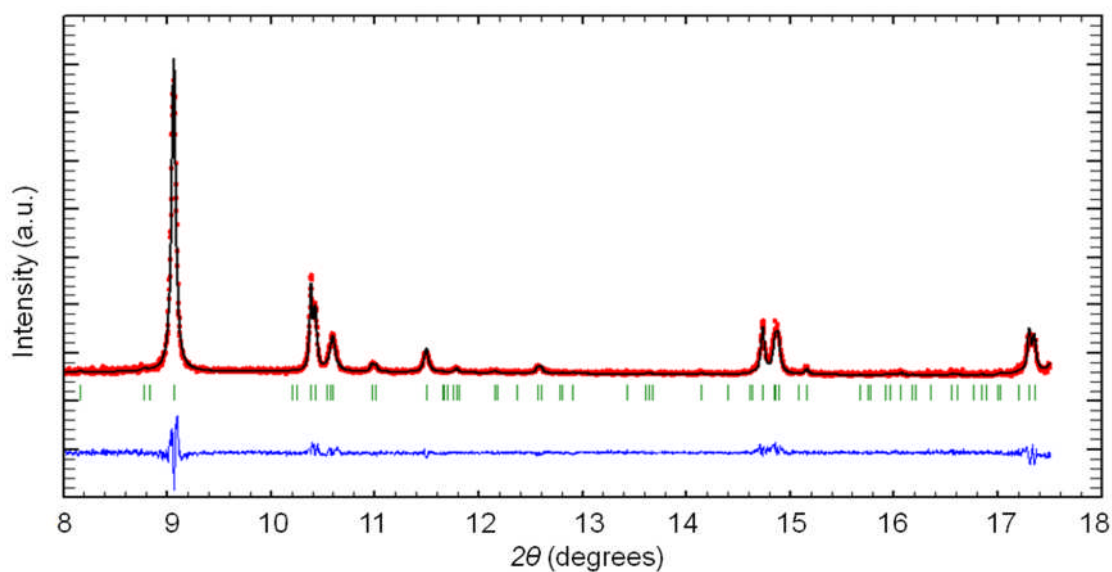


Figure 3-11 Rietveld refinement of XRD data for the crystalline γ - Bi_2MoO_6 formed under hydrothermal conditions from an amorphous gel after 184 min at 160°C . The refinement was carried out using the structural model derived by Theobald et al.^[42]. In this model was necessary to allow anisotropic crystalline size broadening. An observed (black curve) and calculated (red curve) and difference profiles (green curve) are shown.

In contrast to Bi_2O_3 case, the full-width at half maximum (FWHM) of Bragg peaks of several reflections of γ - Bi_2MoO_6 appeared to vary, which was due to the anisotropic shape of crystallites. To take into account this broadening, a linear combination of spherical harmonics of the 4th order^[51] was used, and from the analysis the evolution of crystalline size and morphology was derived. Between ca. 70 and 138 minutes of the reaction at 180°C (Table 3-4), the morphology remained anisotropic, although the growth takes place in all directions. In good agreement with the layered structure of γ - Bi_2MoO_6 , the refinement revealed a platy shape of crystallites. Similar analysis of the data between ca. 20 and 58 minutes resulted in a significant error in the crystallite size due to the presence of both phases. The *a* and *c* parameters of the refined cell of γ - Bi_2MoO_6 phase clearly show a decrease during the crystallization process. The accuracy in the *b* parameter was very poor. Probably the disorder in the stacking of platelets with a very small thickness along [010] is responsible for the lack of intensity in the 0*k*0 reflections.

In a previous study^[31], it was found that an intermediate crystalline phase was formed before $\gamma\text{-Bi}_2\text{MoO}_6$. However, it was not possible to determine the nature of this phase because of the low resolution of the XRD data. In the work presented here, it is shown that the high-quality HRPD data that were obtained enabled the use of Rietveld method to refine each pattern, and thereby gaining new insights of the intermediate and final phases. Nevertheless, the complete structure refinement could not be performed because the data range was restricted to a short d-spacing range due to the requirement of both high spatial resolution and a time resolution which was compatible with the structure formation process. Only the unit cell parameters, the overall Debye-Waller parameters and crystalline sizes were refined.

The evolution of unit cell parameters with time are given in Table 3-2, Table 3-3 and Table 3-4. These results suggest that the a and c axis for the intermediate stage of $\gamma\text{-Bi}_2\text{MoO}_6$ formation, in which two phases coexist, are shorter compared to the pure crystalline phase, that is, $\gamma\text{-Bi}_2\text{MoO}_6$. This can be concluded from the shift of the main Bragg peaks towards higher 2θ values. See Figure 3-12. Figure 3-13 depicts the evolution of the crystallite sizes during isothermal crystallization as a function of time, whereas Figure 3-14 shows changes in the volume fraction of Bi_2O_3 and $\gamma\text{-Bi}_2\text{MoO}_6$ as a function of time during reactions at 160, 170 and 180°C.

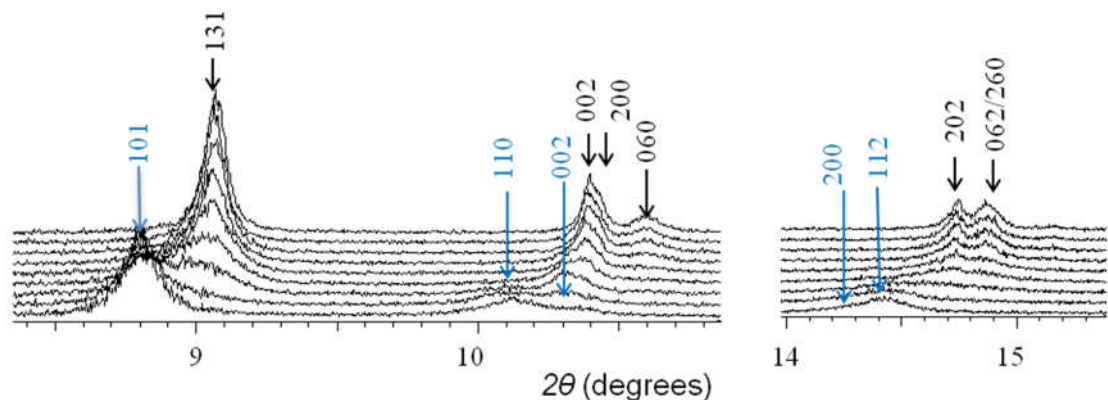


Figure 3-12 Selected HRPD patterns collected during the hydrothermal crystallization of $\gamma\text{-Bi}_2\text{MoO}_6$ at 160°C with the indexing of the Bragg peaks. Bragg Peaks marked with blue arrows correspond to the intermediate phase (Bi_2O_3) formed in a tetragonal unit cell ($a = 4.02 \text{ \AA}$, $c = 5.69 \text{ \AA}$), whereas black arrows are for the final $\gamma\text{-Bi}_2\text{MoO}_6$ crystallizing in an orthorhombic unit cell ($a = 5.50 \text{ \AA}$, $b = 16.25 \text{ \AA}$, $c = 5.42 \text{ \AA}$).

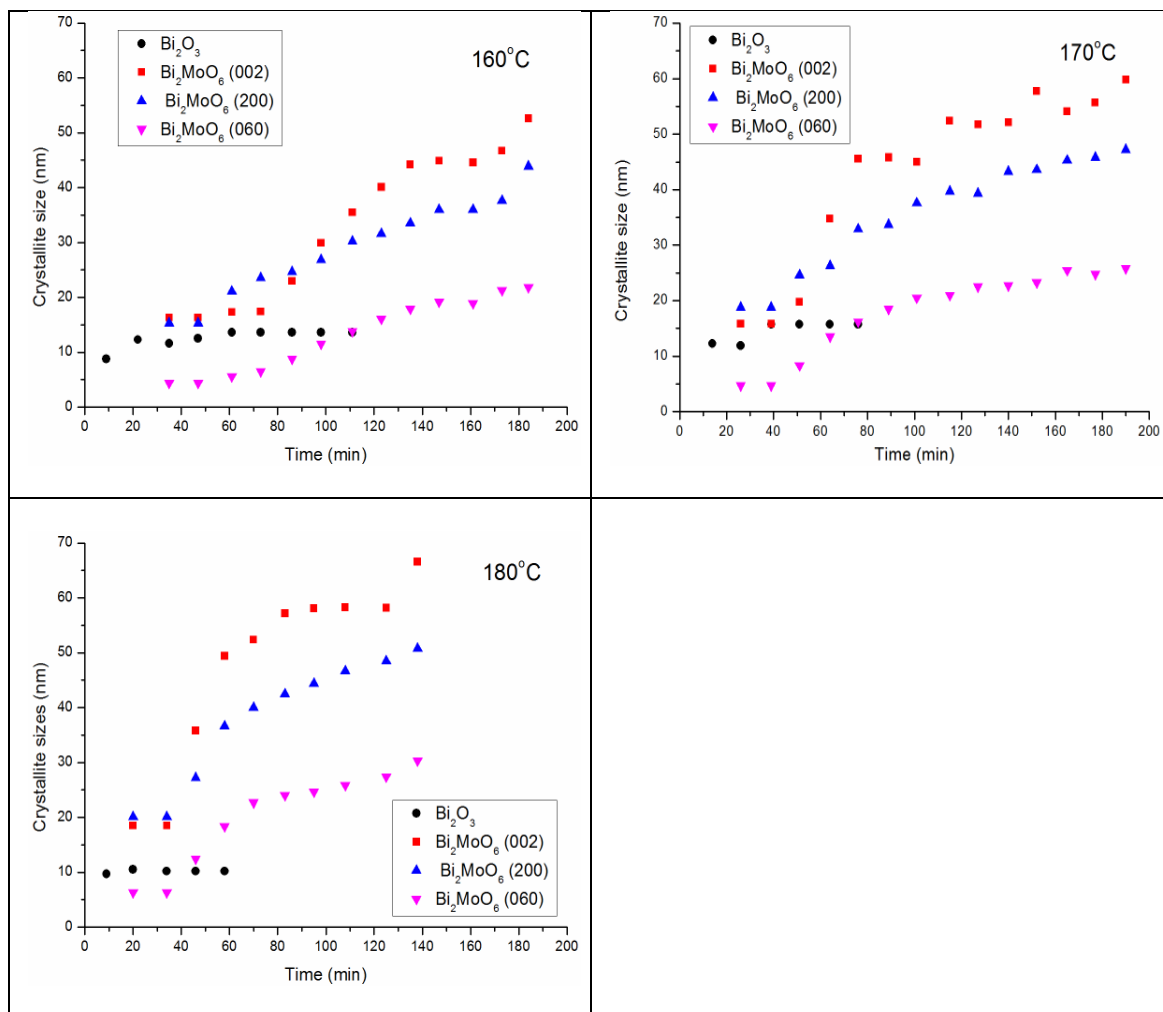


Figure 3-13 Evolution of crystallite sizes formed at different temperatures as a function of time during the hydrothermal synthesis of γ - Bi_2MoO_6 . In the initial stages of the reaction, the crystals are isotropic in the shape with the mean Bi_2O_3 particle sizes of $12.6 \pm 1.6 \text{ \AA}$, $14.5 \pm 1.9 \text{ \AA}$ and $10.2 \pm 0.3 \text{ \AA}$ for temperatures of 160, 170 and 180°C respectively. Thereafter, the anisotropic growth with crystal sizes given in the figure takes place. The uncertainties are smaller than the symbol.

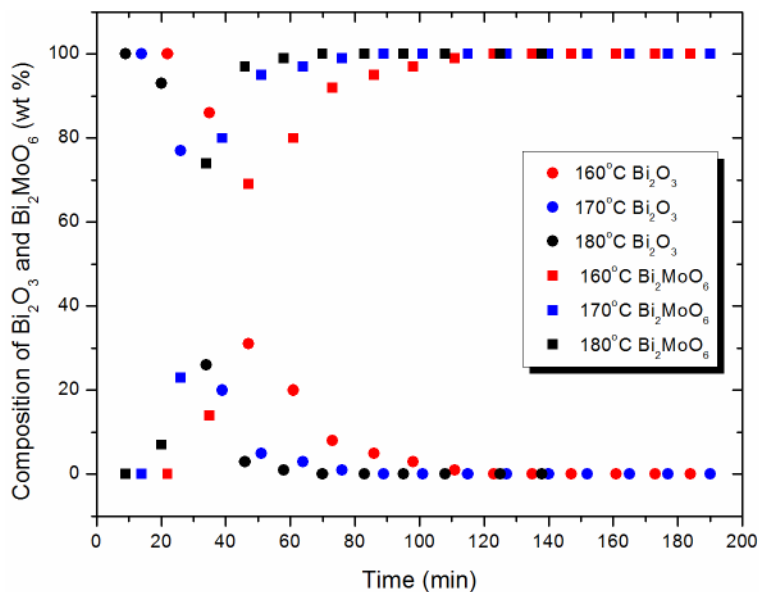


Figure 3-14 Changes in the volume fraction of Bi_2O_3 and $\gamma\text{-Bi}_2\text{MoO}_6$ phases present during the course of the reaction at 160, 170 and 180°C.

Table 3-2 The Rietveld refinement results of HRPD patterns collected at 160°C.

Time (min)	Bi_2O_3		Bi_2MoO_6		
	Cell parameters (Å)		Cell parameters (Å)		
	a	c	a	b	c
9	4.0243(5)	5.556(1)	-	-	-
22	4.0178(4)	5.570(1)	-	-	-
35	4.0185(4)	5.565(1)	5.538(1)	16.267	5.591(4)
47	4.0184	5.564	5.542(1)	16.268	5.577(1)
61	4.0184	5.564	5.5268(6)	16.268(4)	5.5692(7)
73	4.0184	5.564	5.5192(7)	16.259(4)	5.5497(8)
86	4.0184	5.564	5.5139(4)	16.258(2)	5.5380(5)
98	4.0184	5.564	5.5094(4)	16.249(1)	5.5291(4)
111	4.0184	5.564	5.5083(3)	16.255(1)	5.5290(3)
123	-	-	5.5050(3)	16.247(1)	5.5249(2)
135	-	-	5.5057(2)	16.2551(9)	5.5261(2)
147	-	-	5.5032(2)	16.2470(9)	5.5238(2)
161	-	-	5.5047(2)	16.2542(9)	5.5246(2)
173	-	-	5.5024(2)	16.2460(8)	5.5226(2)
184	-	-	5.5036(2)	16.249(1)	5.5246(2)

Table 3-3 *The Rietveld refinement results of HRPD patterns collected at 170°C.*

Time (min)	Bi ₂ O ₃		Bi ₂ MoO ₆		
	Cell parameters (Å)		Cell parameters (Å)		
	a	c	a	b	c
14	4.0191(4)	5.5751(9)	-	-	-
26	4.0154(4)	5.571(1)	5.547(2)	16.289	5.580(3)
39	4.013(1)	5.579(4)	5.5321(9)	16.289(6)	5.567(1)
51	4.013	5.579	5.5174(6)	16.251(2)	5.5374(7)
64	4.013	5.579	5.5093(4)	16.258(1)	5.5292(3)
76	4.013	5.579	5.5050(3)	16.249(1)	5.5253(2)
89	-	-	5.5050(3)	16.254(1)	5.5262(2)
101	-	-	5.5034(2)	16.248(1)	5.5242(2)
115	-	-	5.5042(2)	16.252(1)	5.5257(2)
127	-	-	5.5025(2)	16.2461(9)	5.5228(2)
140	-	-	5.5039(2)	16.2521(9)	5.5251(2)
152	-	-	5.5018(2)	16.2442(9)	5.5228(2)
165	-	-	5.5028(2)	16.2506(7)	5.5247(1)
177	-	-	5.5011(2)	16.2426(7)	5.5228(1)
190	-	-	5.5027(2)	16.2502(8)	5.5245(1)

Table 3-4 *The Rietveld refinement results of HRPD patterns collected at 180°C.*

Time (min)	Bi ₂ O ₃		Bi ₂ MoO ₆		
	Cell parameters (Å)		Cell parameters (Å)		
	a	c	a	b	c
9	4.0206(4)	5.570(1)	-	-	-
20	4.0164(4)	5.5706(9)	5.523(5)	16.228	5.566(7)
34	4.016(2)	5.554(5)	5.5286(7)	16.228(4)	5.5629(8)
46	4.016	5.554	5.5099(4)	16.256(1)	5.5299(3)
58	4.016	5.554	5.5069(2)	16.2536(8)	5.5281(1)
70	-	-	5.5035(2)	16.2451(8)	5.5248(1)
83	-	-	5.5047(2)	16.2517(7)	5.5261(1)
95	-	-	5.5031(2)	16.2456(8)	5.5239(2)
108	-	-	5.5040(2)	16.2511(7)	5.5259(1)
125	-	-	5.5038(1)	16.2524(7)	5.5259(1)
138	-	-	5.5019(2)	16.2449(7)	5.5237(1)

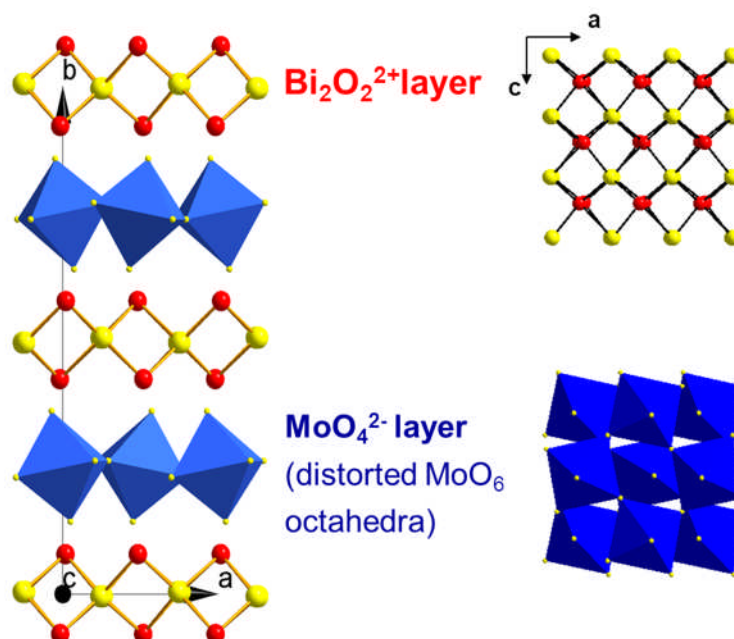


Figure 3-15 The graphical representation of γ - Bi_2MoO_6 Aurivillius type structure viewed down to c -axis (on the left). Corner sharing MoO_6 octahedra along a and c axis form infinite MoO_4^{2-} layers that alternate with Bi_2O_2 layers along b axis. On the right, a detailed view on MoO_4^{2-} and $\text{Bi}_2\text{O}_2^{2+}$ layers viewed along b -axis.

In summary, from XANES and Raman scattering, the presence of isolated tetrahedral molybdenum species, MoO_4^{2-} , were present in the initial stages of the synthesis. In the first step, Raman scattering revealed an elongation of MoO_4 species before their conversion to distorted octahedral, which could not be directly established from the XANES data. Simultaneously to appearance of octahedral species, the γ - Bi_2MoO_6 started to grow. Although it is not possible with the current data to accurately define the atomic architecture of the initial and intermediate phases, it is possible to propose that a distorted fluorite structure acts as a skeleton for the conversion to the γ - Bi_2MoO_6 Aurivillius-type structure, as shown in Figure 3-15. From HRPD data, at the temperature range between 160 and 180°C, the crystal growth of γ - Bi_2MoO_6 occurs in two steps: spherical particles, 10.2±0.3 nm in diameter, first form before the growth of highly anisotropic γ - Bi_2MoO_6 platelets from these particles. However, one cannot exclude the possible presence of molybdenum in the initial Bi_2O_3 structure, in which case its coordination would be tetrahedral.

3.5.3 Combined EXAFS/XRD

Because of complicated HRPD/Raman/XANES setup for following isothermal hydrothermal crystallization at target temperatures described in a previous section, it was necessary to make compromises at the expense of XAS which had to be collected in a short period of time and fluorescence mode. For this reason, experiments were repeated, and high quality XAS data were obtained that could be used for full EXAFS analyses.

Time-resolved Mo K-edge XANES spectra and diffraction data recorded during hydrothermal crystallization of γ -Bi₂MoO₆ gel at 140°C are shown in Figure 3-16 and Figure 3-17 respectively. Both techniques revealed that transformation begins after 92.5±9 min of hydrothermal reaction. The XANES spectrum of the initial γ -Bi₂MoO₆ gel shows a distinct pre-edge peak at 20 010.7 eV (arrow B) and a weak shoulder on the top of the edge at 20 029.3 eV (arrow A) (see Figure 3-16). The features A and B are regarded as characteristic of near edge XAS spectra and corresponds to *1s* to *4d* (arrow B) and *1s* to *5p* (arrow A) quadropole transitions^[43]. Their intensities are used as signatures for determining the coordination environment of molybdenum compounds^[17, 23, 31, 43]. A large pre-edge peak (arrow B) which is a typical for non-centrosymmetric tetrahedral environment, is due to mixing molybdenum *d* and *p* orbitals, while in octahedral environment is its intensity very small. A weak shoulder on the top of the edge (arrow A) is due to *1s* *5p* electronic transition in centrosymmetric octahedral environment. In XRD patterns shown in Figure 3-17 one can observe a gradual shift of all reflections toward higher 2theta values which accounts for formation of γ -Bi₂MoO₆. This shift coincides with a gradual change in Mo⁶⁺ coordination state which is also evident from XANES (Figure 3-16).

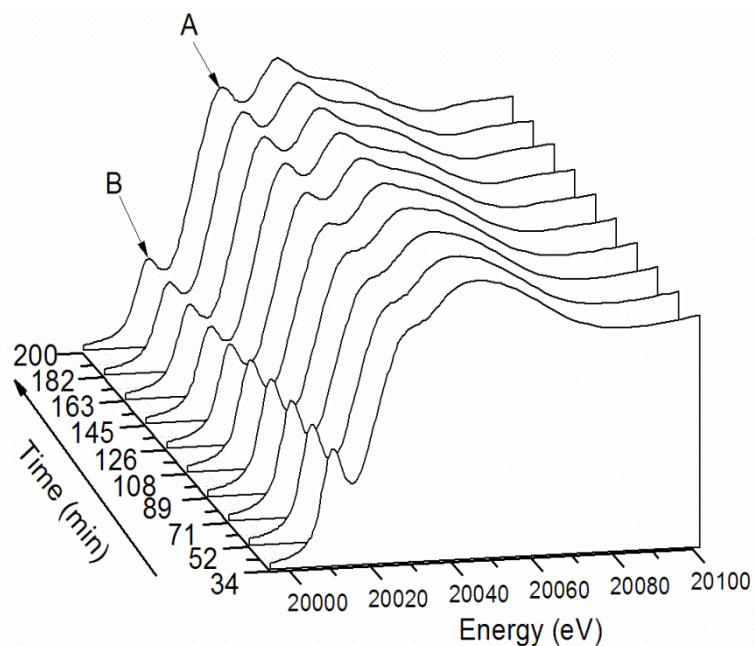


Figure 3-16 Stacked plot of Mo K-edge XANES spectra of γ - Bi_2MoO_6 recorded during hydrothermal crystallization at $140\text{ }^\circ\text{C}$. The pre-edge and the shoulder on the top of the edge are indicated by arrows B and A respectively. For a further explanation see the text.

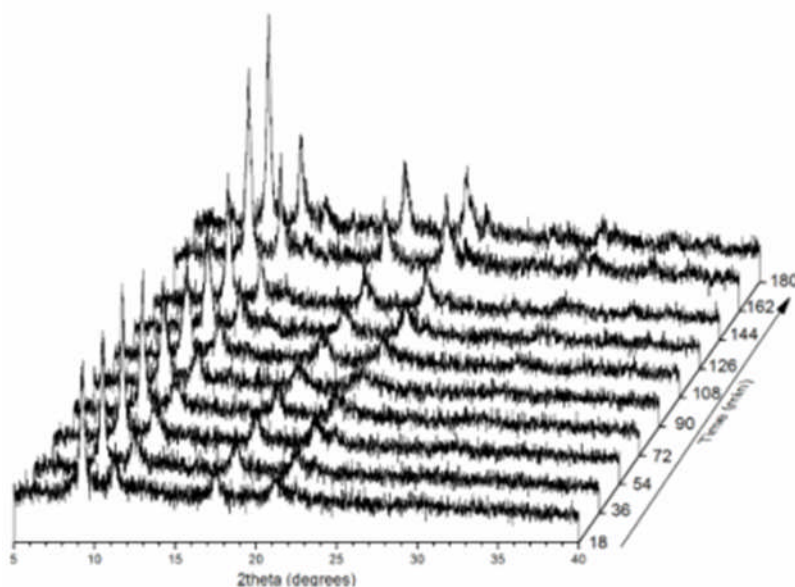


Figure 3-17 Stacked XRD pattern recorded during hydrothermal crystallization of γ - Bi_2MoO_6 gel at $140\text{ }^\circ\text{C}$ with wavelength, $\lambda=0.625\text{ \AA}$. The reflections in the first diffraction pattern can be assigned to Bi_2O_3 phase which is gradually transformed to γ - Bi_2MoO_6 during the course of the reaction.

Comparison of the Mo K-edge XANES, in particular, the pre-edge peak for the starting γ - Bi_2MoO_6 gel with that of $\text{Na}_2\text{MoO}_4 \cdot 2\text{H}_2\text{O}$ model compound suggests, that molybdenum is similar to $\text{Na}_2\text{MoO}_4 \cdot 2\text{H}_2\text{O}$ in terms of local structure (Figure 3-18), while the XRD pattern shows the presence of an amorphous phase. This shows the complementary of using XAS with respect to XRD, since this information can be obtained in gel, amorphous and crystalline phase and is independent of the existence of long range order which is required for useful XRD data. During hydrothermal reaction at the target temperature decay of the distinct pre-edge peak takes place, and thus molybdenum is gradually converted from tetrahedral to octahedral state. Upon completion of the reaction the crystalline product, γ - Bi_2MoO_6 , is formed. XANES suggests that its local structure bears a structural resemblance to the $(\text{NH}_4)_6\text{Mo}_7\text{O}_{24} \cdot 4\text{H}_2\text{O}$ model compound as shown in Figure 3-18.

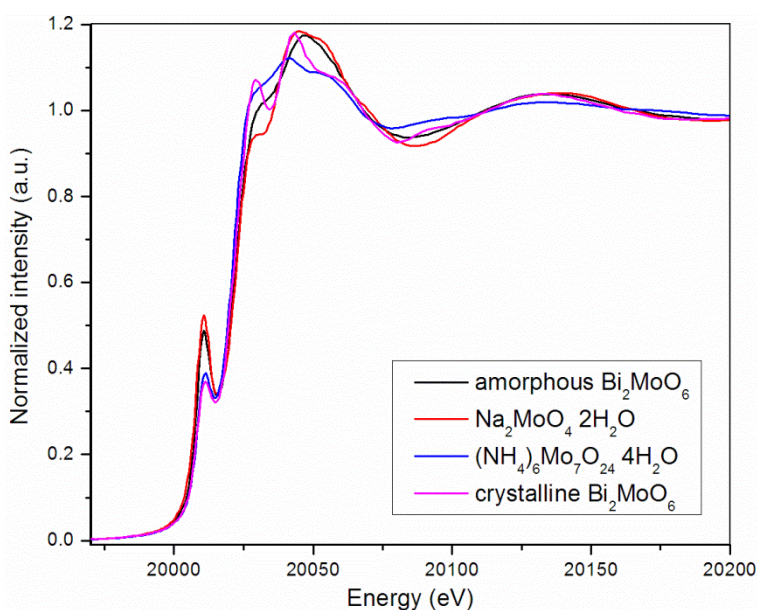


Figure 3-18 Comparison of the Mo K-edge XANES of the amorphous gel and crystalline γ - Bi_2MoO_6 with model compounds, $\text{Na}_2\text{MoO}_4 \cdot 2\text{H}_2\text{O}$ and $(\text{NH}_4)_6\text{Mo}_7\text{O}_{24} \cdot 4\text{H}_2\text{O}$, representing molybdenum in tetrahedral and octahedral geometry respectively.

Hydrothermal crystallizations of γ - Bi_2MoO_6 gel were also carried out at higher temperatures, i.e. 150 and 160°C. Irrespective of the crystallization temperature the coordination of the Mo^{6+} ions changes from tetrahedral to octahedral environment during the reaction^[52].

Figure 3-19 depicts a plot of evolution of intensity of the feature B, i.e. decay of the pre-edge peak as a function of time (from Figure 3-16) for all three crystallization temperatures. The intensity was obtained by direct measurement of maximum value, with a normalization of the XAS data with respect to the edge step and subtracting the smooth background function. The intensity of the pre-edge peak carrying information on amounts of MoO_4^{2-} and MoO_6 species is subsequently used in kinetics analysis (discussed later) for deriving the conversion fraction (α), which is a measure of reaction progress as a function of time.

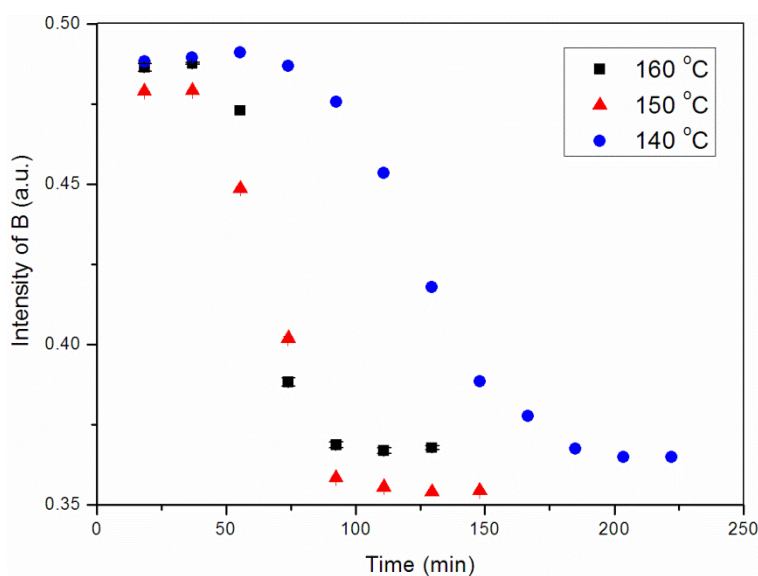


Figure 3-19 The variation of the pre-edge intensity during hydrothermal crystallization at 140, 150 and 160°C with time. The intensity was obtained by direct measurement of the maximum value of the pre-edge peak (arrow B) in XANES spectra plotted in Figure 3-16.

In the XRD experiments, after several minutes the formation of a crystalline phase was observed before $\gamma\text{-Bi}_2\text{MoO}_6$. This intermediate crystalline phase was identified in the section 1.5.2 as Bi_2O_3 . The XRD data quality in these time resolved experiments was not sufficiently high to be able to identify phases and unit cell parameters but sufficient to confirm that this intermediate phase was indeed formed.

XRD measurements were performed on the fully reacted materials in order to identify which crystalline phases were formed. Diffraction data of the fully reacted material is shown in Figure 3-20. The reacted samples were identified as $\gamma\text{-Bi}_2\text{MoO}_6$ ^[42] with an orthorhombic unit cell with $a = 5.50 \text{ \AA}$, $b = 16.25 \text{ \AA}$, $c = 5.52 \text{ \AA}$. The diffraction patterns obtained from freshly prepared Bi_2MoO_6 precursor gel at room temperature showed no evidence for the presence of any crystalline components.

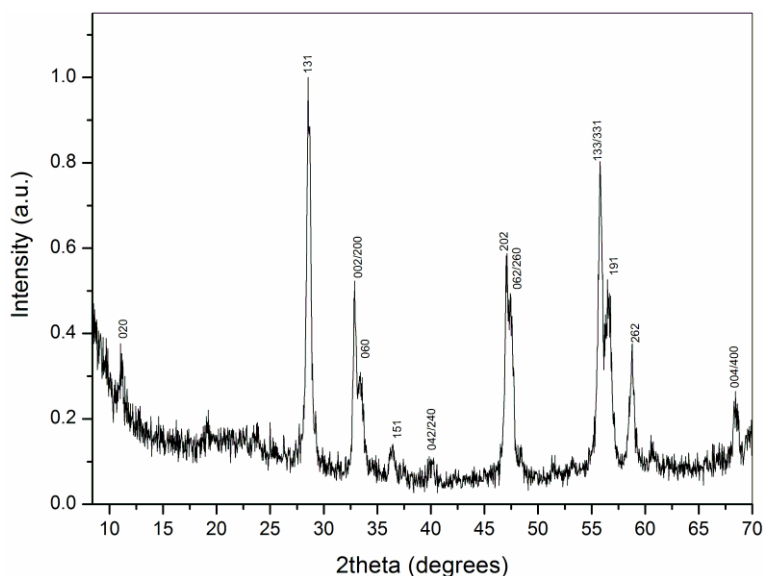


Figure 3-20 Post mortem XRD pattern of the crystalline $\gamma\text{-Bi}_2\text{MoO}_6$ formed at 140°C during in-situ combined XAS/XRD experiment collected with lab XRD machine at the wavelength $\lambda=1.54 \text{ \AA}$. Indeed, the pure phase was formed.

3.5.4 EXAFS

The modelling procedure of the Mo K-edge data of $\gamma\text{-Bi}_2\text{MoO}_6$ was checked by analysing in detail the first shell of the two model compounds, $\text{Na}_2\text{MoO}_4 \cdot 2 \text{H}_2\text{O}$ and $(\text{NH}_4)_6\text{Mo}_7\text{O}_{24} \cdot 4\text{H}_2\text{O}$, representing MoO_4^{2-} and MoO_6 species respectively, as shown in Figure 3-21. In MoO_4^{2-} , the molybdenum atom is surrounded by four tetrahedrally spaced oxygen atoms at 1.76 \AA . In MoO_6 , the molybdenum atom is surrounded by six octahedrally arranged oxygen atoms. The EXAFS fitting results find three oxygen atoms at 1.75 \AA , two at 1.97 \AA and one at 2.17 \AA .

In addition, room temperature Mo K-edge EXAFS data for crystalline γ -Bi₂MoO₆ prepared ex-situ method in Teflon-lined autoclave was obtained (Figure 3-22). This data was fitted with the nearest neighbouring octahedral oxygen shell, in which the four short Mo–O bonds at 1.80 Å along with the two long Mo–O bonds at 2.26 Å were found. In the next cations neighbouring shell were located the two Mo–Mo bonds at 3.82 Å with eight Mo–Bi bonds at 3.92 Å. These bond distances are consistent with structural parameters derived from XRD by Theobald et al.^[42].

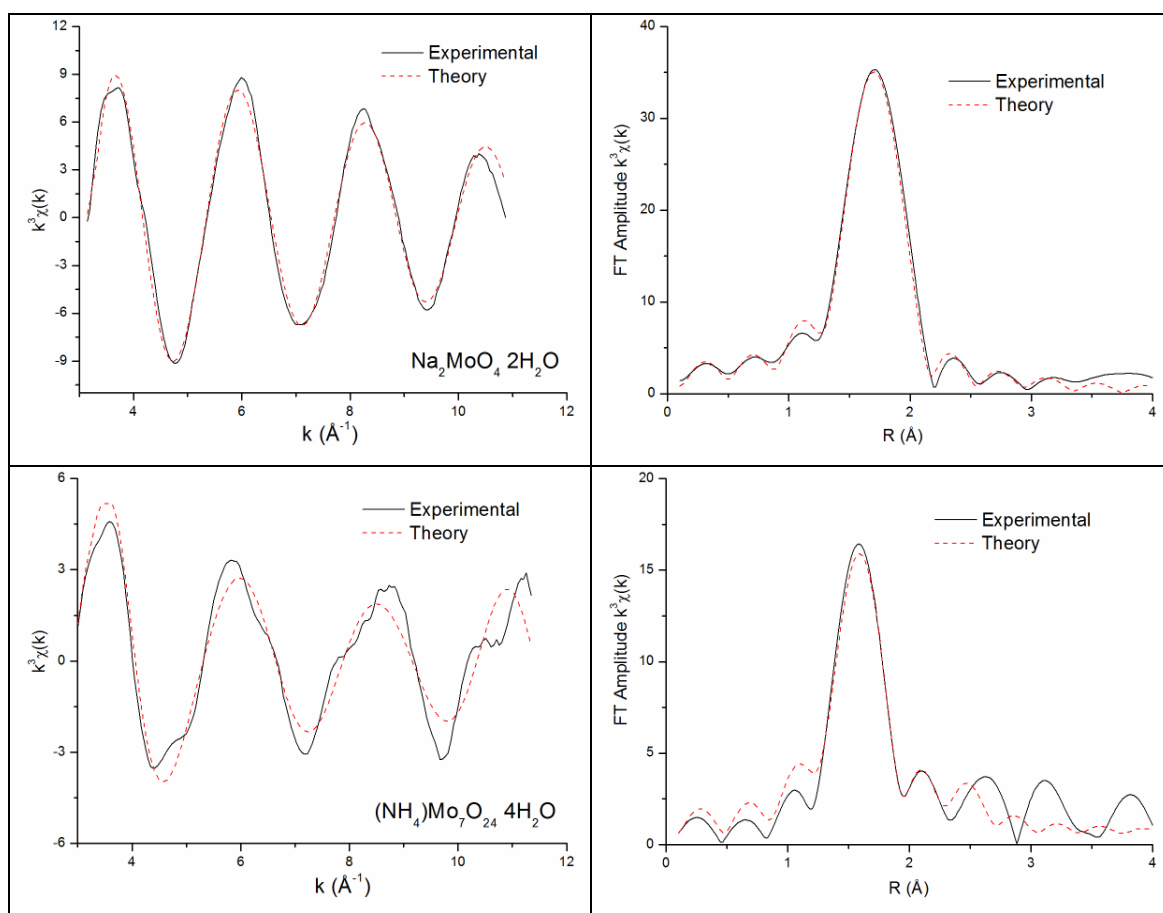


Figure 3-21 Fits to Mo K-edge EXAFS spectra of reference materials analysed in k -space (k^3 -weighted, background subtracted) together with corresponding Fourier transforms. The solid line is the experimental data and the dashed line is the best fit.

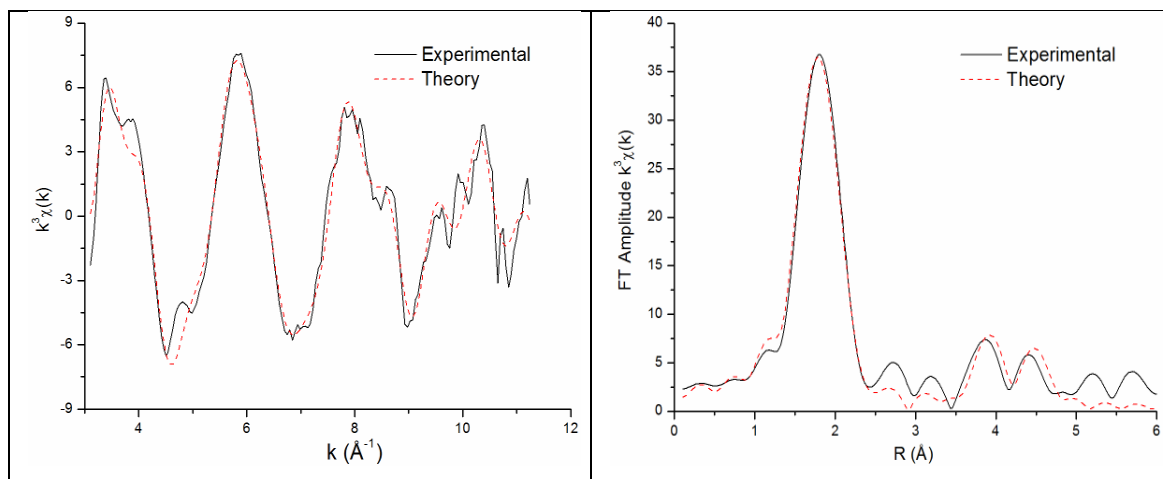


Figure 3-22 A fit to Mo K-edge EXAFS spectrum of ex-situ synthesised $\gamma\text{-Bi}_2\text{MoO}_6$ together with corresponding Fourier transform. Data was analysed in k -space (k^3 -weighted, background subtracted). The solid line is the experimental data and the dashed line is the best fit.

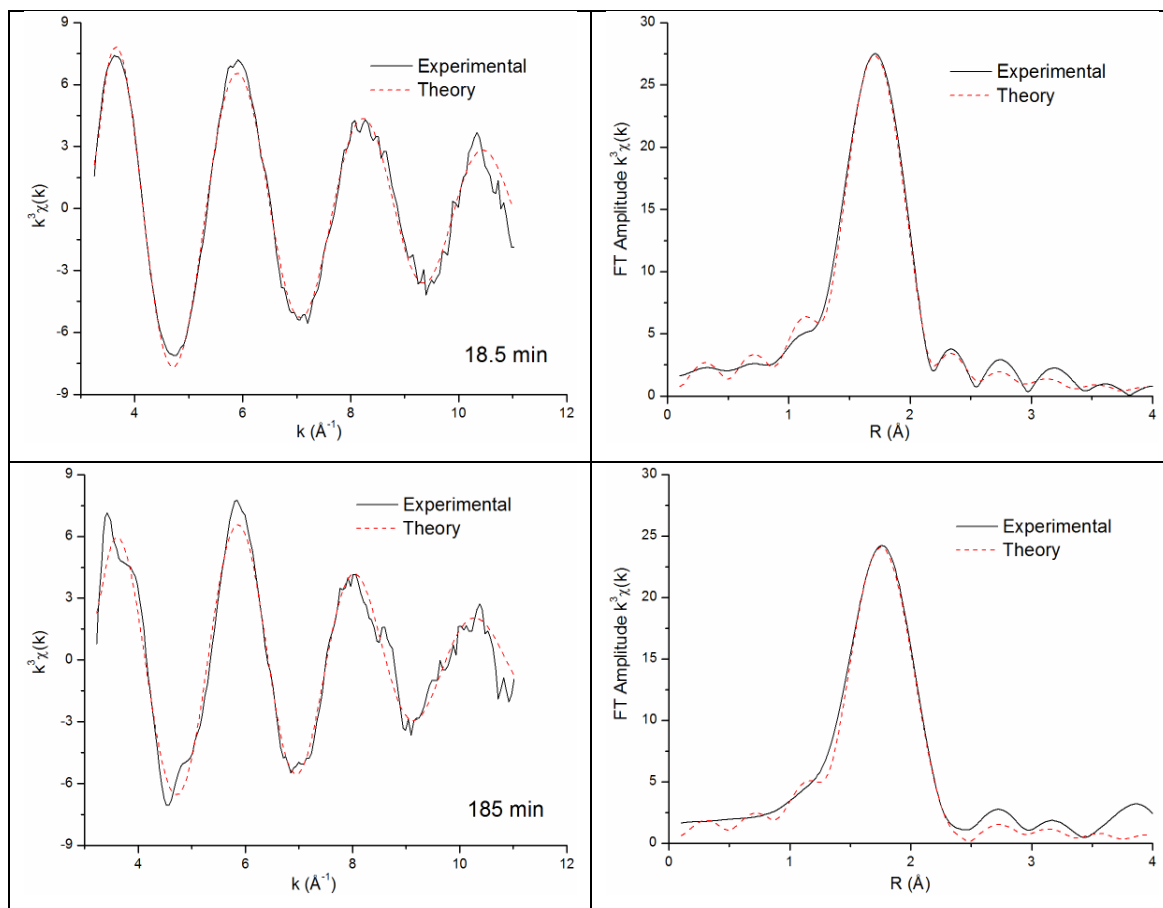


Figure 3-23 A typical fit to Mo K-edge EXAFS spectra of γ - Bi_2MoO_6 recorded after 18 min of the reaction at 140°C and a formed crystalline material upon the reaction completion. Data were analysed in k -space (after background subtraction, k^3 weighted). The solid line is the experimental data and the dashed line is the best fit.

Figure 3-23 depicts typical fits to Mo K-edge EXAFS data analysed in k -space and calculated EXAFS with the corresponding Fourier transforms for the formation of γ - Bi_2MoO_6 at 140°C from an amorphous gel. Comparison of Fourier transforms show that the magnitude of the first Fourier transform peak corresponding to Mo–O distance decreases with crystallization time. These changes are due to a partial transformation in the local atom environment from the tetrahedral Mo^{6+} to octahedral Mo^{6+} coordination as detected by XANES.

While room temperature XRD data taken from the initial γ - Bi_2MoO_6 gel showed only the presence of an amorphous phase, the Mo K-edge EXAFS data revealed that some

short range structure was present and that the molybdenum atom is surrounded by four tetrahedrally arranged oxygen atoms at the bond distance of 1.76 Å.

After 18±9 min of the reaction XRD show four reflections which can be assigned to the Bi₂O₃ phase. The local structure around Mo⁶⁺ ions remains the same, i.e. four tetrahedrally arranged oxygen atoms around molybdenum at the distance of 1.77 Å. Following 90±9 min of the reaction at 140°C, the long Mo–O bonds at 2.27 Å with the four short Mo–O bonds at 1.78 Å are found. The presence of the two long Mo–O bonds that are a typical for a distorted octahedral molybdenum like, for instance, in MoO₃^[53] shows that Mo⁶⁺ ions are converted from tetrahedral to octahedral state. Additionally, this indicates that the Mo⁶⁺ constructs Mo–O–Bi links with the Bi₂O₂²⁺ layers. In the final stages of the reaction, the two long Mo–O bonds are shortening, whereas the short Mo–O bonds are lengthening due to further structural rearrangements. In the formed crystalline material after 185±9 min of the reaction was found the presence of four short Mo–O bonds at 1.80 Å and another two long at 2.26 Å, which are in accordance with those for the material prepared by *ex-situ* and literature^[17, 54]. The purity of the formed crystalline phase was confirmed by XRD as shown in Figure 3-20.

Figure 3-24 depicts changes in bond distances (*R*) and coordination numbers (*N*) during the course of isothermal hydrothermal reaction at the target temperature as a function of time. It is evident that at higher crystallization temperatures is needed less time to convert Mo⁶⁺ ions from tetrahedral to octahedral coordination as evidenced by changes in the Mo–O bond distances and coordination numbers.

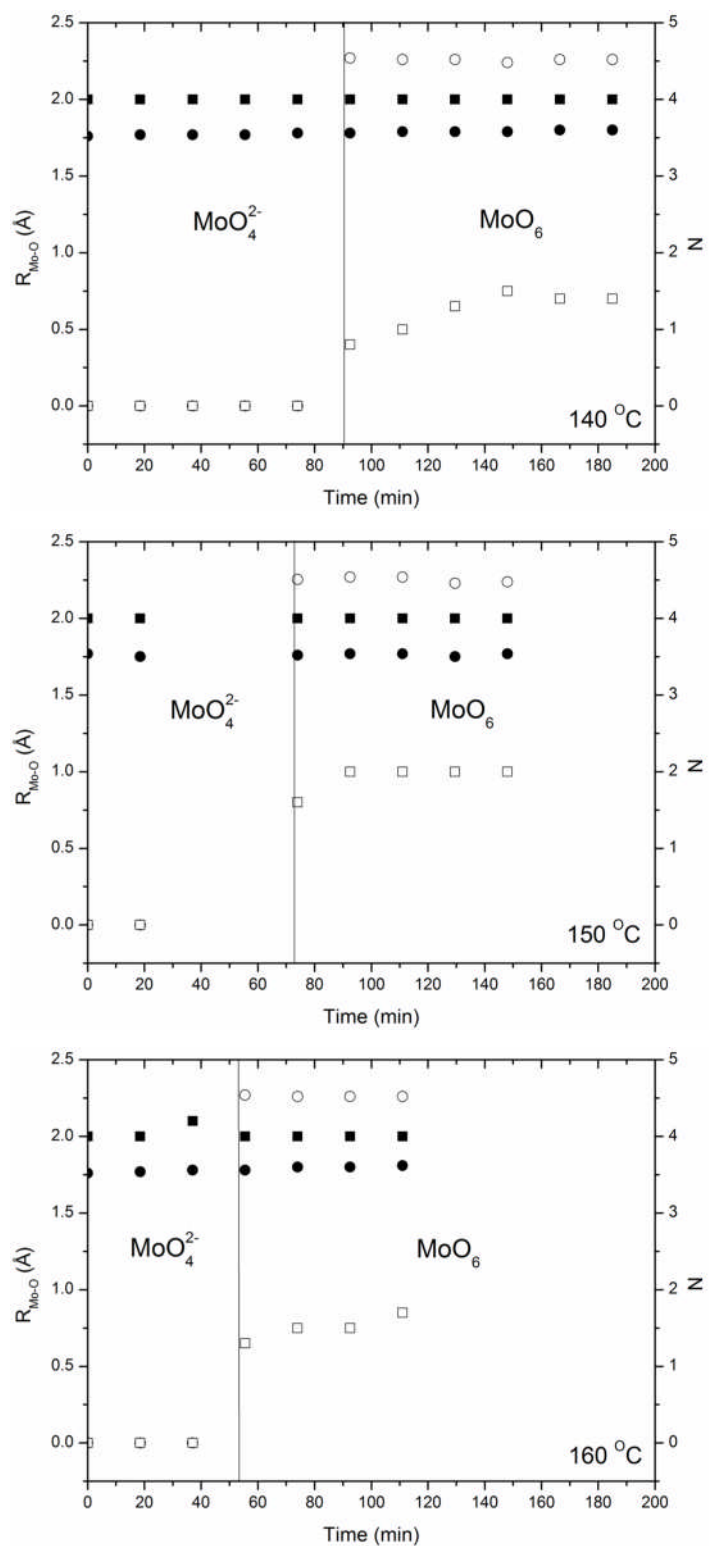


Figure 3-24 Changes in short Mo–O bonds ($R_{\text{Mo-O}}$) (filled circles), long Mo–O bonds (open circles), coordination numbers (N) associated with short bonds (filled squares) and long bonds (open squares) as a function of crystallization time. The error bars are within the size of the used symbol ($\pm 0.01 \text{ \AA}$).

3.5.5 Kinetic analyses

Quantitative information about isothermal crystallization reaction kinetics of γ -Bi₂MoO₆ at different temperatures was obtained by applying the Avrami-Erofe'ev formalism^[55]. With this method the nucleation rates, particle dimensionality and growth mechanism can be linked to the time-dependent extent of reaction. The equation describes conversion of Mo⁶⁺ ions from tetrahedral to octahedral environment as a function of time and temperature,

Equation 3-1 *Avrami-Erofe'ev equation*

$$\alpha = 1 - e^{-(kt)^n}$$

where, α is the conversion fraction describing varying amounts of Mo⁶⁺ ions in tetrahedral or octahedral environment during the reaction, t - time, k - rate related parameter for nucleation and growth and n is the Avrami exponent related to the morphology and the dimensionality of the crystal growth^[56, 57].

Within a narrow temperature range, the temperature dependence of k can be described by the Arrhenius equation:

Equation 3-2 *Arrhenius equation*

$$k = v \exp\left(-\frac{E_A}{RT}\right)$$

where E_A is the activation energy and v the frequency factor (hopping probability) for the process, R universal gas constant, T the absolute temperature.

In general, the pre-edge peak feature has been exploited as signature to determine local geometry and valence states of a variety of transition metals in catalytic materials^[36, 58]. These catalysts are usually subject to thermal treatment at the target temperature in air or gaseous environments and thus the transformation from one phase to another can occur over period of time, which results in variation of the pre-edge peak intensity. Similar behaviours can be seen during formation of materials using hydrothermal reactions, whereby the pre-edge peak can be used as a signature to confirm formation of

a desired phase in time. On the basis of these observations, it is postulated that its intensity has a linear relation with the conversion fraction α , that describes reaction progress as function of time.

It is noteworthy that this pre-edge feature has not been exploited for deriving information on reaction kinetics. So far, it has been reported only studies using in-situ time-resolved XANES for obtaining information on reaction kinetics^[59]. In this case, authors derived the conversion fraction, α , from principal component analysis (PCA) results. The PCA were used to quantify different phases present.

In this work is shown that as an alternative the pre-edge feature in near edge XAS spectra can be used for studying solid state kinetics in the similar manner as other analytical and diffraction methods. The benefits of using it are that one does not only obtain kinetic data but that one also can derive qualitative information about the time evolution of the electronic surroundings of elements of interest.

The conversion fraction, α , describing fraction of the octahedral phase was derived from the XANES pre-edge peak intensity. Since this system contains two phases, i.e. the two phases, MoO_4^{2-} and MoO_6 , coexisting together, then the amount of a single phase (MoO_6) is given as

Equation 3-3 *The amount of a single phase*

$$I_{\text{Oct}} = 1 - I_{\text{Tet}}$$

where I_{Oct} is the amount of octahedral species, MoO_6 ; I_{Tet} is the amount of tetrahedral species, MoO_4^{2-} . Information on kinetics is derived from changes only in the abundance of MoO_6 species as a function of time. The conversion fraction, α , is defined by the following expression

Equation 3-4 *The conversion fraction*

$$\alpha = \frac{(1 - I_{\text{Tet}})_t}{(1 - I_{\text{Tet}})_\infty}$$

where, $I_{(Tet)t}$ is a value of the pre-edge peak intensity, which is linearly related to the MoO_4^{2-} amount, at given time t , and $I_{(Tet)\infty}$ is a value of the pre edge peak intensity when the reaction is completed.

A common method to analyse kinetic data is to linearize the Avrami-Erofe'ev equation by taking 'ln' on both sites, in that a plot of $\ln(-\ln(1-\alpha))$ versus $\ln(t)$ gives a straight line with slope n and intercept $n \ln k$. The plot is usually linear in a fixed α -range and reduced time scale. However, this procedure ignores the beginning and the end of the curve, which makes data analysis incomplete. The simplified linear least square fitting method was proposed by Hancock and Sharp^[60] in 1972. This linear least squares fitting procedures for analysing kinetic data appeals due its simplicity which definitely was an advantage at the time of its conception. However, with modern software tools it is possible to use the entire sigmoidal data without linearization with Avrami-Erofe'ev equation using non-linear least squares fitting procedures and thus benefit from the use of the whole data set. The significance of fitting entire kinetic data using non-linear least squares procedure were discussed and demonstrated by Finney and Finke^[61]. These authors used kinetic data for solid state phase transformations from literature to test the two-step Finke-Watzky model, whereby they tried to deconvolute nucleation rate from autocatalytic growth rate constant. Their fitting results were compared to those obtained by classical Avrami-Erofe'ev model and came to the conclusion that values of n were closed to theirs, whereas the k values are very different.

Kinetic data was fitted to the Avrami-Erofe'ev equation (Equation 3-1) using the non-linear least squares fitting procedure implemented in Origin. Figure 3-25 depicts non-linear least squares fits to kinetic data using Avrami-Erofe'ev equation (Equation 3-1). The solid lines in the plot represent the best fits to $\alpha(t)$ curves for hydrothermal crystallization of γ - Bi_2MoO_6 gel at the three different temperatures. The fitting results presented in Figure 3-25 show that Avrami exponent (n) values lie between 3 and 4. The derived values of Avrami exponent indicate the three-dimensional phase boundary controlled growth with a decreasing nucleation rate^[56]. The conversion process consists of an initial period of nucleation associated with development of stable nuclei followed by growth of these nuclei into crystallites which extends to maximum rate of reaction. Thereafter, the transformation rate of nuclei into crystallites is diminished due to

depletion of the reactants, i.e. one observes a decelerating nucleation which continues until completion of reaction.

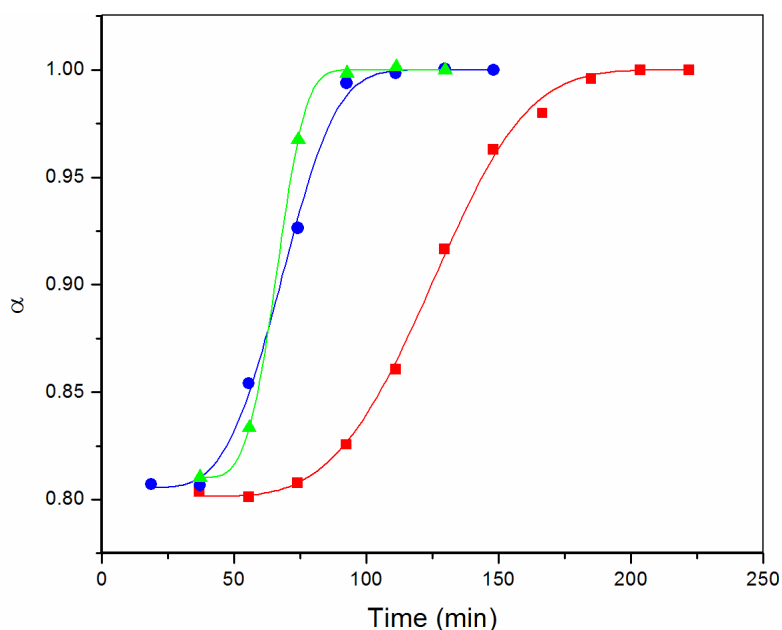


Figure 3-25 Kinetic data for the growth of MoO_6 species from MoO_4^{2-} species. α -time curves were obtained from the isothermal hydrothermal crystallization of $\gamma\text{-Bi}_2\text{MoO}_6$ gel at 140°C (red square), 150°C (blue circle) and 160°C (green triangles). Solid lines are the non-linear least squares fits to Avrami-Erofe'ev expression shown in equation (Equation 3-1) performed in Origin.

Table 3-5 Avrami exponent (n) and rate of crystallization (k) derived from Avrami-Erofe'ev equation.

Temp ($^\circ\text{C}$)	n	$k(\text{min}^{-1})$
140	3.54 ± 0.19	0.0103 ± 0.0001
150	3.45 ± 0.26	0.0182 ± 0.0003
160	3.76 ± 0.10	0.0315 ± 0.0002

From these kinetic analyses, the activation energy for the conversion of molybdenum from tetrahedral to octahedral coordination using the Arrhenius expression (Equation 3-2) was extracted. The plot of $\ln(k)$ versus $1/T$ is shown in Figure 3-26 and yields a

value of $E_a = 83$ kJ/mol which is almost three times higher than the value reported by Beale et al^[23]. This can be due to the fact that different type of a reaction vessel was used.

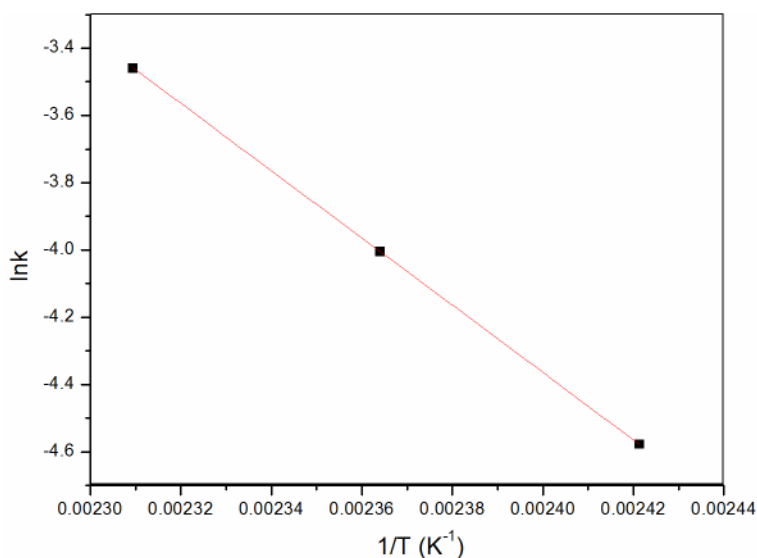


Figure 3-26 Arrhenius plot for determination activation energy.

The results of the kinetic analysis suggest that the overall formation of γ - Bi_2MoO_6 is the three dimensional growth processes with a decreasing nucleation rate. To verify 3D growth mechanism, complementary *ex-situ* studies on γ - Bi_2MoO_6 gel synthesised by hydrothermal method in Teflon-lined autoclave at 180°C for 30 min and 70 min were carried out. The results from SEM, XRD were cross correlated with *in-situ* XAS. SEM micrograph of the γ - Bi_2MoO_6 gel consists of aggregates of nearly spherical particles^[50] which were also confirmed by TEM^[10]. When γ - Bi_2MoO_6 gel is subjected to 30 min of isothermal reaction, the sample exhibits spherical particles (see SEM in Figure 3-27) due to the presence of intermediate phase as evidenced by HRPD. This is in agreement with the *in-situ* EXAFS fitting results which showed slight variations in four short Mo–O bonds due to the presence of isolated tetrahedral MoO_4^{2-} species. If sample was left crystallized for 70 minutes at this temperature, it could be observed not only larger spherical particles but also the formation of irregular thin discs which was evident from SEM, in Figure 3-27. This indicates formation of γ - Bi_2MoO_6 platelets. Compared to *in situ* experiments, XANES shows a shoulder at the top of the edge which is a

characteristic of MoO_6 species. More importantly, EXAFS results showed immediately after formation of the first thin plates the presence of a long Mo–O bonds at 2.26 Å along with four short at 1.78 Å. The long Mo–O bonds, typical for molybdenum in octahedral environment, is shortening during reaction process not only because of growing platelets but also due to ordering molybdenum layers and uniting pre-formed $\text{Bi}_2\text{O}_2^{2+}$ layers. The structural rearrangement of molybdenum layers is related to altering Mo–O bonds until the structure become composed of distorted octahedral molybdenum while preformed $\text{Bi}_2\text{O}_2^{2+}$ layers coming together^[31, 54, 62]. The local structure of bismuth is not altered during the formation process according to Reilly et al^[54], who carried out in-situ Bi L₃-edge EXAFS study of formation of $\gamma\text{-Bi}_2\text{MoO}_6$ from a precursor prepared by precipitation. This was also confirmed by the results from Raman scattering discussed in previous section.

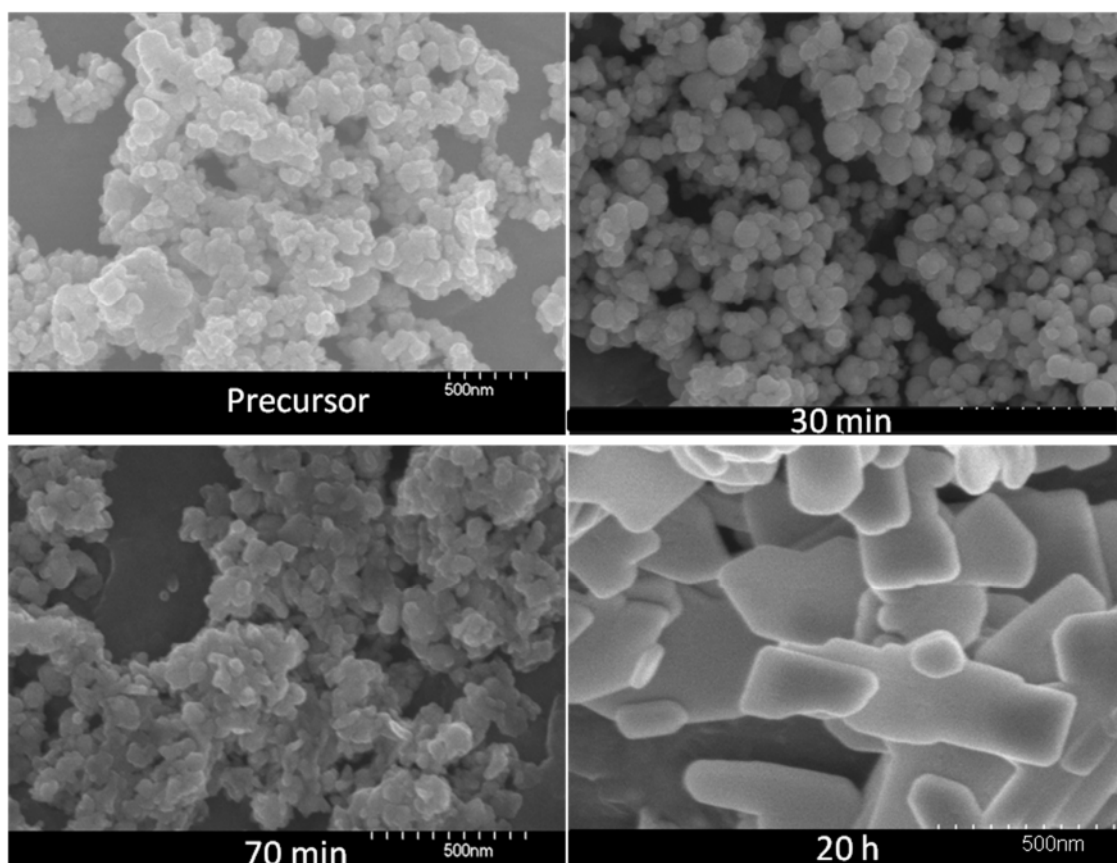


Figure 3-27 SEM pictures of $\gamma\text{-Bi}_2\text{MoO}_6$ gel itself and samples synthesised ex-situ by hydrothermal method at 180°C for 30 min and 70min and 20h.

From SEM micrographs is evident the presence of spherical particles, which are characteristic of 3D growth according to Hulbert^[56]. In summary, overall growth is in three dimensions, whereby from an intermediate phase consisting of Bi₂O₃ particles formed in the initial stage of the reaction are developed γ -Bi₂MoO₆ crystallites^[36]. The growth persists until all available nuclei are consumed during the reaction progress. Moreover, not only the growth of platelets occur but also rearrangement of the structure along c-axis, in that pre-formed Bi₂O₂²⁺ layers coming together. The fact that γ -Bi₂MoO₆ platelets can grow along c-direction is usually overlooked because of its layer structure in which slabs of corner-sharing distorted MoO₆ octahedra are sandwiched between [Bi₂O₂]²⁺ layers^[16]. The growth mechanism of γ -Bi₂MoO₆ that is proposed here is based upon this approach, and thus is different from that reported by Beale et.al.^[23]. In this case, authors investigated only the initial stages of crystallization at much lower temperatures which could lead to a different mechanism, thereby their reactions did not follow sigmoidal paths. This possibly can be attributed to different sources of chemicals for sample preparations as well as type of *in situ* reaction vessels. An alternative explanation might be that the intermediate phase identified in the previous section adds to the diffracted intensity of the XRD peaks used for the kinetics analysis. This would explain why the growth curves in the case of Beale et.al.^[23] do not exhibit a pure sigmoidal shape. By applying the method of using the pre-edge XAS intensity which is not sensitive to the intermediate phase that is being formed, and thereby the data required for the study of the γ -Bi₂MoO₆ formation can be isolated.

3.6 Conclusion

This study has shown that combination of HRPD, XANES and Raman scattering *in situ* techniques is a powerful tool to understand the formation and transformation of phases, which will enable one to control the crystal growth of a crystalline catalytic material. A benefit of using these *in situ* measurements has been demonstrated, by taking the formation of γ -Bi₂MoO₆ from an amorphous gel as an example. It has been found, that it occurs in two steps through the formation of Bi₂O₃ particles in the initial stages, and the growth of highly anisotropic platelets in a second step.

In the second section, it has been shown that the combination of *in-situ* EXAS/XRD with *ex-situ* XRD and SEM can provide complementary information on understanding phase transformations during the formation of γ -Bi₂MoO₆ under hydrothermal conditions. Particularly, EXAFS provides information about changes Mo–O bond distances and coordination numbers during the formation of the crystalline structure which was unavailable from XRD because of a long range ordering requirements. More importantly, EXAFS confirmed the presence of molybdenum species randomly dispersed in Bi₂O₃ matrix and their ordering during the crystallization process. Moreover, the novel approach for deriving the kinetics information using the pre-edge intensity of XAS has been proposed and verified on γ -Bi₂MoO₆ data. As a result of this effort, it was found that the growth of γ -Bi₂MoO₆ crystallites from an amorphous gel is the three dimensional and phase boundary controlled. This growth mechanism is well supported by SEM and HRPD data which confirmed the presence of spherical particles in the initial stages of reaction.

References

- [1] R. K. Grasselli, J. D. Burrington and J. F. Brazdil, *Faraday Discussions of the Chemical Society* **1981**, 72, 203-223; R. K. Grasselli, *Applied Catalysis* **1985**, 15, 127-139.
- [2] J. C. Jung, Heesoo, K., Choi, A. S., Chung, Y. M., Kim, T. J., Lee, J. S., Hoon Oh, S., Song, I. K., *Journal of Molecular Catalysis A Chemical* **2006**, 259, 166-170.
- [3] Hearne G. W. and Adams M., *US Patent* **1948**, 2, 451-485.
- [4] Veath F., Callahan J.L., Milberger E. C. and Foreman R. W., *Actes du deuxieme Congres International de Catalyse* **1961**, 2, 2647; F. Veath, J. L. Callahan, J. D. Idol and E. C. Milberger, *Chemical Engineering Progress* **1960**, 5b, 65.
- [5] R. K. Grasselli, J. D. Burrington, H. P. D.D. Eley and B. W. Paul in *Selective Oxidation and Ammoxidation of Propylene by Heterogeneous Catalysis, Vol. Volume 30* Academic Press, **1981**, pp. 133-163; J. L. Callahan, Foreman, R. W., Veatch, F. in *The SOHIO Process as an Inspiration for Molecular Organometallic Chemistry, Vol. 3044966* (Ed. U. patent), **1962**.
- [6] Callahan J.L. and R. K. Grasselli, *American Institute of Chemical Engineers* **1963**, 9, 755; R. K. Grasselli, *Topics in Catalysis* **2001**, 15, 93-101.
- [7] I. Matsuura, R. Schut and K. Hirakawa, *Journal of Catalysis* **1980**, 63, 152-166.
- [8] D. R. K. Grasselli and Hardman H.F., *US Patent* 3 642 930 **1972**.
- [9] Y. Moro-Oka, W. Ueda, H. P. D.D. Eley and O. H. Werner in *Multicomponent Bismuth Molybdate Catalyst: A Highly Functionalized Catalyst System for the Selective Oxidation of Olefin, Vol. Volume 40* Academic Press, **1994**, pp. 233-273.
- [10] H. Li, C. Liu, K. Li and H. Wang, *Journal of Materials Science* **2008**, 43, 7026-7034.
- [11] Y. Shimodaira, H. Kato, H. Kobayashi and A. Kudo, *The Journal of Physical Chemistry B* **2006**, 110, 17790-17797; R. Gruar, C. J. Tighe, L. M. Reilly, G. Sankar and J. A. Darr, *Solid State Sciences* **2010**, 12, 1683-1686.
- [12] T. Chen and G. S. Smith, *Journal of Solid State Chemistry* **1975**, 13, 288-297.
- [13] M. Egashira, K. Matsuo, S. Kagawa and T. Seiyama, *Journal of Catalysis* **1979**, 58, 409-418.
- [14] T. P. Snyder and C. G. Hill, *Journal of Catalysis* **1991**, 132, 536-555.
- [15] D. J. Buttrey, D. A. Jefferson and J. M. Thomas, *Philosophical Magazine A: Physics of Condensed Matter, Structure, Defects and Mechanical Properties* **1986**, 53, 897.
- [16] R. G. Teller, J. F. Brazdil, R. K. Grasselli and J. D. Jorgensen, *Acta Crystallographica Section C* **1984**, 40, 2001-2005.
- [17] G. Sankar, Roberts, M.A., Thomas, J.M., Kulkarni, G.U., Rangavittal, N., Rao, C.N.R., *Journal of Solid State Chemistry* **1995**, 119, 210-215.
- [18] A. Watanabe, S. Horiuchi and H. Kodama, *Journal of Solid State Chemistry* **1987**, 67, 333-339.
- [19] D. J. Buttrey, T. Vogt, U. Wildgruber and W. R. Robinson, *Journal of Solid State Chemistry* **1994**, 111, 118-127.
- [20] D. J. Buttrey, T. Vogt and B. D. White, *Journal of Solid State Chemistry* **2000**, 155, 206-215.
- [21] A. K. Cheetham and P. Day, *Solid state chemistry: Techniques*, Oxford Science Publications, **1988**, p. 7-89.
- [22] B. C. Gates, Katzer, J.R., Schuit, G.C.A., *Chemistry of catalytic processes*, **1979**, p. 109-128; P. A. Batist and H. J., *Journal of Chemical Technology and Biotechnology* **1979**, 29, 451-466.
- [23] A. M. Beale and G. Sankar, *Chemistry of Materials* **2003**, 15, 146-153.

- [24] G. Sankar and W. Bras, *Catalysis Today* **2009**, *145*, 195-203.
- [25] A. M. Beale, S. D. M. Jacques, E. Sacaliuc-Parvalescu, M. G. O'Brien, P. Barnes and B. M. Weckhuysen, *Applied Catalysis A: General* **2009**, *363*, 143-152.
- [26] A. M. Beale, M. T. Le, S. Hoste and G. Sankar, *Solid State Sciences* **2005**, *7*, 1141-1148; G. Sankar, *Topics in Catalysis* **1999**, *8*, 1-21; W. Bras, G. N. Greaves, M. Oversluizen, S. M. Clark and G. Eeckhaut, *Journal of Non-Crystalline Solids* **2005**, *351*, 2178-2193.
- [27] A. M. Beale, A. M. J. van der Eerden, S. D. M. Jacques, O. Leynaud, M. G. O'Brien, F. Meneau, S. Nikitenko, W. Bras and B. M. Weckhuysen, *Journal of the American Chemical Society* **2006**, *128*, 12386-12387.
- [28] D. C. Koningsberger and R. Prins, *X-ray Absorption: Principles, Applications, Techniques of EXAFS, SEXAFS, and XANES*, Wiley, **1988**, p. 443-572.
- [29] W. Bras, S. Nikitenko, G. Portale, A. M. Beale, A. v. d. Eerden and D. Detollenaere, *Journal of Physics: Conference Series* **2010**, *247*, 012047.
- [30] S. Nikitenko, A. M. Beale, A. M. J. van der Eerden, S. D. M. Jacques, O. Leynaud, M. G. O'Brien, D. Detollenaere, R. Kaptein, B. M. Weckhuysen and W. Bras, *Journal of Synchrotron Radiation* **2008**, *15*, 632-640.
- [31] A. M. Beale, L. M. Reilly and G. Sankar, *Applied Catalysis A: General* **2007**, *325*, 290-295.
- [32] B. Ravel and M. Newville, *Journal of Synchrotron Radiation* **2005**, *12*, 537-541.
- [33] J. Rodriguez-Carvajal, *Commission on Powder Diffraction (IUCr), Newsletter* **2001**, *26*, 12-19.
- [34] P. Thompson, D. E. Cox and J. B. Hastings, *Journal of Applied Crystallography* **1987**, *20*, 79-83.
- [35] C. Kongmark in *Genesis of Bismuth Molybdenum Oxide Catalyst followed by In-situ Techniques and its Use in Catalytic Dense Membrane Reactor, Vol. PhD thesis* Universite des Sciences et Technologies de Lille Lille, **2010**.
- [36] C. Kongmark, V. Martis, A. Rubbens, C. Pirovano, A. Lofberg, G. Sankar, E. Bordes-Richard, R.-N. Vannier and W. Van Beek, *Chemical communications* **2009**, 4850-4852.
- [37] E. Boccaleri, F. Carniato, G. Croce, D. Viterbo, W. van Beek, H. Emerich and M. Milanesio, *Journal of Applied Crystallography* **2007**, *40*, 684-693.
- [38] N. Binsted and S. S. Hasnain, *Journal of Synchrotron Radiation* **1996**, *3*, 185-196.
- [39] S. J. Gurman, N. Binsted and I. Ross, *Journal of Physics C-Solid State Physics* **1984**, *17*, 143-151.
- [40] B. K. Teo, *EXAFS: Basic Principles and Data Analysis*, **1986**, p. 114-157.
- [41] P. A. Batist, J. F. H. Bouwens and G. C. A. Schuit, *Journal of Catalysis* **1972**, *25*, 1-11.
- [42] F. Theobald, A. Laarif and A. W. Hewat, *Ferroelectrics* **1984**, *56*, 219-237.
- [43] M. R. Antonio, R. G. Teller, D. R. Sandstrom, M. Mehicic and J. F. Brazdil, *Journal of Physical Chemistry* **1988**, *92*, 2939-2944.
- [44] I. Nakagawa and J. L. Walter, *The Journal of Chemical Physics* **1969**, *51*, 1389-1397.
- [45] P. R. Graves, G. Hua, S. Myhra and J. G. Thompson, *Journal of Solid State Chemistry* **1995**, *114*, 112-122; R. Murugan, *Physica B: Condensed Matter* **2004**, *352*, 227-232.
- [46] F. D. Hardcastle and I. E. Wachs, *Journal of Raman Spectroscopy* **1990**, *21*, 683-691.

- [47] N. Weinstock, H. Schulze and A. Muller, *The Journal of Chemical Physics* **1973**, 59, 5063-5067.
- [48] J. Min Ku, K. Yong-II, N. Seung-Hoon and W. Seong Ihl, *Journal of Physics D: Applied Physics* **2006**, 39, 5080.
- [49] H. A. Harwig, *Zeitschrift für anorganische und allgemeine Chemie* **1978**, 444, 151-166.
- [50] C. Kongmark, V. Martis, C. Pirovano, A. Löfberg, W. van Beek, G. Sankar, A. Rubbens, S. Cristol, R. N. Vannier and E. Bordes-Richard, *Catalysis Today* **2010**, 157, 257-262.
- [51] M. Jarvinen, *Journal of Applied Crystallography* **1993**, 26, 525-531.
- [52] C. Kongmark in *Genesis of Bismuth Molybdenum Oxide Catalyst by in-situ Techniques and Application in Catalytic Dense Membrane Reactor, Vol. Doctor of Philosophy in Condensed Matter* Universite des Sciences et Technologies de Lille, Lille, **2010**.
- [53] L. Kihlborg, *Arkiv foer Kemi* **1963**, 21, 357-364.
- [54] L. M. Reilly, G. Sankar and C. R. A. Catlow, *Journal of Solid State Chemistry* **1999**, 148, 178-185.
- [55] B. V. C. R. Erofeev, *Doklady of Academy of Sciences of URSS* **1946**, 52, 511-517; M. Avrami, *The Journal of Chemical Physics* **1939**, 7, 1103-1112; M. Avrami, *The Journal of Chemical Physics* **1940**, 8, 212-224; M. Avrami, *The Journal of Chemical Physics* **1941**, 9, 177-184.
- [56] S. F. Hulbert, *Journal of British Ceramic Society* **1969**, 6, 11-20.
- [57] H. Bamford and C. Tipper, *In Comprehensive chemical kinetics*, Elsevier, New York, **1980**, p. 41-113.
- [58] F. Farges, G. E. Brown and J. J. Rehr, *Geochimica et Cosmochimica Acta* **1996**, 60, 3023-3038; G. Sankar, J. M. Thomas and C. R. A. Catlow, *Topics in Catalysis* **2000**, 10, 255-264.
- [59] T. Ressler, J. Wienold, R. E. Jentoft, T. Neisius and M. M. Günter, *Topics in Catalysis* **2002**, 18, 45-52-52.
- [60] J. D. Hancock and J. H. Sharp, *Journal of American Ceramic Society* **1972**, 55, 74-77.
- [61] E. E. Finney and R. G. Finke, *Chemistry of Materials* **2009**, 21, 4692-4705.
- [62] F. Theobald, Laarif A., *Materials Research Bulletin* **1985**, 20, 653-655.

Chapter 4 Characterisation of Chromium doped Fe₂O₃ Catalysts

4.1 Chapter Overview

In this chapter a detailed characterisation of chromium doped iron oxide catalysts using a range of techniques to establish the nature of chromium species in the near surface and bulk of iron oxide, high-temperature shift (HTS) catalysts is described. The methods that have been used are X-ray absorption spectroscopy (XAS) both near edge and extended fine structure data for comparison with chemical and X-ray photoelectron spectroscopy. There was excellent agreement between the techniques in terms of identification and quantification of Cr⁶⁺ and Cr³⁺ species as a function of calcination temperatures between 100 and 500°C. In addition, energy resolved electron yield XAS has been employed to provide to some extent the local surface sensitive information on atoms of interest in catalysts. However, the outcomes of the investigation have not been satisfactory mainly because of poor data quality and the problems in interpreting the data due to this low quality.

4.2 Introduction

Iron and copper based catalysts are widely used for the water-gas shift reactions in which steam and carbon monoxide are reacted to produce hydrogen and carbon dioxide. The operating temperatures for this reaction are between 300 and 450°C^[1]. The majority of high-temperature shift catalysts also contain small amounts of chromium oxide which acts as a stabiliser to prevent sintering of the catalytic particles and hence loss of surface area^[2]. While such benefits are realised using chromium oxide (Cr₂O₃) doping, Cr⁶⁺ can also be detected in addition to Cr³⁺ depending on catalyst preparation conditions. The Cr⁶⁺ causes health hazards as it is carcinogenic and therefore release in the environment should be as small as possible. Although a number of studies have addressed the issue of Cr⁶⁺ and how to avoid its formation, the need remains for improved quantification and also the ability to distinguish how Cr³⁺ and Cr⁶⁺ are distributed between surface and bulk sites^[3, 4]. The water soluble Cr⁶⁺ is highly mobile and very strong oxidant, whereas Cr³⁺ is immobile and quite unreactive.

To determine different chromium speciation, it is required to understand their bulk and near surface structure after different heat treatments. For this, a combination of techniques can be used as their applications provide a reasonably comprehensive picture about the structural properties of these catalysts. Principally, X-ray absorption spectroscopy (XAS) both near edge (XANES) and extended fine structure (EXAFS) as well energy resolved electron yield XANES^[5] (EREY-XAS), with X-ray powder diffraction (XRD), X-ray photoelectron spectroscopy (XPS) and quantitative chemistry are compared.

A quantitative wet chemical method exists to accurately measure levels of Cr⁶⁺ in a Cr⁶⁺/Cr³⁺ mixture. However, this approach cannot discriminate between surface and bulk material. X-ray diffraction methods are ideal for characterising bulk solids, if they are crystalline, but not poorly crystalline components. Furthermore, it is also difficult to distinguish the electronic state of chromium ions in the material using this technique. XAS is an atom-specific technique, widely used in catalytic science to obtain local structure data on crystalline and amorphous materials, but once again this technique provides bulk rather than near-surface information. An alternative technique for obtaining the local structural information that is somewhat surface sensitive is EREY-

XAS. As explained in Chapter 2, this technique probes region less than 100 nm into the material^[6], which is dominant by the bulk than surface. XPS is the ideal technique to gain near-surface information, in that it can distinguish oxidation states of the metal ions but not structural details and it can provide some quantitative information. XPS provides information from the top 1 to 10 nm of the material. Therefore, a combination of all four X-ray techniques have been used to determine local structure and composition of Cr⁶⁺ and Cr³⁺ ions in the HTS catalysts as a function of pre-treatment conditions.

4.3 Aims of the work

The aim of this work is to gain more insights into the differences between the bulk and near-surface structure of the HTS catalysts after different pre-treatments. For this, X-ray techniques such as a conventional XANES and EXAFS, along with EREY–XANES, XRD, XPS and quantitative chemistry are employed. In addition, quantitative determination of chromium species present in the catalysts, including Cr⁶⁺/Cr³⁺ ratio is derived using principal component analysis, the pre-edge peak height method and Vegard's law adapted to EXAFS.

4.4 Experimental part

4.4.1 Catalyst preparation

The iron/chromium oxide catalyst precursors used in this study were prepared using a co-precipitation method. Briefly, iron and chromium nitrate (at a Fe/Cr molar ratio of 9.8) was dissolved in distilled water and precipitated by addition of aqueous sodium carbonate. The brown precipitate was aged under agitation at 70 °C for 1h and washed to remove sodium impurities before separating into five batches for calcination. The five batches were subjected to thermal treatments of 100, 200, 300, 400, 500°C respectively with a 5 hour dwell time at the target temperature. Samples were prepared by Johnson Matthey Technology Centre.

4.4.2 Catalyst characterization

Chemical extraction of the Cr⁶⁺ species was done by heating 3g of the sample with 3g of NaHCO₃ in 150ml of distilled water at 150°C for 1 hour. The Cr⁶⁺ content of the resulting filtrate was determined by iodometric titration.⁷ Chemical analysis was carried out by Johnson Matthey Technology Centre.

XRD data of the materials were collected using a Bruker AXS D8 diffractometer operating with (nickel filtered) Cu K α radiation. Room temperature scans of the samples were performed from $10 < 2\theta < 130^\circ$ with a step size of 0.02° . Data were processed using Bruker AXS Diffrac Plus, EVA V16 software and compared with the ICDD PDF files (PDF2, Release 2003) to identify the phases present in the catalysts. XRD were performed by Johnson Matthey Technology Centre.

XPS measurements were carried out using a Thermo Fischer demonstration Escalab 250 operated with monochromatic aluminium K α radiation as a 650 μ m spot 200 W power. Samples were dusted onto conductive tape mounted on a sample stub. Charge compensation was provided by an argon ion in-lens flood gun at 20 V combined with an in-chamber flood source at 'zero energy' settings. Energy scales were corrected to the carbon 1s signal maxima (285 eV). XPS measurements and data analysis were performed by Johnson Matthey Technology Centre.

The XAS spectra at Cr and Fe K-edges were measured at room temperature on the Dutch Belgium beam line (BM26A)^[7] at the ESRF using a water cooled Si (111) double crystal monochromator with the synchrotron ring operating in 16 bunch mode giving ~60 mA electron current at 6 GeV energy.

Cr K-edge X-ray absorption spectra were measured in the fluorescence mode using Cr K α fluorescence as a function of incident X-ray energy employing a 9-element Ge detector. XAS data were acquired in step scans over a k range from 3 \AA^{-1} to 12 \AA^{-1} using k^3 weighting for the counting time per data point increasing from 5 seconds at 3 \AA^{-1} to 10 sec at 12 \AA^{-1} . Fe K-edge data for HTS catalysts were recorded in transmission mode over a similar k -range. Three scans of each catalyst were recorded and averaged.

The EREY– XAS data were recorded using an electron yield (e-yield) detector^[5]. The e-yield detector, operating with a gas mixture of 25% isobutene and 75% Helium, with a drift voltage of – 1500 V, cathode potential -550 V and with anode held at ground, was measuring a full electron energy spectrum at each incident photon energy. A constant gas flow of 100 ml/min isobutene/He was maintained. The samples were positioned with an inclination of 2.5° with respect to the direct X-ray beam. The horizontal and vertical size of the beam was 5 mm and 1 mm, respectively, which produced a beam spot covering an area around $\sim 115 \text{ mm}^2$ on the sample. In order to maintain the count rate below the saturation level of the detector, the beam intensity was attenuated by placing aluminium sheets in front of the beam exit. A typical pulse height distribution spectrum collected at each photon energy during energy scan of monochromator is shown in Figure 4-1 . The two electron energy windows marked as the bulk and near surface are indicated within which XANES spectra were obtained after integration.

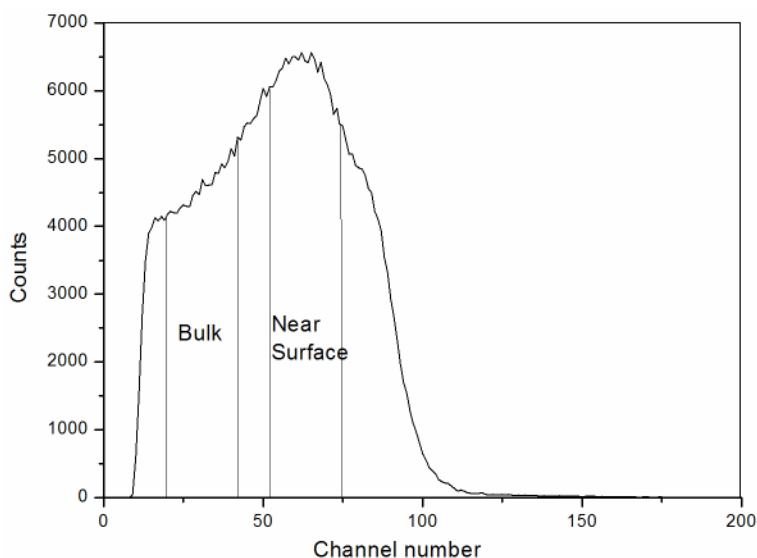


Figure 4-1 A typical Auger electron spectrum obtained at photon energy 6033 eV from HTS-200, whereby two different energy regions are indicated. The low energy region corresponds to Auger electrons escaping from the bulk, whereas in the high energy region they escape from near surface of the catalyst.

4.4.3 XAFS data analysis

Data reduction and the curve fitting analysis of the extended X-ray absorption fine structure (EXAFS) data were performed in Athena^[8] and EXCURVE98^[9] respectively, as described in Chapter 2. Phase shifts and backscattering factors were calculated from atomic potentials using EXCURVE98. The EXAFS data were analysed using the single scattering wave approximation^[10]. Refinement was carried out with k^3 weighting in the range 3.3 to 11.8 Å⁻¹. The AFAC parameter (the amplitude reduction due to many electron processes) was taken from the best fit to EXAFS data from Fe and Cr foils and fixed at 0.7 and 0.9 respectively.

During refinement the coordination numbers were either fixed to crystallographic values or refined. When refined, the error bars on coordination numbers were less than 20%, which is in accordance with values reported in the literature^[11].

During refinements of Fe K-edge EXAFS coordination numbers were fixed to crystallographic values, while Debye-Waller factors and bond distances were refined.

As for Cr K-edge EXAFS, constraints in EXAFS analysis were applied. First, Debye-Waller factors for the first shell were constrained to the same value and during the refinement were not refined. As a result, bond distances together with coordination numbers were obtained. The resulting coordination numbers were not refined in the next step but bond distances together with Debye-Waller factors were allowed to vary during the refinement. Data were refined until reasonable sets of structural parameters were obtained. Quality of fit was assessed on the basis of goodness of fit (R_{FIT}). Good EXAFS fit has $R_{FIT} < 25\%$.

In addition, to determine the nature of chromium species and the amount of Cr⁶⁺ in the catalyst, principal component analysis (PCA) was performed on the near edge spectra (XANES) using model compounds, Cr₂O₃ and K₂Cr₂O₇, representing Cr³⁺ and Cr⁶⁺ respectively. Each normalized XANES spectrum of the catalysts was fitted to normalized data from the Cr³⁺ and Cr⁶⁺ model compounds using Athena software^[8]. The least squares fittings of the data were performed in the range of -20 to -2 eV. During the

fitting procedures constraints such as weights between 0 and 1, force weights to sum 1 and all standards use the same value of E_o were applied.

4.5 Results and discussion

The results of quantitative chemical analysis are shown in Table 4-1. The data indicate that total Cr^{6+} levels are low ($<0.05\%$) for material calcined at 100°C . The level then increases markedly up to 400°C , when over 50 % of the Cr appears to be Cr^{6+} , and subsequently diminishes after heating to 500°C . This variation with temperature is discussed alongside data from other techniques below.

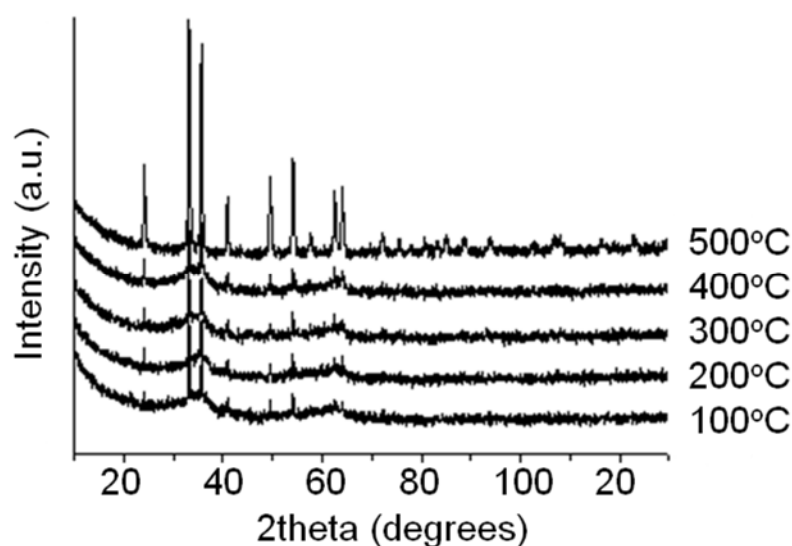


Figure 4-2 XRD patterns of HTS catalysts calcined at various temperatures showing crystalline and amorphous components. The crystalline component in samples was identified as haematite. The amorphous halo centred around $2\theta = 27^\circ$ is much reduced in the sample calcined at 500°C whilst the crystalline peaks have increased. This indicates a considerable increase in the degree of crystallinity.

XRD patterns recorded at room temperature (Figure 4-2) reveal that the samples calcined at temperatures below 500°C contains both amorphous and crystalline components, while the sample calcined at 500°C appears to be highly crystalline. The

crystalline component is identified as Fe_2O_3 (haematite) in all samples. There was no evidence of any significant X-ray peak shifts to confirm Fe/Cr/O solid solution formation or stoichiometric differences in any of these samples, as evidenced by the calculated lattice parameter data obtained through Rietveld analysis (TOPAS software). However, Cr^{3+} and Fe^{3+} ionic radii are very similar, both form α -alumina oxides structure and here Cr is very much the minority species. Furthermore, interatomic potential computational modelling has indicated ready solubility of Cr^{3+} in haematite^[12].

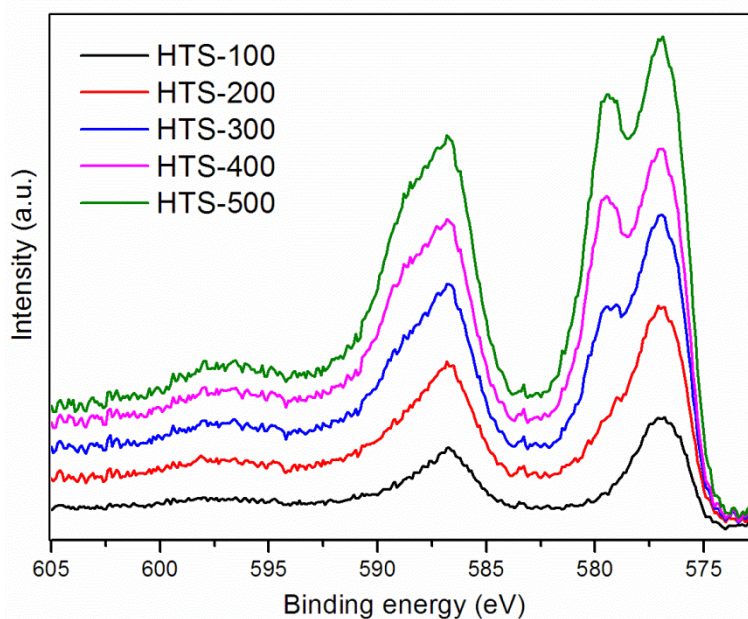


Figure 4-3 XPS data of the chromium containing iron oxide samples heated at various temperatures. For clarity only the Cr 2p spectra are shown which are normalised and corrected using carbon 1s binding energy. The split in the peaks between 575 and 580 eV indicates the presence of both Cr^{3+} and Cr^{6+} .

The results of XPS analysis, which are derived from the spectra in Figure 4-3 by curve fitting, are shown in Table 4-1. The spectra clearly indicate the presence of both Cr^{3+} (binding energy 576.8 eV) and Cr^{6+} (binding energy 579.4 eV) although the relative amounts vary strongly with calcination temperature. The ratio of Cr to Fe data in Table 4-1 suggest that the total amount of Cr at the surface slightly increases as a function of calcination temperature. This observation would be in agreement with the electron microscopy analysis by Edwards et.al.^[4], who measured composition variation from

6.3±2.3 wt% at the centre of a catalyst grain to 10.7±2.3 wt % at the edge. The Cr⁶⁺ concentration matches that measured by bulk chemical analysis with perhaps a slight surface excess up to 400°C. After calcination at 500°C the XPS data indicate a strong surface excess of Cr⁶⁺.

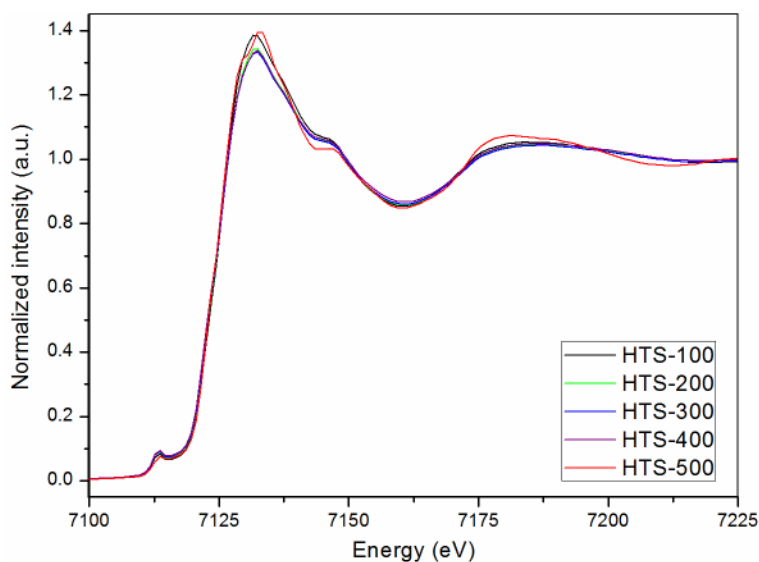


Figure 4-4 Transmission Fe K-edge XANES spectra of HTS catalysts calcined at various temperatures. The small pre-edge peak indicates the presence of octahedrally coordinated Fe³⁺ ions.

Normalized transmission Fe K-edge XANES of HTS catalysts are depicted in Figure 4-4. The small pre-edge feature appearing in XANES spectra at ~7113 eV can be assigned to *1s* to *3d* electron transition and indicates the presence of octahedrally coordinated Fe³⁺ ions. This electronic transition is particularly sensitive to the oxidation state and geometry of the iron atom. The peak at ~7132 eV on the rising edge is due to *1s* to *4p* electronic transition, while the weak peak at 7147 eV is due to *1s* to *4s* electronic transition^[13]. Small variation in white line intensity can be due to calcination of catalysts at various temperatures.

Normalized Cr K-edge XANES spectra recorded in the fluorescence mode for the chromium containing iron oxide catalysts are shown in Figure 4-5 along with two model compounds, Cr₂O₃ and K₂Cr₂O₇, representing Cr³⁺ and Cr⁶⁺ oxidation states respectively. The XANES spectra for the two model compounds containing Cr³⁺ and

Cr^{6+} ions are distinctly different with the Cr_2O_3 data showing a pre-edge doublet (~5994 eV) with very low intensity compared to $\text{K}_2\text{Cr}_2\text{O}_7$ which has an intense single pre-edge peak. This latter feature has been reported in several publications and identified as a $1s - 3d$ transition. Although this quadrupole transition is not allowed according to the selection rules, due to mixing of p and d states coupled with local coordination symmetry and density of unoccupied states, the transition becomes allowed. This pre-edge feature has been exploited as a signature identifying tetrahedral coordination geometry in a variety of d^0 transition metals states in catalytic materials^[14, 15]. In addition, Cr K-edge EREY–XANES obtained from the near-surface and bulk of HTS-catalysts are shown in Figure 4-6. The EREY–XANES spectra are nearly identical to the XANES fluorescence data and are therefore not further discussed.

Comparison of the XANES for HTS-100 (red solid line) with that of the Cr_2O_3 model compound suggests that the chromium in the catalyst is similar to Cr_2O_3 , in terms of local structure even though it lacks the long range structural crystalline order (Figure 4-2) and Cr is only a minority dopant. The two small pre-edge features at 5993 eV and 5995 eV can be assigned to the $1s - 3d(t_{2g})$ and $1s - 3d(e_g)$ electronic transitions respectively^[15-18]. The 2 eV separation of the Cr^{3+} pre-edge features agrees with the 2–3 eV octahedral crystal field splitting between the t_{2g} and e_g levels measured for several Cr^{3+} compounds in local octahedral coordination^[16]. However, the pre-edge XANES for the catalysts calcined above 100°C are distinctly different to Cr_2O_3 in that they show the strong pre-edge feature indicating the presence of Cr^{6+} in widely varying amounts as a function of calcination temperature.

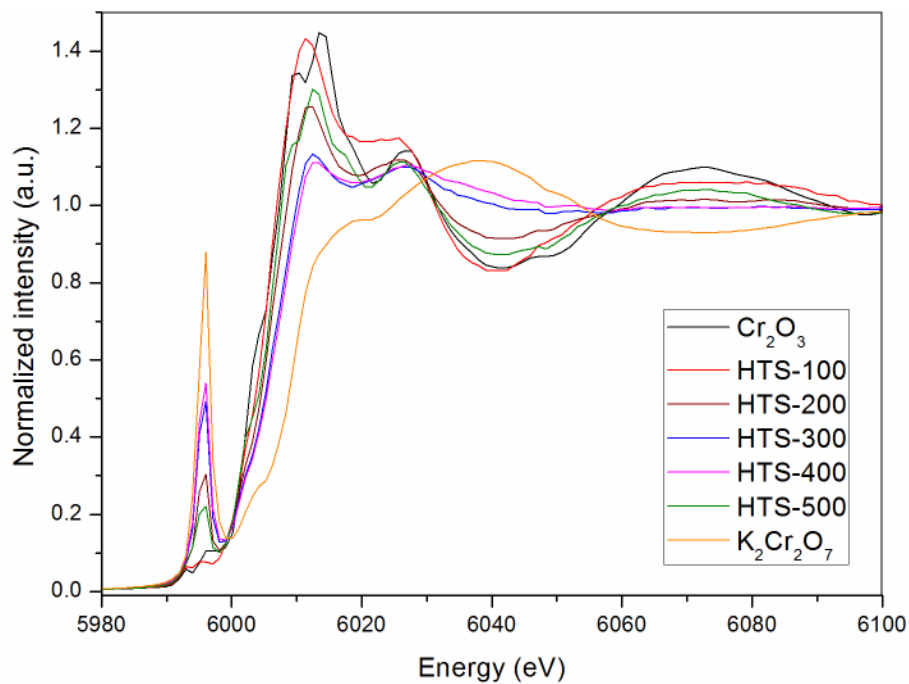


Figure 4-5 Cr K-edge XANES of HTS catalysts and the reference materials containing Cr^{6+} and Cr^{3+} representing tetrahedral and octahedral geometry respectively. The pre-edge peak is used as signature identifying the coordination geometry of chromium species. (See text for further explanation).

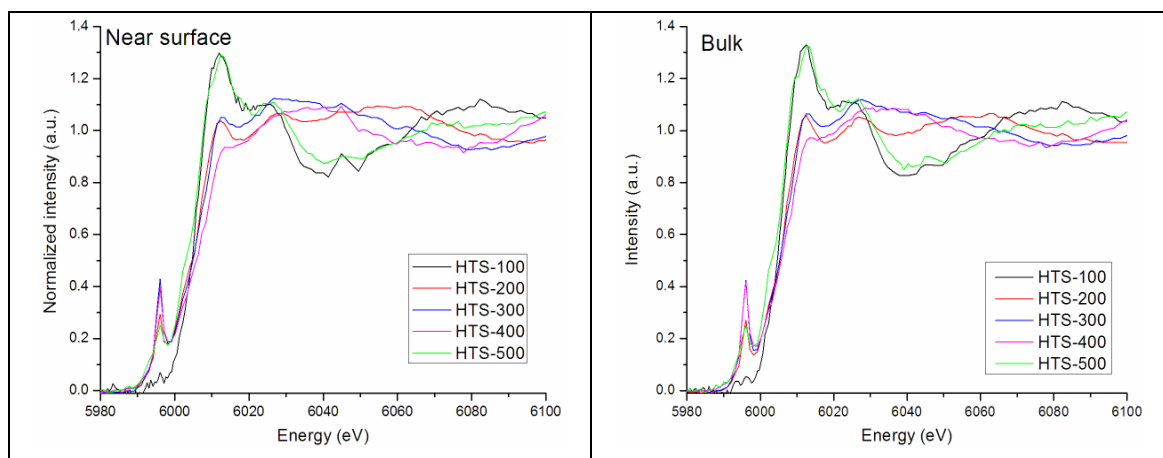


Figure 4-6 Cr K-edge EREY-XANES for HTS catalysts obtained from the near surface and bulk. The pre-edge peak indicates the coordination geometry of chromium species. See text for further explanation.

Quantification of the fluorescence XANES data was carried out using principal component analysis (PCA) by taking Cr_2O_3 and $\text{K}_2\text{Cr}_2\text{O}_7$ as model compounds to obtain the best linear combination fit. A typical fit to the catalyst data (HTS-500) is depicted in Figure 4-7.

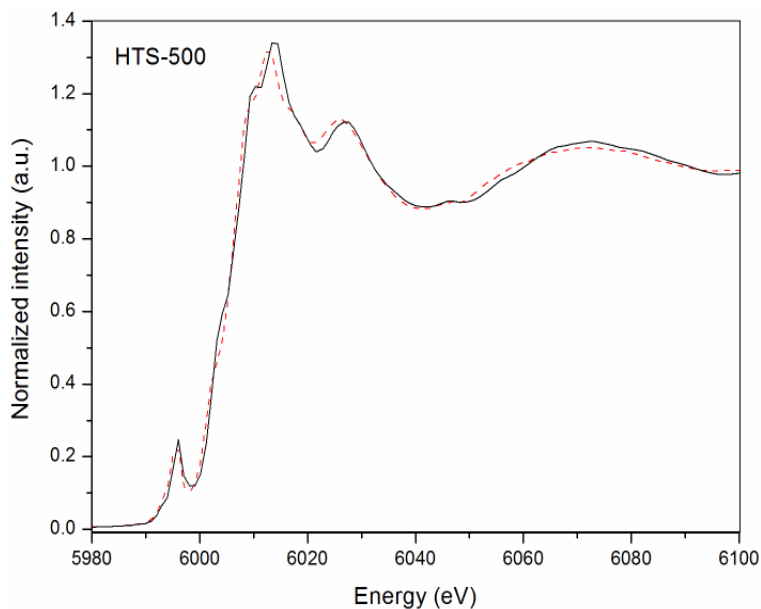


Figure 4-7 *Cr K-edge fluorescence XANES of HTS-500 catalyst (solid line) and the fitted profile (dashed line) obtained by a linear combination least square fit to the Cr_2O_3 and $\text{K}_2\text{Cr}_2\text{O}_7$ reference materials. The catalyst contains 18% of Cr^{6+} and 82% of Cr^{3+} .*

The variation of the ratio of Cr^{6+} to Cr^{3+} derived by this method (Table 4-1) shows a similar pattern to that displayed by the results of bulk chemical analysis, i.e. a minimal amount of Cr^{6+} at 100°C rising to a maximum at 400°C and then a decrease in the ratio after 500°C calcination, when Cr^{6+} becomes unstable and reduces to Cr^{3+} . This pattern of behaviour differs in one respect from that observed by XPS, which is a surface sensitive technique, in that the latter indicates a considerable excess of Cr^{6+} at the surface after calcination at 500°C compared to the bulk. This suggests that surface Cr^{3+} re-oxides during cooling to room temperature.

Table 4-1 Relative amounts of Cr^{6+} and Cr^{3+} in catalysts calcined at various temperatures. XANES and EXAFS refers to data measured in fluorescence.

Calcination Temp. (°C)	Bulk analysis			Surface analysis	
	Chemical	XANES	EXAFS	XPS	
	Cr ⁶⁺ /Cr ³⁺ atom ratio				Total Cr/Fe **
100	0.05	*	*	*	0.08
200	0.32	0.39	0.37	0.48	0.07
300	0.83	1.16	1.00	1.01	0.09
400	1.18	1.48	1.50	1.46	0.11
500	0.21	0.22	0.30	0.82	0.13

* Too low to measure.

** Bulk Cr/Fe formulation 0.11.

An alternative approach for determination of chromium speciation in HTS catalysts can be applied using the pre-edge height method^[17]. For this, XANES spectra of appropriate mechanical mixtures of Cr^{3+} and Cr^{6+} model compounds containing 0, 20, 40, 60, 80 and 100 % Cr^{6+} /Total Cr are collected and subsequently used for deriving quantifying proportion of Cr^{6+} /total Cr content from XANES.

Cr K-edge data for model compounds containing only Cr^{3+} (Cr_2O_3) and Cr^{6+} ($K_2Cr_2O_7$) were collected under identical conditions as the HTS catalysts. However, the mechanical molar mixtures of Cr^{3+} and Cr^{6+} were not measured during experiments. Therefore, the molar mixtures were simulated using XANES spectra of model compounds, Cr_2O_3 and $K_2Cr_2O_7$, and normalized as shown in Figure 4-8.

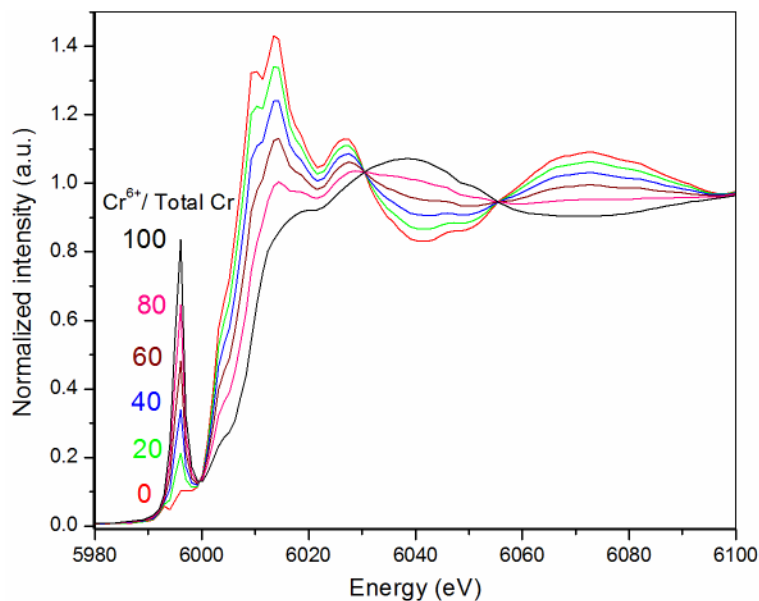


Figure 4-8 Variation of the pre-edge peak height of Cr K-edge XANES as a function of $\text{Cr}^{6+}/\text{Total Cr}$. Total Cr is defined as mixture of Cr^{3+} and Cr^{6+} . Spectrum in red is without Cr^{6+} i.e. 100 mol % Cr^{3+} , in green contains 20 mol % of Cr^{6+} , in blue 40 mol% of Cr^{6+} , in brown 60 mol% of Cr^{6+} , in pink 80 mol% of Cr^{6+} and in black is solely Cr^{6+} .

The resulting simulated spectra are in good agreement with published data by Brown et.al.^[19] and Peterson et.al.^[20]. The pre-edge peak heights are plotted against known $\text{Cr}^{6+}/\text{total Cr}$ contents and then are fitted with a polynomial function, as shown in Figure 4-9. Use of this correlation reproduces known $\text{Cr}^{6+}/\text{total Cr}$ contents $\pm 3\%$ ^[17]. Accuracy in the test was defined as the difference between the calculated fraction of Cr^{6+} given by the PCA or the pre edge peak height method and the known fraction of Cr^{6+} in mixtures of model compounds containing Cr^{3+} and Cr^{6+} that were mechanically mixed together with an appropriate molar ratios. The PCA analyses yield the fraction of Cr^{6+} species with an accuracy $\pm 8\%$ ^[17]. Based upon these results a calibration curve (Figure 4-9) can be constructed which can be then used to determine the ratio of Cr^{6+} to Cr^{3+} in HTS catalysts.

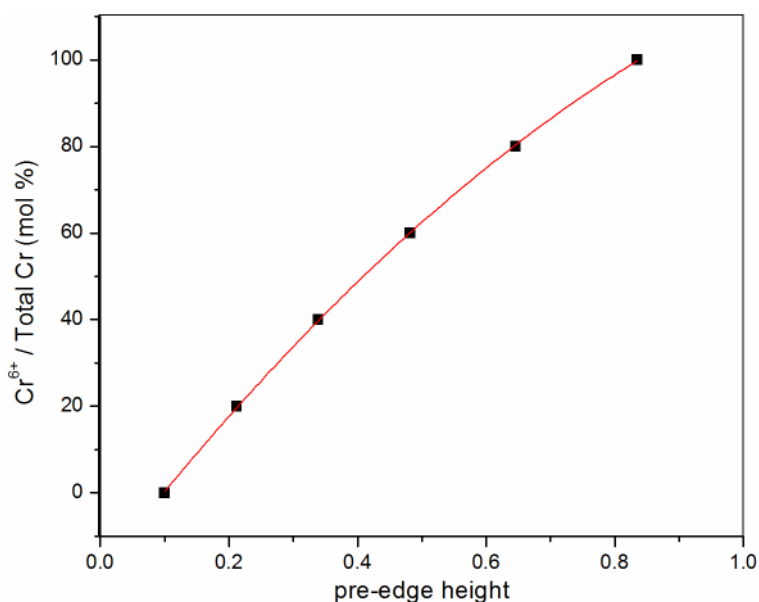


Figure 4-9 Plot of $Cr^{6+}/Total\ Cr$ versus pre-edge height. Data were fitted with a polynomial function $y=A+B_1x+B_2x^2$, where $A=-18.2\pm 0.6$, $B_1=191.3\pm 2.9$, $B_2=-59.9\pm 3.0$ and $R=0.99$.

In Table 4-2 results are compared for the determination of the Cr^{6+} fraction from fluorescence and EREY–XANES data using the pre-edge peak height method and PCA. The ratio Cr^{6+}/Cr^{3+} obtained from fluorescence data using the pre-edge peak method (Table 4-2) shows that the fraction of Cr^{6+} species is $27\pm 0.02\%$ higher in catalysts pre-treated between 100 and 400°C compared to that by PCA. Interestingly, the fraction of Cr^{6+} species in HTS-500 is only $20\pm 0.01\%$ higher. Unsurprisingly, there are differences in Cr^{6+}/Cr^{3+} ratio obtained from EREY data using both methods. The overall results indicate a similar trend to that of fluorescence, minimum amount of Cr^{6+} at 100 and 500°C with a maximum for temperatures between 200 and 400°C. Indeed, there are differences in Cr^{6+} fraction for catalysts calcined at 300 and 400°C but it has not been possible to find an explanation for this. In addition, it is supposed that poor data quality and difficulties to operate e-yield detector during measurements led to experimental errors which are responsible for these potentially misleading results.

Table 4-2 Determination of Cr^{6+}/Cr^{3+} atom ratio in HTS catalysts from fluorescence and EREY–XANES data using the pre-edge peak method and PCA. The resulting values are with an accuracy of 3%^[21] for the pre-edge peak method and 8% for PCA.

Calcin. Temp. (°C)	Cr^{6+}/Cr^{3+} atom ratio					
	Pre-edge peak height			PCA		
	Fluores	Bulk	Near-surf	Fluores	Near-surf	Bulk
100	0.00	0	0	0.00	0.00	0.00
200	0.52	0.41	0.47	0.39	0.33	0.27
300	1.56	1.08	1.13	1.16	0.77	0.72
400	2.13	1.08	0.89	1.48	0.76	0.70
500	0.27	0.35	0.35	0.22	0.25	0.35

In order to investigate further the scope for XAS methods to derive information on the occurrence of Cr^{6+} , a third approach has been examined, the quantification of bulk transmission EXAFS data. For this Vegard law^[22] is used. The law is an approximate empirical rule which states that a linear relation exist, at constant temperature, between the lattice constants of materials such as alloys, solid solutions and the concentrations of the constituents elements^[23]. In this case it is assumed that that there is linear relationship between bond distances of HTS catalysts obtained by EXAFS analyses and the concentrations of Cr^{6+} and Cr^{3+} ions. The EXAFS results showed the fraction of Cr^{3+} is dominant in HTS-100 as EXAFS found Cr–O bonds at 1.99 Å. Thus fraction of Cr^{3+} ions in catalysts can be estimated from the different average Cr–O bond distances using Equation 4-1,

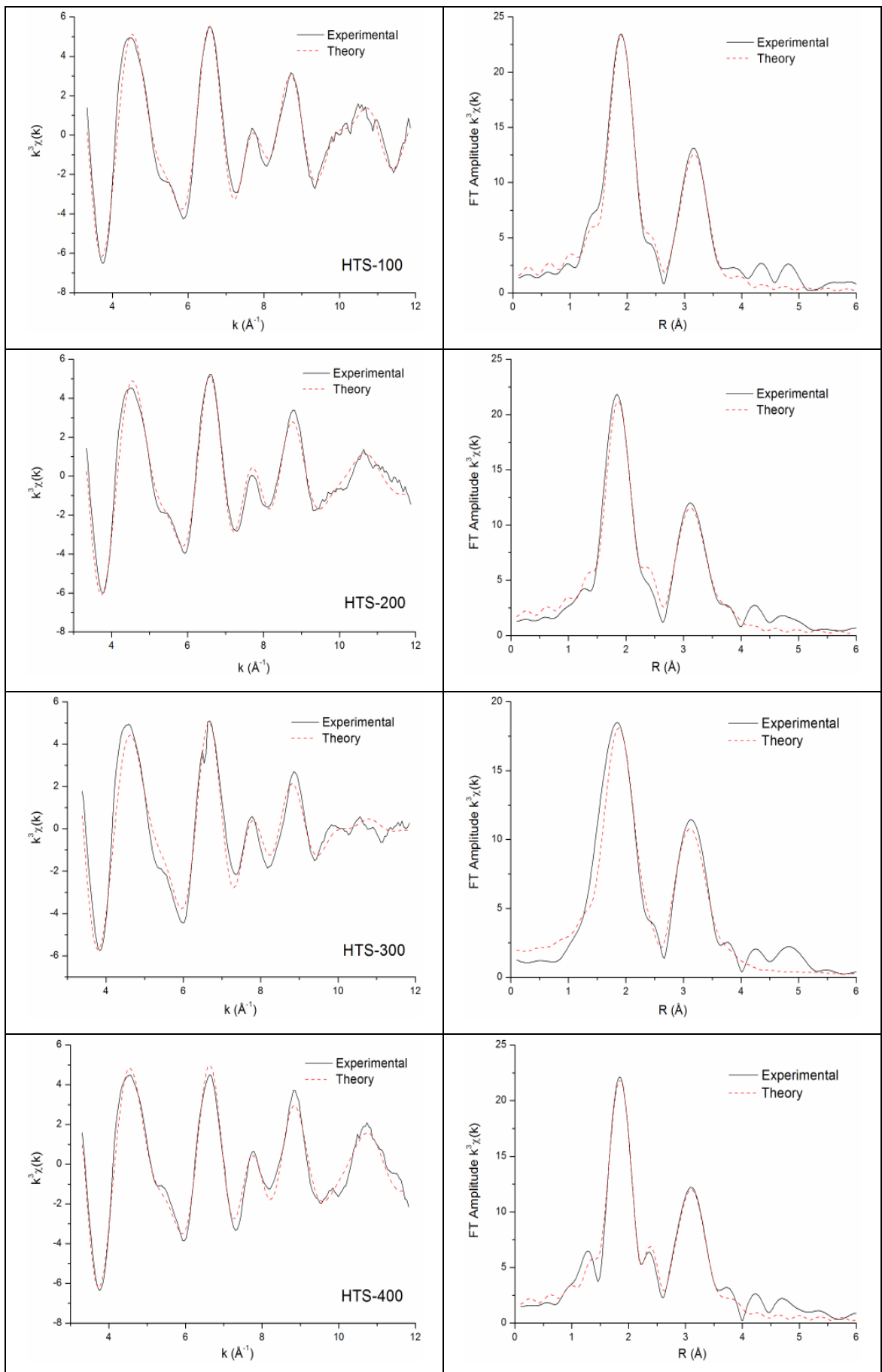
Equation 4-1 Vegard expression for EXAFS

$$R^* = R_1x + R_2(1 - x)$$

where, R^* is the average bond distance, R_1 is the bond distance Cr^{3+} –O, R_2 represents Cr^{6+} –O and x is the fraction of Cr^{3+} in a catalyst.

Hence, the fraction of Cr^{6+} ions present in HTS catalysts can be easily derived. The estimated values of Cr^{6+}/Cr^{3+} ratio are summarized in Table 4-1.

Fe K-edge and Cr K-edge EXAFS analysis Figure 4-10 and Figure 4-13 show the best fit between the calculated and experimental Fe K-edge and Cr K-edge EXAFS data respectively. The EXAFS fitting results for both Fe K-edge and Cr K-edge are summarized in Table 4-3. All the samples, except for the one heated at 500°C, showed a large amorphous component by XRD in addition to the presence of haematite. In order to determine whether the amorphous component also has similar local environment to that of the crystalline part, the Fe K-edge EXAFS data of all the samples were analysed in detail. The structural parameters obtained from Fe K-edge EXAFS data for HTS catalysts revealed that the structure of HTS-100 catalysts is very close to the haematite structure $\alpha\text{-Fe}_2\text{O}_3$ ^[24]. The iron oxygen distances are found to be $R_{\text{Fe-O}} = 1.96 \text{ \AA}$ and $R_{\text{Fe-O}} = 2.09 \text{ \AA}$, and the iron-iron distances $R_{\text{Fe-Fe}} = 2.89 \text{ \AA}$, 3.05 \AA , and 3.40 \AA . These inter atomic distances are in good agreement with the structure of haematite^[24]. The FeO_6 octahedra in haematite share one face ($R_{\text{Fe-Fe}} = 2.89 \text{ \AA}$), three edges ($R_{\text{Fe-Fe}} = 2.97 \text{ \AA}$), three double corners ($R_{\text{Fe-Fe}} = 3.37 \text{ \AA}$) and six double corners $R_{\text{Fe-Fe}} = 3.7 \text{ \AA}$. The inter-atomic iron-oxygen distances of, $R_{\text{Fe-O}}$, and iron – iron, $R_{\text{Fe-Fe}}$, in HTS-200, -300, -400, -500 are similar to those in the crystal structure of haematite.



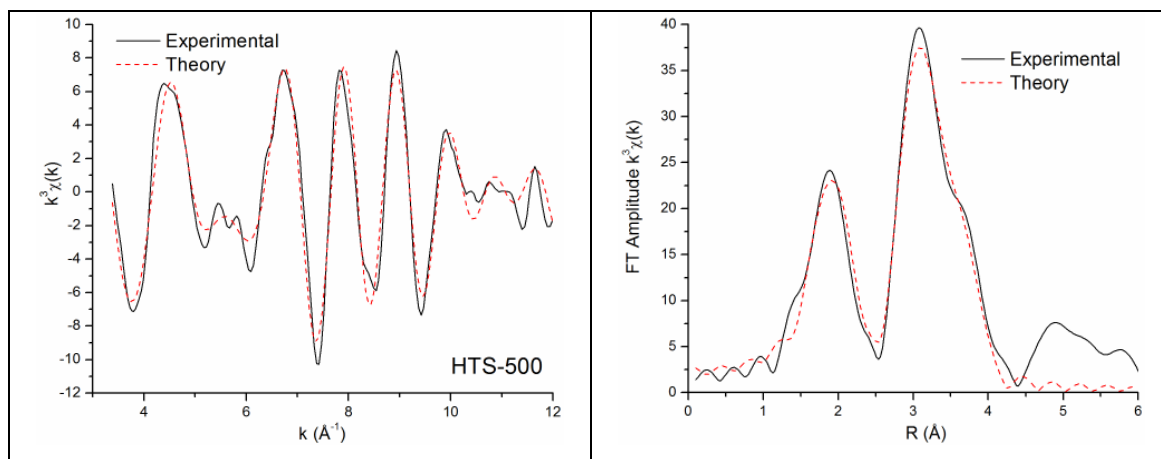


Figure 4-10 *Fe K-edge EXAFS spectra analysed in k -space (after background subtraction, k^3 -weighted) of HTS catalysts together with corresponding Fourier transforms. The solid line is experimental data and the dashed line is the best fit.*

Before the Cr K-edge data were analysed, the modelling procedure including calculated phase shift and amplitude factors was tested by analysing in detail the two model compounds, $K_2Cr_2O_7$ and Cr_2O_3 . In $K_2Cr_2O_7$ the chromium atom is surrounded by four tetrahedrally arranged oxygen atoms at a distance of $R_{Cr(VI)-O} = 1.61 \text{ \AA}$. The chromium-chromium distance was found to be at $R_{Cr(VI)-Cr} = 3.14 \text{ \AA}$. In Cr_2O_3 the chromium atom is surrounded by six octahedrally spaced oxygen atoms at $R_{Cr(III)-O} = 1.99 \text{ \AA}$; the chromium-chromium distances are $R_{Cr(III)-Cr} = 2.65, 2.89, 3.42, 3.65 \text{ \AA}$. The EXAFS fitting results for $K_2Cr_2O_7$ and Cr_2O_3 are consistent with the reported structural models derived from XRD^[25].

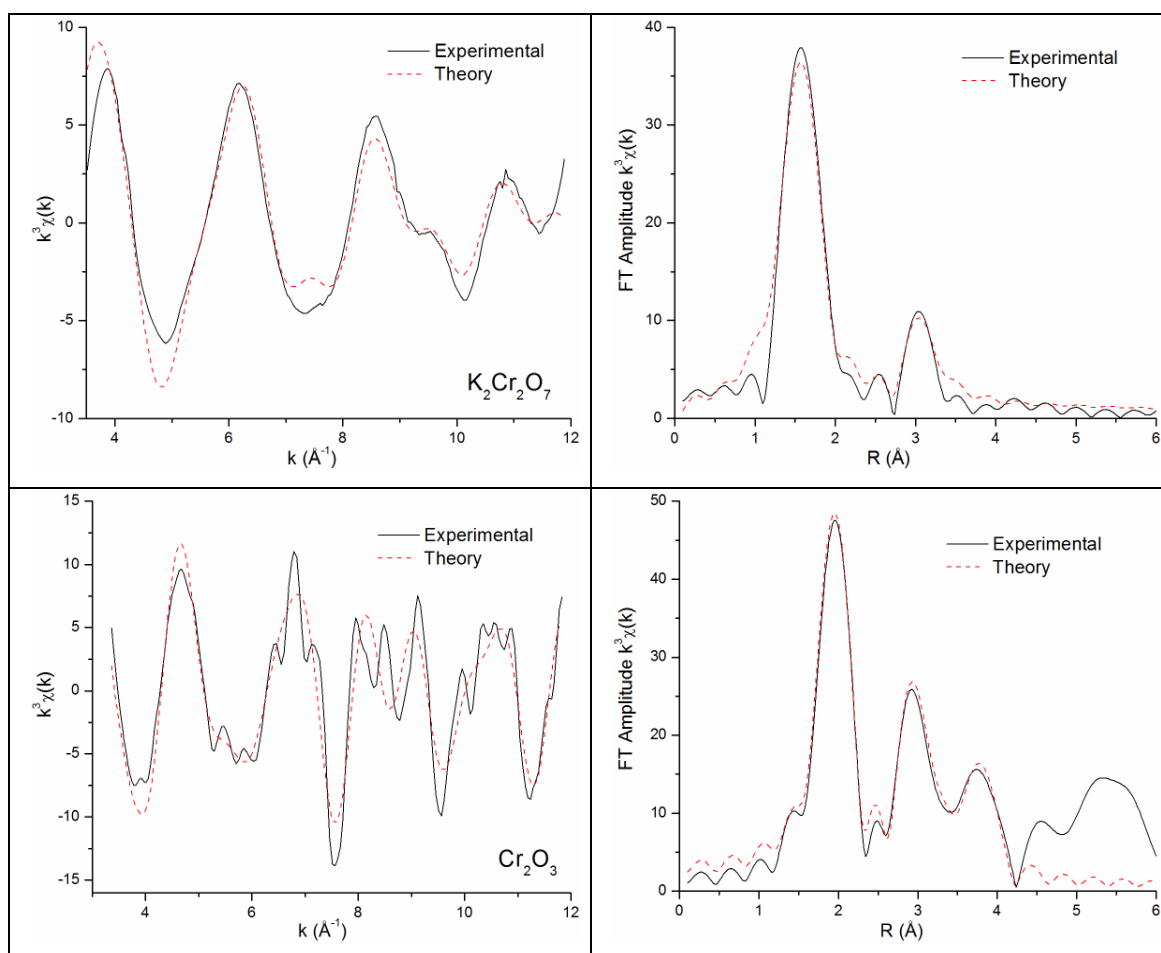


Figure 4-11 Cr K-edge EXAFS spectra of reference materials, $K_2Cr_2O_7$ and Cr_2O_3 , analysed in k -space (after background subtraction, k^3 -weighted) and Fourier transforms of corresponding EXAFS spectra. The solid line is the experimental data and the dashed line is the best fit.

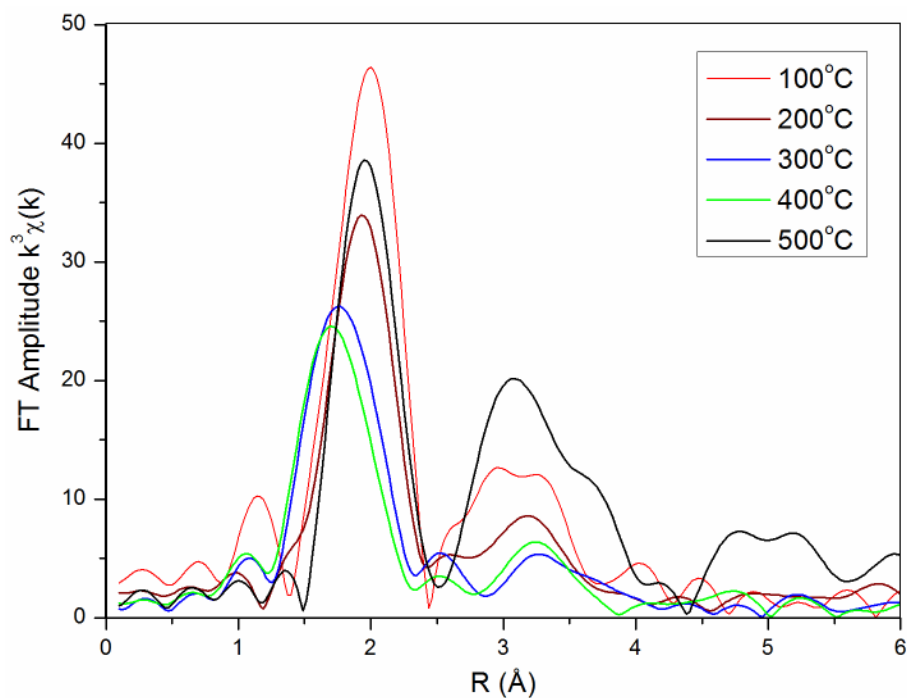


Figure 4-12 Fourier transforms of k^3 weighted Cr K-edge EXAFS as a function of the atomic distance, R , for HTS catalysts calcined at various temperatures. See text for further explanation.

Comparison of the Fourier transforms of HTS-100, -200, -300, and -400 (Figure 4-12) clearly show that the magnitude of the Fourier transform peaks corresponding to the Cr–O distance at $\sim 2\text{\AA}$ decreases with calcination temperature. The thermally induced changes correspond to a partial transformation from the octahedral Cr^{3+} to tetrahedral Cr^{6+} coordination as detected by XANES and supported by chemical and XPS analysis. Furthermore, Figure 4-12 confirms that this process is reversed on heating to 500°C , i.e. the level of Cr^{6+} is significantly reduced.

While the EXAFS data in Figure 4-10 for the Fe K-edge from the four largely amorphous materials, HTS-100, -200, -300 and -400 look broadly similar and obviously different to that for crystalline haematite (HTS-500), the Cr K-edge data show significant differences. These structural changes in the local environment around Cr reflect the large differences in relative amounts of Cr^{6+} and Cr^{3+} detected by other techniques as discussed above. The results of detailed curve fitting for the Cr K-edge EXAFS data are shown in Table 4-3. It is important to note when viewing Table 4-3

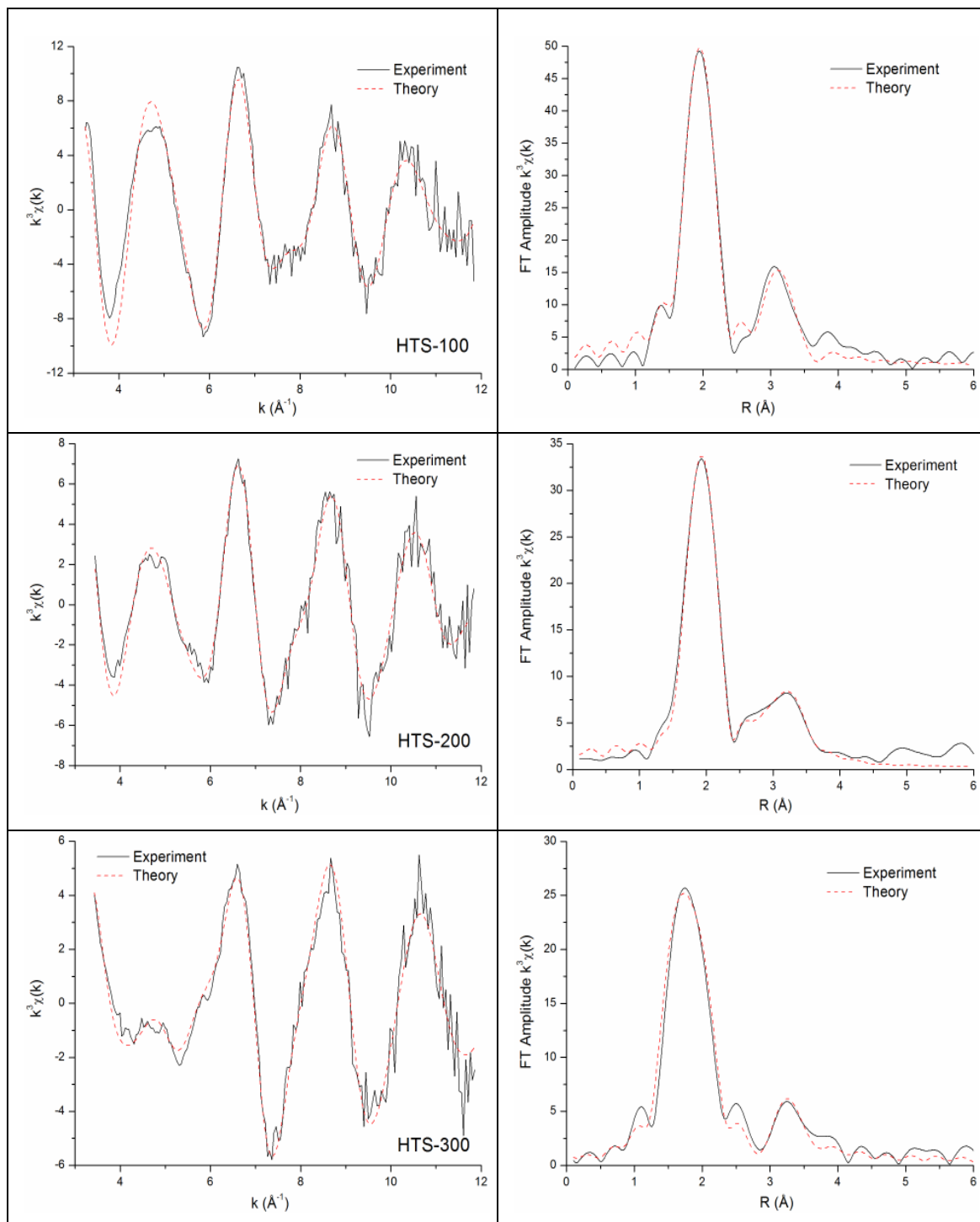
that it is not possible to distinguish Fe and Cr as backscatters since they have similar X-ray scattering power.

For HTS-100 the nearest neighbour oxygen shell can be fitted with a single octahedral shell with a Cr–O distance of 1.99 Å which is similar to Cr₂O₃ and close to the average value from the Fe K-edge in HTS-100. For the next nearest neighbour cations three shells were fitted following a similar pattern to the Fe K-edge in HTS-100 rather than Cr₂O₃, i.e. cations at 3.00 Å (1Fe), 3.12 Å (3Fe), and 3.45 Å (3Fe). The XANES data has already confirmed the sole presence of Cr³⁺ and these two results would suggest that Cr³⁺ substitutes for Fe³⁺ in the amorphous matrix in agreement with predictions from computational modelling^[12].

Accurate Cr K-edge EXAFS fitting results for HTS-200, -300 and -400 can only be obtained by introducing two Cr–O distances of ~1.64 Å (similar to K₂Cr₂O₇) and ~2.0 Å, (similar to Cr₂O₃). The results obtained for the short Cr–O distance are consistent with the Cr⁶⁺–O tetrahedral distance in K₂Cr₂O₇ and the long Cr–O distance agrees with the octahedral distance found in Cr₂O₃. The variation in the relative number of O atoms in the two first shell sites reflects the changes in the relative amount of Cr⁶⁺ and Cr³⁺ as a function of calcination temperature. Indeed, the relative oxygen occupation in the two sites, tetrahedral and octahedral, can provide a quantitative estimate of the amount of the two Cr oxidation states as shown in Table 4-1. For the second shell of HTS-200 and -300 EXAFS fitting finds three cations atoms, one at a short distance of 2.97 Å and the other two/three at a longer distance of 3.13 Å plus three iron(chromium) atoms at 3.40 Å. This pattern is broadly similar to data for the Fe K-edge. While the next nearest neighbour cation shells are slightly different for HTS-200 and -300, the data for HTS-400 seems very different reflecting the large amount of Cr⁶⁺ compared to Cr³⁺ and the presence of tetrahedral geometry. However, the radii of the fitted cation shells match the average values derived for HTS-200 and -300, i.e. the overall structure is dominated by the Fe–O octahedral matrix.

HTS-500 has been already identified by XRD as crystalline haematite. It is not surprising therefore that EXAFS data for the Cr K-edge bears some resemblance to the Fe K-edge. However, a short Cr–O distance (1.63 Å) contribution to the EXAFS can be

detected corresponding to the presence of Cr^{6+} . XPS data discussed above indicates this oxidation state is located primarily at the surface.



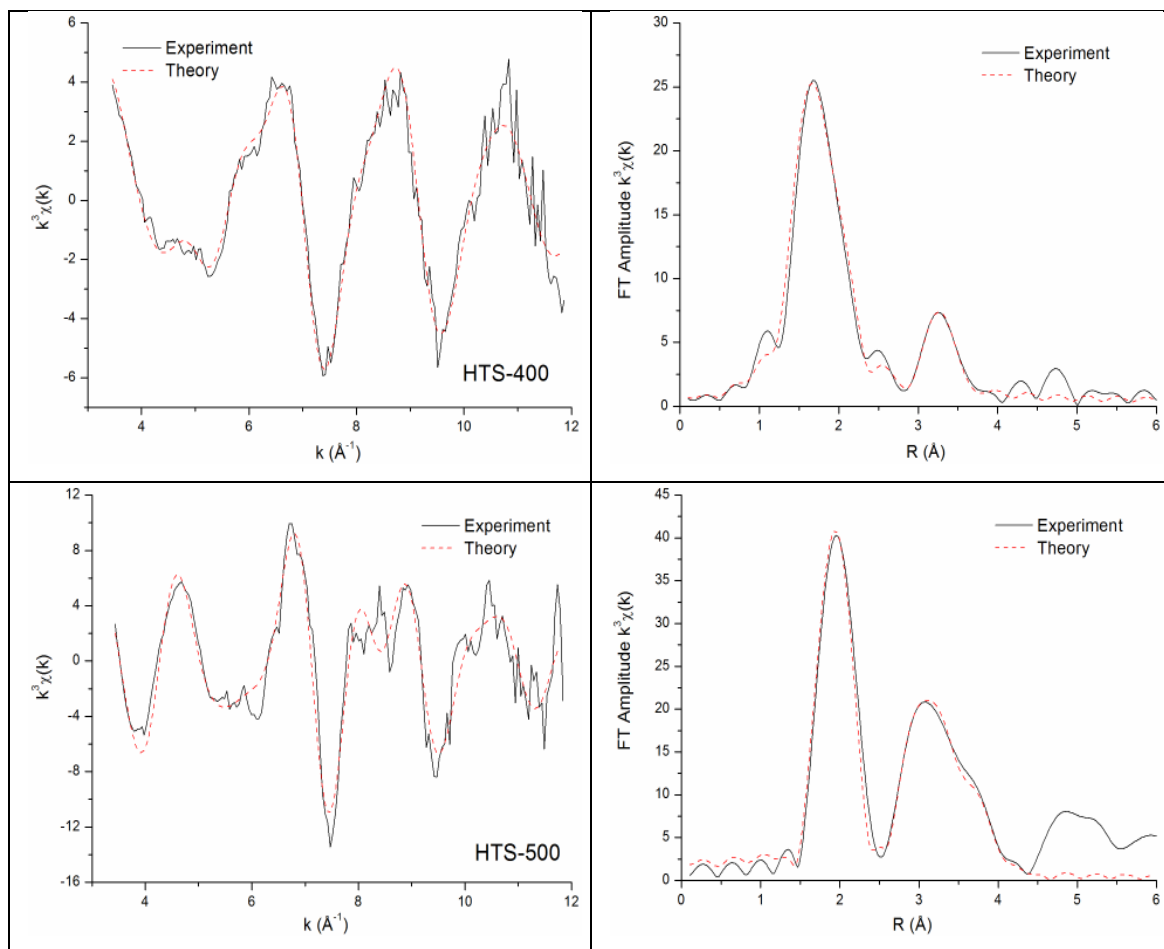


Figure 4-13 Cr K-edge EXAFS spectra analysed in k -space (after background subtraction, k^3 -weighted) of HTS catalysts and Fourier transform of corresponding EXAFS spectra. The solid line is an experimental data and the dashed line is the best fit.

Table 4-3 Fe K-edge and Cr K-edge EXAFS results for the HTS catalysts and chromium containing model compounds, where N is coordination number, R – inter-atomic distance between atom pairs, σ^2 – Debye Waller factor and R_{Fit} – goodness of fit.

Catalyst	Fe K-edge					Cr K-edge				
	Sc.	N	R (Å)	σ^2 (Å ²)	R_{Fit}	Sc.	N	R (Å)	σ^2 (Å ²)	R_{Fit}
HTS-100	O	3	1.96±0.004	0.004	16	O	6	1.98±0.003	0.005	25
	O	3	2.09±0.008	0.012		Fe(Cr)	1	2.99±0.018	0.003	
	Fe	1	2.89±0.005	0.004		Fe(Cr)	3	3.11±0.175	0.012	
	Fe	3	3.05±0.005	0.007		Fe(Cr)	3	3.43±0.038	0.018	
	Fe	3	3.40±0.015	0.022						
HTS-200	O	4	1.95±0.003	0.005	19	O	1	1.64±0.010	0.003	23
	O	2	2.14±0.005	0.005		O	4	1.98±0.010	0.005	
	Fe	1	2.92±0.010	0.005		Fe(Cr)	1	2.96±0.015	0.005	
	Fe	3	3.06±0.005	0.010		Fe(Cr)	3	3.13±0.020	0.012	
	Fe	3	3.41±0.010	0.016		Fe(Cr)	3	3.42±0.025	0.015	
HTS-300	O	2	1.89±0.010	0.004	28	O	2	1.64±0.002	0.004	22
	O	3	2.03±0.010	0.007		O	3	1.98±0.003	0.005	
	Fe	1	2.89±0.015	0.007		Fe(Cr)	1	3.05±0.020	0.010	
	Fe	3	3.03±0.010	0.011		Fe(Cr)	2	3.14±0.020	0.014	
	Fe	3	3.38±0.015	0.016		Fe(Cr)	3	3.40±0.015	0.016	
HTS-400	O	4	1.95±0.003	0.005	18	O	2	1.64±0.003	0.004	20
	O	2	2.15±0.005	0.004		O	2	1.98±0.003	0.004	
	Fe	1	2.90±0.010	0.005		Fe(Cr)	1	3.03±0.010	0.010	
	Fe	3	3.05±0.005	0.009		Fe(Cr)	2	3.38±0.010	0.014	
	Fe	3	3.38±0.010	0.017						
HTS-500	O	3	1.94±0.010	0.004	26	O	1	1.63±0.010	0.007	33
	O	3	2.09±0.010	0.004		O	5	1.99±0.004	0.005	
	Fe	1	2.88±0.070	0.004		Fe(Cr)	3	2.96±0.010	0.008	
	Fe	3	2.97±0.025	0.004		Fe(Cr)	1	3.12±0.150	0.011	
	Fe	3	3.37±0.005	0.005		Fe(Cr)	3	3.40±0.015	0.007	
	Fe	3	3.68±0.010	0.005		Fe(Cr)	3	3.71±0.015	0.010	
K ₂ Cr ₂ O ₇	O	4	1.61±0.005	0.008		O	4	1.61±0.005	0.008	29
	Cr	1	3.14±0.010	0.004		Cr	1	3.14±0.010	0.004	
Cr ₂ O ₃	O	6	1.99±0.005	0.005		O	6	1.99±0.005	0.005	39
	Cr	1	2.65±0.020	0.006		Cr	1	2.65±0.020	0.006	
	Cr	3	2.89±0.008	0.005		Cr	3	2.89±0.008	0.005	
	Cr	3	3.42±0.010	0.005		Cr	3	3.42±0.010	0.005	
	Cr	6	3.65±0.010	0.008		Cr	6	3.65±0.010	0.008	

4.6 Conclusion

Analysis of Cr doped Fe₂O₃ catalysts chemically and by XPS, XANES, XRD and EXAFS has revealed that Cr³⁺ is the dominant species for the largely amorphous material calcined at 100°C. However upon heating to 400°C the levels of Cr⁶⁺ increase markedly. There is good agreement between the four techniques in terms of identification and quantification of the relative levels of the two Cr species. On heating to 500°C, when the material crystallises to form haematite, the Cr⁶⁺ becomes unstable and is reduced again to Cr³⁺. XPS indicates that the residual Cr⁶⁺ after 500°C calcination is mainly located at the surface and is probably formed from re-oxidation of Cr³⁺ during a cooling to room temperature. However, the total Cr/Fe ratio measured by XPS suggests that Cr³⁺ is incorporated in the haematite lattice.

It has also been shown that both the pre-edge peak analysis method along with principal component analysis of XANES data and modelling EXAFS data differentiating Cr⁶⁺ and Cr³⁺ oxygen distances provide good methods of analysing mixed oxidation states. The attempt to probe the near surface layer of catalysts using the EREY technique was unfortunately not successful.

References

- [1] L. Lloyd, D. E. Ridler and M. V. Twigg, *Catalyst Handbook*, Wolfe Publishing, **1989**, p. 283-339; C. Ratnasamy and J. P. Wagner, *Catalysis Reviews: Science and Engineering* **2009**, *51*, 325-440; C. Rhodes, G. J. Hutchings and A. M. Ward, *Catalysis Today* **1995**, *23*, 43-58.
- [2] G. C. Chinen, R. H. Logan and M. S. Spencer, *Applied Catalysis* **1984**, *12*, 89-96; R. L. Keiski and T. Salmi, *Applied Catalysis A: General* **1992**, *87*, 185-203.
- [3] F. Domka, A. Basinska and R. Fiedorow, *Surface Technology* **1983**, *18*, 275-282; J. Y. Lee, D.-W. Lee, K.-Y. Lee and Y. Wang, *Catalysis Today* **2009**, *146*, 260-264; P. Kappen, J.-D. Grunwaldt, B. S. Hammershøi, L. Tröger and B. S. Clausen, *Journal of Catalysis* **2001**, *198*, 56-65; G. Doppler, A. X. Trautwein, H. M. Zietzen, E. Ambach, R. Lehnert, M. J. Sprague and U. Gonser, *Applied Catalysis* **1988**, *40*, 119-130.
- [4] M. A. Edwards, D. M. Whittle, C. Rhodes, A. M. Ward, D. Rohan, M. D. Shannon, G. J. Hutchings and C. J. Kiely, *Physical Chemistry Chemical Physics* **2002**, *4*, 3902-3908.
- [5] T. Rayment, S. L. M. Schroeder, G. D. Moggridge, J. E. Bateman, G. E. Derbyshire and R. Stephenson, *Review of scientific instruments* **2000**, *71*, 3640-3645.
- [6] L. M. Schroeder, G. D. Moggridge, R. M. Lambert and T. Rayment, *In Spectroscopy for Surface Science (Advances in Spectroscopy)* **1998**, Vol. 26, Clark, R.J.H., Hester R.E., Eds., John Wiley & Sons: Chichester, p. 1-29.
- [7] S. Nikitenko, A. M. Beale, A. M. J. van der Eerden, S. D. M. Jacques, O. Leynaud, M. G. O'Brien, D. Detollenaere, R. Kaptein, B. M. Weckhuysen and W. Bras, *Journal of Synchrotron Radiation* **2008**, *15*, 632-640.
- [8] B. Ravel and M. Newville, *Journal of Synchrotron Radiation* **2005**, *12*, 537-541.
- [9] N. Binsted and S. S. Hasnain, *Journal of Synchrotron Radiation* **1996**, *3*, 185-196.
- [10] S. J. Gurman, N. Binsted and I. Ross, *Journal of Physics C-Solid State Physics* **1984**, *17*, 143-151.
- [11] B. K. Teo, *EXAFS: Basic Principles and Data Analysis*, **1986**, p. 114-157; G. Bunker, *Introduction to XAFS: A Practical Guide to X-ray Absorption Fine Structure Spectroscopy*, Cambridge University Press, **2010**, p. 134-188.
- [12] S. Benny, *Doctoral thesis (EngD)*, University College London (UCL) **2010**.
- [13] G. Sankar, P. R. Sarode and C. N. R. Rao, *Chemical Physics* **1983**, *76*, 435-442; T. E. Westre, P. Kennepohl, J. G. DeWitt, B. Hedman, K. O. Hodgson and E. I. Solomon, *Journal of the American Chemical Society* **1997**, *119*, 6297-6314; L. A. Grunes, *Physical Review B* **1983**, *27*, 2111.
- [14] F. Farges, G. E. Brown and J. J. Rehr, *Geochimica et Cosmochimica Acta* **1996**, *60*, 3023-3038; C. Kongmark, V. Martis, A. Rubbens, C. Pirovano, A. Lofberg, G. Sankar, E. Bordes-Richard, R.-N. Vannier and W. Van Beek, *Chemical communications* **2009**, 4850-4852; G. Sankar, J. M. Thomas and C. R. A. Catlow, *Topics in Catalysis* **2000**, *10*, 255-264; F. Farges, *Physical Review B* **2005**, *71*, 1-14.
- [15] M. L. Peterson, J. G. E. Brown, G. A. Parks and C. L. Stein, *Geochimica et Cosmochimica Acta* **1997**, *61*, 3399-3412.
- [16] Burns R.G., *Mineralogical applications of crystal field theory*, 2nd ed. Cambridge Univ. Press **1993**, 7-43.
- [17] M. L. Peterson, G. E. Brown and G. A. Parks, *MRS Proceedings* **1996**, *432*, 75-80.
- [18] A. M. Beale, D. Grandjean, J. Kornatowski, P. Glatzel, F. M. F. de Groot and B. M. Weckhuysen, *Journal of Physical Chemistry B* **2006**, *110*, 716-722.
- [19] G. E. Brown, Jr. and N. C. Sturchio, *Reviews in Mineralogy and Geochemistry* **2002**, *49*, 1-115.

- [20] M. L. Peterson, G. E. Brown and G. A. Parks, *Colloids and Surfaces A: Physicochemical and Engineering Aspects* **1996**, *107*, 77-88.
- [21] S. D. Kelly, D. Hesterberg and B. Ravel, *Analysis of Soils and Minerals Using X-ray Absorption Spectroscopy, in Methods of Soil Analysis - Part 5 Mineralogical Methods*, SSSA Book Series 5, **2008**, p. 388-464.
- [22] L. Vegard, *Zeitschrift für Physik* **1921**, *5*, 17.
- [23] A. R. Denton and N. W. Ashcroft, *Physical Review A* **1991**, *43*, 3161-3164.
- [24] R. L. Blake, R. E. Hessevick, T. Zoltai and L. W. Finger, *American Mineralogist* **1966**, *51*, 123-129.
- [25] J. K. Brandon and I. D. Brown, *Canadian Journal of Chemistry* **1968**, *46*, 933-941;
R. E. Newnham and Y. M. de Haan, *Zeitschrift fuer Kristallographie, Kristallgeometrie, Kristallphysik, Kristallchemie* **1962**, *117*, 235-237.

Chapter 5 EREY–XAS and transmission XAS investigation of CoAlPOs

5.1 Chapter overview

In this chapter, experiments on hydrothermally prepared cobalt substituted aluminophosphates (AlPOs) with AEI and CHA (chabazite) type structures are discussed. It is postulated that the activity and selectivity of these catalysts can be attributed the presence of Co^{2+} species at tetrahedral sites in the AlPO frameworks. Conversely, low catalytic activity is due to extra-framework Co^{2+} species located at the outer surface or occluded within the micropores of catalysts. Hence, a spectroscopic technique which can discriminate between framework and extra-framework transition metal ions has been used. In addition, conventional X-ray Absorption spectroscopy (XAS) is applied to obtain detailed structural information about transition metal ions.

5.2 Introduction

X-ray Absorption Fine Structure (XAFS) is a powerful tool in catalyst research for describing the local structure of catalytic active transition metal ions. In many cases, there is still a lack of understanding of this local structure and it is difficult to gather accurate experimental information due to a low concentration of the active metal ions and the presence of a mixture of amorphous and polycrystalline phases^[1]. XAFS provides information on the short range order around a target atom, which is particularly useful for metal ions whose size is in the range of 1–2 Å^[2]. For instance, catalytically active metal ions inside zeolite channels or cages are limited by the size of the zeolite cavities. These metal ions can have long range structural ordering but are often too small to be studied with for instance X-ray diffraction (XRD). Most of the other conventionally used characterisation techniques have difficulties to detect metal ions of such dimensions and thus can provide only a limited amount of structural information. XAFS is sensitive to the oxidation state, coordination chemistry, the distances, coordination number and species of the atoms immediately surrounding the selected element and thus is an ideal tool for the study of catalysts.

Conventional transmission and fluorescence XAFS does not discriminate between bulk and surface structure since X-rays penetrate in matter. In the case that one wants to obtain surface specific or depth resolved near surface information Energy Resolved Electron Yield X-ray Absorption Spectroscopy (EREY–XAS) is the method of a choice. This technique probes the local coordination environment of a metal atom present in the near surface layer of materials up to the escape depth of the electrons^[3]. Electron yield XAFS is normally carried out in high vacuum conditions due to the limited path length of electrons in the solid state or gas. An innovation by Rayment et.al.^[4] demonstrated that detection of electrons under non-vacuum conditions is possible by using the environmental gas as an electron amplification medium like in a proportional counter^[5]. In this case, an electron detection using an energy resolving electron-yield (e-yield) detector allows one to obtain depth resolved information. The basic concept of the technique is that Auger electrons, which are emitted during the decay of the excited atomic states produced by X-ray absorption events, lose energy by various inelastic processes, as they propagate to the surface. Consequently, the energy of the detected electrons contains information regarding the depth at which the electron has been

generated. Energy-selective detection of the electron yield signal thus enables recording of EREY–XAS from the ‘high energy’ region, in which Auger electrons escaping from the near surface of a material, and the ‘low energy’ region for Auger electrons generated in the bulk of the material. Typical escape depths of Auger electrons are between 100 and 1000 Å^[6] which indicate the near surface range over which useful information can be obtained.

So far, EREY–XAS has been used for studying NiO thin films^[7] and dense metal oxides catalysts^[8]. To ascertain capabilities and limiting factors of the technique, it is interesting to apply this technique to other materials on which its sensitivity can be demonstrated.

Cobalt substituted aluminophosphates (CoAlPOs) belonging to a family of zeotype materials were identified as being suitable for this purpose. Particularly, CoAlPO-18 and CoAlPO-34 are used as model catalysts in this study because not only they are well suited for this testing but also because of the relevance of their catalytic activity for methanol to light olefins reactions^[9, 10].

Microporous materials are prepared by hydrothermal crystallization process from inorganic aqueous solutions with “correct” pH at temperatures below 200°C in the presence of an organic molecule, especially amines and quaternary ammonium cations, which acts as structure directing agent (SDA), called templates^[9]. The structure directing effect of organic molecules can be ascribed to the charge distribution, the size and geometric shape of a template. During “templating” either the gelation or the nucleation process occurs, whereby the organic molecule organizes AlO₄ and PO₄ units into particular geometric topology around itself and thus provides the initial building blocks for the crystallization of specific types of structures^[11]. Hence, during the course of crystallization the organic molecules can be encapsulated into either channels and cages or entrapped between layers. Their role is to provide the stability of the material through the development of non-bonded interactions. Large pore materials are produced from bulky SDA molecules, whereas small organic molecules are used for formation of small pore materials^[12]. CoAlPO-18 can be synthesised using tetraethylammonium hydroxide (TEAOH) or N, N,-diisopropyl ethylamine (DIPE) as the SDA. DIPE is more favourable SDA than TEAOH, since there is possibility that CoAlPO-34 is formed in

the presence of cobalt ions as a competing phase during the synthesis of CoAlPO-18^[13, 14]. CoAlPO-34 can be easily prepared using triethylamine (TEA) or TEAOH^[15]. The resulting solid product can contain framework and extra-framework Co²⁺ ions. The framework Co²⁺ ions are tetrahedrally coordinated, whilst extra-framework Co²⁺ ions yield different geometries. To use such microporous materials as catalysts, the organic template has to be removed calcination in air or oxygen.

Although CoAlPO catalysts have been studied extensively in the last decade, there still exists controversy^[16] regarding the nature and location of transition metal ions incorporated into the framework sites of AlPO molecular sieves. There is no sufficient evidence to support an argument of truly isomorphous substituted transition metal ions, and thus rule out the presence of extra-framework transition metal oxides. Also information about the presence and coordination of the metal ions in the surface (the top layer of ~ 50Å) and near surface region (50–100 Å) is still lacking. The structural and electronic properties from these regions can play an important role in understanding the relationship between catalytic properties, their structures and chemical compositions. Moreover, the understanding of chemistry of such materials can lead to the design of novel catalysts. For direct methods of examining the incorporation of the metal ions into the framework, the spectroscopic techniques such as Ultraviolet–visible spectroscopy (UV–VIS)^[17], Infrared spectroscopy (IR)^[18] and XAFS^[15, 17, 19-21] have been employed.

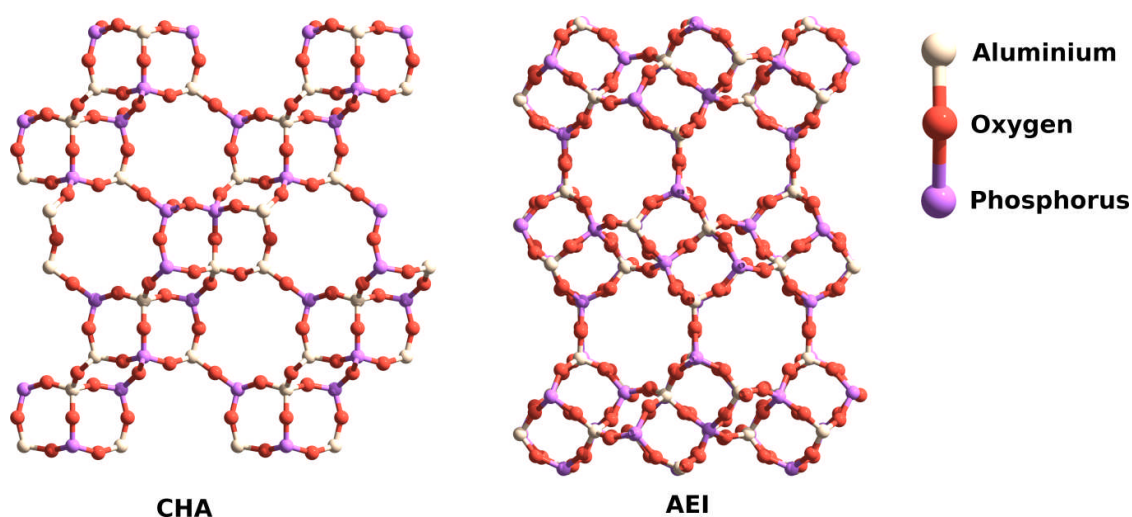


Figure 5-1 The 3D representation of the pore framework structures of AlPO-34 (CHA) and AlPO-18 (AEI), whereby cobalt will be introduced into the framework by the isomorph substitution for framework aluminium. Both structures have chabazitic cages as side pockets along the 0.38 nm diameter pores^[13].

The framework structures of AIPO-34 and AIPO-18 are depicted in Figure 5-1. AIPO-18 is classified as an AEI-type molecular sieve according to Framework Type Code (FTC) used in the International Zeolite Association database (IZA)^[22]. AIPO-34 has a chabazite (CHA-type) structure, which is structurally similar to AIPO-18 (AEI). Both structures can be described as a 3-dimensional channel networks consisting of six member rings with average pore size ≈ 0.38 nm. The difference between these two structures is in the stacking sequence and orientation of the double six rings^[13].

The aluminophosphate (AIPO) structure is built from strict alternation of corner-sharing Al^{3+}O_4 and P^{5+}O_4 tetrahedra^[22] (where $\text{Al}:\text{P} = 1$), which results in a electro-neutral framework. The isomorphic substitution of aluminium by transition metals in the AIPO framework can introduce both negative and positive charge in the framework^[9, 23]. In cobalt substituted aluminophosphates, Co^{2+} ions (≤ 10 w%) substitute for Al^{3+} ions at tetrahedral sites. This results in the formation of a negatively charged framework, Brönsted acid sites^[13], which implies that each Co^{2+} cation incorporated in the structure is charge compensated by a proton, as shown in Figure 5-2.

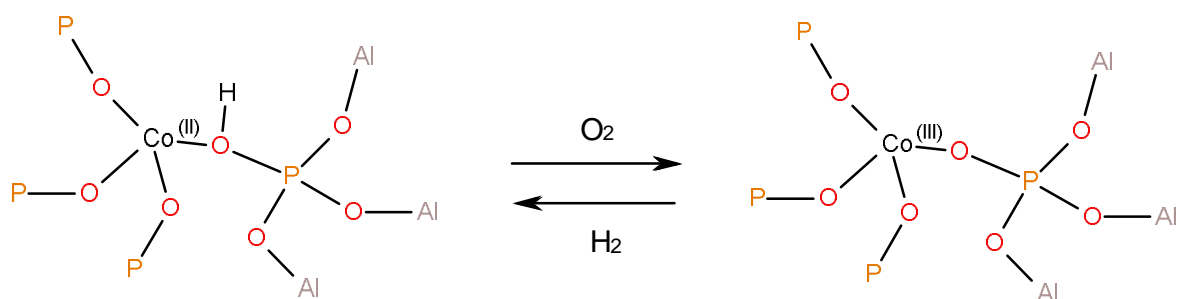


Figure 5-2 The generation of Brönsted acid sites in cobalt substituted aluminophosphates. The negatively charged framework is balanced by an equivalent number of positively charged extra-framework species such as quaternary ammonium cations and protonated amines^[13].

However, if the solids are heated at moderate temperatures in air or oxygen, the cobalt oxidation state changes to 3+, and thus the acid site disappears. Consequently, an electroneutral framework is created. Earlier studies showed that higher amounts of

cobalt doping (> 20 w% Co) has a loss of crystallinity and densification during calcination as side effect ^[15].

5.3 Aims of the work

Besides the investigation if the EREY–XAS is a suitable characterization method for the differences between the bulk and surface of CoAlPO, the aim of the work described in this chapter is to verify that isomorphous substitution of Co²⁺ for Al³⁺ ions in AEI and CHA structures indeed takes place, and distinguish between framework and extra-framework Co²⁺ ions.

5.4 Experimental part

5.4.1 Hydrothermal preparation of CoAlPO-18 and CoAlPO-34

A typical preparation of these catalysts is described elsewhere^[9, 13, 24]. Samples for this study were prepared by Sankar's group and were not used for any other studies.

CoAlPO-18 was prepared using N,N-diisopropylethylamine (DIPE) as the structure directing agent. The relative molar composition of the gel was calculated employing the formula $0.9\text{Al}^{3+} : 0.1\text{Co}^{2+} : 1\text{P}^{5+} : 0.8 \text{ DIPE} : 25\text{H}_2\text{O}$, where cobalt acetate was used as a Co^{2+} source. The initial gel was prepared by dissolving aluminium hydroxide hydrate ($\text{Al}(\text{OH})_3 \cdot x\text{H}_2\text{O}$, Sigma-Aldrich) in a solution of phosphoric acid (H_3PO_4 , 85%, Sigma-Aldrich) with deionised water. An aqueous solution of cobalt(II) acetate tetrahydrate ($(\text{CH}_3\text{COO})_2\text{Co} \cdot 4\text{H}_2\text{O}$, 98 %, Sigma-Aldrich) was then added to the mixture. After rigorous stirring of the gel for two hours, *N,N-Diisopropylethylamine* ($[(\text{CH}_3)_2\text{CH}]_2\text{NC}_2\text{H}_5$, 99.5 %, Sigma-Aldrich) was added to form the final gel which was stirred for several hours. The gel was then placed in an autoclave and heated at 160°C for four days.

CoAlPO-34 samples were prepared using tetratethylammonium hydroxide (TEAOH) as SDA^[25]. The relative molar composition of gels used in this study was calculated employing the formula $0.9\text{Al}^{3+} : 0.1\text{Co}^{2+} : 1\text{P}^{5+} : x \text{ TEAOH} : 25\text{H}_2\text{O}$, where $x = 0.8$ and 1 . The samples were then heated at 170°C for three days. The molar ratios of the gels are given in Table 5-1.

Table 5-1 Synthetic conditions of CoAlPO-34 preparation; tetratethylammonium hydroxide was used as a template.

Sample	Molar composition					Conditions
	Co	Al	P	TEAOH	H ₂ O	
A	0.1	0.9	1	0.8	25	170°C , 3 days
B	0.1	0.9	1	1.0	25	170°C , 3 days

5.4.1 XRD characterization

Although XRD is not a convenient tool for the determination of the structure of the active metal particles, it is suitable for the structural elucidation of the carrier framework. For an accurate structural determination of the materials X-ray powder diffraction patterns were obtained. X-ray diffraction measurements were performed on a Bruker D4 diffractometer Cu K α radiation at room temperature. The XRD patterns were collected using a position sensitive detector in 5 - 50° 2 θ range with a 0.02 Å step size. The powders were closely packed onto a flat-plate sample holder.

5.4.2 Transmission and Energy-Resolved Electron Yield XAS

Co K-edge EREY and transmission XAFS spectra were collected on the Dutch Belgium beam line (BM26A)^[26] at the ESRF using a water cooled Si(111) double crystal monochromator with the synchrotron ring operating in 4 bunch mode giving ~40 mA electron current at 6 GeV energy. Room temperature transmission XAS data were acquired in step scans over a k range from 3 - 12 Å⁻¹ using k^3 weighting for the counting time per data point increasing from 1 sec at 3 Å⁻¹ to 5 sec at 12 Å⁻¹. To achieve better statistic, three XAFS spectra were recorded for each sample in the transmission geometry.

The EREY–XAS (see chapter 2 for further details) data were recorded using e-yield detector over a similar k range as was used in the XAFS experiments. The e-yield detector was operating with a gas mixture of 10% Isobutene and 90% Helium, a drift voltage of -1500 V, cathode potential -550 V and a grounded anode. The e-yield detector measured a full electron energy spectrum at each incident photon energy. An example of a typical energy electron spectrum is shown in Figure 5-3. A constant flow of 100 ml/min Isobutene/He mixture was maintained through the vessel. The sample was set at an inclination of 2.5° with respect to the X-ray beam. The horizontal and vertical size of the beam was 4 and 0.7 mm respectively, and produced a beam foot print on the sample covering an area of around ~80 mm² on the sample. In order to maintain the count rate below the detector saturation level, the beam intensity was, when required, attenuated by placing aluminium sheets before the sample.

5.4.3 XAFS data analysis

The EREY–XAS from the bulk and near surface of samples were obtained by summing all Auger electron spectra collected for each photon energy during the energy scan of the monochromator. This is followed by integration within the electron energy regions indicated in Figure 5-3. TEY spectra were obtained by integrating a whole area of the Auger electron energy spectrum.

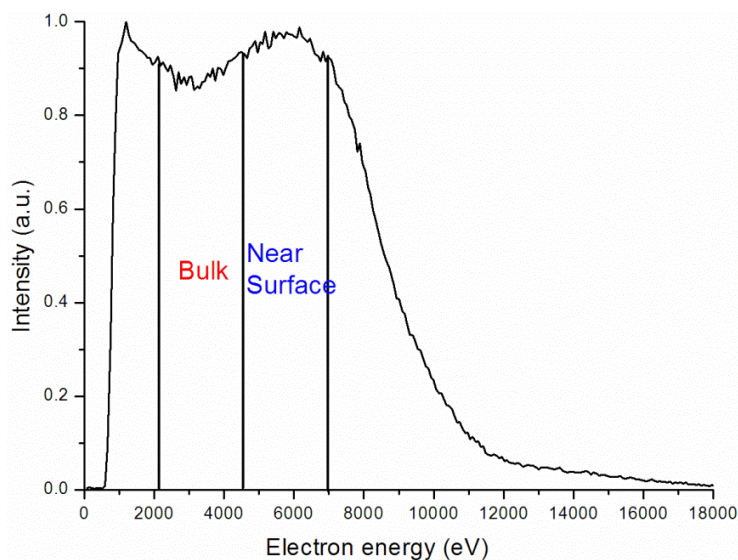


Figure 5-3 Auger electron spectrum obtained at photon energy of 7 903 eV from CoAlPO-34 A, whereby two different energy regions are indicated. The low energy region, in which Auger electrons escape from the bulk, whereas the higher energy electrons emanate from the near surface region of the sample.

Transmission XAS as well as EREY–XAS data were normalized in Athena^[27] (See Chapter 2 for more details about procedure). The non-linear least squares fittings of EXAFS and EREY–EXAFS data were performed in EXCURVE98^[28]. The EXAFS and EREY–EXAFS data were analysed using the single scattering wave approximation^[29]. Phase shift and backscattering factors were calculated from atomic potentials using EXCURVE98. The non-structural parameter AFAC (the amplitude reduction due to many electron processes) was taken from the best fit to transmission EXAFS from Co-foil and fixed at 0.85. The same value of AFAC was used for EREY–EXAFS analysis. The refinement of transmission EXAFS data was carried out with k^3 weighting in the

range 3.3 to 12.8 Å⁻¹. The refinement of EREY– EXAFS data was carried out with k^3 weighting in the range 3.3 to 8.5 Å⁻¹. During the refinement the coordination numbers were fixed to crystallographic values, however bond distances and Debye-Waller factors were allowed to vary.

5.5 Results and discussion

In Figure 5-4 and Figure 5-5 diffraction patterns of CoAlPO-34 A and B and CoAlPO-18 respectively are shown. The XRD patterns could be indexed to the respective structures, and no extra reflections arising from other phases were found. XRD patterns of the as-prepared CoAlPO-34 A and B catalysts are identical regarding positions of the reflections and their intensities indicating identical crystalline structures. Due to the low concentration and random substitution of cobalt ions in the AlPO framework, XRD is not able to provide the structural information about how the cobalt atoms are incorporated in the crystalline framework. This information is crucial in the determination of the relationship between structure and catalytic activity of these catalysts^[30].

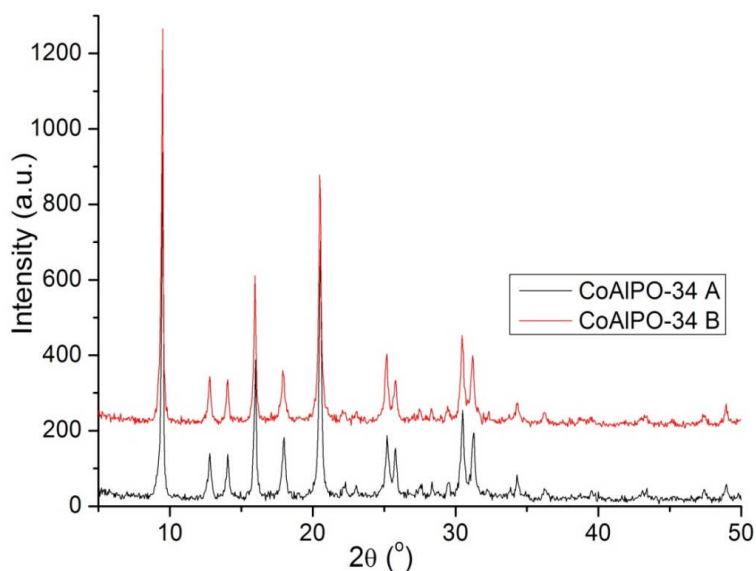


Figure 5-4 XRD patterns of the CoAlPO-34 samples A and B. The patterns are nearly identical which indicates that the crystalline framework of both materials is nearly identical.

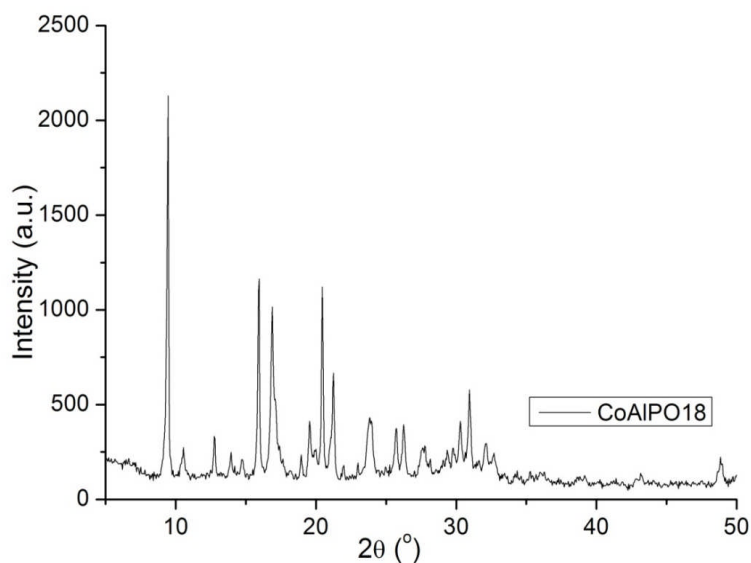


Figure 5-5 XRD pattern of the CoAlPO-18 sample which resembles to AlPO-18^[31] pattern, monoclinic *C2/c* space group.

First, the Co K-edge transmission X-ray absorption near edge spectra (XANES) of reference materials and CoAlPO catalysts will be discussed, followed by EREY-XANES. The XANES spectra are used for distinguishing between framework and extra-framework Co^{2+} species in CoAlPO samples. From previous work on the cobalt substituted aluminophosphates it is known that Co^{2+} species can be either incorporated into the framework in the tetrahedral coordination or be present as the extra-framework ions in octahedral coordination^[32, 33]. Accordingly, cobalt acetate ($\text{C}_4\text{H}_6\text{CoO}_4$) and cobalt aluminate (CoAl_2O_4), representing Co^{2+} in octahedral and tetrahedral environments respectively were chosen as reference materials. The reference Co K-edge XANES spectra are shown in Figure 5-6. The Co^{2+} ions are tetrahedrally coordinated in CoAl_2O_4 ^[34], and the XANES spectrum displays a pre-edge peak at ~ 7708 eV. On the other hand, the pre-edge peak is absent in octahedrally coordinated Co^{2+} ions in cobalt acetate and there is a shift in the main edge towards higher energies. The pre-edge peak in cobalt aluminate is due to the $1s$ to $3d$ electronic transition, which is much stronger for Co^{2+} in the tetrahedral environment compared to that of octahedral. This occurs during relaxation in the non-centrosymmetric environment, in which d and p Co–O molecular orbital are mixed together. A typical characteristic of Co^{2+} in octahedral environment is a strong white line intensity, a feature at 7722 eV (main edge intensity), that arises due to linear O–Co–O bonds from $1s$ to $4p$ absorption transition.

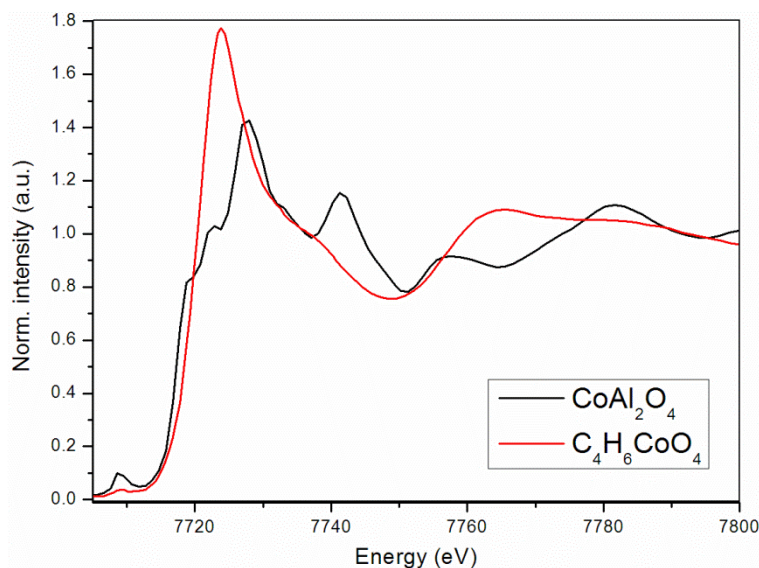


Figure 5-6 *Co K-edge XANES of CoAl_2O_4 and $\text{C}_4\text{H}_6\text{CoO}_4$ which have been used as reference materials representative of the tetrahedral or octahedral coordinated Co^{2+} ions.*

Figure 5-7 depicts the comparison of the transmission and TEY XANES spectra of the CoAl_2O_4 along with as-prepared cobalt substituted aluminophosphates. Since EREY-XAS is not a well-established technique in comparison to conventional transmission or fluorescence methods, it is required to compare these spectra and avoid uncertainties regarding data normalization. The comparisons of the XANES spectra collected by the two techniques suggest that the spectra are similar. There is no shift of the main edge and only minor changes of the white line intensity on the top of the main edge can be observed. The slight white line intensity decrease in EREY-XANES of CoAl_2O_4 can be due to ‘self-absorption’ effect analogous to what is found in fluorescence yield spectra when insufficiently diluted samples are used for measurements^[35]. Furthermore, the slight increase of the white line intensity of CoAlPO-18 and CoAlPO-34 B can be due to the near surface disorder, or changes in the local geometry of Co^{2+} ions, particularly in CoAlPO-18 (for further explanations see discussion on EXAFS data).

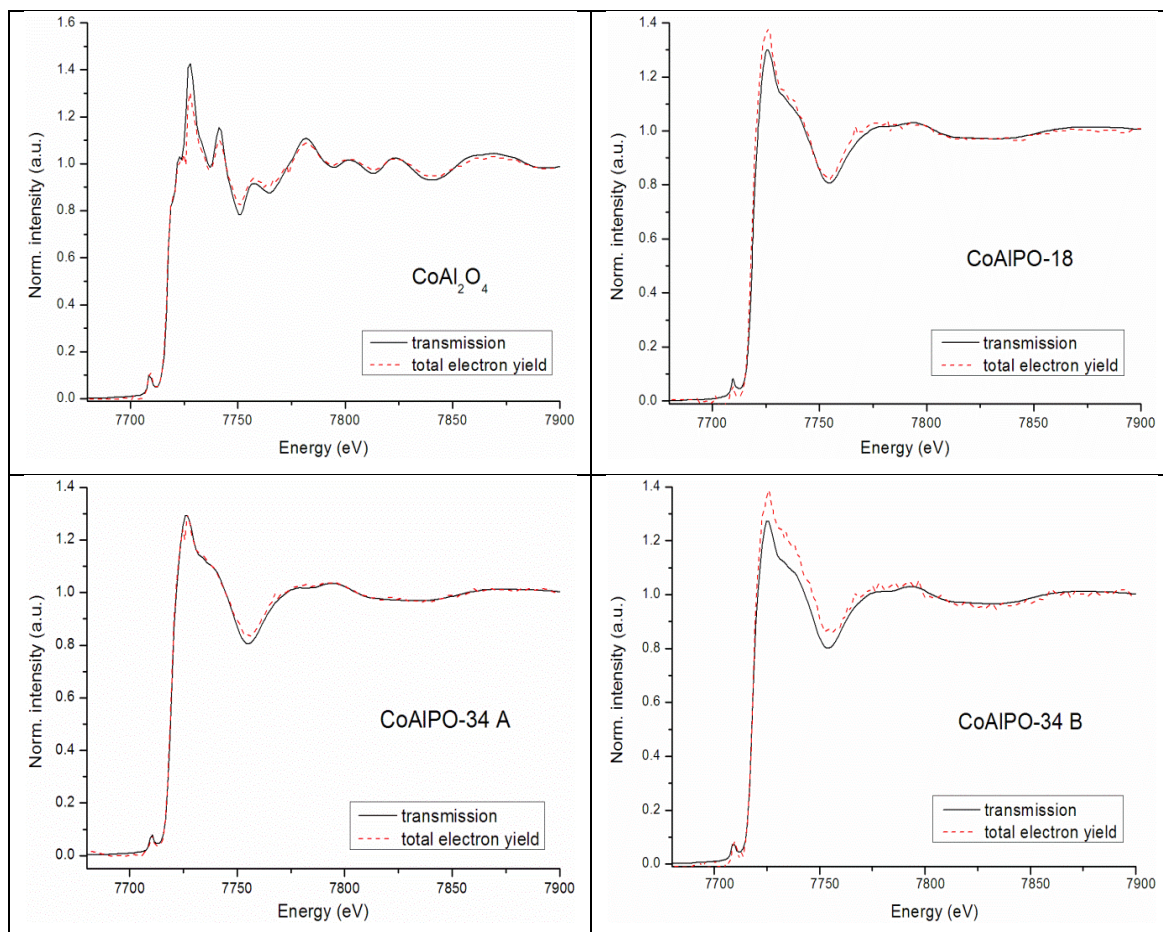


Figure 5-7 Comparison of the Co K-edge transmission and TEY-XAS spectra of CoAl_2O_4 , as-prepared CoAlPO-18 and as-prepared CoAlPO-34 A and B . The comparison shows that spectra are very similar regarding the pre-edge feature and position of the main edge.

Co K-edge EREY-XANES obtained from the near surface and bulk as well as transmission XANES spectra of the as-prepared CoAlPO-34 A and B samples along with CoAlPO-18 are shown in Figure 5-8. The pre- and main-edge peak position of all CoAlPOs samples matches well that of the reference CoAl_2O_4 . This indicates that Co^{2+} ions are present at tetrahedral sites in the framework of the material. As for the transmission XANES data, it can be seen that spectra of CoAlPO-34 A and B and CoAlPO-18 are identical. The EREY-XANES obtained from the near surface and bulk of the catalysts also suggest that there are no significant differences; within the experimental error the spectra look identical. This indicates that Co^{2+} species are uniformly,

independent of the bulk or near surface, incorporated into the AlPO framework in the tetrahedral geometry.

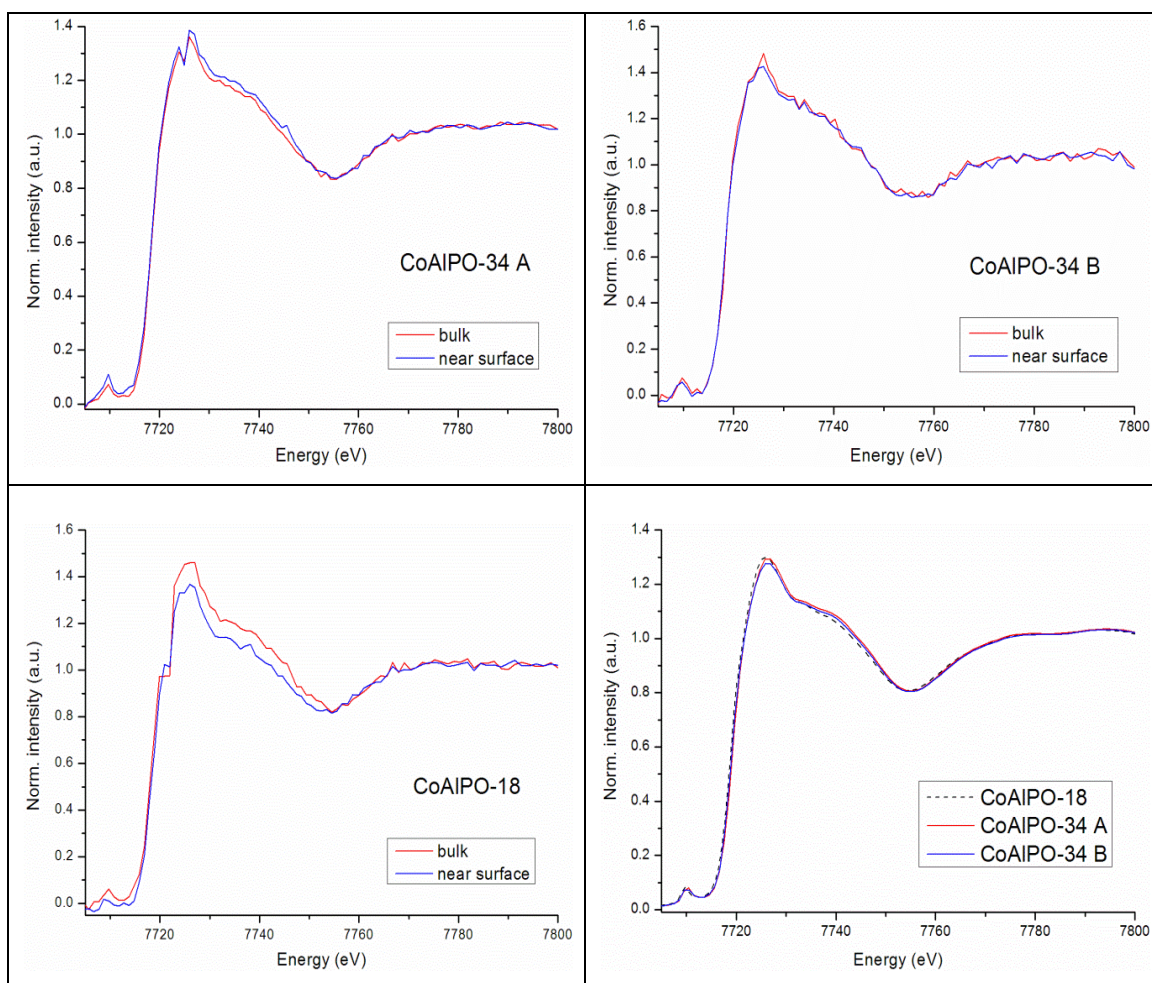


Figure 5-8 Co K-edge EREY-XANES for CoAlPO-34 A, CoAlPO-34 B and CoAlPO-18, where the spectrum from the bulk is plotted in red, whereas from the near surface is in blue. Co K-edge transmission XANES of all catalysts are shown in bottom right corner. The marginal differences indicate that there is no difference between the bulk and near edge with respect to the Co^{2+} coordination.

From the EXAFS curve fitting analysis on a reference cobalt foil and by fixing coordination numbers to the crystallographic values, the amplitude reduction factor due to electron processes (named in EXCURVE98 as AFAC) was determined to be 0.85. It represents the average proportion of excitations which contribute to EXAFS. In order to quantitatively determine structural parameters of the cobalt environment, the fitting

procedure was performed on transmission Co K-edge EXAFS data of the model compounds, tetrahedral Co^{2+} in CoAl_2O_4 ^[34] and octahedral Co^{2+} in $\text{C}_4\text{H}_6\text{CoO}_4$ ^[36]. To avoid strong correlations between Debye-Waller factors and coordination numbers, the coordination numbers were kept fixed to the crystallographic values during refinements. In CoAl_2O_4 ^[32], the Co^{2+} ions are surrounded by four tetrahedrally spaced oxygen atoms at 1.94 ± 0.01 Å. In $\text{C}_4\text{H}_6\text{CoO}_4$, the Co^{2+} ions are surrounded by six octahedrally arranged oxygen atoms at 2.08 ± 0.005 Å. Based upon transmission EXAFS data, the local structure around the cobalt atom in CoAlPO-34 A and B samples along with CoAlPO-18 can be accurately described by four tetrahedrally spaced oxygen atoms at a distance of 1.94 ± 0.003 Å. This bond distance, typical for Co^{2+} in tetrahedral environment, is in good agreement with values found in CoAl_2O_4 and the literature^[15]. The results are summarized in Table 5-2.

Table 5-2 Structural parameters obtained from analysis of transmission Co K-edge EXAFS data for the as-prepared catalysts and model compounds, where N is coordination number, R –bond distance, σ –standard deviation of bond distance, σ^2 –Debye-Waller factor and R_{Fit} –goodness of fit.

Sample	Scatter	N	R (Å)	σ^2 (Å ²)	R_{Fit}
CoAlPO-34 A	O	4	1.94 ± 0.003	0.005	24
CoAlPO-34 B	O	4	1.94 ± 0.003	0.005	24
CoAlPO-18	O	4	1.94 ± 0.003	0.006	28
CoAl_2O_4	O	4	1.94 ± 0.010	0.004	38
$\text{C}_4\text{H}_6\text{CoO}_4$	O	6	2.08 ± 0.005	0.007	31

Before EREY–EXAFS fitting result can be discussed, it is important to mention that the experimentally determined k -range of the data is shorter with a limited number of independent data points^[37], N_I , but there is still sufficient information for fitting the first oxygen shell. The N_I defines the number of parameters that can be reliably obtained from the fitting of EXAFS spectrum. In the case of transmission data, EXAFS analyses were only performed on the first shell, since the primary aim of this work is to understand the immediate local environment around cobalt in the bulk and near surface.

The EREY-EXAFS results for CoAlPO-34 A and B also found Co-O bonds at $1.94 \pm 0.01 \text{ \AA}$, which is a typical for Co^{2+} ions in tetrahedral environment as evidenced by EXAFS fitting results for CoAl_2O_4 . This indicates that the presence of extra-framework Co^{2+} species in the near surface region of the catalysts can be ruled out within the surface sensitivity limit of this technique. It seems that all Co^{2+} ions are placed in the framework exclusively at tetrahedral sites, as it is also evidenced by XANES. In addition, changes in the Al/P ratios for these two samples did not have an influence on the incorporation of Co^{2+} ions into the framework. Room temperature Co K-edge transmission and EREY-EXAFS spectra of as-prepared CoAlPO-34 samples with associated Fourier transforms and their fits are shown in Figure 5-9 and Figure 5-10. In these figures is demonstrated that EREY-EXAFS amplitude are comparable to that of transmission. In addition, EREY-EXAFS are little bit noisier but data quality was sufficient to perform full EXAFS analyses. The fitting results are summarized in Table 5-3.

Table 5-3 Structural parameters obtained from the analysis of energy resolved Co K-edge EXAFS data for as-prepared catalysts, where N is coordination number, R – bond distance, σ –standard deviation of bond distance, σ^2 –Debye-Waller factor and R_{Fit} –goodness of fit.

	Sample	Scatter	N	R (Å)	σ^2 (Å ²)	R_{Fit}
CoAlPO-34 A	near-surface	O	4	1.94±0.005	0.004	38
	bulk	O	4	1.93±0.010	0.003	44
	TEY	O	4	1.95±0.010	0.006	42
CoAlPO-34 B	near-surface	O	4	1.93±0.01	0.005	50
	bulk	O	4	1.94±0.01	0.004	50
	TEY	O	4	1.94±0.01	0.005	45
CoAlPO-18	near-surface	O	4	1.96±0.01	0.005	53
	bulk	O	4	1.97±0.02	0.005	58
	TEY	O	4	1.98±0.01	0.007	53

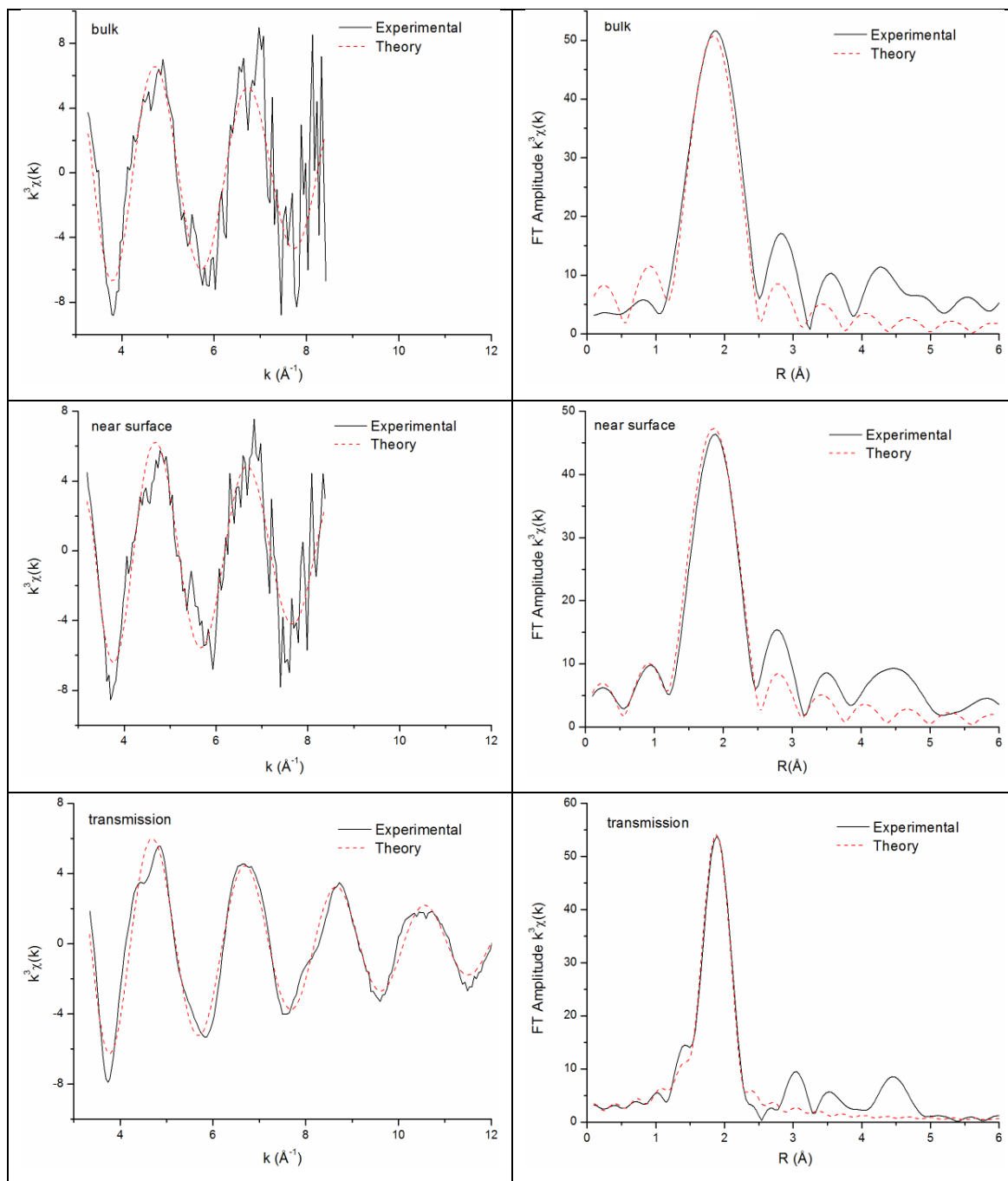


Figure 5-9 Comparison of Co K-edge EREY and transmission EXAFS together with corresponding Fourier transforms for CoAlPO-34 A. Data were analysed in k -space (after background subtraction, k^3 -weighted). The solid line is the experimental data and the dashed line is the best fit. It can be clearly observed that EREY-EXAFS amplitudes are comparable of that transmission. The EREY-EXAFS spectra are noisier, particularly at higher k -values.

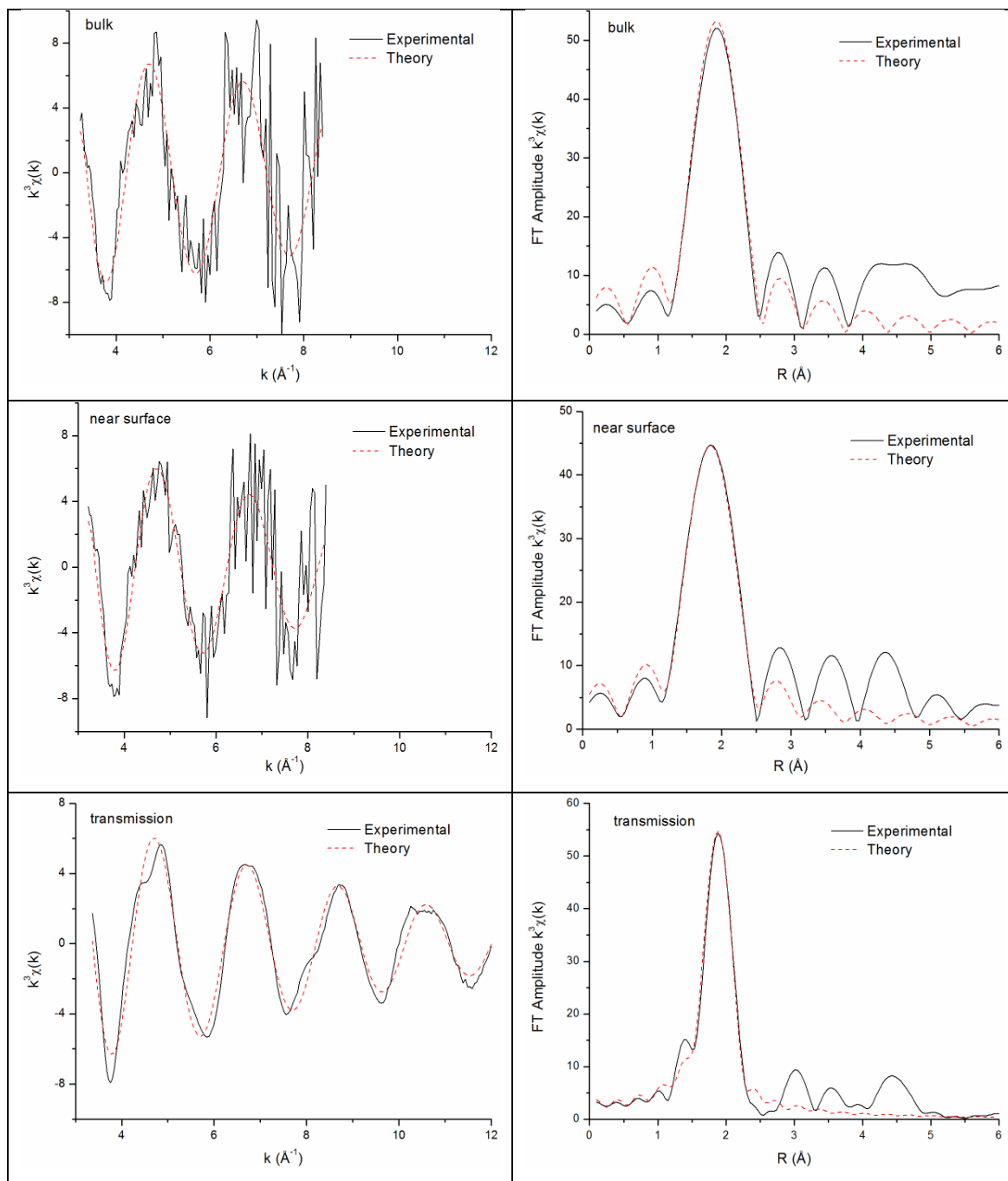


Figure 5-10 Comparison of Co K-edge EREY and transmission EXAFS together with corresponding Fourier transforms for CoAlPO-34 B. Data were analysed in k -space (after background subtraction, k^3 -weighted). The solid line is the experimental data and the dashed line is the best fit. It can be clearly observed that EREY-EXAFS amplitudes are comparable of that transmission. The EREY-EXAFS spectra are noisier, particularly at higher k -values, but the data quality is sufficient for full EXAFS analyses.

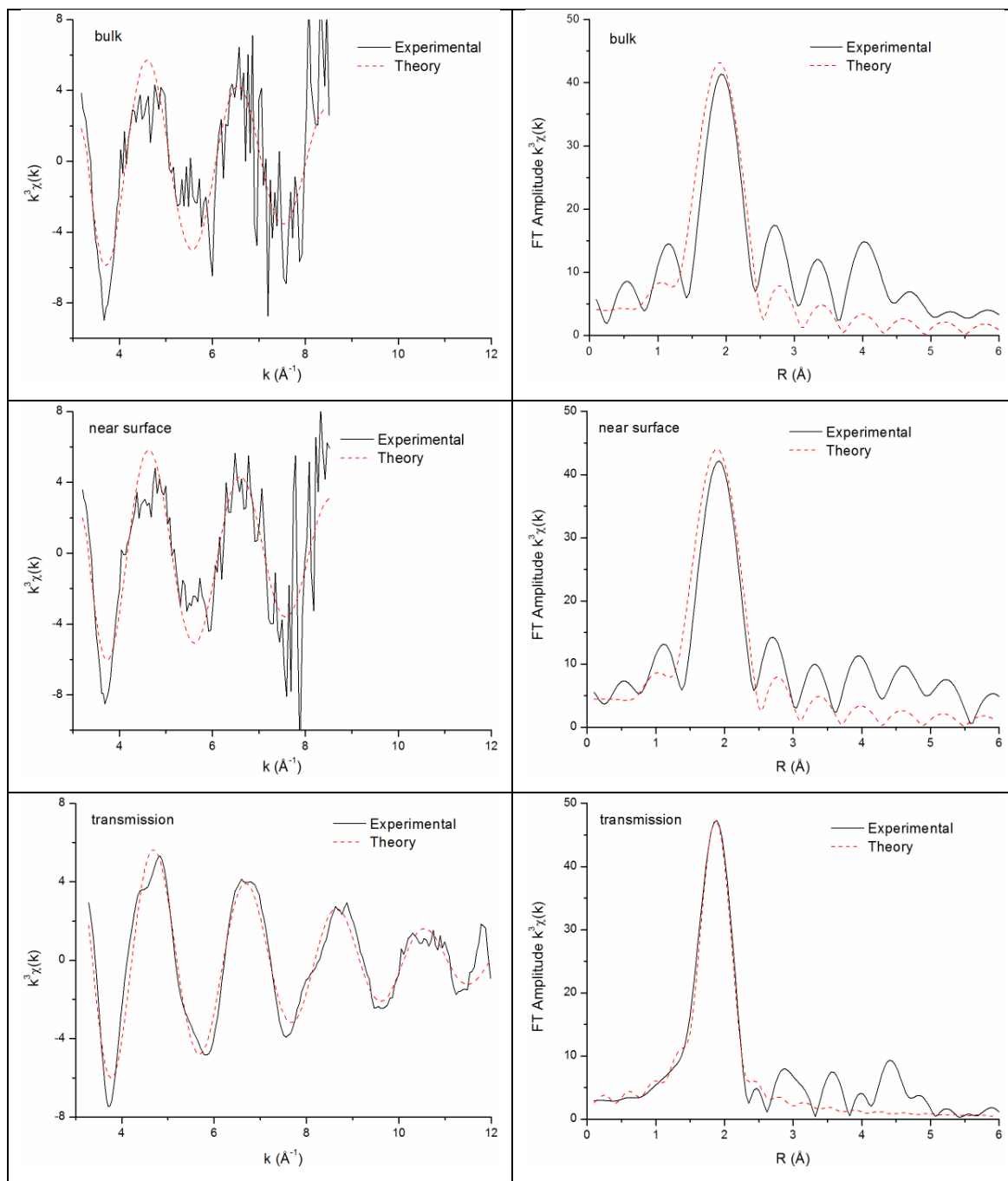


Figure 5-11 Comparison of Co K-edge EREY and transmission EXAFS together with corresponding Fourier transforms for CoAlPO-18. Data were analysed in k -space (after background subtraction, k^3 -weighted). The solid line is the experimental data and the dashed line is the best fit. It can be clearly observed that EREY-EXAFS amplitudes are comparable to that of transmission. The EREY-EXAFS spectra are much noisier, particularly at higher k -values, but data quality is sufficient for full EXAFS analyses.

EREY–EXAFS results for CoAlPO-18 found in the bulk and near surface four Co–O bonds at 1.96 ± 0.01 Å and 1.97 ± 0.01 Å respectively. The values from the transition region between the surface and bulk of the catalyst are in disagreement with bond distances obtained from transmission EXAFS probing the bulk of the catalyst. One can argue that an increase in coordination numbers should be observed, but on the other hand this can also be rationalized by the fact that these species are located near the surface, where they are not necessarily entirely bonded. This suggests that not all cobalt atoms are incorporated into the tetrahedral lattice of AlPO-18 framework during the synthesis. The fact that only a limited amount of Co^{2+} species is present as extra-framework atoms is supported by the XRD pattern showing that a pure phase of CoAlPO-18 was obtained. A similar phenomena was reported in the literature in EXAFS study on Co/MCM-41^[38], where Co^{2+} ions are not in tetrahedral lattice positions but form finely dispersed cobalt oxide clusters. The local structure of extra-framework cobalt in as-prepared material was described by four Co–O bonds at 1.97 Å. Moreover, EREY–XANES from the near surface showed also a small decrease in the pre-edge peak intensity and the increase of white line intensity (Figure 5-7), which indicates the presence of Co^{2+} species in different coordination geometry. This can account for the presence of a mixture of tetrahedral and octahedral coordination^[39]. The other reasonable explanation can be that in a regular octahedral coordination are Co^{2+} ions surrounded by water molecules, whereas in a less symmetrical, pseudo-octahedral, coordination some of the coordinating oxygen atoms bridge between two cations (P^{5+} –O– Co^{2+})^[19]. However, the possibility that this discrepancy is a consequence of the lower data quality cannot entirely be ruled out in this case, and also the fact that the local structural information is obtained only from the transition region between the near surface and bulk of the catalysts. Nevertheless, on the bases of these findings, it can be postulated that a small amount of the cobalt atoms can be present as small cobalt oxide particles on the surface of the catalyst.

To prove the presence of these small oxide particles on the surface and also gain insights about their chemical states, it requires employing low energy electron diffraction (LEED) or X-ray photoelectron spectroscopy (XPS), but this was beyond the scope of this work. In contrast, several reports in the literature^[17, 18, 21, 33] probing mainly the bulk of such materials using spectroscopic techniques claimed that Co^{2+} ions are incorporated into the tetrahedral framework sites by synthesis. The presence of extra-

framework cobalt species was not discussed in detail. It was postulated that if extra-framework Co^{2+} ions present in the AlPO frameworks their structure collapse, and Co^{2+} species are octahedrally coordinated with an average Co–O bonds of 2.06 Å^[32, 33].

5.6 Summary and Conclusion

Cobalt substituted AlPO-34 A, B and AlPO-18 catalysts were synthesised by hydrothermal method. The formation of the desired crystalline phases was confirmed by XRD. XAFS spectra were used to provide information on the incorporation of cobalt into the framework, whereas EREY–XAFS spectra were used to distinguish between framework and extra-framework Co^{2+} species. The structural information about Co^{2+} species in as-prepared CoAlPO-34 A and B obtained using a conventional transmission technique confirmed that Co^{2+} ions are embedded in the CHA structure at tetrahedral sites of the catalysts. More importantly, the results from EREY–XAS did not show any evidence of the presence of extra-framework Co^{2+} species in the near surface region of the catalysts. This indicates that Co^{2+} isomorphly substituting for Al^{3+} ions are uniformly distributed at the tetrahedral sites of the AlPO-34 framework. In contrast, EREY–XAS results for CoAlPO-18 showed that a small amount of Co^{2+} ions is located near the surface of the catalyst and acts as extra-framework Co^{2+} which is not substituting for Al^{3+} in the AlPO-18 framework. The extra-framework Co^{2+} ions do not influence the long range ordering of the structure as evidenced by XRD, and transmission EXAFS that confirmed the presence of tetrahedrally coordinated Co^{2+} ions in the AlPO-18 framework.

References

- [1] A. I. Frenkel, C. W. Hills and R. G. Nuzzo, *The Journal of Physical Chemistry B* **2001**, *105*, 12689-12703.
- [2] A. Y. Khodakov, W. Chu and P. Fongarland, *Chemical Reviews* **2007**, *107*, 1692-1744; R. B. Gregor and F. W. Lytle, *Journal of Catalysis* **1980**, *63*, 476-486.
- [3] J. Stohr, C. Noguera and T. Kendelewicz, *Physical Review B* **1984**, *30*, 5571-5579; P. H. Citrin, P. Eisenberger and R. C. Hewitt, *Physical Review Letters* **1978**, *41*, 309-312; Koningsberger D.C. and Prins R., *X-ray absorption. Principles applications, techniques of EXAFS, SEXAFS, and XANES*, Jon Wiley & Sons, **1992**, p. 443-572.
- [4] T. Rayment, S. L. M. Schroeder, G. D. Moggridge, J. E. Bateman, G. E. Derbyshire and R. Stephenson, *Review of scientific instruments* **2000**, *71*, 3640-3645.
- [5] Ertl G. and Kuppers J., *Low Energy Electrons and Surface Chemistry*, Verlag Chemie, Weinheim, **1974**, p. 2-47; M. G. Lagally and J. A. Martin, *Review of scientific instruments* **1983**, *54*, 1273-1288; G. F. Knoll, *Radiation detection and measurement*, Wiley, **1989**, p. 160-198.
- [6] L. M. Schroeder, G. D. Moggridge, R. M. Lambert and T. Rayment, *In Spectroscopy for Surface Science (Advances in Spectroscopy)* **1998**, Vol. 26, Clark, R.J.H., Hester R.E., Eds., John Wiley & Sons: Chichester, p. 1-29.
- [7] B. Abbey, J. D. Lipp, Z. H. Barber and T. Rayment, *Journal of Applied Physics* **2006**, *99*, 124914-124919.
- [8] A. Vollmer, J. D. Lipp, J. R. I. Lee, G. E. Derbyshire and T. Rayment, *Analytical Chemistry* **2003**, *75*, 6571-6575.
- [9] J. Chen and J. M. Thomas, *Journal of the Chemical Society, Chemical Communications* **1994**, 603-604.
- [10] J. M. Thomas, R. Raja, G. Sankar and R. G. Bell, *Nature* **1999**, *398*, 227-230; Y. Xu, C. P. Grey, J. M. Thomas and A. K. Cheetham, *Catalysis Letters* **1990**, *4*, 251-260.
- [11] B. M. Lok, T. R. Cannan and C. A. Messina, *Zeolites* **1983**, *3*, 282-291.
- [12] A. B. Pinar, L. Gomez-Hortiguela and J. Perez-Pariente, *Chemistry of Materials* **2007**, *19*, 5617-5626.
- [13] J. Chen, P. A. Wright, J. M. Thomas, S. Natarajan, L. Marchese, S. M. Bradley, G. Sankar, C. R. A. Catlow and P. L. Gai-Boyes, *The Journal of Physical Chemistry* **1994**, *98*, 10216-10224.
- [14] G. Muncaster, A. T. Davies, G. Sankar, C. R. A. Catlow, J. M. Thomas, S. L. Colston, P. Barnes, R. I. Walton and D. O'Hare, *Physical Chemistry Chemical Physics* **2000**, *2*, 3523-3527.
- [15] G. Sankar, J. K. Wyles and C. R. A. Catlow, *Topics in Catalysis* **2003**, *24*, 173-184.
- [16] M. Hartmann and L. Kevan, *Chemical Reviews* **1999**, *99*, 635-664; B. M. Weckhuysen, R. R. Rao, J. A. Martens and R. A. Schoonheydt, *European Journal of Inorganic Chemistry* **1999**, *1999*, 565-577; U. Lohse, B. Parltitz, D. Muller, E. Schreier, R. Bertram and R. Fricke, *Microporous Materials* **1997**, *12*, 39-49; M. Hartmann and L. Kevan, *Research on Chemical Intermediates* **2002**, *28*, 625-695.
- [17] G. Sankar, S. Fiddy, A. M. Beale, I. Harvey, S. Hayama and G. Bushnell-Wye, *AIP Conference Proceedings* **2007**, *882*, 585-587.
- [18] G. Sankar, R. Raja and J. M. Thomas, *Catalysis Letters* **1998**, *55*, 15-23.
- [19] K. Simmance, G. Sankar, R. G. Bell, C. Prestipino and W. v. Beek, *Physical Chemistry Chemical Physics* **2009**, *12*, 559-562.
- [20] P. A. Barrett, G. Sankar, C. R. A. Catlow and J. M. Thomas, *Journal of Physical Chemistry* **1996**, *100*, 8977-8985.

- [21] G. Sankar, R. Raja, S. L. Scott, C. M. Crudden and C. W. Jones in *On the Structure of Cobalt-Substituted Aluminophosphate Catalysts and Their Catalytic Performance Nanostructured Catalysts, Vol.* (Ed. D. J. Lockwood), Springer US, **2003**, pp. 195-212.
- [22] S. T. Wilson, B. M. Lok, C. A. Messina, T. R. Cannan and E. M. Flanigen, *Journal of the American Chemical Society* **1982**, *104*, 1146-1147.
- [23] R. Xu, W. Pang, J. Yu, Q. Huo and J. Chen in *Vol.* John Wiley & Sons Pte Ltd, Singapore, **2009**, pp. 191-251; H. O. Pastore, S. Coluccia and L. Marchese, *Annual Review of Materials Research* **2005**, *35*, 351-395.
- [24] G. Sankar, J. K. Wyles and C. R. A. Catlow, *Topics in Catalysis* **2003**, *24*, 173-184.
- [25] B. M. Lok, C. A. Messina, R. L. Patton, R. T. Gajek, T. R. Cannan and E. M. Flanigen, *Journal of the American Chemical Society* **1984**, *106*, 6092-6093.
- [26] S. Nikitenko, A. M. Beale, A. M. J. van der Eerden, S. D. M. Jacques, O. Leynaud, M. G. O'Brien, D. Detollenaere, R. Kaptein, B. M. Weckhuysen and W. Bras, *Journal of Synchrotron Radiation* **2008**, *15*, 632-640.
- [27] B. Ravel and M. Newville, *Journal of Synchrotron Radiation* **2005**, *12*, 537-541.
- [28] N. Binsted and S. S. Hasnain, *Journal of Synchrotron Radiation* **1996**, *3*, 185-196.
- [29] S. J. Gurman, N. Binsted and I. Ross, *Journal of Physics C-Solid State Physics* **1984**, *17*, 143-151.
- [30] G. Sankar and J. M. Thomas, *Topics in Catalysis* **1999**, *8*, 1-21; G. Sankar, J. M. Thomas and C. R. A. Catlow, *Topics in Catalysis* **2000**, *10*, 255-264.
- [31] A. Simmen, L. B. McCusker, C. Baerlocher and W. M. Meier, *Zeolites* **1991**, *11*, 654-661.
- [32] P. A. Barrett, G. Sankar, C. Richard, A. Catlow and J. M. Thomas, *Journal of Physics and Chemistry of Solids* **1995**, *56*, 1395-1405.
- [33] P. A. Barrett, G. Sankar, R. H. Jones, C. R. A. Catlow and J. M. Thomas, *Journal of Physical Chemistry B* **1997**, *101*, 9555-9562.
- [34] K. Toriumi, M. Ozima, M. Akaogi and Y. Saito, *Acta Crystallographica Section B* **1978**, *34*, 1093-1096.
- [35] S. L. M. Schroeder, G. D. Moggridge, R. M. Lambert and T. Rayment, *Journal de Physique IV France* **1997**, *7*, 92-96.
- [36] J. N. van Niekerk and F. R. L. Schoening, *Acta Crystallographica* **1953**, *6*, 609-612.
- [37] E. A. Stern, *Physical Review B* **1993**, *48*, 9825-9827.
- [38] A. Jentys, N. H. Pham, H. Vinek, M. Englisch and J. A. Lercher, *Microporous Materials* **1996**, *6*, 13-17.
- [39] G. Sankar, J. M. Thomas, F. Rey and G. N. Greaves, *Journal of the Chemical Society, Chemical Communications* **1995**, 2549-2550; D. Grandjean, A. M. Beale, A. V. Petukhov and B. M. Weckhuysen, *Journal of the American Chemical Society* **2005**, *127*, 14454-14465.

Chapter 6 Effects of X-rays on crystal nucleation in Lithium disilicate

6.1 Chapter Overview

The effects of exposure to a monochromatic 10 keV X-ray beam on thermally induced crystallization of lithium disilicate glass has been investigated and rendered two unexpected findings. First, it was found that an extended exposure during the nucleation heat treatment increased the number of nucleation sites. Second, it was observed that the effects extended far beyond the sample region that was directly exposed to the X-ray beam. The effects were confined to the direction perpendicular to the polarization of the synchrotron radiation beam that was used. The effects could be attributed to photo electrons created not only by the direct X-ray beam but also by the scattered radiation.

6.2 Introduction

The use of synchrotron radiation based X-ray techniques to follow the evolution of materials in time has become quite common in the last decade. The time domains available depend on which specific technique is used, but broadly speaking one can state that the most time resolved experiments are performed at a rate of around 1-60 seconds/frame. Obviously, there are experiments where higher time resolution is required and also can be achieved but these are not numerous. However, in many cases it is not required or desirable to carry out experiments with too high a time resolution. Common sense suggests that when studying the drying of, for instance, cement it is not too sensible to take data at a millisecond time frame rate. The same is true for many studies in catalysis or crystallization. Therefore, in many experiments, for example, hydrothermal synthesis of dense metal oxides catalysts at constant temperature or phase transformation during heating at elevated temperatures is a sample exposed to the X-ray beam in an approximate energy range 5 – 20 keV for several minutes or hours.

In general, the danger of sample modification due to interactions with the X-ray beam is assumed to be relatively benign compared to, for instance, electron microscopy. However, the danger for damage due to radiation by X-rays in this photon energy range is known but apart from in the protein crystallography community not very well documented^[1]. The key to combat the damage problem in organic crystals is to cool the samples to cryogenic temperatures where the damage causing processes are arrested. Unfortunately, the cooling strategy does not work when it is necessary to study time-resolved processes of samples where water is the solvent or where temperature is one of the controlling factors such as in crystallization processes.

In general, the influence of exposure to radiation with photons with energies 5-20 keV has a destructive tendency on either the molecules themselves or on the crystals formed from these molecules. Monochromatic X-ray beams of third generation synchrotrons do not induce sufficient local heating effects to be the cause of this damage, and the effect has more to be sought in the radiolysis products liberated by X-ray absorption^[2]. However, in crystallization studies on polymers^[3] or in the solid state^[4], the effects of the interaction of the X-rays with the sample have so far been ignored apart from

microfocus experiments where the local dose is so high that not only the crystallization process is influenced but actually the sample can be destroyed^[5].

There are exceptions to the destructive effect of X-rays reported in the literature. In some cases, the X-ray beam actually caused particles to be formed^[6] but these experiments were carried out with a pink beam. The latter is partially monochromated and consequently a very high radiation dose is a possible case for local heating. For experiments where monochromatic radiation was used, very few references of the interference of the X-rays with the crystallization process can be found. A report on radiation induced crystallization of sucrose due to 8 keV photons from a sealed tube Cu source can be found^[7]. However, these authors worked on a system of 'dried raspberry flavoured Jell-O (gelatine)' in which the gelatine inhibited the formation of sucrose crystals. Once the sample was exposed to radiation for several hours, crystallization occurred. Although the authors do not provide an explanation for this phenomenon, it could well be that the radiation damaged the gelatine matrix sufficiently for the sucrose to become mobile and start crystallization. When exposed to microwave radiation (100 W, 2.4 GHz, 10-15 minute exposures), the authors found a similar effect.

Several other cases have been reported in which radiation helped to induce structure formation. The initiation of pyramidically shaped crystals on the surface of 0.5 micron thick amorphous, mechanically buckled, Barium Titanate film when exposed to a dose of 10^{10} photons/sec, 24 keV in a $12 \times 12 \mu\text{m}^2$ spot is the only example so far where radiation is assumed to induce crystallization in the solid state^[8]. The authors dismiss the possibility that this might be due to local sample heating but instead make a reasonable case that the electrons created by the photoelectric effect increase the vibration amplitude in, mainly, the light atoms. Recently, an effect was reported in which the authors claimed to have found bundle formation under the influence of radiation^[9]. X-rays of around 8.5 keV are reported to have an effect on the glass transition temperature in Polymethylmethacrylate (PMMA),^[10] which could indicate an effect on the crystallization kinetics as well.

In this chapter are reported some serendipitous findings of the interaction of 10 keV X-ray photons with a lithium disilicate ($\text{Li}_2\text{Si}_2\text{O}_5$) glass. The crystallization kinetics of this type of glass is widely studied through the years, and it is believed that crystallization is homogeneous throughout the bulk of the material^[11]. The idea of the experiment was to

subject the sample to two-step heat treatment in which the first step would induce the crystallization nucleation centres and the second, higher temperature treatment, would allow the nucleation centres to develop into crystallites. By performing combined SAXS/WAXS experiments, one can gain insights into the growth of the particles and the crystalline volume fraction. In this way, the crystallization kinetics can be studied with, for instance, Avrami type methods^[12] provided that the sample temperature is homogeneous and the newly formed crystallites are randomly oriented to avoid texture effects. In the case that texture due to surface crystallization exists, kinetic studies are more difficult because the texture degree might not remain the same during the experiment, and therefore one would observe peak intensity variations due to both growth as well as changing texture with little hope of being able to deconvolute the two effects^[4, 13].

There are commercial materials on the market, Fotoform and Fotoceram, which are based on $\text{Li}_2\text{Si}_2\text{O}_5$ that can be crystallized by exposure to ultraviolet radiation. However, a prerequisite for this behaviour is that the glass is doped with both Ce as well as Ag^[14]. The mechanism involved is that upon irradiation the Ce releases electrons, which subsequently reduce the Ag to a metallic state. Upon raising the temperature the Ag atoms become mobile and form metallic clusters, which in turn acts as the nucleus for the $\text{Li}_2\text{Si}_2\text{O}_5$ crystal to grow. In this work, crystallization studies of pure $\text{Li}_2\text{Si}_2\text{O}_5$ without any dopant are reported.

6.3 Aims of the work

The aim of this work is to investigate effects of exposure to a 10 keV monochromatic beam on lithium disilicate glass which was subjected to different treatments during on-line experiments. For this, high resolutions powder diffraction (HRPD) and scanning electron microscopy (SEM) is used. To avoid uncertainty regarding contamination of samples by Pt and Au, X-ray absorption spectroscopy (XAS) measurements in fluorescence geometry are carried out. In addition, the photon flux and an adiabatic temperature rise are calculated.

6.4 Experimental part

$\text{Li}_2\text{Si}_2\text{O}_5$ glass was prepared by batch melting (1 kg batch) of high-purity Li_2CO_3 and SiO_2 reagents in Pt crucible at 1550°C for 6 h. The melt was poured on graphite to form 0.5 cm thick patty that was subsequently annealed at 450°C for 30 minutes and cooled down to room temperature by shutting off the furnace power. The patty was stored in a desiccator. Several plates of dimension 0.2 x 1.0 cm were cut from this patty using a Buehler diamond saw. Thin platelets (100 μm) were cut, and the surfaces were slightly polished using SiO_2 as polishing powder (SPL, Zaandam, Netherlands) to remove any inhomogeneity, which could act as surface nucleation centres. Because this material is slightly hygroscopic, care was taken to store the materials in a desiccator and to perform both the cutting as well as the polishing water free. Samples for this study were prepared at University of California (S. Sen).

Fluorescence XAS measurements at the Pt L-edge and Au L-edge using a 9-element Ge detector were performed at DUBBLE (BM26A) at the European Synchrotron Radiation Facility (ESRF) to establish contamination levels due to materials from crucibles used for the sample preparation becoming incorporated into the sample. Concentration of Pt and Au in the sample was below the detectable level of the detector ($<100\text{ppm}$), and therefore elemental contamination is assumed to be irrelevant for these studies.

SAXS/WAXS experiments were performed on BM26A at the ESRF^[15]. BM26A is designed as an EXAFS station but also has a SAXS/WAXS capability^[15]. The storage ring was operated in 7/8+1 filling mode with current between 160 and 200 mA at 6 GeV electron energy. Measurements were performed with monochromatic beam produced by Si(111) at energy of 10 KeV. The acquisition time for frames was set to 60 sec/frame. The full width beam spot on the sample was about 0.3 x 1.0 mm^2 (VxH), which was verified by measuring a beam mark on the green paper. In the vertical direction, there are no relevant intensity ‘tails’^[16].

For a typical experiment the average photon flux on the samples was 3.8×10^9 photons/sec ($E = 10 \text{ keV}$) from which around $(2.0 \pm 0.1) \times 10^9$ photons/sec were absorbed in the sample. The absorbed energy, W_{abs} , will only marginally increase the sample temperature in the irradiated spot at room temperature^[8, 17]. An upper limit of the

temperature increase due to the X-ray absorption can be determined by assuming that there is no heat exchange between the irradiated volume and the surrounding matrix. The heat capacity and density of the material are, respectively, $C_p \approx 200 \text{ J/g}\cdot\text{K}$ and $\rho \approx 2.47 \times 10^{-3} \text{ g/mm}^3$. The irradiated volume is $V_{\text{irr}} \approx 0.05 \text{ mm}^3$. With the measured photon energy (10 keV), photon flux, and absorption this leads to an adiabatic temperature rise (ATR).

Equation 6-1 *Adiabatic temperature rise*

$$ATR = \frac{1}{\rho V_{\text{irr}} C_p} \cdot W_{\text{abs}} \approx 1.4 \times 10^{-4} \text{ K/s}$$

During 3 hours nucleation heat treatment, the temperature will therefore rise at most 1.5° K.

The glass samples were mounted on the beam line in a ‘cage furnace’ in order to avoid temperature gradients over the sample^[18]. In this furnace, the samples are positioned with a slight angle with respect to the direct beam. Therefore, the vertical beam footprint is about 25% larger than the actual vertical beam size. The temperature was measured by a Pt-Rh thermocouple placed close to the actual sample. The samples were subject to a two-step heat treatment on-line, that is, the Tammann method^[19]. The first nucleation induction step of three hours was carried out at $450 \pm 2^\circ\text{C}$. The temperature was reached within 30 min at rate $15^\circ\text{C}/\text{min}$. During this period, the samples absorbed a total radiation dose of $4.3 \times 10^{13} \text{ photons/mm}^2$. No crystallization occurred during this initial thermal treatment. The second (crystallisation) step was at a higher temperature ranging between experiments from 560 ± 2 to $650 \pm 3^\circ\text{C}$. The duration of the second step was determined by a combination of the temperature and the storage ring operation schedule. 10 hours at 650°C (fully crystallized, LidiSi-1); 5 hours at 620°C (not fully crystallized, LidiSi-2); 4 hours at 600°C (not fully crystallized, LidiSi-3); 10 hours at 580°C (LidiSi-4); 12 hours at 560°C (LidiSi-5).

The use of the combined SAXS/WAXS set-up with the high temperature furnace does not guarantee a sufficiently accurate sample positioning with respect to the curved Inel detector. After being cooled, the samples were re-measured at room temperature on the Swiss-Norwegian beam line (BM1A) at the ESRF using a MAR345 image plate detector with a monochromatic beam ($\lambda = 0.7955 \text{ \AA}$). The sample–detector distance was 1968 mm. The X-ray beam size was set to $500 \times 500 \mu\text{m}$ (V x H). With this beam size, it was possible to obtain diffraction data from both the areas exposed to X-rays during the on-line experiments as well as from non-exposed areas. Each pattern was collected during 5 second exposure. Analyses of diffraction data were carried out using FULLPROF software^[20]. The input parameters for the Rietveld refinement were based on the atomic coordinates determined from diffraction data for $\text{Li}_2\text{Si}_2\text{O}_5$ by de Jong^[21]. From least-squares fittings was found that peak shapes can be the best described by pseudo–Voigt function^[22]. Only unit cell parameters, the overall Debye-Waller factor parameter and crystalline size were refined. In the case of XRD data for samples that were not exposed to X-ray beam during pre-heat and crystallisation, a good fit was obtained only when the structure was compress along [001] direction. Therefore, the March function^[23] was used to correct intensities for the preferred orientation in Debye–Scherrer geometry.

Scanning Electron Microscopy (SEM) images were taken with fully digital field-emission LEO Gemini 1530 (Carl Zeiss SMT) Scanning Electron Microscope using an acceleration voltage of 20 keV. For the SEM sample preparation, the platelets were embedded in epoxy and subsequently cut with a diamond saw. The cross sections of the platelets were studied.

6.5 Results and discussion

It should be remarked that no evidence for crystal formation was found in the samples during the initial nucleation heat treatment at 450°C . In all cases, crystallization only started when the sample were brought to the higher crystallization temperature.

When the samples were removed from the sample holder after the experiments, an obvious coloration showed where the sample was exposed to the X-ray beam. The samples had lost transparency and, depending on the exposure time, became ‘frosty white’, as shown in Figure 6-1. This white area was in the vertical direction on either side around 200 μm larger than the footprint of the X-ray beam on the sample. In the vertical direction, the intensity in the beam ‘tails’ is known to be negligible and does not extend beyond 10 μm ^[16]. In the horizontal direction, there is hardly a discoloration beyond the area exposed to the beam. At the position where the X-ray beam has hit the sample, the affected area is around 15 μm larger than the actual X-ray footprint, which is consistent with the extent of the beam ‘tail’ in this direction.

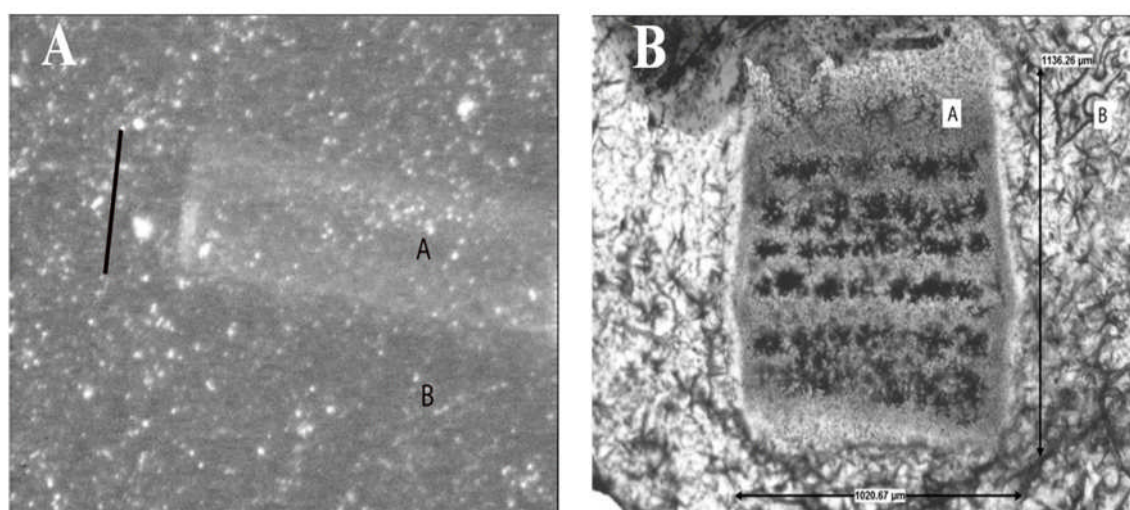


Figure 6-1 *Optical microscopy from samples exposed to a 0.4 x 4.0 mm² (panel A) and a 0.4 x 1.0 mm² sized X-ray beam (panel B). Panel A (left hand side) shows a not fully crystallized sample (heat treatment like sample LidiSi-3), panel B (right hand side) shows LidiSi-1 (fully crystallized). Only the central part of the areas marked ‘A’ in both panels have been exposed to the beam during the crystallization experiment (vertical direction). The areas marked ‘B’ have not been exposed to the direct beam. The black bar in panel A is 1 \pm 0.05 mm in length.*

It is not uncommon that solid state samples that have been kept at elevated temperatures on a synchrotron beam are discoloured at the position where the sample intercepts the X-ray beam. Oxidation effects can possibly play a role here, and it is generally assumed

that these are surface effects, while the bulk of the material is not altered. However, there is an unexpected finding here in that the affected area ($\sim 1000\mu\text{m}$) is larger than the actual X-ray beam footprint on the sample ($\sim 400\mu\text{m}$) in the vertical direction. This is the case for both the fully as well as the partially crystallized samples. In the horizontal direction, the discoloured region is commensurate with the beam footprint. This has been verified by repeating the experiment with different horizontal slit settings while subjecting the samples to a heat treatment like sample LidiSi-3.

To establish if there are any structural differences between the exposed and non-exposed parts of the samples, scanning electron microscopy (SEM) on a cross cut through a not exposed part of the LidiSi-3 sample were performed. This sample should according to the heat treatment be only partially crystallised. In this sample, the presence of a textured surface layer is observed, as shown in Figure 6-2. $\text{Li}_2\text{Si}_2\text{O}_5$ is a material that is supposed to exhibit bulk crystallization in preference over surface crystallization, but this finding is reproducible over several samples. The occurrence of the surface crystallisation is not uncommon in this type of experiment. In the bulk of the not fully crystallized sample, small droplets of around $1\mu\text{m}$ can be seen. On the basis of known bulk crystallization rates^[24], these are assumed to be small crystallites, although the required sample treatment to prove this by either X-ray or electron diffraction would be difficult and beyond the scope of this work.

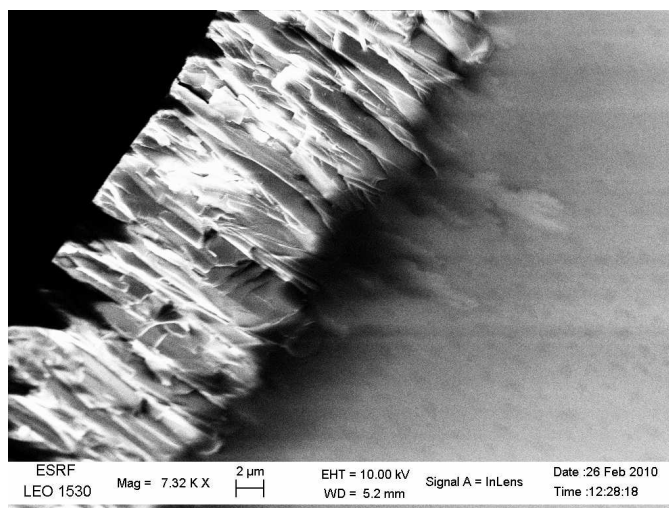


Figure 6-2 SEM micrograph of a freshly cleaved LidiSi-3, which has not been exposed to the X-ray beam. The black area is the epoxy in which the sample was embedded. A textured surface layer is observed. In the bulk, small fairly monodisperse droplets can be seen. These are assumed to be homogeneously nucleated bulk crystallites.

There are two striking differences, when the SEM micrographs (Figure 6-3) of sample of the ‘exposed’ with the ‘non-exposed’ areas are compared. ‘Exposed’ in this context means ‘exposed to X-rays during both the nucleation as well as the crystallization heat treatment’. The surface layer that is observed in the non-exposed area is much reduced in size or even completely absent in the exposed area. The second difference is that the morphology in the non-exposed area is coarser as compared to the exposed area. The average crystallite size is estimated to be roughly twice as large.

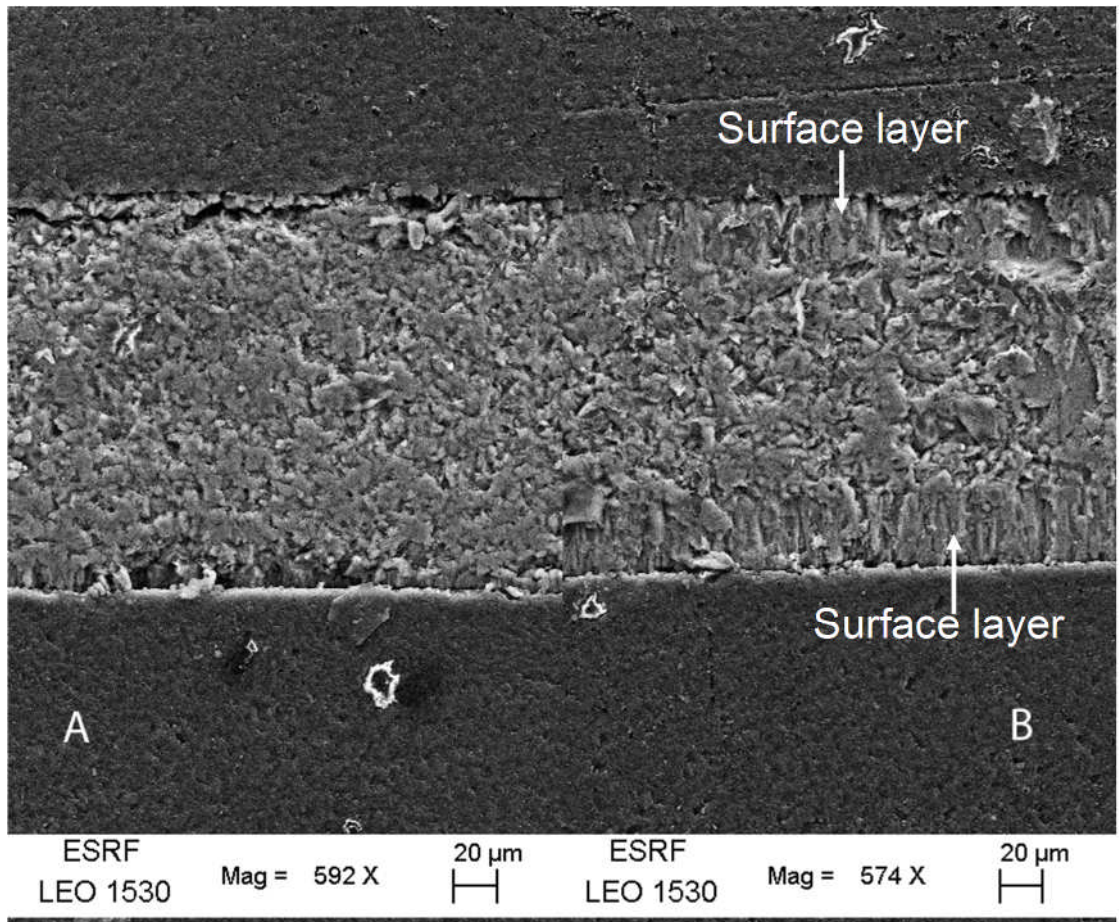


Figure 6-3 SEM micrographs of the cross section of an area exposed to X-rays during the on-line experiment (panel A) and a non-exposed area (panel B) for LidiSi-5 embedded in epoxy (dark regions top and bottom of figure). The surface layers in the non-exposed sample are indicated by arrows. In the exposed area, there is hardly any evidence of a surface layer and the morphology is finer.

In order to eliminate any uncertainty, a SEM micrograph for LidiSi-2 from the transition zone of the exposed to non-exposed area has been obtained. This is shown in Figure 6-4. From this result can be concluded that the influence of the X-rays is not limited to the surface but that the bulk of the material is also altered.

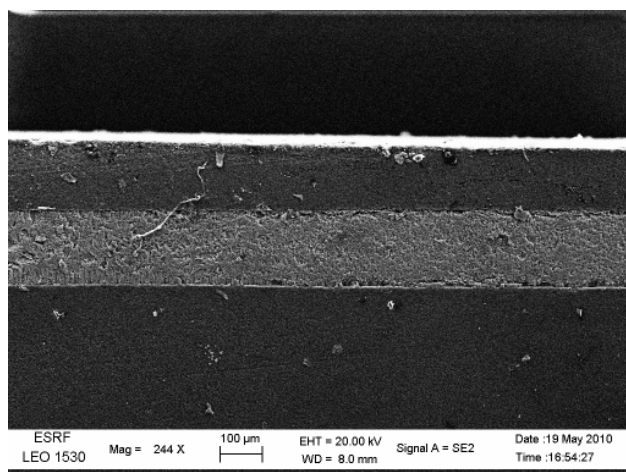


Figure 6-4 SEM micrograph of LidiSi-5 of the transition region between the non-exposed region (marked A) towards the exposed area (marked B). The non-exposed area clearly shows the surface layer and the coarse morphology, while in the exposed area the surface layer is absent and the morphology is finer.

Powder diffraction patterns of all samples both from the exposed as well as the non-exposed sample areas were obtained. An example of patterns from LidiSi-2 that was not yet fully crystallized before the experiment was terminated is shown in Figure 6-5, where panel ‘A’ shows the diffraction pattern from a sample area which has been exposed to the X-ray beam and ‘B’ corresponds to a non-exposed area.

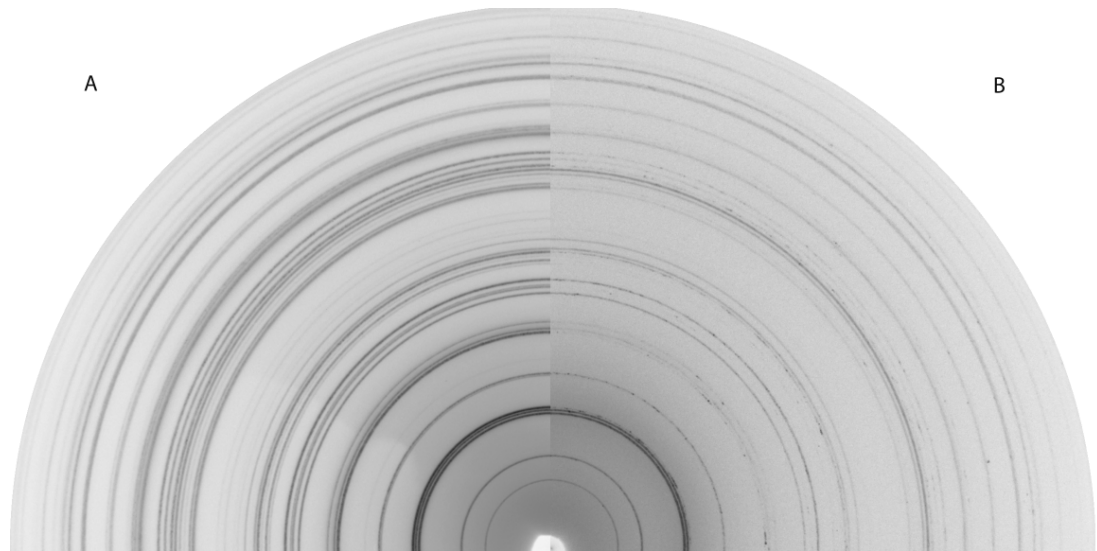


Figure 6-5 *The two dimensional diffraction patterns from a not fully crystallised sample (LidiSi-2) for the area exposed to the X-rays during the experiment (panel A) and the non-exposed area (panel B). The irregular radial intensity in panel B is typical for coarse grained samples.*

In the area that was exposed to the X-rays during the experiment, one finds a regular powder pattern without the irregular intensity variations that occur in samples that consist of coarse grains in which too few grains have been exposed to the X-ray beam to generate a fully isotropic pattern. However, for the same sample in a region not exposed to the X-rays during the experiment a rather irregular radial intensity distribution is found, which is indicative of coarse crystals. In the non-exposed area, there is also an absence or severe intensity reduction in a number of diffraction peaks. This indicates the existence of crystallographic texture in the sample.

A radial integration will obviously not render accurate intensities in the case of the textured pattern. However, this can still be used for unit cell determinations. Since this sample was not fully crystallized, there is still scattering intensity remaining from the amorphous glass. In Figure 6-6, the result of a radial integration is shown.

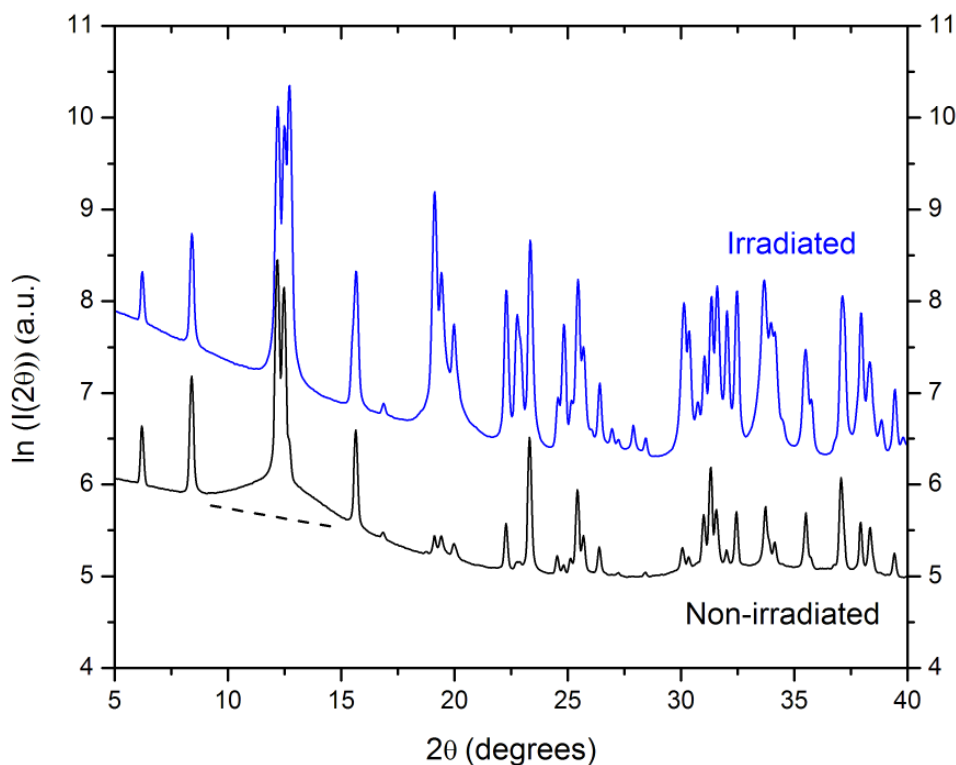


Figure 6-6 Powder diffraction data from the non-exposed area (black curve) around $2\theta = 12^\circ$ scattering intensity is observed, which is due the amorphous halo (the dotted line is a guide to the eye). This intensity is absent in the curve taken in the exposed area (blue curve). The X-ray wavelength used was $\lambda = 0.7955 \text{ \AA}$.

In the diffraction pattern of the non-exposed area, remnants of the scattering halo due to the amorphous glass are found, which is consistent with the degree of crystallisation that should have developed due to the thermal treatments. However, in the diffraction pattern obtained from the exposed area, this halo is absent. In fully crystallized samples, the amorphous halo is completely absent in both the exposed and non-exposed areas. From these observations, the conclusion can be drawn that inside the exposed area the crystallization progresses faster than outside the exposed area.

The powder diffraction unit cell characterization showed no difference between regions that that were grown whilst irradiating or in the absence of the beam but confirmed the presence of a single crystalline phase. Therefore, the surface layer crystallizes in the same phase as the bulk even though the morphology appears to be different. The room temperature parameters of this crystalline phase are: orthorhombic, space group $Ccc2$,

$a = 5.8299 \pm 0.0005 \text{ \AA}$, $b = 14.6012 \pm 0.001 \text{ \AA}$, $c = 4.7832 \pm 0.0005 \text{ \AA}$. A typical fit to diffraction data of LidiSi-1 using the Rietveld refinement with input parameters based on the atomic coordinates derived by de Jong et.al.^[21] is depicted Figure 6-7.

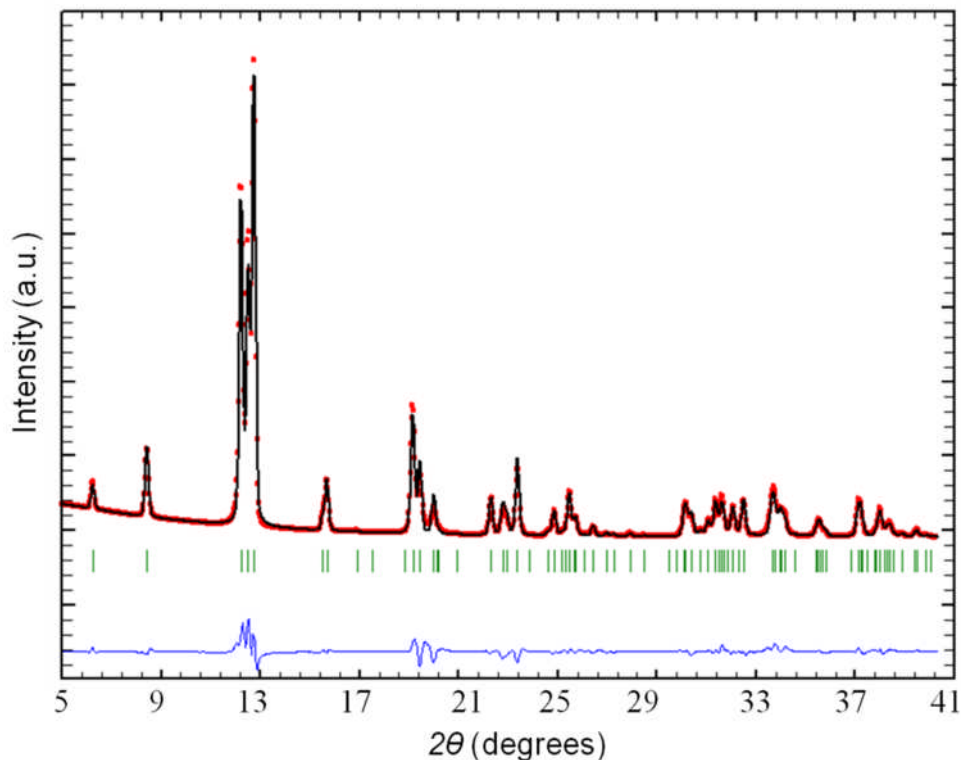


Figure 6-7 An example of Rietveld refinement plot of XRD data in this case for LidiSi-1, using the atomic coordinates derived by de Jong et.al.^[21], Ccc2 space group. An observed (black curve) and calculated (red curve) and difference profiles (blue curve) along with green lines indicating position of Bragg peaks are shown.

A further investigation was made on samples that were non-exposed, only exposed during the crystallization heat treatment, and a sample that was exposed during both the pre-heat as well as the crystallization treatment. The results of this is given are given in Figure 6-8 in which the respective diffraction curves are shown. In this figure, the peak intensities are normalized on the 130 diffraction peak. In the inset in the figure, a systematic intensity decrease can be seen in the 040 and 111 diffraction peaks. The curve related to the nonexposed area has the lowest intensity, while the pattern corresponding to an area that was irradiated during both the nucleation as well as the

crystallization heat treatment has diffraction intensities, which compare well with the powder diffraction data that are found in the literature^[21].

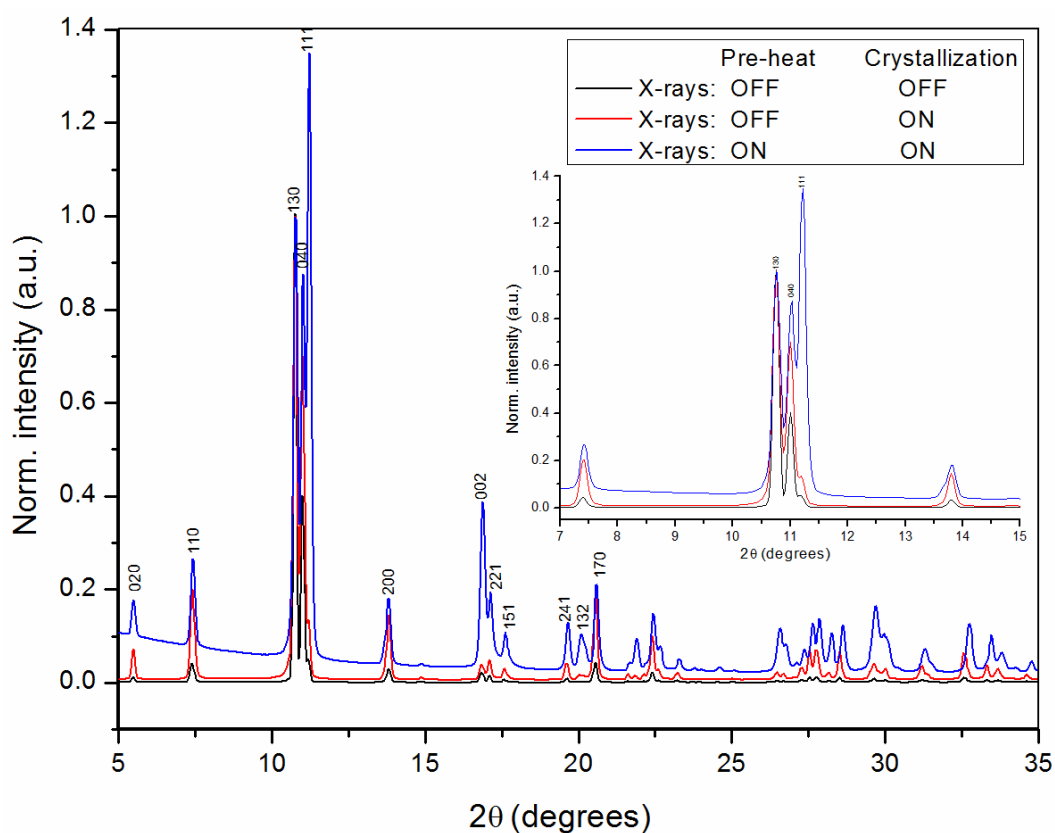


Figure 6-8 Powder diffraction data comparisons between samples areas exposed to X-rays at different stages of the thermal treatment. The peak intensities are normalized on the 130 diffraction peak. The inset shows a magnified range where weaker 040 and 111 peaks are observed in the diffraction curves for the areas that were less or not exposed to X-rays during the experiment.

In Table 6-1, the results of the Rietveld refinement are shown as obtained with the software package Fullprof^[20]. The March function^[25] implemented in FULLPROF is used to correct intensities for the preferred orientation in Debye–Scherrer geometry and renders the March parameter G_I^{-2} value equal to 1 means perfect isotropic powder, <1 can in this case be related to the ‘platy’ morphology and >1 indicates the presence of texture. The degree of texture, η , can be determined from the March parameter^[26].

Table 6-1 March parameter G_I^{-2} and the degree of the texture η as a function of the exposure to X-rays during the two step thermal treatment. The columns ‘pre-heat’ and ‘crystallization’ indicate if the sample was exposed to the radiation during these thermal stages.

X-rays		G_I^{-2}	η (%)
pre heat	crystallization		
on	on	0.93 ± 0.02	4
off	on	1.13 ± 0.02	7
off	off	2.06 ± 0.07	40
on	off	Not performed	

The relevance here is not so much the actual degree of texture but the presence or absence of texture as function of the exposure to the X-ray beam. It should not be forgotten that the samples were platelets, but from these results it is clear that the samples that were exposed to the X-rays during both the pre-heat treatments as well as the crystallization treatment have a ‘platy’ type of morphology, which is in agreement with earlier findings^[27]. The samples that were only exposed during the crystallization have a somewhat textured morphology, and the samples that were not exposed to X-rays are rather heavily textured.

The morphology of $\text{Li}_2\text{Si}_2\text{O}_5$ glass that is subjected to a two-step heat treatment is found to be different as function of exposures to X-rays during the different steps. In the case that the sample is not exposed, a surface layer and a bulk morphology with coarse crystallites is formed, which is heavily textured. If the same sample is exposed to the X-rays only during the crystallization step but not during the nucleation step, a lighter textured morphology is obtained. The most interesting phenomenon is found when the sample is exposed both during the nucleation as well as the crystallization step. Then, an isotropic diffraction pattern is found with the earlier reported ‘platy’ morphology^[21]. There is also a marked difference in the amorphous glass content of samples that have been allowed to partially crystallize. The degree of crystallinity in the exposed areas of such samples is higher than that in the non-exposed areas. Because of a lack of samples in the batch that have been used, it has not been possible to study samples that were

only exposed during the nucleation heat treatment. From this data, it is clear that the X-rays influence the crystallization process. The fact that one finds a finer morphology and a faster crystallization rate when the sample is exposed during the nucleation heat treatment provides strong evidence to an increase in the number of crystallization nucleation sites that are being created in this step. What exactly the mechanism is by which this takes place is unclear. It has been reported that photoluminescence can be induced in $\text{Li}_2\text{Si}_2\text{O}_5$ after exposure to low energy X-rays but^[28], however, no influence on structure formation has been observed.

It has been found that in mechanically stressed amorphous BaTiO_3 films nonthermal crystallization occurred upon exposure to rather high doses of 24 keV X-rays^[8]. The authors explain this by an increase of the thermal vibration energy due to interactions with energetic photo electrons. This could increase the hopping probability, of especially the lighter atoms present in the sample. However, in the BaTiO_3 case, the effects were confined to the surface and to the area directly exposed to the X-rays. However, the recoil energy transmitted by the electrons is still rather low, and electronic excitations (photo excitation and subsequent Auger decay) might play a much more important role. Noteworthy, these processes are known to be the main contributor for X-ray induced atom or ion desorption from surfaces.

Studies of crystalline materials with amorphous zones created by ion implantation irradiated by low energy electrons have shown that even far below the energy required to induce atomic displacements it is possible that recrystallization is induced. Interactions that create dangling bonds are sufficient and do not have to be supported by kinetic energy transfer from either the photons or electrons to allow migration of atomic species^[29]. This is a plausible explanation for the phenomena that is observed with respect to the increased crystallisation.

In the optical microscopy data, it is found that the spot affected by the X-ray beam is substantially larger than the size of the beam itself. An area with the same horizontal size as the X-ray beam footprint but extending around $125\mu\text{m}$ in the vertical direction on either side of the directly irradiated region is discoloured and has the same fine morphology as the area directly exposed to the X-ray beam. It is worth noting that no sizeable extension is observed in the horizontal direction. The path length of both

elastically as well as inelastically scattered electrons in the solid state is at most some micrometers and therefore not sufficient to explain the rather large extension in the vertical plane. A possible explanation can possibly be found in the fact that synchrotron radiation is polarized in the horizontal, that is, electron orbit, plane. Both elastically as well as inelastically scattered photons will scatter in the vertical direction. The scattered photons will have an energy distribution with a maximum of the original 10 keV photons energy and, assuming a density of 2.35 g/cm^3 for the glass, an attenuation path length of around $275 \mu\text{m}$ in this sample. Photons that are initially inelastically scattered will have a shorter range. Photo electrons can be created anywhere in the volume throughout which the X-rays are scattered so that the nucleating effects do not have to remain confined to the direct exposed area of the sample.

The absence of a surface layer with a different texture but identical crystalline phase could also be explained in this scenario. Apparently surface nucleation is not completely irrelevant for these samples and has been observed by other authors as well^[30]. If the samples have been exposed to X-rays during the nucleation heat treatment, sufficient nucleation sites could have been formed throughout the sample and thus also near the surface, to ensure that the surface nucleation would become less important. A test of this hypothesis could be to expose a thick sample to the X-ray beam so that only a single surface of the sample platelet would receive sufficient flux.

6.6 Conclusion

The data that were collected on $\text{Li}_2\text{Si}_2\text{O}_5$ samples provides strong evidence that an exposure to monochromatic synchrotron radiation even from a bending magnet source increases the crystallization nucleation rate if the sample is exposed to the radiation during the crystallization experiment. This is a rather unexpected finding since in general one finds the effects of high flux X-rays to be destructive instead of inducing crystallization.

The crystallization progresses faster in regions that have been exposed to X-rays. The two explanations that are feasible are that the crystal nucleation rate is higher or that the

crystallization process itself is assisted by the X-rays. The latter option is rather unlikely, and the fact that a finer morphology in the samples is found where they have been exposed to X-rays favours the explanation that the nucleation sites are more abundant in the exposed area. What exactly the mechanism is that induces the nucleation is not clear at present, but local heating due to X-ray absorption and structural changes due to the kinetic energy of photoelectrons, created by absorption of the X-rays, can be ruled out. The most plausible explanation is that this is caused by the influence of the photo electrons on dangling bonds.

The experiments show that the effects due to radiation extend spatially well beyond the area directly exposed to X-rays in the direction at right angles to the X-ray beam polarization. The only explanation for the spatial extension of radiation effects beyond the directly exposed spot is that this is due to the absorption of X-rays that already have been scattered. The intensity of this scattered radiation is several orders of magnitude lower as compared to the direct beam, but when using a (medium intensity) beamline on a third generation synchrotron radiation source the number of scattered photons apparently is still numerous enough to interfere in a non-negligible way with the samples in both the solid as well as the liquid state.

The original aim of the experiment was to study the crystallization kinetics of lithium disilicate samples when subjected to a two-step heat treatment by on-line SAXS/WAXS experiments. This two-step treatment was intended to separate the nucleation events from the crystallization growth and induce heterogeneous nucleation in the bulk of the material. These results show that this approach for this particular glass can only be applied when care is taken to minimize the radiation dose and especially avoid the exposure to X-rays during the thermal treatment intended to induce crystallisation nuclei.

References

- [1] C. Nave and E. F. Garman, *Journal Of Synchrotron Radiation* **2005**, *12*, 257-260; E. F. Garman and S. M. McSweeney, *Journal Of Synchrotron Radiation* **2007**, *14*, 1-3.
- [2] R. Roots and S. Okada, *Radiation Research* **1975**, *64*, 306-320.
- [3] J. P. A. Fairclough, S. M. Mai, M. W. Matsen, W. Bras, L. Messe, S. C. Turner, A. J. Gleeson, C. Booth, I. W. Hamley and A. J. Ryan, *Journal of Chemical Physics* **2001**, *114*, 5425-5431.
- [4] W. Bras, S. M. Clark, G. N. Greaves, M. Kunz, W. van Beek and V. Radmilovic, *Crystal Growth & Design* **2009**, *9*, 1297-1305.
- [5] R. J. Davies, M. Burghammer and C. Riekkel, *Macromolecules* **2008**, *41*, 7251-7253.
- [6] J. G. Mesu, A. M. J. van der Eerden, F. M. F. de Groot and B. M. Weckhuysen, *Journal of Physical Chemistry B* **2005**, *109*, 4042-4047.
- [7] G. Susich, A. O. King and L. M. Dogliotti, *Science* **1959**, *130*, 567-568.
- [8] Y. Feldman, V. Lyahovitskaya, G. Leitus, I. Lubomirsky, E. Wachtel, V. A. Bushuev, G. Vaughan, Z. Barkay and Y. Rosenberg, *Applied Physics Letters* **2009**, *95*, 3.
- [9] H. G. Cui, E. T. Pashuck, Y. S. Velichko, S. J. Weigand, A. G. Cheetham, C. J. Newcomb and S. I. Stupp, *Science* **2010**, *29*, 555-559.
- [10] H. R. Keymeulen, A. Diaz, H. H. Solak, C. David, F. Pfeiffer, B. D. Patterson, J. F. van der Veen, M. P. Stoykovich and P. F. Nealey, *Journal of Applied Physics* **2007**, *102*, 013528
- [11] A. L. Greer and K. F. Kelton, *Journal of the American Ceramic Society* **1991**, *74*, 1015-1022; V. M. Fokin, E. D. Zanutto, N. S. Yuritsyn and J. W. P. Schmelzer, *Journal of Non-Crystalline Solids* **2006**, *352*, 2681-2714; P. F. James, *Physics and Chemistry of Glasses* **1974**, *15*, 95-105.
- [12] H. Bamford and C. Tipper, *In Comprehensive chemical kinetics*, Elsevier, New York, **1980**, p. 41-113.
- [13] W. Bras, G. N. Greaves, M. Oversluizen, S. M. Clark and G. Eeckhaut, *Journal of Non-Crystalline Solids* **2005**, *351*, 2178-2193.
- [14] V. P. Veiko, Q. K. Kieu, N. V. Nikonorov, V. Y. Shur, A. Luches and S. Rho, *Applied Surface Science* **2005**, *248*, 231-237.
- [15] S. Nikitenko, A. M. Beale, A. M. J. van der Eerden, S. D. M. Jacques, O. Leynaud, M. G. O'Brien, D. Detollenaere, R. Kaptein, B. M. Weckhuysen and W. Bras, *Journal of Synchrotron Radiation* **2008**, *15*, 632-640.
- [16] R. van Silfhout, A. Kachatkou, N. Kyele, P. Scott, T. Martin and S. Nikitenko, *Optics Letters* **2011**, *36*, 570-572.
- [17] A. C. Cheng and M. Caffrey, *Biophysical Journal* **1996**, *70*, 2212-2222.
- [18] A. J. Dent, M. Oversluizen, G. N. Greaves, M. A. Roberts, G. Sankar, C. R. A. Catlow and J. M. Thomas, *Physica B* **1995**, *209*, 253-255.
- [19] G. Tammann, *Zeitschrift fur Physikalische Chemie* **1898**, *28*, 441-479.
- [20] J. Rodriguezcarvajal, *Physica B* **1993**, *192*, 55-69.
- [21] B. De Jong, H. T. J. Super, A. L. Spek, N. Veldman, G. Nachtegaal and J. C. Fischer, *Acta Crystallographica Section B-Structural Science* **1998**, *54*, 568-577.
- [22] P. Thompson, D. E. Cox and J. B. Hastings, *Journal of Applied Crystallography* **1987**, *20*, 79-83.
- [23] C. J. Howard and E. H. Kisi, *Journal of Applied Crystallography* **2000**, *33*, 1434-1435.
- [24] P. C. Soares Jr, E. D. Zanutto, V. M. Fokin and H. Jain, *Journal of Non-Crystalline Solids* **2003**, *331*, 217-227.

- [25] W. Dollase, *Journal of Applied Crystallography* **1986**, *19*, 267-272.
- [26] E. Zolotoyabko, *Journal of Applied Crystallography* **2009**, *42*, 513-518.
- [27] D. U. Tulyaganov, S. Agathopoulos, I. Kansal, P. Valerio, M. J. Ribeiro and J. M. F. Ferreira, *Ceramics International* **2009**, *35*, 3013-3019.
- [28] A. Doi, *Japanese Journal of Applied Physics* **1978**, *17*, 279-282.
- [29] I. Jencic, M. W. Bench, I. M. Robertson and M. A. Kirk, *Journal of Applied Physics* **1995**, *78*, 974-982; J. Frantz, J. Tarus, K. Nordlund and J. Keinonen, *Physical Review B* **2001**, *64*.
- [30] L. L. Burgner, M. C. Weinberg, P. Lucas, P. C. Soares and E. D. Zanotto, *Journal of Non-Crystalline Solids* **1999**, *255*, 264-268.

Chapter 7 Conclusion and future work

The work presented in this thesis is primarily focused on the characterization of multicomponent metal oxides, in particular, Bi_2MoO_6 , $\text{Fe}_2\text{O}_3/\text{Cr}_2\text{O}_3$, CoAlPO-18 and CoAlPO-34 along with $\text{Li}_2\text{Si}_2\text{O}_5$. A variety of synchrotron radiation based techniques were employed, in particular, X-ray Absorption Spectroscopy (XAS), near edge structure (XANES), extended fine structure (EXAFS) and X-ray Diffraction (XRD). In addition to these synchrotron techniques, the development of the Energy Resolved Electron Yield (EREY) XAS technique has been extended.

From the work presented in Chapter 3, it has been shown that the combination of High Resolution Powder Diffraction (HRPD) with Raman and XANES in a single experiment is a powerful tool for understanding the formation of Bi_2MoO_6 from an amorphous gel under mild hydrothermal conditions. The data from the HRPD experiments demonstrated that the formation of Bi_2MoO_6 takes place in two steps, starting with the formation of Bi_2O_3 particles followed by the growth of highly anisotropic Bi_2MoO_6 platelets. Using XANES and Raman spectroscopy, it was possible to follow the phase transformation of tetrahedrally coordinated molybdenum species present in the initial gel. These were gradually transformed to have octahedral coordination upon the reaction completion. In addition, independent *in-situ* EXAFS/XRD experiments performed under identical conditions confirmed the presence of molybdenum species randomly distributed in the Bi_2O_3 matrix and their ordering during the crystallization process.

A new approach for deriving the reaction kinetics using the XAS pre-edge intensity is presented and verified using data from the Bi_2MoO_6 experiments. Using this method, the growth of Bi_2MoO_6 crystallites from an amorphous gel was found to be three dimensional and phase boundary controlled. This growth mechanism is in good agreement with HRPD and SEM data, which confirmed the presence of spherical particles in the initial stages of the reaction.

The results presented in this chapter demonstrated that combined time-resolved *in-situ* experiments are advantageous for understanding the structure formation process of

materials. Such determinations are crucial for engineering new crystalline materials with properties tailored to specific chemical processes.

Therefore, in the future it would be interesting to prepare and investigate the structure of Bi_2MoO_6 doped with metal cations such as Co^{2+} , Ni^{2+} , Fe^{3+} . Another interesting area of research would be to look at the structure of multi-component Bi_2MoO_6 catalysts, prepared through the incorporation of phases such as cobalt molybdate and iron molybdate (which were successfully synthesised using the hydrothermal method). However, due to the limited time allotted to this project, it was not possible to prepare multi-component Bi_2MoO_6 catalysts. By understanding the structural properties of multi-component bismuth molybdate catalysts (in particular, the local structure of transition metals), one can determine how each constituent of the catalyst influences the catalytic function. In addition, it is possible to investigate the placement of the transition metals within the matrix during on-line catalytic reactions using the high pressure gas rig described in Appendix A. Appendix A also includes a description of a possible future study on the preparation of a Bi_2MoO_6 catalyst using a steam assisted synthesis method.

In Chapter 4, a combination of techniques was employed to establish the nature of chromium species in the bulk and near surface of chromium doped iron oxide catalyst. The experiments (XPS, EXAFS, XRD and chemical analysis) on the pre heat treated catalysts provided clear insight into the oxidation character of the chromium for samples in the range of 100-500°C. Also it was found that the different techniques demonstrated impressive agreement with each other, which served to validate both the results and the techniques themselves.

It has also been shown that either pre-edge peak analysis or principal component analysis of the XANES data in combination with modelling EXAFS data (to distinguish Cr^{6+} and Cr^{3+} oxygen bond distances) can provide good methods of analysing mixed oxidation states.

Due to the limited beam-time available for experiments, it was not possible to follow the structural changes during *on-line* calcination in air. Therefore, some follow up work is required to perform *in-situ* time-resolved XAS experiments. Since the high pressure

gas rig is in operation, it would also be of interest to look at the behaviour of chromium species during catalytic reactions under operando conditions. Lastly, it would be valuable to look at the local structure of a catalyst taken out from the reactor and compared to one taken during the start of the reaction.

The fifth chapter reports an experimental setup that is capable of measuring local structural parameters, while distinguishing between the near surface and bulk of a sample. This method known as EREY–XAS has been used to distinguish between framework and extra-framework Co^{2+} species in CoAlPO-18 and CoAlPO-34 catalysts. The results were compared with the bulk transmission data. The transmission EXAFS results showed that Co^{2+} ions are embedded in the porous structure at the tetrahedral sites of the catalysts. However, the EREY–XAS data did not provide any evidence of the presence of extra-framework Co^{2+} species in the near-surface region of the catalyst. This indicates that when isomorphly substituting Co^{2+} for Al^{3+} , ions are uniformly distributed at the tetrahedral sites of the AlPO-34 framework. In contrast, EREY–XAS results for CoAlPO-18 showed that a small number of Co^{2+} ions are located near the surface of the catalyst and act as extra-framework Co^{2+} i.e. the Co^{2+} ions are not substituting for Al^{3+} . This indicates that Co^{2+} ions form small cobalt oxide particles on the surface which do not influence the long range ordering of the structure as evidenced by XRD and transmission EXAFS, which confirmed the presence of tetrahedrally coordinated Co^{2+} ions in the AlPO-18 framework.

In order to get a deeper understanding of the behaviour of Co^{2+} ions in CoAlPO-18 and CoAlPO34 catalysts during activation, it is essential to obtain local structural information near to the surface and within the bulk. Comparison of the results for the as-prepared and activated catalysts will provide new insights about the relationship between structure and function.

Although this technique still has a long way to go before it will be routinely applied to XAS measurements, it is a promising method for structural studies on catalysts under real conditions at ambient pressures (for seeking information about the near-surface region). In addition, it can provide structural information when the conventional fluorescence and transmission method cannot be used e.g. in studies of thin films deposited on substrates, which are covered with a layer of metal (Ni) and overlaid with

metal oxide (NiO). Such samples are too thick for the transmission of the X-ray beam. Data obtained from fluorescence techniques most directly relates to the bulk (Ni). However, data suffers from severe self-absorption effects.

Though it was shown that it can be a useful tool in materials science, EREY–XAS data collection is still challenging compared to conventional XAS techniques, as shown in Chapter 5 in the HTS catalyst studies. Moreover, data reduction can now be carried out more easily because of newly developed software (Reduce) but it is still not straightforward. To summarize, this technique can be applied to ‘special’ samples which cannot be measured with traditional XAS techniques. To further develop the EREY–XAS technique, work is needed to improve the data quality, reduce the noise and to make the methodology more user-friendly for others to work with.

In the future, the ERAY–XAS method may be beneficial for investigating the interactions of inorganic materials with gas molecules.

Finally, an unexpected finding involving the interaction of a synchrotron X-ray beam with a sample is documented. In this instance, the effects of exposure to a monochromatic 10 keV X-ray beam on thermally induced crystallization of lithium disilicate glass were investigated. First, it was found out that an extended exposure during the nucleation heat treatment increased the number of nucleation sites. Second, it was observed that the effects extended far beyond the sample region that was directly exposed to the X-ray beam. The effects were confined to the direction perpendicular to the polarization of the synchrotron radiation beam. The effects could be attributed to a photo electron created not only by the direct X-ray beam but also by the scattered radiation thus extending the affected sample volume beyond the volume that is directly exposed to the X-ray beam.

Because of a lack of samples in the batch, it was not possible to study samples that were only exposed during the nucleation heat treatment. Accordingly, it would be interesting to perform these experiments, and obtain a complete picture of this phenomenon.

Another consideration is the effects on the samples of the X-ray beam itself. The effect could be investigated by exposing the samples to more intense X-ray beams, which can be provided by undulators.

Appendix A High pressure gas rig

The aim of the work is to use *in-situ* XAS/XRD techniques to understand the process that takes place during the steam assisted crystallisation. A series of multicomponent mixed metal oxide molybdate catalysts are used as a test materials. From this study a deeper understanding of structural modifications that take place during the growth process can be obtained and intermediate phases determined. In order to perform this study, the experimental setup had to be designed to be capable of delivering steam and gases at pressures in the range of 1 to 50 bars and temperatures from 25 to 240°C, i.e. a high pressure has rig.

In this new method for preparation of materials, solid precursors are formed from co-precipitating bismuth nitrate and ammonium heptamolybdate. The solid precursor is loaded into a capillary reactor. The steam is passed through the sample at temperatures between 200 and 240°C, thus converting the amorphous precursor to a crystalline solid over a period of time.

Due to the length of time for the project and unexpected problems at the beamline during beamtime, these *in-situ* experiments could not be performed. However, the high pressure gas rig that was installed on the beamline is in operation and routinely used for following catalytic reactions under real conditions. The project was jointly funded by DUBBLE and Dutch users.

Figure A shows a scheme of the high pressure gas rig which is permanently installed in the EXAFS experimental hutch (BM26A). The gas rig consists of two parts. The first part that is installed outside of the experimental contains:

- Two panels accommodating pressure controllers with gas cylinders support below
- Gas cabinet for toxic gases
- Flexible stainless steel hoses for connecting gas cylinders and pressure regulators
- 8 gas lines

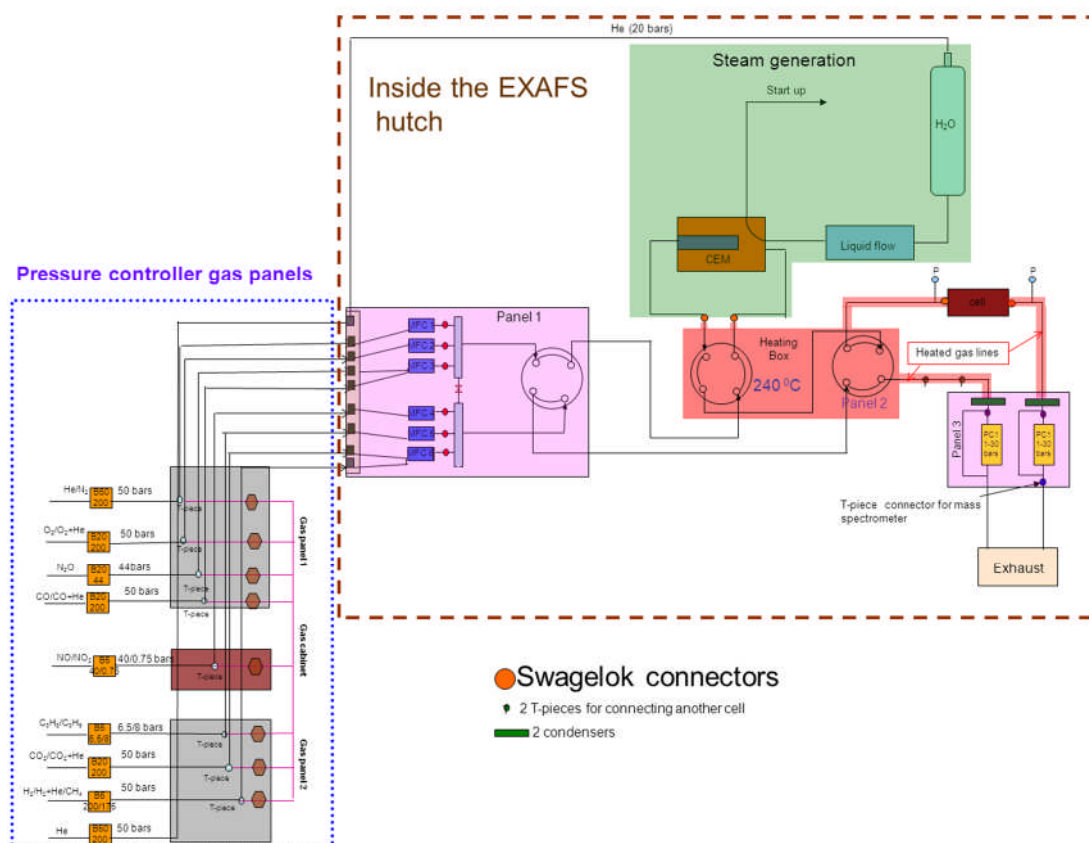


Figure A-1 The scheme of the high pressure gas rig built at DUBBLE.

The second part contains three panels that are installed inside the experimental hutch. Main components are manual valves, pneumatic valves, fast switching valves that can operate at temperatures of up to 240°C (Panel 2), 2 mixing cylinders, 6 mass flow controllers, 4 back pressure controllers and 2 condensers.

Panel 1 contains manual valves that are used for gas leak tests and maintenance. Pneumatic valves are used for safety and protection of Mass Flow Controllers (MFCs) as flow of the gas can be stopped remotely in case of unauthorised action. Mixing cylinders are filled in SiC powder to ensure good mixing of gases. The volume of each cylinder is 2ml.

Gas flow rates are controlled using six Brooks 5850A MFCs, with pre-programmed calibration curves for common gases (See Table A-1). If a MFC is operated with gas other than it was calibrated, new gas conversion factors have to be inserted. Each MFC has an option to enter a value of gas conversion factor manually, since all MFCs were

calibrated using N₂. It is worth noting that each MFC is calibrated to specific types of gases that are used so that high flow (1-100 ml/min), medium flow (1-30ml/min) and low flow (1-10ml/min) ranges are covered. The MFCs are organised into the group of three covering each flow range (see Panel 1 in Figure 1).

The 4-way fast switching valve is used for switching between gases. The benefit of using the 4-way fast switching valve is that one can rapidly switch between dry and wet gases. For instance, while a sample is pre-treated in dry gas during *on-line* reaction, the wet gas can be prepared using a second line bypassing a capillary reactor. If one works with steam, the gas lines towards the capillary reactor are heated using heating tapes up to 200°C in order to avoid condensation in the lines while working at high pressures. The sample in the capillary reactor is heated using a heating gun. The temperature is controlled using thermocouples at different points of the heating lines.

Panel 2 contains two 4-way fast switching valves which can operate at temperatures of 240°C. The second 4-way fast switching valve is connected to the steam generation system. The benefit is that mixture of steam and gas can be produced in a closed loop without interfering with the rest of the setup.

The third panel accommodates four Brooks 5866 pressure controllers which can accurately control the pressure of the flowing gas. They are calibrated in the ranges of 1 to 5 bars and 1 to 50 bars. They are connected to 4-way manual valves. The position of the valve selects whether the gas flows through one of the back pressure controllers or directly to exhaust. If steam is used, the gas has to pass through condensers to avoid condensation in the pressure controllers.

Pneumatic valves, MFC, 4-way fast switching valves, temperature settings for heating the lines and pressure controllers are operated remotely using specially developed software.

Table A-1 Gas flow rates achievable by MFCs calibration curves for various gases.

MFC	Gas or gas mixtures	minimum flow (mlN/min)	maximum flow (mlN/min)
MFC1	He	5	100
	N ₂	5	100
	O ₂	5	100
	O ₂ in He	5	100
	CO	5	100
	5- 10% CO in He	5	100
	CO ₂ in He	5	100
MFC2	O ₂	0.3	10
	5% -10% O ₂ in He,	1	30
	N ₂ O	0.3	10
	N ₂ O in He	1	25
MFC3	CO	0.3	10
	5% CO in He	1	25
	CO ₂	0.3	10
	CO ₂ in He	1	25
MFC4	NO	0.4	12
	NO ₂	0.3	10
	NO ₂ (0-10)% in He	1	25
MFC5	C ₃ H ₆	1	20
	C ₃ H ₈	1	20
	C ₂ H ₆	1	30
	C ₂ H ₄	1	30
	CH ₄	1	30
	(5-10)% H ₂ in He	1	25
	H ₂	0.3	12
MFC6	H ₂	5	100
	5-10 % H ₂ in He	5	100
	He	5	100
	N ₂	5	100

The steam generation system is shown in Figure 2. It contains a water storage tank, a flow control part and an evaporator unit.

The water storage tank contains distilled water which should be at a pressure of a few bars higher than the pressure required in the upstream system. The water flow from this tank is continuously measured by the Liquiflow which is connected to the E7000 unit. A control valve on top of the Controlled Evaporator Mixer (CEM) is subsequently activated in order to obtain the desired flow. Dry feed gas is added through the top of the CEM. Inside the CEM water is evaporated and mixed with the feed gas resulting in a continuous stream of the desired steam/gas mixture.

On the top of the water tank a three way valve is positioned with an open outlet. With this valve it is possible to depressurize the system and to purge air from the tank.

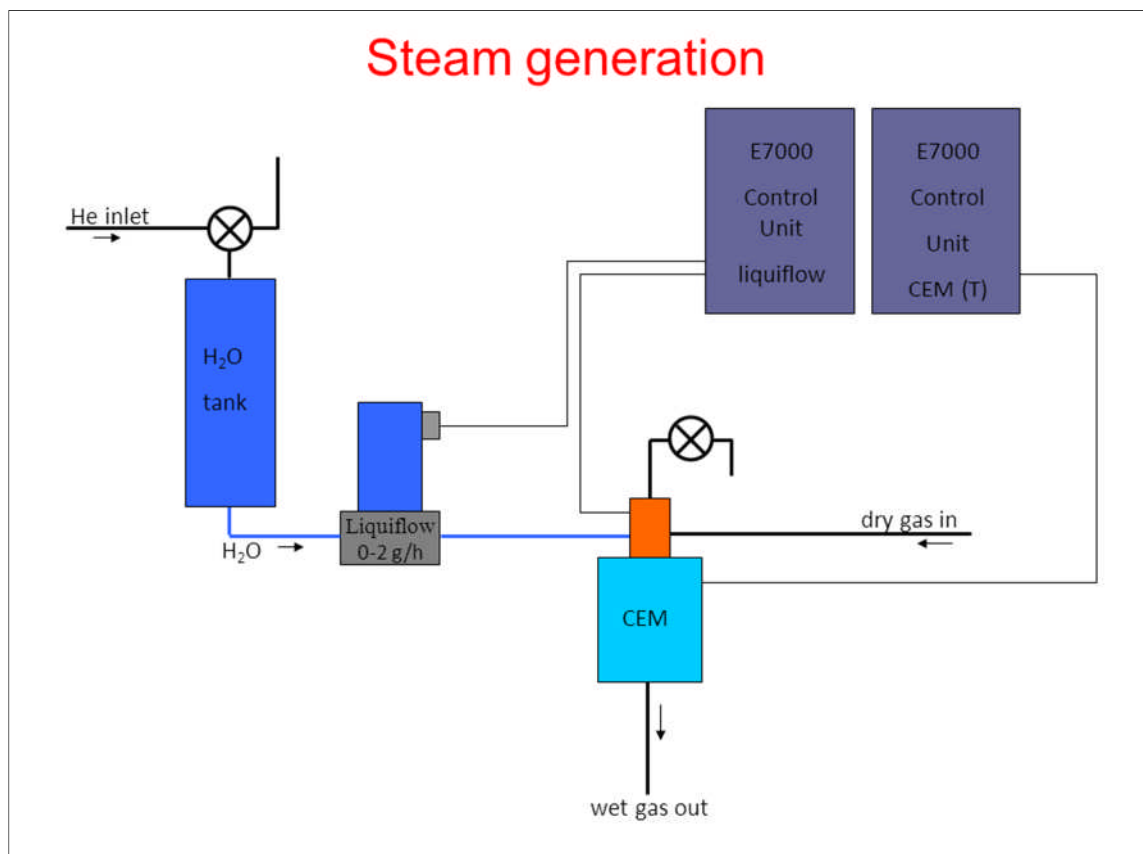


Figure A-2 Steam generation system (see text for further explanation).